A Physiologically Based Pharmacokinetic Model Study of the Biological Fate, Transport, and Behavior of Engineered Nanoparticles

by

Dingsheng Li

A dissertation submitted in partial fulfillment
of the requirements for the degree of
Doctor of Philosophy
(Environmental Health Sciences)
in the University of Michigan
2015

Doctoral Committee:

Professor Olivier J. Jolliet, Co-Chair
Professor Andrew D. Maynard, Co-Chair
Clinical Adjunct Professor Claude Emond, University of Montreal
Assistant Research Professor Masako Morishita
Associate Professor Patrick Nelson, Lawrence Technological University
Professor Margaret S. Wooldridge

Acknowledgement

This work marks the finishing line of my days as a student for the past 21 years, which is close to 80% of my entire life so far. Along all these years, there are many people I am thankful for their support. Without them, I wouldn't be able to see the results of my education crystallized in this thesis.

I start with my parents because, it is physiologically impossible for me to stand in front of the audience to defend my thesis if not for them giving me life nearly three decades ago. Of course, they have done much more for me. As my role models in life, they have taught me to be kind to others, patient with problems, perseverant in difficulties, and hopeful for future. My father being a Ph.D. himself also inspired me to pursue this degree near the end of my undergraduate study, just to be sure not to appear undereducated in front of him if not for anything else. My mother being a doctor infused me with interest of protecting people's health, which led me choosing environmental health sciences as my major.

There is a Chinese idiom, "一日为师，终身为父", which can be translated to something like "once a teacher, for life a father-figure". I think this fits perfectly well with my relationship with my advisor, Olivier Jolliet. Before I started my Ph.D. studies, I never thought there would be an advisor like him. Hours and hours we have spent in his office or mine discussing one question to another. I still remember once we started around 3 pm and finished close to 9 pm taking neither a break nor a bite. And I will never forget when I was pushing for this dissertation a few days before my Defense in the office, he came by at 11 pm, and worked with me on the problems I

had until 2 am in the morning. Curiosity for the unknown, passion for the answers, prudence for the results – I see these qualities essential for me becoming a scientist who may push the boundaries of our knowledge one day in him. I also learned that, I should probably work out more in order to have the stamina he still possess now in his 50s and surviving his illness when I may be the advisor to my Ph.D. students sometime in the future.

I may not be that interested in science if not for my undergraduate advisor, Prof. Mei Li (李梅). It was she who showed me the way of scientific research in my junior year of college. She dispelled the mystical mist shrouding the laboratory for me and made me confident that I can make a scientific contribution to our field of studies. Under her supervision, I got the chance to have my first experience in carrying out a hypothesis orientated experiment and writing a scientific paper for publication. If Olivier is the one who guided me becoming a mature researcher, then Prof. Li is the one who led me on this path of scientific exploration.

I have also received tremendous help from a number of collaborators and friends for my Ph.D. thesis. As a novice of PBPK model four year ago, Claude Emond, Gunnar Johanson, and Ulrika Carlander taught me from the very basic physiology that I erred at the beginning such as not having the blood flow from the spleen going to the liver through portal vein. Gunnar also generously hosted me as a visiting researcher at the prestigious Karolinska Institutet during 2013, which then gave me a chance to tour Europe and feast my eyes in the summer. It was the collaborative effort from Margaret Wooldridge, Mohammad Fatouraie, Ethan Eagle, and James Barres that made the system generating those nanoparticles worked and well characterized after many glitches in different parts of that system. Masako Morishita, James G. Wagner, Kaitlin Cornwell, David Ciciora, Gina Sancricca, and Kathryn Thompson spent many

hours on collecting and analyzing the biological samples from the experiments again and again. Without these two groups of people, Chapter 3 would not exist in this thesis and it would be impossible for me to complete my work. Andrew Maynard served as the co-chair of my Ph.D. Committee and helped me appreciate the bigger picture of nanotoxicology and the challenges for assessing the health risks of nanoparticles. Patrick Nelson introduced me to many quantitative methodologies in PBPK model and other approaches in modeling the biodistribution of chemicals in the body.

Beyond my Ph.D. thesis, I am grateful for Chuanwu Xi, who helped me greatly in my career development and offered many invaluable advices when it comes to choosing my path after my Ph.D. Mark A. J. Huijbregts and Manuele Margni both acted as my mentor and helped me through critical phases of the projects I was working on during the time when Olivier was not available due to his illness.

I would also like to thank all the members of Olivier's group at University of Michigan, past and current, for supporting me and sharing happy moments together. Jinglan Hong was my first contact within the group and to Olivier when I was applying for graduate school. Shanna Shaked was my GSI when I took my course in Life Cycle Assessment and taught me this intriguing field attracted me here in the first place. As an expert of Matlab, Cedric Wannaz carefully designed mini-courses for us although I'm sorry to say that my brain didn't keep much of what he taught. Andrew Henderson and I worked on two other projects together and if I have to rate you on scale, you're definitely bacon. Yvan Wenger, although we never met in person, working on you legacy produced two papers for me and I truly appreciate your help when we were exchanging ideas over emails and Skype. Alexi Ernstoff edited the English of many papers written by Olivier and me – both non-native speakers. Susan

Csiszar lightened up our moods many times with her cute cute baby Toby. Karin Veltman and I shared joyful moments watching the demise of Joffrey Baratheon. Katerina Stylianou officially introduced my taste buds to authentic Greek food. Lei Huang and I came to this Department together in 2009 and we fought through the many mandatory courses for the first two years, and yes, I envy you for becoming a Dr. almost a year before me.

To my friends in China and elsewhere, I thank you all for your encouragements and supports for all these years. No matter you were there for my personal life or my academic studies. No matter if you cheered me on with words like “You can do it!” or taunted me with teases like “You’re never going to make it, told you so”, which only fueled me with more energy to keep on going.

Lastly, Qiu Qiu, during my final days writing this dissertation, some of our chats may have deprived me a few hours of much needed sleep. But if the clock can be turned, I would not choose otherwise and miss the happiness coming out from our conversations. Thank you for crossing those things off my wish list of what I wanted to do before leaving Ann Arbor with me and I can’t wait to cross many more things off our list in the future with you.

Table of Contents

List of Tables

List of Figures

List of Appendices

List of Abbreviations

AUC: Area under curve

CeO_2: Cerium oxide

GI tract: Gastrointestinal tract

PAA-peg: Polyethylene glycol-coated polyacrylamide

PBPK model: Physiologically based pharmacokinetic model

PCs: Phagocytizing cells

SMPS: Scanning mobility particle sizer

Abstract

Though the use of engineered nanoparticles has been exponentially increasing, little attention has been given to the nanoparticles biodistribution in the body. This thesis aims to establish a physiologically based pharmacokinetic (PBPK) model that accounts for nano-specific biobehaviors in order to understand the biodistribution of various types of nanoparticles.

I start with experimental data for polyethylene glycol-coated polyacrylamide (PAA-peg) nanoparticles intravenously injected to rats. By accounting for the phagocytosis process, the PBPK model successfully predicts the dynamics of PAA-peg nanoparticles between and within organs. According to the model, phagocytizing cells (PCs) quickly capture nanoparticles until saturation and constitute a major reservoir for nanoparticles.

The PBPK framework is then adapted to address cerium oxide (CeO_2) nanoparticles. A system of experimental apparatus is designed to integrate the generation, aging, and inhalation exposure of CeO_2 nanoparticles to rats. The amounts found in organs are further analyzed with a mass balance approach to gain a holistic understanding of the biodistribution. The PBPK model is then slightly modified to accommodate unique phenomenon for inhaled nanoparticles including mucociliary clearance and entry into the systemic circulation by penetrating the alveolar wall. The recovered amount is predominantly in lungs and feces, with extrapulmonary organs contributing less than 2% in recovery rate. No differences in biodistribution patterns are found between fresh and aged CeO_2 nanoparticles. The model predicts the biodistribution well and

finds PCs in the pulmonary region are accountable for most of the nanoparticles not eliminated by feces.

To expand the model's applicability, additional biodistribution data of nanoparticles collected from literatures are used for parameterization, including three polymers nanoparticles, three different sizes of silver nanoparticles, and one CeO_2 nanoparticles. Only parameters physiologically linked with the characteristics of nanoparticles are changed. Overall the model maintains its robustness by having a R^2 of 0.69 – 0.97 between the $\log_{10}$ of measured and predicted results. The changes of certain parameters also offer insights on the relationship between nanoparticles' characteristics and biodistribution.

In summary, this work highlights the importance of phagocytosis as a major determinant of nanoparticles biodistribution and provides a tool for better evaluating the human health risks posed by nanoparticles.

CHAPTER 1

Introduction

1.1 Motivation

1.1.1 Nanoparticles in the modern world

Humans have been exposed to airborne particles at nanosize (diameter < 100 nm) from natural origins such as forest fires for thousands of years. However, anthropological origins of these particles, such as internal combustion engines and power plants, became the major sources of exposure after the Industrial Revolution (Oberdörster et al. 2005). More recently, engineered nanoparticles (materials with at least one dimension of 100 nm or less are designed and produced by humans intentionally) emerged as a rapidly developing field of study for both scientific research and industrial application (Oberdorster et al. 2005). Engineered nanoparticles have demonstrated possessing unique properties in comparison with their bulk counterparts due to their small size, surface structure, solubility, shape, and aggregation (Nel et al. 2006). These properties have led to the wide use of nanoparticles as an emerging technology in various industries such as medicine, energy, textile, food, metallurgy, etc. (Smith et al. 2013; Chakrabarti et al. 2014; Chen et al. 2014; Irzhak et al. 2014; Wijnhoven et al. 2009).

1.1.2 Potential health risk from nanoparticles

However, there is a growing concern about the potential toxicity of nanoparticles. Studies reported the potential toxicities of nanoparticles including oxidative stress

(Sayes et al. 2006; Warheit et al. 2007; Yu et al. 2014) as well as possible genotoxic effects (Lee et al. 2013; Martinez Paino et al. 2012). Human exposure to nanoparticles can come from the manufacturing phase of products having ingredients of nanoparticles such as workers' occupational exposure (Wu et al. 2014), the use phase of products such as clothing or drugs (Lee et al. 2014), and disposal phase of these products after which nanoparticles may enter human bodies via different environmental compartments (Walser et al. 2012; Sun et al. 2014).

Considering the observations of toxicity of nanoparticles and the potential human exposure, concerns about the human health risks of nanoparticles have been raised (Warheit et al. 2008; Khanna and Kumar 2014) and it requires innovative researches to provide scientifically sound basis to better assess the health risks of nanoparticles.

1.1.3 Relationship between characteristics and hazards of nanoparticles

Conventionally, the hazards of chemicals to human are mainly determined by the exposed mass and chemical composition. However, studies have shown that the extent of exposure and toxicity of nanoparticles to the biologic system could be affected by a wide range of characteristics of nanoparticles, even those with the same chemistry (Maynard 2007). Similarly, the biodistribution of nanoparticles within the body exhibits different patterns from that of the bulk counterparts due to the physical forms specific to nanoparticles such as size and shapes (Maynard et al. 2011).

Toxicity of nanoparticles has been found to be linked with certain characteristics of the nanoparticles (Maynard 2007; Maynard et al. 2011). The toxic dose response relationship of nanoparticles with similar chemistry may be dependent on surface areas instead of mass (Oberdorster et al. 1994). Nanoparticles with the same surface areas but altered surface chemistry also induced different inflammatory responses (Maynard and Kuempel 2005). Differences in structures of aggregates for the same

primary nanoparticle could result in different biological responses (Shvedova et al. 2005).

Unlike their bulk counterparts, certain nanoparticles have been shown to migrate into the systemic circulation after deposition into either the lungs (Oberdörster et al. 2002; Nemmar et al. 2002; Semmler et al. 2004; He et al. 2010; Geraets et al. 2012; Aalapati et al. 2014) or the gut (He et al. 2010; Bockmann et al. 2000). The degree of penetration from the respiratory system to extrapulmonary organs may have a negative correlation with the size of nanoparticle (Oberdörster et al. 2005; Kreyling et al. 2002; Kreyling et al. 2009). Additionally, nanoparticles have been reported to translocate directly from the olfactory epithelium to the brain (Oberdörster et al. 2004; Elder et al. 2006). Certain surface modifications on nanoparticles could also affect the biobehaviors of nanoparticles inside the body, such as phagocytosis (Moghimi et al. 2001; Liu et al. 2008).

1.1.4 Importance of understanding the biodistribution of nanoparticles systematically

Previous findings demonstrate that some nanoparticles are able to cross biological barriers and thus reach sensitive target organs while their bulk counterparts may not. Yet the determinants of these nano-specific phenomena remain barely explored in a systematic manner. It is therefore necessary to determine the extent to which and the modes of action by which nanoparticles become bioavailable, potentially bioaccumulate, and translocate from point of exposure to organs. Given the influences of different characteristics of nanoparticles on their biobehavior within the body, it is also critical to study how these characteristics may affect those determinants of the biodistribution of nanoparticles. In addition, combining with the information of what characteristics may lead to higher toxicities of nanoparticles, there is the potential for

developing a screening protocol based on their characteristics to identify nanoparticles that we should have high concerns on their hazards to human health.

1.2 Physiologically basked pharmacokinetic modeling (PBPK) as a tool

1.2.1 Brief introduction to PBPK

PBPK models are built to mathematically describe the absorption, distribution, metabolism, and elimination of chemicals in the body based on quantitative interrelations among critical determinants of these processes with the aim of predicting the biodistribution of chemicals in the body (Krishnan 2007).. PBPK models are widely used for drug development (Grillo et al. 2012), animal toxicity testing designs (Lipscomb et al. 2012), and human health risk assessments (Lu et al. 2008). PBPK models have been developed to successfully model the behaviors of toxicants and drugs since the 1930s (Teorell 1937; Jain et al. 1981; Gerlowski and Jain 1983; Ramsey and Andersen 1984).

1.2.2 Past efforts using PBPK on nanoparticles

With the rapid development of nanotechnology and attentions attracted to the risk of nanoparticles, PBPK models focusing on various nanoparticles emerged: Lin et al. (2008) provided a first PBPK for quantum dots based on experimentally-derived blood to tissue distribution ratios but did not offer clear explanation of these ratios; Lee et al. (2009) were able to predict the long-term persistency of quantum dots in mice and rats but were not able to capture the early biodistribution dynamics of these nanoparticles; Lankveld et al. (2010) presented a PBPK model for silver nanoparticles but did not specify the mechanisms governing the biodistribution processes; Li et al. (2012) developed a detail PBPK model for poly(lactic-co-glycolic) acid nanoparticles

but cannot be directly adapted to other types of nanoparticles. Up to this point, each of these models has been developed for a specific type of nanoparticle, without looking in further details at the ability to model various types of nanoparticles within a consistent framework. There is therefore a clear need to explore how a common framework can be adapted and parameterized in a parsimonious way to account for nanoparticle specificities.

1.3 Bridging the gap

1.3.1 Taking phagocytosis into account in PBPK models

As demonstrated in a number of *in vivo* experiments, the reticuloendothelial system comprises a major clearance route for micrometer and nanometer-scale materials of biologic or anthropogenic origin (Moghimi et al. 2001; Cho et al. 2009). For example, nanoparticles intended for medical use may be modified with structural functionalizations with the specific aim to prevent or reduce phagocytosis (Moghimi et al. 2001; Liu et al. 2008).

Despite the recent developments of PBPK models with nanoparticles, these models have not specifically addressed the role of cellular phagocytosis (Lin et al. 2008; Lee et al. 2009; Lankveld et al. 2010; Li et al. 2012). Phagocytosis of nanoparticles has been modeled based on *in vitro* experiments (Wilhelm et al. 2002; Luciani et al. 2009), but this mechanism has hitherto not been incorporated in the attempts to describe the overall biodistribution in the body. Wenger et al. (2011) developed a rat model based on experimental mass-balance correlations suggesting the importance of macrophage uptake saturation of phagocytosis in the organs. Nevertheless, the model lacks a physiological approach and brings limited understanding on the processes affecting biodistribution.

1.3.2 Scientific questions to be answered by this work

To advance our knowledge in the biodistribution of nanoparticles in the body, this work was designed to answer the following scientific questions:

A) How to account for nano-specific phenomena, such as phagocytosis in the biodistribution of nanoparticles?

B) How to relate inhaled doses to nanoparticles uptake and how to describe the dynamics of nanoparticles between and within organs?

C) What are the most influential determinants affecting the biodistribution and how these parameters need to be adapted to describe the specific behavior of various nanoparticles?

By answering these questions, we can deepen our understanding of the biodistribution of nanoparticles and therefore enhance our ability to comprehensively assess their human health risks.

1.3.3 Addressing various types of nanoparticles in a common framework

This study proposes the use of PBPK model to answer the scientific questions above. To develop and test a model that can be easily adapted to different nanoparticles, the following strategy is proposed. First, two specific nanoparticles involving first hand data collected at the University of Michigan will be examined in depth in order to build the PBPK model that provides a common framework for other nanoparticles. Then, this PBPK model will be tested for its robustness by extending to other nanoparticles using a wider range of experimental results from published literature.

Detailed biodistribution data of polyethylene glycol-coated polyacrylamide (PAA-peg) nanoparticles were collected and reported previously (Wenger et al. 2011). The PAA-peg nanoparticles were administrated to rats via intravenous injection of a single dose. The concentrations of PAA-peg nanoparticles in various organs were then measured

over 120 hours. Saturation of PAA-peg nanoparticles was observed in most of the organs, which indicates the possibility of phagocytosis of nanoparticles. This study will use this intravenous injection of PAA-peg nanoparticles dataset to build up the initial PBPK model framework that takes into account the important role of phagocytosis in order to predict and explain the biodistribution of intravenously injected PAA-peg nanoparticles.

A project was set up and financed by US-EPA to study the generation, characterization, and biodistribution in rats via inhalation of freshly combusted/UV light aged cerium oxide (CeO_2) nanoparticles. This CeO_2 nanoparticles project first designs an experimental apparatus that connects the generation and aging of CeO_2 nanoparticles and the exposure chamber directly, with a series of instruments to characterize the nanoparticles. After the rats are exposed to the CeO_2 nanoparticles for four hours, feces, lungs, and extrapulmonary organs were analyzed for nanoparticles concentrations at different time points. This study will analyze the data collected in this joint project to reconstitute the mass balance of recovered amounts of nanoparticles and analyze the biological fate of inhaled CeO_2 nanoparticles. Then, the PBPK model framework built from the PAA-peg nanoparticles data will be expanded for inhalation exposure with minimum modifications to the model's structure. This inhalation PBPK model will be parameterized with the CeO_2 nanoparticles data to address specific biobehavior of nanoparticles inside the body following inhalation exposure.

After establishing the PBPK framework that can model exposures to nanoparticles by either intravenous injection or inhalation, additional biodistribution data for various types of nanoparticles will be gathered from the literature. These additional data will be employed to further parameterize the PBPK model developed in this study. To

keep the parsimony of the model framework, only parameters that reflect the specific characteristics of the different types of nanoparticles will be changed. The relationship between these parameters and the specific characteristics of each type of nanoparticles will also be explored empirically.

1.4 Objectives of this thesis

1.4.1 Specific aims

The general objective of this thesis is to develop and evaluate a PBPK model that accounts for biobehaviors specific to nanoparticles whether exposed by intravenous injection or inhalation. The predictability of this PBPK model will be first established and tested using observed biodistribution of PAA-peg and CeO_2 nanoparticles, in order to then be extended to different types of nanoparticles with minimum changes to the model itself.

More specifically, this work aims to address the following Specific Aims:

Specific Aim 1 – PBPK model for PAA-peg nanoparticles

Specific Aim 1 aims to develop a PBPK model for PAA-peg nanoparticles intravenously injected in rats, accounting for nanoparticles phagocytosis as a sequestration process influencing the biodistribution throughout the body. It is hypothesized that sequestration by phagocytizing cells of the reticuloendothelial system is the most important pathway for regulating nanoparticles in blood and organs at sub-saturation doses.

This Specific Aim 1 will more specifically address the following goals:

a) Appropriately account for nano-specific phenomena, such as phagocytosis.
b) Successfully describe the dynamics of nanoparticles between and within organs.

c) Identify the most influential determinants affecting the biodistribution of PAA-peg nanoparticles.

Specific Aim 2 – PBPK model for CeO_2 nanoparticles

Specific Aim 2 aims to extend the PBPK model from Specific Aim 1 to study the biodistribution of CeO_2 nanoparticles in rats exposed by inhalation, starting with a mass balance analysis. We hypothesize that inhaled nanoparticles small enough could penetrate the alveolar wall and enter the systemic circulation. Translocation from the lungs to the gastrointestinal tract (GI tract) by mucociliary clearance and then excreted by feces could also be an important pathway of elimination of inhaled nanoparticles. This Specific Aim 2 will more specifically address the following goals:

a) Examine whether the characteristics and biobehavior of CeO_2 nanoparticles will change significantly after the UV-light aging process.
b) Analyze the biodistribution of CeO_2 nanoparticles after inhalation exposure, including main organs and feces to enable a mass balance calculation.
c) Develop, parameterize, and evaluate a PBPK model that combines pulmonary deposition with internal biodistribution able to predict the biobehavior of CeO_2 nanoparticles following inhalation exposure.

Specific Aim 3 – Adaptation of the PBPK model to other nanoparticles

Specific Aim 3 aims to test whether the PBPK model developed in this thesis can accommodate various types of nanoparticles with minimum changes. The PBPK model developed in Specific Aim 2 and 3 will be adapted to other experimental data for different types of nanoparticles gathered from the literature. Data for both intravenous injection and pulmonary exposure pathways will be examined to test the robustness of the model. Parameterization of the model to different nanoparticles will

also be used to explore how different characteristics of nanoparticles may influence the most important parameters that govern the biodistribution of nanoparticles. This Specific Aim 3 will address the following goals:

a) Extend the current PBPK model framework to other types of nanoparticles with minimum changes to the model itself while maintain the robustness of the model.
b) Evaluate the ability of the model to accommodate for unique characteristics of certain nanoparticles.
c) Explore how different characteristics of the nanoparticles would impact the most influential parameters determining the biodistribution.

1.4.2 Outline of this thesis

This thesis is structured according to the above Specific Aims. Following the present introductory Chapter 1, Chapters 2, 3, and 4 address each of the three Specific Aims, following the format of a journal paper supplemented by additional information in Appendices 2, 3, and 4 respectively. Chapter 5 summarizes how the scientific questions asked in this work have been answered and proposes research topics that are worth exploring in the future. This work has generated a number of papers (both published and in preparation) and conference presentations (see publication list in Appendix 1). The contents of Chapter 2 have been published as a full research paper in the journal *Nanotoxicology*. The contents of Chapter 3 will be submitted to the journal of *Particles and Fibre Toxicology* as a full research paper. In a much more condensed format, the contents of Chapter 4 have been published as a conference proceedings paper at the International Conference on Safe Production and Use of Nanomaterials 2012. In addition to the core objective of the thesis focused on the development of PBPK of nanoparticles, I published a paper dedicated to the health

impacts modeling of polycyclic aromatic hydrocarbons. This publication is enclosed in Appendix 5 to illustrate the wider range of tools and experience I have apprehended during my PhD studies.

CHAPTER 2[1]

Physiologically based pharmacokinetic modeling of polyethylene glycol-coated polyacrylamide nanoparticles in rats

2.1 Introduction

Wide production and use of nanoparticles increase the likelihood of unintentional exposure at workplaces and through the general environment (Abbott and Maynard 2010; Li et al. 2010; Cassee et al. 2011; Lee et al. 2011; Weinberg et al. 2011). *In vivo* and *in vitro* studies have shown that nanoparticles have the potential to induce several health effects including oxidative stress, leading to inflammatory reactions as a function of nanoparticles properties (Oberdörster et al. 2005; Sayes et al. 2006; Warheit et al. 2007; Zhang et al. 2011). The degree of inflammatory response to nanoparticles depends on the biodistribution of nanoparticles in the body (Warheit et al. 2007; Cho et al. 2009). A literature review suggests that various types of inhaled (Oberdörster et al. 2002; Nemmar et al. 2002; Semmler et al. 2004) or intravenously injected (Oberdörster et al. 2002; Wenger et al. 2011; Panagi et al. 2001) nanoparticles can migrate to, and deposit in different organs via systemic circulation. Knowledge in this field of research remains however limited (Li et al. 2010; Khlebtsov and Dykman 2011). The various physiological determinants of nanoparticles behavior within the body must be systematically explored to better understand pharmacokinetic mechanisms.

[1] The content of this chapter has been published as a full research paper in *Nanotoxicology*. Li, D.; Johanson, G.; Emond, C.; Carlander, U.; Philbert, M.; Jolliet, O. Physiologically based pharmacokinetic modeling of polyethylene glycol-coated polyacrylamide nanoparticle in rats. *Nanotoxicology* **2014**, *8(S1)*, 128-137.

Physiologically based pharmacokinetic (PBPK) models have investigated the behavior of exogenous chemicals within the body (Teorell 1937). Recently, several studies have employed PBPK models to describe the biodistribution of nanoparticles (Lin et al. 2008; Lee et al. 2009; Lankveld et al. 2010; Li et al. 2012). These models have not specifically addressed the role of cellular phagocytosis, a process of phagocytizing cells such as macrophages and monocytes internalizing the nanoparticles, although it is a key process affecting nanoparticles biodistribution (Moghimi et al. 2001; Cho et al. 2009). For example, nanoparticles intended for medical use may be modified with structural functionalizations with the specific aim to prevent or reduce phagocytosis (Moghimi et al. 2001; Liu et al. 2008). Phagocytosis of nanoparticles has been modeled based on *in vitro* experiments (Wilhelm et al. 2002; Luciani et al. 2009), but this mechanism has hitherto not been incorporated in the attempts to describe the overall biodistribution in the body. Wenger et al. (Wenger et al. 2011) developed a rat model based on experimental mass-balance correlations suggesting the importance of macrophage uptake saturation of phagocytosis in the organs. Nevertheless, the model lacks a physiological approach and brings limited understanding on the processes affecting biodistribution.

Specific issues need to be addressed in the nanoparticle PBPK models: a) how to account for nano-specific phenomena, such as phagocytosis; b) how to describe the dynamics of nanoparticles between and within organs; and c) what are the most influential determinants affecting the biodistribution?

Here we have developed a PBPK model in rats incorporating the nanoparticles phagocytosis mechanism and to explore the biodistribution of intravenous exposure of polyethylene on glycol-coated polyacrylamide (PAA-peg) nanoparticles. PAA-peg is an example of a nanoparticle engineered for intracellular delivery of sensory and

pharmaceutically active agents (Kuruppuarachchi et al. 2011). Our study provides a significantly improved understanding of the key determinants of nanoparticles biodistribution in rats with a more physiologically relevant PBPK framework. This framework provides a sound basis for further extension to other exposure routes, types of nanoparticles, and for subsequent evaluation of biodistribution of nanoparticles in humans.

2.2 Methods

2.2.1 Experimental data

The PBPK model was developed based on anatomical and physiological considerations and on an experimental biodistribution study published by Wenger et al. (Wenger et al. 2011), where five groups of rats (n = 3) received a single intravenous dose of 7 000 μg ^{14}C-labeled PAA-peg nanoparticles. The PAA-peg nanoparticles had a hydrodynamic radius of 35 ± 7 nm and a surface charge of + 2.31 ± 0.77 mV. Urine, feces, blood samples, and cage residues, were collected at sequential times and tissue samples of the liver, spleen, kidneys, heart, lungs, brain, lymph nodes (mesenteric, inguinal, and popliteal), and bone marrow (both femurs) were collected following euthanasia by CO_2. Radioactivity levels were determined by liquid scintillation counting with correction for background chemiluminescence. Hepatic phagocytosis was visually observed by microscopy approach (Fig. 2.1).

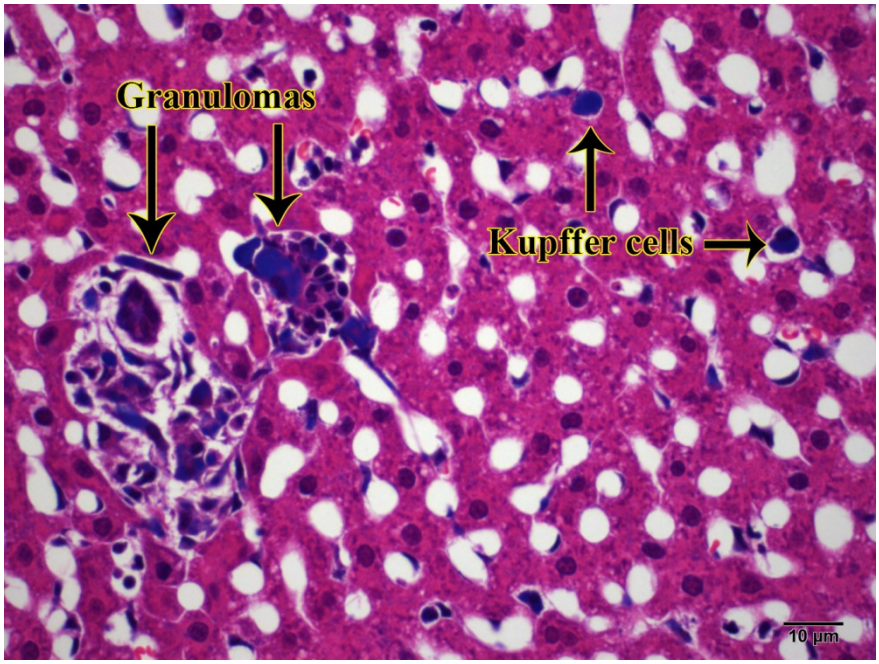

Fig. 2.1 Light micrograph of liver from a rat exposed through the caudal vein to polyacrylamide hydrogel nanoparticles (35nm mean hydrodynamic radius) containing covalently bound Coomassie Blue (1%). This figure demonstrates that most of the nanoparticles are phagocytized, necrotic foci (arrows) incorporating nanoparticle laden macrophages (blue) and individual Kupffer cells being engorged with aggregates of nanoparticles. [Stain, H&E – 5um].

2.2.2 PBPK model

The PBPK model consists of 10 compartments: arterial blood, venous blood, lungs, spleen, liver, kidneys, heart, brain, bone marrow, and the rest of the body (skin, muscle, skeleton, etc.). All compartments are interconnected via systemic circulation (Fig. 2.2). Within each organ compartment, there are three sub-compartments representing capillary blood, tissue, and phagocytizing cells (PCs). The arterial blood and venous blood compartments also have phagocytizing cells sub-compartments.

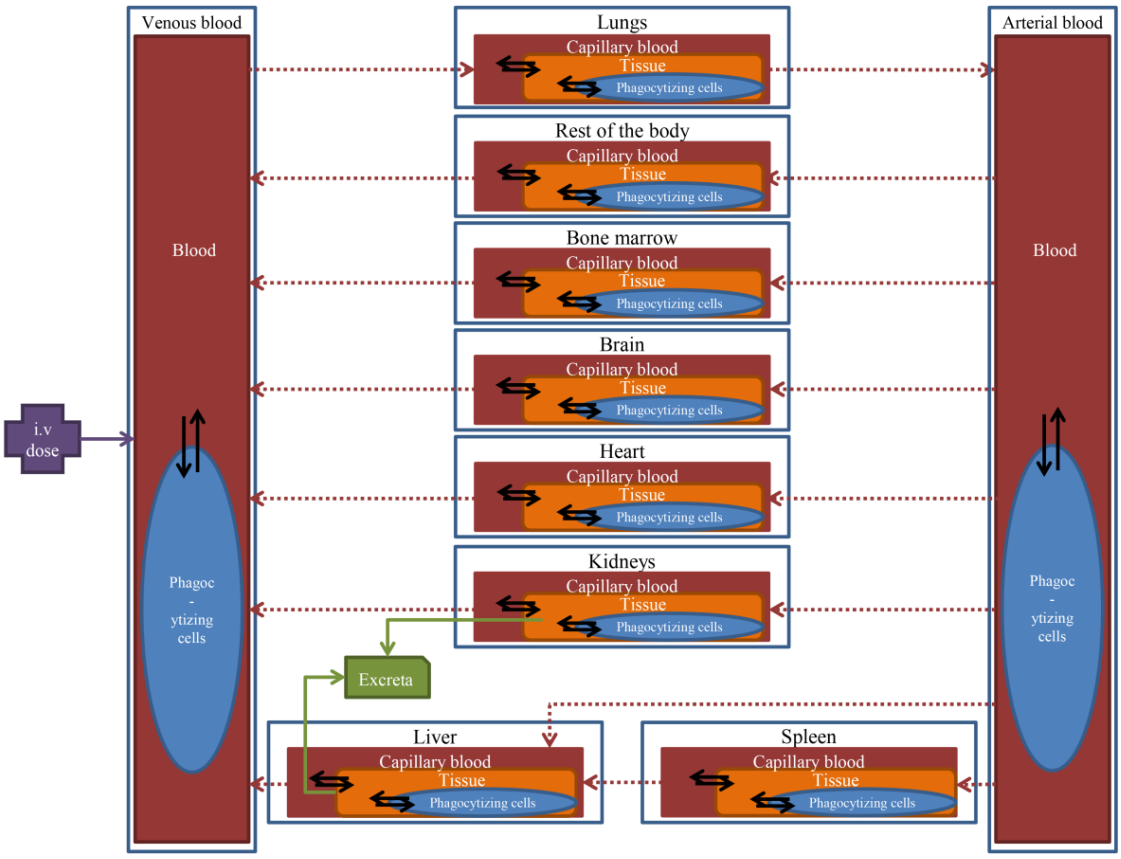

Fig. 2.2 Structure of the nanoparticle PBPK model, with phagocytizing sub-compartment in each tissue.

The exchange of nanoparticles between blood and tissue in each organ is described as a flow- and diffusion-limited process. Diffusion between blood and tissue is controlled by a permeability coefficient, which limits the effective blood flow (Krishnan 2007). We assume the same permeability coefficient for lungs, spleen, liver, kidneys, heart, and bone marrow. This permeability coefficient for the brain compartment is set to zero, under the assumption of a highly efficient blood-brain barrier.

Most plasma proteins cannot pass the capillary membranes, hence the composition of interstitial fluid differs from that of plasma. As a consequence, the composition of the biocorona formed around the nanoparticles will differ between these two locations (Nel et al. 2009; Lundqvist et al. 2008). This may make the blood environment energetically more favorable than the interstitial fluid, resulting in an uneven

distribution between blood and interstitial fluid at steady-state (Mason et al. 1992). The uneven distribution of large anionic plasma proteins may also contribute to the uneven distribution of nanoparticles via the Gibbs-Donnan effect. The distribution between interstitial fluid and plasma is accounted for by fitting a tissue: blood partition coefficient. Although the composition of interstitial varies between tissues, the tissue: blood partition coefficient is assumed to be the same for all tissues.

A fraction of the nanoparticles entering the tissue is sequestrated by PCs. When the amount of captured nanoparticles increases, the PCs can eventually be saturated. The PCs saturation level is organ specific, reflecting the variation in the density of PCs as well as differences in uptake capacity for different types of PCs among different organs. The effective uptake rate by PCs is a function of a maximum uptake rate and decreases as the PCs become saturated. This maximum uptake rate is the same for all compartments except for the spleen, due to its mesh-like structure that could trap nanoparticles in the spleen marginal zones and delay their contact with the splenic phagocytizing cells (Demoy et al. 1999; Moghimi 2002). Nanoparticles can also re-enter the tissue after desorption from PCs by processes such as exocytosis (Chithrani and Chan 2007; Keighron et al. 2012).

Excretion of nanoparticles occurs from liver tissue and capillary blood of kidneys. Biodegradation is considered negligible for the time-scale of this study due to the low biodegradability of cross-linked polyacrylamide (Smith et al. 1996, 1997). More details describing the dynamics of the model and the mathematical representations can be found in the method section and in the supplementary material.

2.2.3 Main mathematical description of the model

We present here three main model equations describing the mass balances of a tissue *t* and of the PCs in this tissue. A more comprehensive mathematical representation of the model is given in the supplementary material (Appendix A2.1).

Tissue: Since the model assumes a diffusion-limited process, the capillary blood and tissue in the organ should be described separately. As a result, the dynamic of nanoparticles in the tissue sub-compartment results from the net transfer with capillary blood, instead of the direct exchange between arterial blood and venous blood as in perfusion-limited process. A fraction of nanoparticles is captured by PCs and may re-enter the tissue by desorption. In certain organs, excretion of nanoparticles occurs as a clearance route from the body. The equation describing these processes is:

$$\frac{dM_t}{dt} = \overbrace{PA_t \times (C_{t,b} - C_t / P)}^{\text{net transfer with capillary blood}} - \overbrace{(W_t \times C_t \times k_{t,ab} - M_{t,m} \times k_{de})}^{\text{interaction with PCs}} - \overbrace{\frac{dM_{e,ex}}{dt}}^{\text{clearance by excretion}} \qquad 2.1$$

where,

M_t [µg] – Amount of nanoparticles in the tissue of organ *t*.

W_t [g] – Weight of organ *t*.

C_t [µg per g] – Concentration of nanoparticles in the tissue of organ *t*.

$C_{t,b}$ [µg per g] – Concentration of nanoparticles in the capillary blood of organ *t*.

PA_t [mL per hour] – Permeability coefficient-surface area cross-product. It is approximated as the product of permeability coefficient between capillary blood and tissue (unitless) and regional blood flow (mL per hour), $\chi_\alpha \times Q_t$, in this model, assuming the surface area is proportional to the regional blood flow.

P [unitless] – Partition coefficient of nanoparticles between tissue and blood.

$M_{t,m}$ [µg] – Amount of nanoparticles captured by PCs in organ *t*.

$k_{t,ab}$ [per hour] – Current uptake rate of nanoparticles by PCs in organ *t*.

k_{de} [per hour] – Desorption rate of nanoparticles from PCs to tissue.

$M_{e,ex}$ [μg] – Amount to excreta from source *e*. *e* only applies to tissue in liver and capillary blood in kidneys.

To eliminate the sub-compartment of capillary blood and simplify the model, Eq. 2.1 can be transformed to Eq. 2.2 that expresses the dynamic in different organs directly as a function of the arterial blood (C_{art}) and permeability coefficient (χ_α). Details of this transformation can be found in the supplementary material (Appendix A2.1).

$$\frac{dM_t}{dt} = \frac{\chi_\alpha \times Q_t}{(1+\chi_\alpha)}(C_{art} - C_t / P) - (W_t \times C_t \times k_{t,ab} - M_{t,m} \times k_{de}) - \frac{dM_{e,ex}}{dt} \qquad 2.2$$

Phagocytizing cells: The change in mass of nanoparticles in PCs is the uptake from the tissue minus desorption from PCs back to tissue. The uptake rate $k_{t,ab}$ will decrease as the amount captured approaches the total PCs saturation level characterized by the PCs uptake capacity per unit weight. The equation describing these behaviors is:

$$\frac{dM_{t,m}}{dt} = \overbrace{W_t \times C_t \times k_{ab0} \times (1 - \frac{M_{t,m}}{M_{t,cap} \times W_t})}^{uptake\ from\ tissue} - \overbrace{M_{t,m} \times k_{de}}^{desorption\ back\ to\ tissue} \qquad 2.3$$

where,

k_{ab0} [per hour] – Maximum uptake rate by PCs.

$M_{t,cap}$ [μg per g] – PCs uptake capacity for nanoparticles per organ *t* weight.

2.2.4 Implementation of the model

The PBPK model was implemented in Berkeley Madonna™ version 8.3.18 (Berkeley, CA) and acslX™ version 3.0.2.1 (Huntsville, AL). Parameters with unknown values were optimized by fitting the unknown model parameters against the experimental data given by Wenger et al. (Wenger et al. 2011) using the Nelder-Mead method in acslX™. To create the most parsimonious model possible, we used a common generic parameter for most organs. We only differentiated parameters between compartments

when it was indispensable to explain the dynamics of the PAA-peg concentration in that compartment in a physiologically meaningful way. The following parameters were fitted: clearance rates from kidneys and liver, the fraction of residual capillary blood left in organs when analyzed for nanoparticles contents, partition coefficient between tissue and blood (same for all compartments), permeability coefficients between blood to tissue (same for all compartments but brain and rest of the body), PCs uptake capacity per organ weight (one for each compartment), the maximum uptake rate (same for all compartment but spleen) and desorption rate by PCs (same for all compartment). All other parameter values were taken from the scientific literature (Krishnan 2007; Travlos 2006; Brown et al. 1997; Bernareggi and Rowland 1991; Brookes 1967). Values of all parameters and their standard deviations are listed in Table 2.1.

2.2.5 Analysis of model accuracy and identifying influential parameters

For the model evaluation we determine the deviation from the line of unity between the $\log_{10}$ of measured and predicted values (McKone 1993), and calculate the corresponding R^2.

We determine the most influential input parameters by performing a systematic sensitivity analysis using two approaches. First, we multiply or divide each parameter by a factor of 2 or 100 and compare the nanoparticles amount in a given compartment over time. Second, we analyze the relative sensitivity of the area under the mass-time curve (*AUC*) to different model parameters by comparing the relative change in *AUC* divided by a 1% relative change in parameter *p*:

$$\text{Relative sensitivity} = \frac{dAUC / AUC}{dp / p} \qquad 2.4$$

The relative sensitivities were calculated both for 10 hours and for 120 hours, to capture fast and slow processes, respectively.

2.3 Results

2.3.1 Model's predictions of the biodistribution

The model's predictions fit well with measured data (R^2 =0.97), as seen in Fig. 2.3, and illustrated in Fig. A2.1 in the Appendix (Appendix A2.2). The model suggests that 83% of the total nanoparticles found in richly perfused organs are stored in the PCs 120 hours after injection. As shown in Table 2.1, the specific PCs uptake capacity per organ weight for different organs varies by more than two orders of magnitude, consistently with the expected densities of PCs that are the highest in spleen and liver.

Table 2.1 Descriptions and values of parameters for the model.

Parameter (unit)	Description	Generic values [a]	Spleen (s)	Liver (l)	Bone marrow (bm)	Lungs (lu)	Heart (h)	Kidneys (k)	Rest of the body (rest)	Brain (br)	Blood (blood)
W_t (g) [b]	Weight of organs	N/A	0.779 ± 0.101	10.0 ± 1.02	7.60	1.20 ± 0.109	0.873 ± 0.0877	2.37 ± 0.196	213	1.35 ± 0.139	16.5 ± 0.522
$W_{t,b}$ (g) [c]	Weight of capillary blood in organ	N/A	0.0172	2.11	0.760	0.432	0.226	0.379	8.51	0.0945	N/A
Q_t (mL per h) [d]	Blood flow to organ	N/A	72.7	1245	133	4980	254	702	2473	99.6	4980
$M_{t,cap}$ (μg per g) [e]	Phagocytizing cells uptake capacity per organ weight	N/A	631 ± 8.50	74.8 ± 0.203	41.2 ± 0.799	25.5 ± 0.0671	5.03 ± 0.0521	1.08 ± 0.00835	17.6 ± 0.155	0.0827 ± 12.2	0.0396 ± 0.000374
χ_α (unitless) [e]	Permeability coefficient between blood to tissue	1.06×10^{-3} ± 1.12×10^{-5}	generic	generic	generic	generic	generic	generic	8.25×10^{-5} ± 4.41×10^{-7}	0	N/A
P (unitless) [e]	Partition coefficient between tissue and blood	0.147 ± 0.00191	generic	generic	generic	generic	generic	generic	generic	generic	1
k_{ab0} (per h) [e]	Maximum uptake rate by phagocytizing cells	16.1 ± 0.306	0.112 ± 0.000990	generic	generic	generic	generic	generic	generic	generic	generic
k_{de} (per h) [e]	Desorption rate by phagocytizing cells	4.90×10^{-19} ± 7.26×10^{-17}	generic	generic	generic	generic	generic	generic	generic	generic	generic
CLE_e (per h) [e]	Clearance rate to excreta	N/A	N/A	1.18×10^{-2} ± 2.92×10^{-4}	N/A	N/A	N/A	6.56×10^{-3} ± 5.35×10^{-5}	N/A	N/A	N/A
fr_β [e]	Fraction of capillary blood of organs left when analyzed	0.177 ± 0.0257	generic	generic	generic	generic	generic	generic	generic	0.346 ± 0.0208	N/A

[a] $\chi\alpha$, P, k_{ab0}, k_{de} have generic values for most compartments. "generic" indicates the corresponding generic value for each parameter

[b] Values expressed in average ± standard deviation from experimental data, except for bone marrow (assumed to be 3% of the total body weight [Travlos 2006]), and the rest of the body (the result of subtracting all other organs' weights from total body weight). The average values are used in the model

[c] Values obtained by multiplying the literature estimates of the percentage (w/w) of capillary blood in the organs (Brown et al., 1997) with the experiment values of organ weights. The percentage for bone marrow is estimated in this study

[d] Values obtained from literature (Brookes 1967; Bernareggi and Rowland 1991; Krishnan 2007). For the rest of the body, it is assumed to be the difference between total cardiac output and the sum of blood flows through other organs

[e] Values expressed in optimized value ± standard deviation obtained from parameterization by acslX™ (version 3.0.2.1)

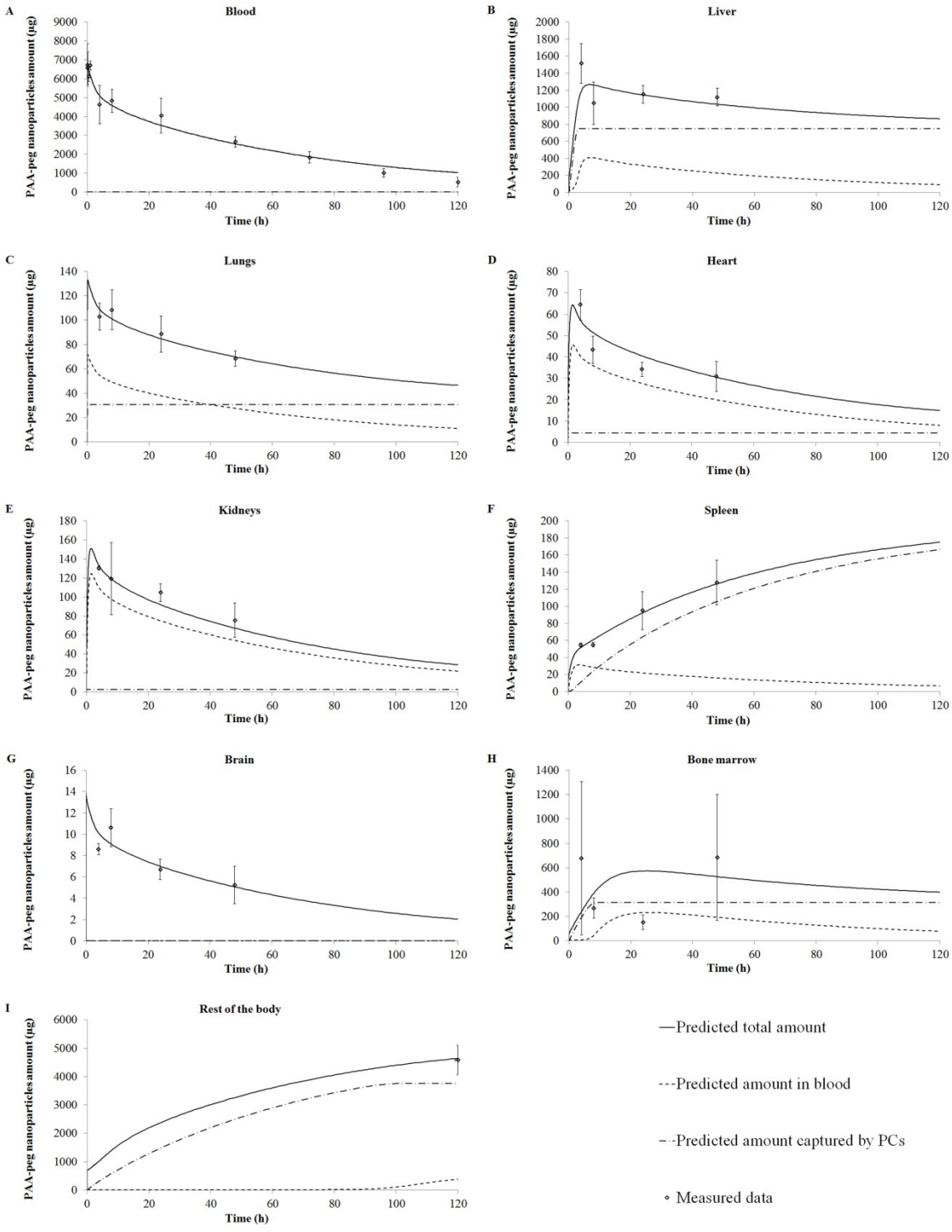

Fig. 2.3 Amount of PAA-peg nanoparticles predicted by the PBPK model predicted versus measured data in different organs. Error bars show the standard deviation of measured data. "PCs" is the abbreviation for phagocytizing cells. (A) blood. (B) liver. (C) lungs (D) heart. (E) kidneys. (F) spleen. (G) brain. (H) bone marrow. (I) rest of the body

The time course of nanoparticles amount in the *blood* compartment (arterial and venous blood combined) exhibits two phases (Fig. 2.3A). During the first four hours

after dosing, the amount in blood decreases quickly as the nanoparticles rapidly distribute to the organs, whereafter they are internalized by the PCs. After about four hours, a slower decay is observed as the PCs in the richly perfused organs are saturated and the nanoparticles diffuse into the rest of the body.

For the *liver*, *lungs*, *heart*, and *kidneys* (Fig. 2.3B, 2.3C, 2.3D, and 2.3E), the nanoparticles in the capillary blood of each compartment are transferred into the tissue and captured by the PCs in a relatively fast process, which reaches saturation plateau within 30 minutes to four hours. After saturation, PCs loaded with nanoparticles represent the major storage depot.

The *spleen* acts similarly to the organs discussed above except the PCs within have a lower uptake rate which delays the time for saturation (see Fig. 2.3F), due to the mesh-like structure of the spleen.

The blood-brain barrier blocks most of the nanoparticles from entering the tissue in the *brain* compartment (see Fig. 2.3G). Less than 0.2% of the injected nanoparticles were found in the brain. In accordance with other studies describing nanoparticles biodistribution (Oberdörster et al. 2002; Yokel et al. 2012; Sadauskas et al. 2007), this restricted amount of nanoparticles in the brain may well be explained by the nanoparticles content of residual capillary blood not entirely removed from the brain samples.

In contrast to all other tissues, the model is less suited to describe the experimentally observed time courses in *bone marrow* (Fig. 2.3H). In the original experiment, Wenger et al. (Wenger et al. 2011) reported only 0.02 g of bone marrow sampled, which is less than 3% of the total bone marrow weight (Travlos 2006), suggesting poor recovery. In addition, the standard deviations of the measured amount of nanoparticles were far higher for bone marrow than for the other tissues, suggesting a

high variability in the measurements. Additional data with a higher recovery rate and more precise measurements are needed to develop more accurate predictions for the bone marrow.

Due to the lower permeability coefficient between capillary blood and tissue, the kinetics of the *rest of the body* exhibits a different dynamic than the other organs (Fig. 2.3I). The nanoparticles are transferred from capillary blood rather slowly into the tissue and captured by PCs. Due to its large share (84%) of the whole body weight the rest of the body represents a major depository with 65% of the injected dose at the end of the experiment. Though the nanoparticles amount in the rest of the body has only been measured at the end of the experiment, the evolution of this amount is consistent with observed data in other organs and the mass balance of nanoparticles in the entire body.

2.3.2 Influential parameters

The most influential parameters affect the biodistribution of PAA-peg nanoparticles as follows.

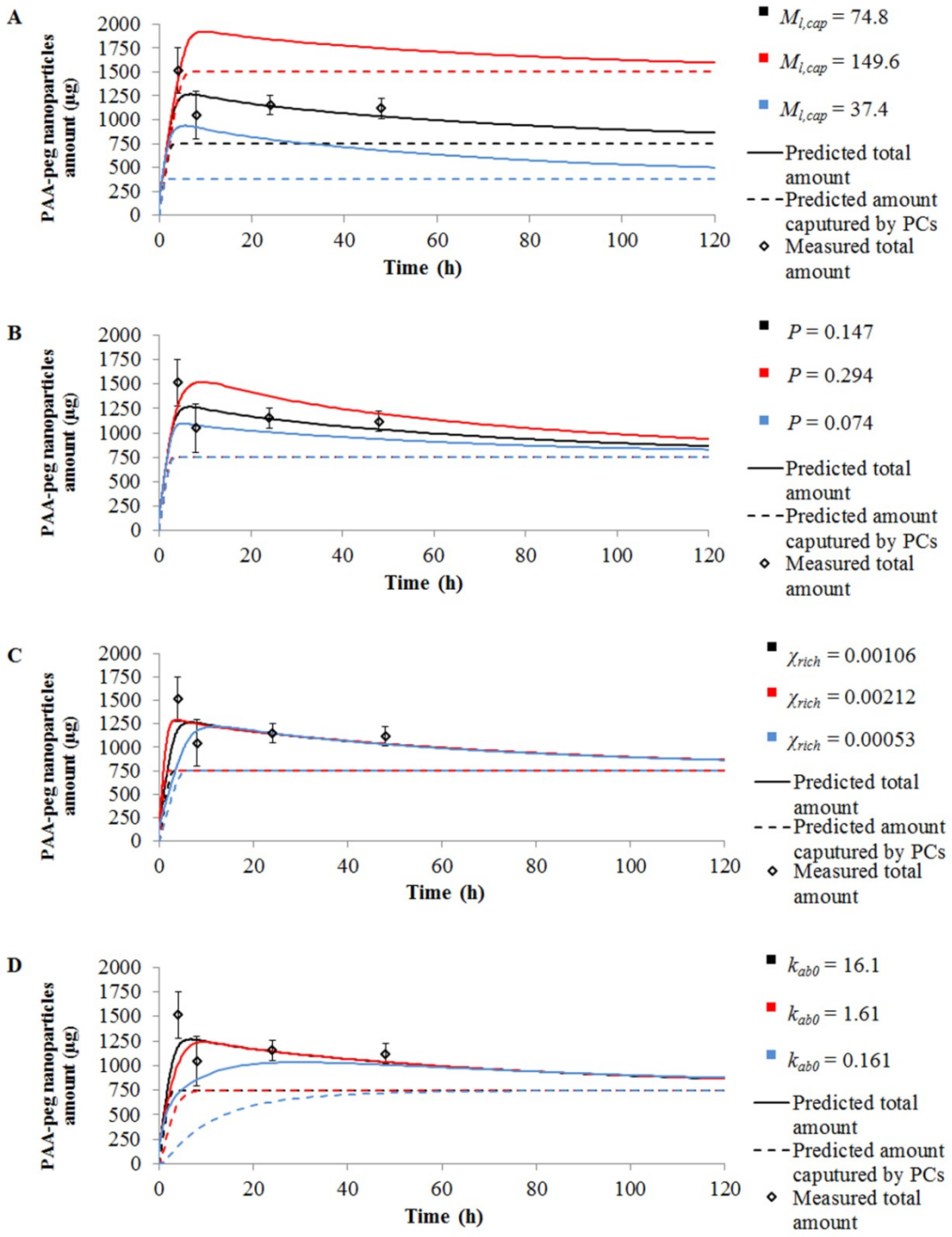

Fig. 2.4 Sensitivity analysis of the amount of nanoparticle in liver to the four most influential parameters. (A) PCs uptake capacity per liver weight ($M_{l,cap}$) . (B) partition coefficient between tissue and blood (P). (C) permeability coefficient between capillary blood and tissue in liver (χ_{rich}). (D) maximum uptake rate by PCs (k_{ab0}). Error bars show the standard deviation on measured data. "PCs" is the abbreviation for phagocytizing cells. Reference values from Table 2.1 are in black and sensitivity study are shown in red and blue.

Table 2.2 Relative sensitivities (unitless) for the most influential parameters [a].

Organ	$M_{t,cap}$		P		χ_{rich}		χ_{rest}		k_{ab0}	
	10 hours	120 hours	10 hours	120 hours	10 hours	120 hours	10 hours	120 hours	10 hours	120 hours
Blood	0.00	0.00	-0.07	-0.12	-0.08	-0.01	-0.06	-0.50	0.00	0.00
Liver	0.41	0.69	0.17	0.17	0.20	0.02	-0.03	-0.13	0.01	0.00
Lungs	0.27	0.44	0.45	0.32	-0.05	-0.01	-0.04	-0.28	0.00	0.00
Heart	0.07	0.15	0.60	0.54	-0.04	-0.01	-0.05	-0.42	0.00	0.00
Kidneys	0.02	0.04	0.71	0.69	-0.04	-0.01	-0.06	-0.48	0.00	0.00
Spleen	0.00	0.10	0.51	0.63	0.16	0.10	-0.05	-0.33	0.18	0.62
Brain	0.00	0.00	-0.07	-0.12	-0.08	-0.01	-0.06	-0.50	0.00	0.00
Bone marrow	0.06	0.57	-0.03	0.57	0.71	0.07	-0.04	-0.19	0.01	0.00
Rest of the body	0.00	0.02	-0.06	-0.06	0.11	-0.01	0.28	0.41	0.00	0.00

[a] For descriptions of the parameters, please refer to Table 2.1

The *PCs uptake capacity* of nanoparticles per unit weight ($M_{t,cap}$) is the most influential parameter in the liver. It determines the maximum PAA-peg nanoparticles amount and the model is highly sensitive to this parameter throughout the entire time-course (Fig. 2.4A), with high relative sensitivities of 0.41 and 0.69 over 10 and 120 hours respectively (Table 2.2). Once captured by PCs, nanoparticles will not be easily transferred to other compartments since the desorption of nanoparticles from the PCs back into the tissues are rather slow. Therefore a near constant nanoparticle storage in PCs is reached once the PCs are saturated (Fig. 2.4A dashed lines). Similar effects are shown in lungs and bone marrow (Table 2.2), which have high values for $M_{t,cap}$ (Table 2.1). On the contrary, $M_{t,cap}$ is not a sensitive parameter for blood, heart, kidneys and brain (Table 2.2) since the majority of nanoparticles in these organs are not captured by the PCs. The PCs in the spleen and the rest of the body do not reach saturation for most of the 120 hours, and are therefore not sensitive to $M_{t,cap}$ (Table 2.2).

The *partition coefficient between tissue and blood* (P) has a moderate influence on the short-term kinetics in the liver and virtually no influence on the long-term kinetics (Fig. 2.4B and Table 2.2). This is due to the fact that for liver, the amount of nanoparticles in the tissue represent about one third of the nanoparticles in the early phase, but is strongly reduced later as the concentration in the blood is itself reduced. The partition coefficient between tissue and blood has a dominant influence on lungs, heart, kidneys, spleen. These organs have a higher proportion of nanoparticles in the tissues and the spleen does not reach saturation in PCs (Table 2.2).

The *permeability coefficient between capillary blood and tissue* (χ_α) determines the speed of nanoparticles passage from capillary blood into the tissue. This parameter only affects the short-term kinetics in liver (Fig. 2.4C), with moderate relative

sensitivity of 0.20 for 10 hours *AUC* (Table 2.2). Among organs, the influence of χ_α is only large in bone marrow (Table 2.2) because of lower blood flow rate relative to organ weights. This permeability coefficient (χ_{rest}) has also a large influence on both the short-term and long-term kinetics of the rest of the body (Table 2.2, more details can be found in Appendix A2.3).

In the considered range, lowering the *maximum uptake rate by PCs* (k_{ab0}) has little influence on most organs, unless it is reduced by two orders of magnitude and thus becomes a limiting factor to the capture of nanoparticles by PCs, as observed in the spleen (Table 2.1 and Table 2.2).

For the brain, the model considers the residual capillary blood left in the brain responsible for the detected nanoparticles and therefore the relative sensitivities are similar for blood and brain (Table 2.2). All parameters have low to moderate influences on blood except the *permeability coefficient to the rest of the body* χ_{rest} for the 120 hour *AUC*. This is because most nanoparticles in blood migrate to the rest of the body after the phagocytizing saturation capacity is reached in richly perfused organs.

This analysis of the most influential parameters reveals that the partition coefficient between tissue and blood, the permeability coefficient between capillary blood and tissue, and the maximum uptake rate by PCs have a relatively small influence on the long-term biodistribution of PAA-peg nanoparticles for most organs.

2.4 Discussion

We have observed large variations in uptake capacity of up to two orders of magnitude. These are consistent with the expected densities of phagocytizing cells (PCs): we also find the highest PCs uptake capacities for spleen, liver, bone marrow, and lungs in accordance with other studies (Lang and Dobrescu 1991; Hyafil et al. 2007) that indicated these organs have the highest density of PCs. For the distribution of PAA-peg nanoparticles among organs, the uptake capacity is especially important to spleen, liver, bone marrow, and lungs. The importance of the uptake capacity might be lower or even negligible in organs with lower density of PCs. The high uptake capacity value for the rest of the body seems counter-intuitive as the rest of the body is not known for high level of phagocytizing cells. This could suggest that the uptake capacity parameter also represents other mechanisms in addition to phagocytosis. For example, protein binding is also proposed as an explanation for the intracellular uptake saturation for gold nanoparticles (Chithrani et al. 2006). This possibility of multiple mechanisms being responsible for the saturation phenomenon requires further investigation.

The tissue-specific phagocytizing capacities are in relation to the observed PAA-peg nanoparticles time course in the corresponding tissues. It is therefore important to validate that the fitted capacities are consistent with other similar experimental studies, i.e. using the same route of administration, same, strain, age and identical nanoparticles. According to the present model, the PCs uptake capacity per liver weight is about 74.8 μg per g of tissue. Considering that there are about 27 million macrophages per gram of rat liver (Alpini et al. 1994) and assuming that all PCs in the liver are macrophages, the uptake capacity of the liver PCs corresponds to 2.8 pg or 3.8 million PAA-peg nanoparticles per macrophage (the average molar mass of the

PAA-peg nanoparticle in this study was 440 000 g/mole). This is consistent with other *in vitro* studies finding 3.2 to 48 million nanoparticles per macrophage (Wilhelm et al. 2003; Robert et al. 2011).

Nanoparticles uptake by PCs has several implications on the toxicity of nanoparticles. First, by storing the nanoparticles, the PCs could prevent the organs from being directly damaged when exposed to potential toxic nanoparticles. Second, during the nanoparticles sequestrations, the PCs can be stressed, impairing the body's immune system. Third, the nanoparticle-loaded PCs could slowly release nanoparticles back to the tissue over time and serve as a long-term internal source of nanoparticles inside the body, extending organs exposure duration even after external nanoparticles sources are eliminated.

A better understanding of the mode of action concerning the uptake of nanoparticles by PCs is crucial not only regarding bioaccumulation and toxicity, but also with respect to pharmacologic effects and drugs therapeutic threshold. Nanopharmaceuticals drugs preparation might end up being captured by PCs before reaching their target thus and inhibiting or reducing their pharmacological effects. PCs saturation by non-toxic nanoparticles might nevertheless reduce the immune response to pathogens and increase the body's vulnerability to diseases.

Our model has the advantage compared to previous biodistribution models for nanoparticles (Lin et al. 2008; Lee et al. 2009; Lankveld et al. 2010; Li et al. 2012; Wenger et al. 2011) in that it describes the interactions between PCs and nanoparticles in a more detailed and, as we believe, a more physiologically based manner. For example the distribution coefficient given by Lin et al. (2008) is empirical rather than physiological and represents an amalgamation of several processes such as deposition, protein binding, transport through capillaries, phagocytosis, transcytosis, and

endocytosis. By providing a more detailed representation of the different mechanisms, our model enables us to identify the critical processes that determine the behavior and biodistribution of nanoparticles. In our opinion, this forms a sound basis for further refinement and adaptation to other types of nanoparticles and other species including human.

This work points out an important limiting step driving the equilibrium constant of polyacrylamide nanoparticles, namely the *partition coefficient* between tissue and blood, the diffusibility parameter (namely *permeability coefficient)* between capillary blood and tissues, the *uptake capacities* of PCs, and the *uptake rate* of PCs. These are the major unknown estimates that require optimization in order to model the biodistribution of other nanoparticles.

Despite the PAA-peg nanoparticles concentration in the organs being generally higher than the concentration in blood, the introduction of PCs compartments within each tissue implies that the apparent *partition coefficient* between tissue (excluding PCs) and blood may be smaller than 1, thus the partition coefficient of 0.15 obtained by best fit (Table 2.1). The apparent partition coefficient between tissue and blood may be linked to the composition of the biocorona formed around the nanoparticles. Various properties of the nanoparticles, e.g. size, surface charge, and ligands, and crystallinity can influence the composition of the biocorona and therefore affect the interaction between nanoparticles and the biological system (Nel et al. 2009). The low apparent partition coefficient implies that, disregarding the redistribution due to phagocytosis, the modeled nanoparticles have a preference for blood.

A limiting amount of nanoparticles in the brain could be explained by a residual capillary blood containing nanoparticles not entirely removed from the brain samples. The assumption of zero *permeation* value used for the brain is in accordance with the

prediction obtained using the PBPK model. However, we cannot exclude that minor permeation occurs. Higher amounts in the brain have been reported for other intravenous exposure to nanoparticles (Oberdörster et al. 2004; Elder et al. 2006; Yokel et al. 2012; Hardas et al. 2010), suggesting higher permeation in brain for other nanoparticles such as cerium oxide.

The absolute *uptake rates and capacities* of PCs are expected to vary across different types of nanoparticles as influenced by nanoparticles size, surface modification, surface charge and chemical reactivity (Moghimi et al. 2001; Wilhelm et al. 2002; Walkey et al. 2012). The relative abundance and types of PCs in different organs are intrinsic anatomical-physiological and animal dependent. It could also be related to defensive immune response triggered by a pathological response. It will therefore be interesting to test the hypothesis that the relative PCs uptake capacities vary similarly across organs as a function of nanoparticles properties. Individual types of PCs have different uptake capacities for the same type of nanoparticles. For example, the uptake capacity of monocytes is about 50 times lower than those of macrophages as suggested in the literature (Luciani et al. 2009). In our model, the uptake capacity represents the overall uptake of all types of PCs. In the future, it would be of interest to differentiate the uptake for each main type of PCs. The *desorption rate* of PAA-peg nanoparticles from the PCs back to tissue plays a negligible role since it is orders of magnitude lower than the uptake rate, which agrees with the findings of Luciani et al. (2009).

Although this model considers phagocytosis to be solely responsible for the saturation phenomenon observed in the experiment, we cannot exclude other mechanisms, such as protein binding, that would result in similar outcome. The parameter $M_{t,cap}$ may thus represent a mixture of different mechanisms rather than phagocytosis only.

Figure 1 nevertheless shows that phagocytosis plays a dominating role in the distribution of PAA-peg nanoparticles in the liver.

Future efforts should therefore focus on these most influential parameters affecting the biodistribution of nanoparticles, and how these parameters depend on nanoparticles properties such as type, size and surface charge. Better knowledge is especially needed about the PCs, their uptake kinetic for nanoparticles and their quantitative abundance in different organs. Other potentially important mechanisms such as protein binding should also be investigated further. Obtaining experimental values is a priority for the partition coefficient between tissue and blood, the permeability coefficient between capillary blood and tissues.

2.5 Conclusions

According to the PBPK model developed in this work, the PCs are the major reservoir of PAA-peg nanoparticles in the organism. Because of the high net uptake by phagocytizing cells, nanoparticles will only accumulate in organ tissues after the saturations of PCs occurred. When extrapolating this model to human, certain physiological parameters such as blood flow, organ weight, etc. can be directly adapted for a human's setting while the partition coefficient, permeability coefficient, and parameters governing the PCs behavior should be investigated further before making predictions with this model.

Acknowledgements to this chapter:

This chapter is based on the paper titled "Physiologically based pharmacokinetic modeling of polyethylene glycol-coated polyacrylamide nanoparticles in rats" published in the journal of *Nanotoxicology*.

This study was funded by the U.S. Environmental Protection Agency under EPA STAR Program (grant No. RD-83486001), the University of Michigan Risk Science Center, the Swedish Research Council for Health, Working Life and Welfare (Forte, grant No. 2010-0702), Sweden, and the European Union Seventh Framework Programme under the project NANoREG (grant No. 310584). The authors would also like to thank Alexi Ernstoff for proof reading and commenting on the manuscript.

CHAPTER 3[2]

Physiologically based pharmacokinetic modeling of cerium oxide nanoparticles by inhalation exposure in rats

3.1 Introduction

Nanoparticles emerged as a type of innovative material that holds multiple promising features when compared to their bulk counterparts (Nel et al. 2006). Commercial applications of nanomaterials may expose human to nanoparticles and raise concerns about potential human health impacts, given toxic effects of nanoparticles were observed (Wang et al. 2014; Choi et al. 2009; Kendall and Holgate 2012). This paper focuses on exposure and biodistribution of Cerium oxide (CeO_2) nanoparticles, which are mainly used as a diesel fuel additive to improve combustion efficiency (Wakefield et al. 2008) and can be released to the environment by diesel engines. Several *in vitro* and *in vivo* studies have shown that these CeO_2 nanoparticles can generate reactive oxygen species that induce oxidative stress and inflammatory responses, which can cause adverse human health effects (Aalapati et al. 2014; Thill et al. 2006). To better understand the toxic effects of CeO_2 nanoparticles, it is necessary to first characterize the biodistribution of CeO_2 nanoparticles in the entire body.

Several studies have shown that intravenously injected CeO_2 nanoparticles could be found in all major organs in rats following systemic circulation even 90 days after injection (Yokel et al. 2012; Hardas et al. 2010; Yokel et al. 2009). An intratracheal instillation study found that besides of lungs, the largest quantity of instilled CeO_2

[2] The content of this chapter will be submitted as a full research paper to *Particle and Fibre Toxicology*.

nanoparticles was in the feces in the first two days after exposure (He et al. 2010). Recently conducted inhalation studies on CeO_2 nanoparticles showed that the lungs are the major deposit organ while CeO_2 nanoparticles could penetrate from the lungs into the systemic circulation as they were found in other extrapulmonary organs (Geraets et al. 2012; Aalapati et al. 2014). However, these inhalation studies did not include feces and fail to provide a more comprehensive mass balance of the inhaled dose of CeO_2 nanoparticles. In addition, diesel fuel combustion and refining processes emit SO_2 that may be physically associated with CeO_2 nanoparticles. There is therefore a need to characterize environmental transformation and physicochemical properties of aged CeO_2 nanoparticles using their interactions with UV radiation and ambient air co-pollutants, and compare them to freshly-combusted CeO_2 nanoparticles. To better understand exposure, provide insights on the main mechanisms responsible for biodistribution and possibly extrapolate biobehavior from rodent models to humans, it is useful to complement biodistribution experimental data with pharmacokinetic modeling. Physiologically based pharmacokinetic (PBPK) models have been used to study and predict the biodistribution of chemicals inside the body for decades (Krishnan 2007). Several PBPK models have been specifically developed for nanoparticles (Lin et al. 2008; Lee et al. 2009; Lankveld et al. 2010; Li et al. 2012) but failed to specifically address the role of phagocytosis, which was observed as a key process of nanoparticle biodistribution (Moghimi et al. 2001; Cho et al. 2009; Luciani et al. 2009). Li et al (2014) built a whole body PBPK model that incorporated phagocytosis but the model was limited to intravenous injection of nanoparticles. One PBPK model for inhalation exposure of nanoparticles has been developed for silver nanoparticles by Bachler et al (2013), but this model only considers biliary excretion from the liver to feces and cannot explain the high amount of nanoparticles found in

feces in a previous pulmonary *in vivo* study (He et al. 2010). Currently, there is no detailed PBPK model describing the biodistribution of inhaled CeO_2 nanoparticles. There is therefore a need for developing a PBPK model parameterized for CeO_2 including deposition in the respiratory system and translocation/excretion.

The objectives of this study are:

1. Generate and characterize both fresh and UV-light aged CeO_2 nanoparticles.
2. Measure the biodistribution of CeO_2 nanoparticles in an *in vivo* rat inhalation study, including main organs and feces and analyze the mass balance.
3. Develop, parameterize, and evaluate a PBPK model that combines pulmonary deposition with internal biodistribution, able to predict the biodistribution kinetic of CeO_2 nanoparticles.

3.2 Methods

3.2.1 Experimental apparatus

Fig. 3.1 shows the schematic of the entire experimental apparatus located at Michigan State University consisting of a nanoparticle generation facility, a photochemical chamber, a series of instruments that characterize the aerosol flow, and a nose-only inhalation exposure chamber for rats.

Generation of CeO_2 nanoparticles: CeO_2 nanoparticles with a density of 6.96 g/cm^3 were generated using the University of Michigan combustion synthesis (UMCS) facility was transported to Michigan State University for animal exposure. The UMCS facility uses a multi-element H_2/O_2 diffusion flame burner to provide a high-temperature oxidizing environment for cerium acetate (cerium(III) acetate hydrate; Sigma-Aldrich, 99.99% trace metals basis) precursor decomposition, oxidation, and particle formation. The burner was operated continuously to generate appropriate

quantities of nanoparticles for analysis. Further information on the synthesis facility can be found in Bakrania et al. (2007a; 2007b), Miller et al. (2005), and Hall et al. (2004).

Photochemical chamber: The atmospheric reaction chamber is a 500-L fluorinated ethylene propylene Teflon bag designed in collaboration with Ingeniven Inc. (North Hampton, NH, United States). Thirty (UVA-340) fluorescent lamps (40 W each) were used to simulate sunlight in the short wavelength region from 365 nm down to the solar cutoff of 295 nm. These lamps were placed beside the chamber to simulate ~250 W/m^2 of direct UV flux in the chamber, which is equivalent to five times solar UV flux. Reflections from the interior surface of the enclosure are expected to significantly increase this figure and actual UV flux levels were measured with a UV meter.

Nanoparticle characterization: A scanning mobility particle sizer (SMPS) with an electrostatic classifier (TSI-3080, TSI Inc., Shoreview, MN, USA) was used to monitor the aerosol number density and particle size distribution as a function of time during the animal exposure studies. Specifically, the size distribution of the aerosol was monitored during the experiments in real time using a differential mobility analyzer (DMA) (TSI-3081, TSI Inc., Shoreview, MN, USA) connected to a condensation particle counter (CPC) (TSI-3010, TSI Inc., Shoreview, MN, USA). The SMPS uses a particle size impactor filter to remove particles >~0.5 μm in size. Additionally, a cascade impactor filter (Sioutas Impactor, SKC Inc., Eighty Four, PA, USA) was incorporated after the photochemical chamber, upstream of the exposure carousel, filter packs and SPMS, to remove larger particles and agglomerates.

Gas sampling (GS) was used to measure the NO_x, CO, O_3, and CO_2 levels in the nanoparticles carrier gas. These gases were by-products of the combustion process

used to generate the ceria nanoparticles, and also represent gases found at ambient conditions in urban environments. Additional measurement of post combustion O_2 levels were performed using an emission analyzer (MEXA-584L, HORIBA Instruments, Ann Arbor, MI, USA) to ensure that the oxygen was at atmospheric levels, i.e. near 20% on a mole fraction basis.

The nanoparticles mass during each exposure study was measured using filter pack assemblies. Four 47-mm Teflon (PTFE) filters (Gelman Science) in Teflon/Teflon-coated aluminum filter packs were attached to two ports of the exposure chamber to determine the total nanoparticle mass deposited during sampling times corresponding to the exposure studies. The filter packs were used according to the Federal Reference Method (U.S. EPA 1999). Four pumps were used to control the flow rates to the exposure carousel, the filter packs, the SMPS and the GS system. Additional details on the aerosol transport system, including dimensions and flow rates, can be found in Fatouraie et al. (2015).

Transmission electron microscopy (TEM) was performed at the University of Michigan's electron microbeam analysis laboratory using a high resolution electron microscope (JEOL 3011, JEOL USA Inc., Peabody, MA, USA) in order to characterize the nanoparticles morphology and size distribution. The nanoparticles were sampled on copper grids (carbon film, 300 mesh copper, Electron Microscopy Sciences, Hatfield, PA, USA) placed in the aerosol flow after the impactor filter. Bulk properties such as crystalline structure and the average crystallite size were analyzed using powder x-ray diffraction (XRD) equipment (Bruker D8 Discover with GADDS, BRUKER AXS Inc., Madison, WI, USA). Details on the sample preparation for the nanoparticle materials analysis can be found in Fatouraie et al. (2015).

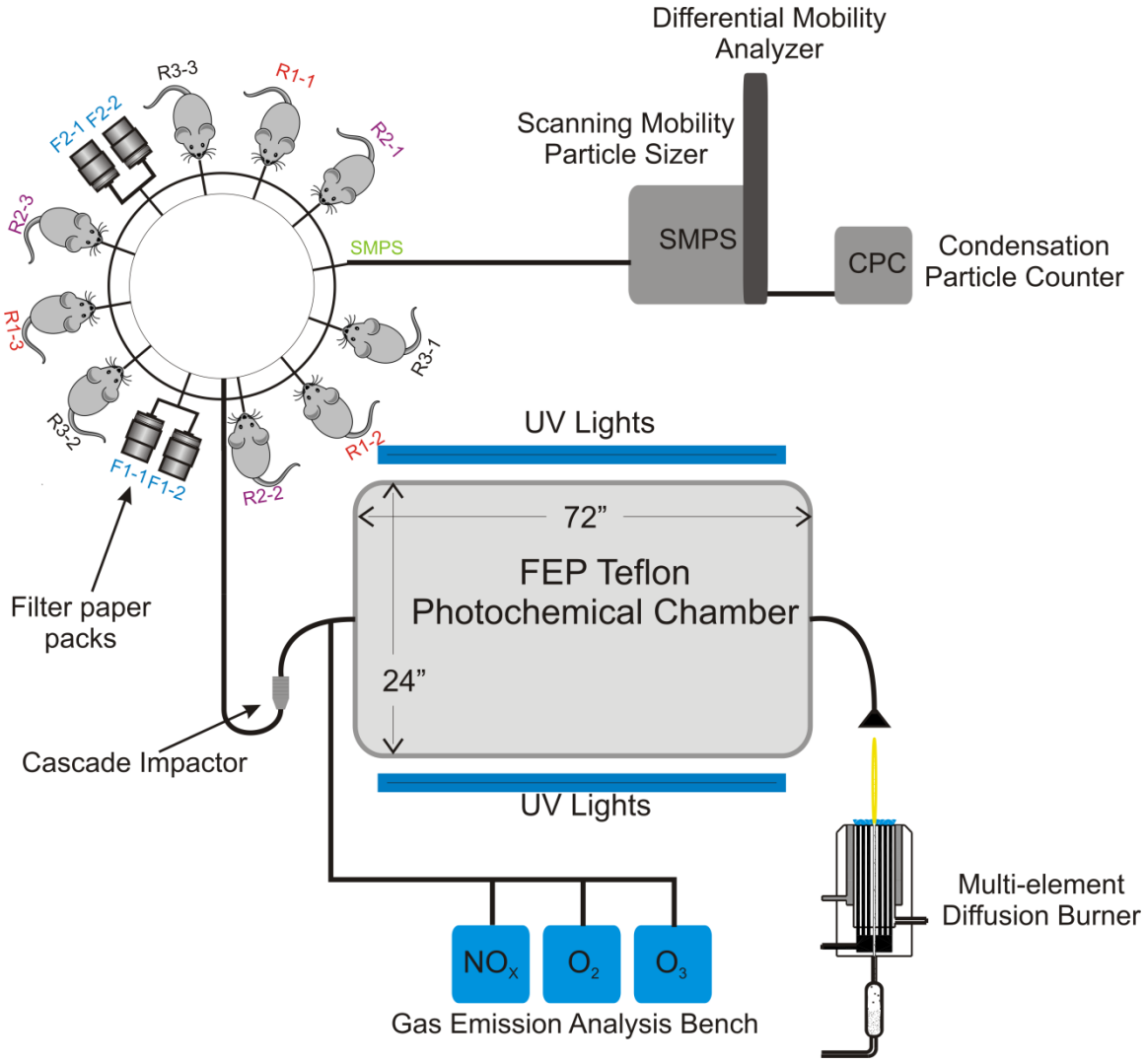

Fig. 3.1 Schematic representation and photo of the experimental apparatus. The dimensions are not to scale.

3.2.2 Animal study design

Animals and inhalation exposure: Male Sprague-Dawley rats 200 – 235 g, 9 weeks of age, were obtained from Charles River Laboratories (Portage, MI, United States) and

housed for at least seven days in shoebox-style cages prior to experimental protocols with access to food and water *ad libitum*. Study protocols were approved by the Institutional Animal Care and Use Committee of Michigan State University, an AAALAC accredited institution.

Rats were acclimated to nose-only restraining devices (CH Technologies, Westwood, NJ, USA) in the days preceding exposure. Nine rats were exposed to CeO_2 nanoparticles in a 12-port nose-only exposure system (CH Technologies) for a single four hour exposure. Three ports of the system were used to collect nanoparticle samples. The exposure environmental conditions were 25±3°C, 50±15% humidity, and the dilution levels in the burner were controlled to achieve oxygen concentration of 20% on a mole fraction basis with the thresholds of 25 ppb for O_3 and 50 ppb for NOx. Two runs of nine rats per run were used for both freshly generated CeO_2 nanoparticles and aged CeO_2 nanoparticles. After exposure, 3 rats each were sacrificed after 15 min, 24h, and seven days (n = 3 per time point per run). Blood, lungs, liver, kidneys, heart, brain, olfactory bulb, spleen, feces, and urine were collected for CeO_2 nanoparticles concentration analysis. Feces and urine were collected only for the first 24 h post exposure.

Determination of CeO_2 nanoparticle concentrations in organs/feces/urine: All equipment and supplies used for trace element analysis were rigorously acid-cleaned in a 5-step, 11-day procedure. Detailed procedures on the lung tissue digestion and the analysis were documented previously (Harkema et al. 2004; Morishita et al. 2004). In brief, all biological samples were weighed and then acid-digested in concentrated nitric acid. Sample extracts were then diluted and analyzed for Ce using inductively coupled plasma–mass spectrometry (ELEMENT2, Thermo Finnigan, San Jose, CA, USA). The detection limit of this method is 0.002 ng/mL. The background cerium

levels in all sampled organs were determined in a preliminary study with two control rats which were not exposed to the CeO_2 nanoparticle aerosol. All background levels were below detection limit.

3.2.3 PBPK modeling

Model framework: The foundation of this PBPK is based on our previously developed PBPK model for intravenously injected nanoparticles (Li et al. 2014), extending it for inhalation exposure. The present PBPK model consists of 10 compartments: arterial blood, venous blood, lungs, spleen, liver, kidneys, heart, brain, GI tract, and rest of the body. All compartments are interconnected via systemic circulation (Fig. 3.2). Within each organ compartment, there are three sub-compartments representing capillary blood, tissue, and phagocytizing cells (PCs). The arterial blood and venous blood compartments also have phagocytizing cells sub-compartments. Nanoparticles are inhaled by the rats when exposed. Following inhalation, the nanoparticles are deposited into three different regions of the respiratory system: head region, tracheobronchial region, and pulmonary region. The deposition fractions in these three regions were modeled as a function of the density and size distribution of nanoparticles recorded by the SMPS using the Multiple-Path Particle Dosimetry Model (MPPD v 2.11; http://www.ara.com/products/mppd.htm) (see Appendix A3.1 for detailed calculation).

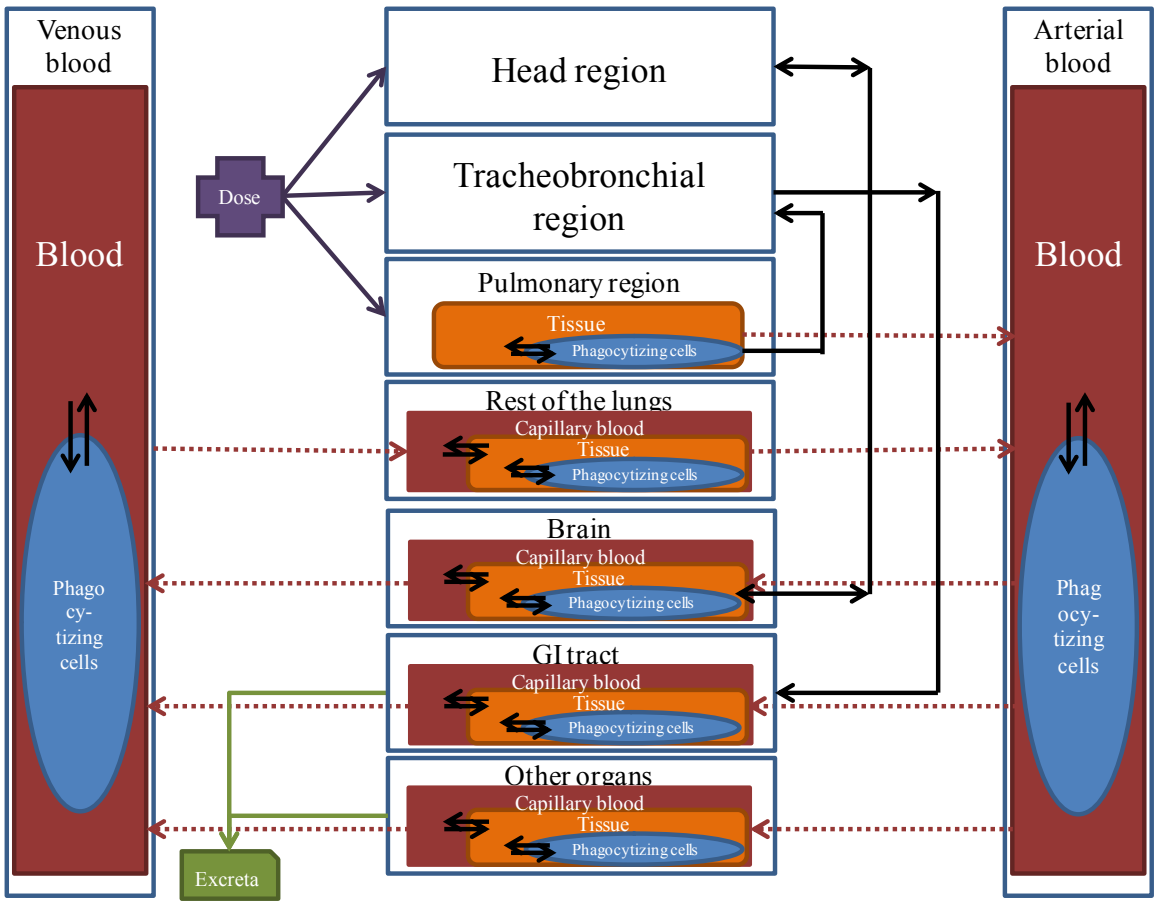

Fig. 3.2 Structure of the nanoparticle PBPK model for inhalation, with phagocytizing cells sub-compartment in each tissue.

After deposited in the head region, nanoparticles could be exchanged with the brain via olfactory bulb. Nanoparticles deposited in the tracheobronchial region could be transferred to the pharynx by mucociliar, then swallowed down to the GI tract and eventually excreted via feces. The mass balance analysis of observed data (see Fig. 3.4B in the results section) led us to made the assumption that the small enough nanoparticles (diameter < 70 nm) are those which predominantly have the potential to penetrate the alveolar wall and enter the systemic circulation. During exposure, a fraction of these small nanoparticles are directly transferred from the pulmonary region to the blood; once deposited in the pulmonary region, the small nanoparticles are also transferred to the blood at a different rate. Phagocytizing cells (PCs) loaded

with nanoparticles could also be transferred to the tracheobronchial region by mucociliary transportation.

The exchange of nanoparticles between blood and tissue in each organ is described as a flow- and diffusion-limited process. The flow limited process is controlled by a permeability coefficient, which limits the effective blood flow (Krishnan 2007). Except for brain, we assume the same permeability coefficient for all organs. The permeability coefficient for the brain compartment is set to zero, under the assumption of a highly efficient blood-brain barrier as observed by (Hardas et al. 2010). The diffusion-limited process is controlled by the tissue: blood partition coefficient and assumed to be the same for all organ tissues (Li et al. 2014).

A fraction of the nanoparticles entering the tissue is sequestrated by PCs until the PCs are eventually saturated. The PCs saturation level is organ specific, reflecting the variation in the abundance of PCs as well as differences in uptake capacity for different types of PCs among different organs. The effective uptake rate by PCs is a function of a maximum uptake rate and decreases as the PCs become saturated. This maximum uptake rate is the same for all compartments except for the spleen, due to its mesh-like structure that could trap nanoparticles in the spleen marginal zones and delay their contact with the splenic PCs (Demoy et al. 1999; Moghimi 2002). Nanoparticles can also re-enter the tissue after desorption from PCs by processes such as exocytosis (Chithrani and Chan 2007; Keighron et al. 2012). For a given animal species, the uptake capacity and uptake rate for each PC may vary between different nanoparticles, while the relative abundance of PCs densities in different organs was taken the same for all nanoparticle type.

Excretion of nanoparticles occurs from head region, GI tract, liver tissue, and capillary blood of kidneys. Degradation of CeO_2 nanoparticles is considered negligible for the time-scale of this study.

Main mathematical description of the model: We present here three main model equations describing the mass balances of a tissue *t* and of the PCs in this tissue. A more comprehensive deduction of the mathematical representation of the model is given in Appendix A3.2.

The dynamic of nanoparticles in the tissue sub-compartment can be majorly described in two parts: 1) the transfer between arterial blood and venous blood and; 2) interaction with the PCs. In certain organs, excretion of nanoparticles occurs as a clearance route from the body. The equation describing these processes is:

$$\frac{dM_t}{dt} = \overbrace{\frac{\chi_\alpha \times Q_t}{(1+\chi_\alpha)} \times (C_{art} - C_t / P)}^{transfer\,between\,arterial/venous\,blood} - \overbrace{(W_t \times C_t \times k_{t,ab} - M_{t,m} \times k_{de})}^{interaction\,with\,PCs} - \overbrace{\frac{dM_{e,ex}}{dt}}^{clearance\,by\,excretion} \qquad 3.1$$

where,

M_t [µg] – Amount of nanoparticles in the tissue of organ *t.*

χ_α [unitless] – Permeability coefficient between capillary blood and tissue.

Q_t [mL per hour] – Regional blood flow in organ *t*.

C_{art} [µg per g] – Concentration of nanoparticles in arterial blood.

C_t [µg per g] – Concentration of nanoparticles in the tissue of organ *t*.

P [unitless] – Partition coefficient of nanoparticles between tissue and blood.

W_t [g] – Weight of organ *t*.

$M_{t,m}$ [µg] – Amount of nanoparticles captured by PCs in organ *t*.

$k_{t,ab}$ [per hour] – Current uptake rate of nanoparticles by PCs in organ *t.*

k_{de} [per hour] – Desorption rate of nanoparticles from PCs to tissue.

$M_{e,ex}$ [μg] – Amount to excreta from source *e*. *e* only applies to tissue in liver and capillary blood in kidneys. The elimination of nanoparticles directly from the GI tract is described separately (Appendix A3.2).

The change in mass of nanoparticles in PCs is the uptake from the tissue minus desorption from PCs back to tissue. The uptake rate $k_{t,ab}$ will decrease as the amount captured approaches the total PCs saturation level characterized by the PCs uptake capacity per unit weight. The equation describing these behaviors is:

$$\frac{dM_{t,m}}{dt} = \overbrace{W_t \times C_t \times k_{ab0} \times (1 - \frac{M_{t,m}}{M_{t,cap} \times W_t})}^{uptake\,from\,tissue} - \overbrace{M_{t,m} \times k_{de}}^{desorption\,back\,to\,tissue} \qquad 3.2$$

where,

k_{ab0} [per hour] – Maximum uptake rate by PCs.

$M_{t,cap}$ [μg per g] – PCs uptake capacity for nanoparticles per organ *t* weight.

In addition, a series of equations describing the deposition and transfer of nanoparticles in different regions of the respiratory system can be found in the Appendix A3.2.

Model implementation: The PBPK model was implemented in Berkeley Madonna™ version 8.3.18 (Berkeley, CA). Parameters with unknown values were optimized by fitting the unknown model parameters against the experimental data. To create the most parsimonious model possible, we used a common generic parameter for most organs. We only differentiated parameters between compartments when it was indispensable to explain the dynamics of the CeO_2 concentration in that compartment in a physiologically meaningful way. The parameters fitted in this study are bolded in Table 3.1. The fraction of residual capillary blood left in organs when analyzed for nanoparticles contents and the PCs uptake capacities in organs were taken from our

previous model (Li et al. 2014). All other parameter values were taken from the scientific literature (Krishnan 2007; Travlos 2006; Brown et al. 1997; Bernareggi and Rowland 1991; Brookes 1967). Values of all parameters are listed in Table 3.1 below.

Evaluation of the model and identification of key parameters: The same model evaluation approach was applied as in Li et al. (2014): we determined the deviation from the line of unity between the $\log_{10}$ of measured and predicted values (McKone 1993), and calculated the corresponding R^2 and squared geometric standard deviation from the unity line.

Table 3.1A Description and values of parameters for the model that have the same values across all runs. Values in bold are fitted for this experiment.

Parameter (unit)	Description	Generic values [a]	Spleen (s)	Liver (l)	Lungs (lu)	Heart (h)	Kidneys (k)	GI tract (gi)	Brain (br)	Rest of the body (rest)	Blood (blood)
W_t/WB *(unitless)* [b]	% of organ weight to body weight	-	0.0031	0.040	0.0047	0.0034	0.0094	0.044	0.0053	0.84	0.050
$W_{t,b}/W_t$ (unitless) [c]	% of capillary blood in organ to organ weight	-	0.22	0.16	0.10	0.18	0.32	0.10	0.070	0.017	-
frQ_t (unitless) [d]	Fraction of cardiac output to organ	-	0.015	0.046	1	0.051	0.14	0.21	0.02	0.51	1
$M_{t,cap}$ (μg per g) [e]	Phagocytizing cells uptake capacity per organ weight	-	634	74.8	25.5, 32.5 [f]	5.03	1.08	0.0014	0.083	17.6	**0.016**
χ_α (unitless)	Permeability coefficient between blood to tissue	**0.30**	generic	generic	generic	generic	generic	generic	0	**0.018**	-
P (unitless) [e]	Partition coefficient between tissue and blood	**0.074**	generic	generic	generic	generic	generic	generic	generic	generic	1
k_{ab0} (per h) [e]	Maximum uptake rate by phagocytizing cells	**0.98**	**0.54**	generic	generic	generic	generic	generic	generic	generic	generic
k_{de} (per h) [e]	Desorption rate by phagocytizing cells	4.90×10^{-19}	generic	generic	generic	generic	generic	generic	generic	generic	generic
CLE_e (per h) [e]	Clearance rate to excreta	-	-	0.006	**2.70, 0.0017** [g]	-	0.0019	0.072	-	-	-
fr_β (unitless) [e]	Fraction of capillary blood of organs left when analyzed	0.144	generic	generic	generic	generic	generic	generic	0.37	generic	-

[a] $\chi\alpha$, P, k_{ab0}, k_{de} have generic values for most compartments. "generic" indicates the corresponding generic value for each parameter.

[c] Values were obtained by from Wenger et al. (2011) except for the GI tract, which was obtained from Bernareggi and Rowland (1991).

[c] Values were obtained from literature estimates of the percentage (w/w) of capillary blood in the organs (Brown et al., 1997) except for lungs and GI tract, which were estimated by the authors.

[d] Values obtained from literature (Brookes 1967; Bernareggi and Rowland 1991; Krishnan 2007).

[e] Values obtained from Li et al. (2014) and He et al. (2010), see Chapter 4 for details.

[f] 22.5 is for the lungs tissue, 32.5 is for the pulmonary region of the lungs.

[g] 2.70 is for direct clearance out of the body from the head region, 0.0017 is for clearance out of the body from the pulmonary region.

Table 3.1B. Descriptions and values of parameters for the interactions between different regions of the respiratory system and other organs for the four runs. Values in bold are fitted for this experiment.

Parameter (unit)	Description	Fresh 1	Fresh 2	Aged 1	Aged 2
fr_{head} (unitless) [a]	Fraction of inhaled nanoparticles deposited in the head region	0.098	0.11	0.096	0.097
fr_{tra} (unitless) [a]	Fraction of inhaled nanoparticles deposited in the tracheobronochial region	0.037	0.034	0.034	0.036
fr_{pul} (unitless) [a]	Fraction of inhaled nanoparticles deposited in the pulmonary region	0.16	0.14	0.14	0.16
fr_{gi} (unitless) [b]	Fraction of inhaled nanoparticles deposited in the GI tract	**0.62**	**0.90**	**0.91**	**1.41**
fr_{s} (unitless) [a]	Fraction of nanoparticles smaller than 70 nm in diameter	0.080	0.032	0.045	0.082
		Generic parameters			
k_{giab} (per h)	Absorption rate of GI tract	**0.0035**			
k_{pulb} (per h)	Transfer rate from pulmonary region to blood	**6.00E-06**			
k_{headbr} (per h)	Transfer rate from head region to brain	**0.0097**			
k_{brhead} (per h)	Transfer rate from brain to head region	**0.10**			
$k_{pulmtra}$ (per h) [c]	Transfer rate of inactive phagocytizing cells from pulmonary region to tracheobronchial region	**0.0011**			
k_{gi} (per h) [c]	Transfer rate from tracheobronchial region to GI tract	**0.056**			
$fr_{airblood}$ (unitless)	Direct transferred fraction from nanoparticles in air to blood	**0.26**			
$delay_{gi}$ (h)	Time delay for nanoparticles to travel from respiratory system to GI tract	**2**			
$delay_{f}$ (h) [d]	Time delay for nanoparticles in feces to be excreted out	8			

[a] Values calculated based on size distribution of SMPS data and MPPD model.

[b] This fraction (or the sum of this fraction with those for the respiratory system) could be higher than 1 due to uncertainty in the data caused by various factors such as ingestion of nanoparticles.

[c] Values obtained from He et al. (2010), see Chapter 4 for details.

[d] Value obtained from Wenger et al. (2011)

3.3 Results

3.3.1 Characterization of CeO_2 nanoparticles

The real time characterization of particle size distribution during an exposure study, as measured using the SMPS, is shown in Fig. 3.3A, for second study of aged nanoparticles. The individual distributions are shown for 60, 120, and 180 minutes after the start of the experiments as well as the average particle size distribution over the 240 minutes of particle generation. The size distribution indicates a slightly bi-modal distribution with peaks around 25 nm and 90 nm, with ~90% of the particles less than 200 nm in size. The estimates for the particle diameters are based on the equivalent diameter of a spherical particle with the same mass. The same size distribution trends were observed for both the fresh and aged particles. Additional details on the time history of the particle size distribution are provided in Fatouraie et al. (2015). After converting the number based concentrations to mass based concentrations, the size distribution for all four runs follow a log-normal distribution (Fig. A3.1, Appendix A3.1) with the following geometric means and 95% confidence intervals: 146 nm (95% CI, 50, 334), 195 nm (95% CI, 66, 334), 174 nm (95% CI, 61, 338), and 151 nm (95% CI, 52, 322), for fresh 1, fresh 2, aged 1, and aged 2 runs respectively.

The exposure concentrations based on filter pack measurements of CeO_2 nanoparticles for runs fresh 1, fresh 2, aged 1, and aged 2 were 172 $\mu g/m^3$, 585 $\mu g/m^3$, 483 $\mu g/m^3$, and 439 $\mu g/m^3$, respectively. During the fresh 2 run, exposure levels varied between an initial period of 197 minutes at low exposure level to fix an experimental problem, and a subsequent period of 163 minutes with much higher exposure, with 585 $\mu g/m^3$ being the time averaged concentration for the entire six

hours of exposure. The duration of the other three experiments was four hours. The exposure concentrations based on SMPS were 351 μg/m^3, 1 250 μg/m^3 during 163 minutes, 416 μg/m^3, and 433 μg/m^3, for runs fresh 1, fresh 2, aged 1, and aged 2 respectively. These SMPS based concentrations were highly consistent with the filter packs measured concentrations except for run fresh 1. Based on the size distribution recorded by the SMPS, the exposure concentrations of nanoparticles smaller than 70 nm for runs fresh 1, fresh 2, aged 1, and aged 2 were 27.9 μg/m^3, 38.9 μg/m^3 during 163 minutes 26.4 μg/m^3, and 35.6 μg/m^3, respectively, showing less variation between runs than the total concentrations.

TEM images are presented in Fig. 3.3B for typical fresh nanoparticles. The images show the nanoparticles are highly agglomerated structures which consist of small primary particles. TEM image analysis indicates the average diameter of the primary particles is 2 – 3 nm. Consistent with the SMPS data, analysis of the TEM images revealed no significant differences between the fresh and aged particles in terms of primary particle size or the agglomerated morphology.

Bulk powder samples collected on the impactor surfaces were used for XRD analysis and to determine the phase, composition and average crystallite size of the nanoparticles. Because the nanoparticles were sampled on the impactor surface (to acquire sufficient material for analysis), the results are biased to larger particle sizes than the particles transported to the exposure chamber. However, the results are expected to be consistent for composition and phase data. Typical XRD spectra for fresh nanoparticles are presented in Fig. 3.3C. All peaks in the spectra correlate well with the crystallographic reference database for CeO_2 [*Powder diffraction file, compiled by JCPDS. International Centre for Diffraction Data, Swarthmore, PA (1990)]*. The reference spectra are provided in Fig. 3.3C for comparison. Average

crystallite size was determined based on the spectral peak broadening according to the Scherrer equation using the methods described in Bakrania et al. (2007b). Detailed analysis was performed for the [111] and [220] features. An average crystallite size of 6.67 ±0.06 nm was determined, which is as expected, slightly higher than the TEM values of primary particle diameter.

Together the SMPS, TEM and XRD data indicate both the fresh and aged nanoparticles are agglomerates of small primary particles of CeO_2 approximately 2 – 3 nm in size, and the agglomerate dimensions (based on the SMPS data) span a size distribution up to ~200 nm in size.

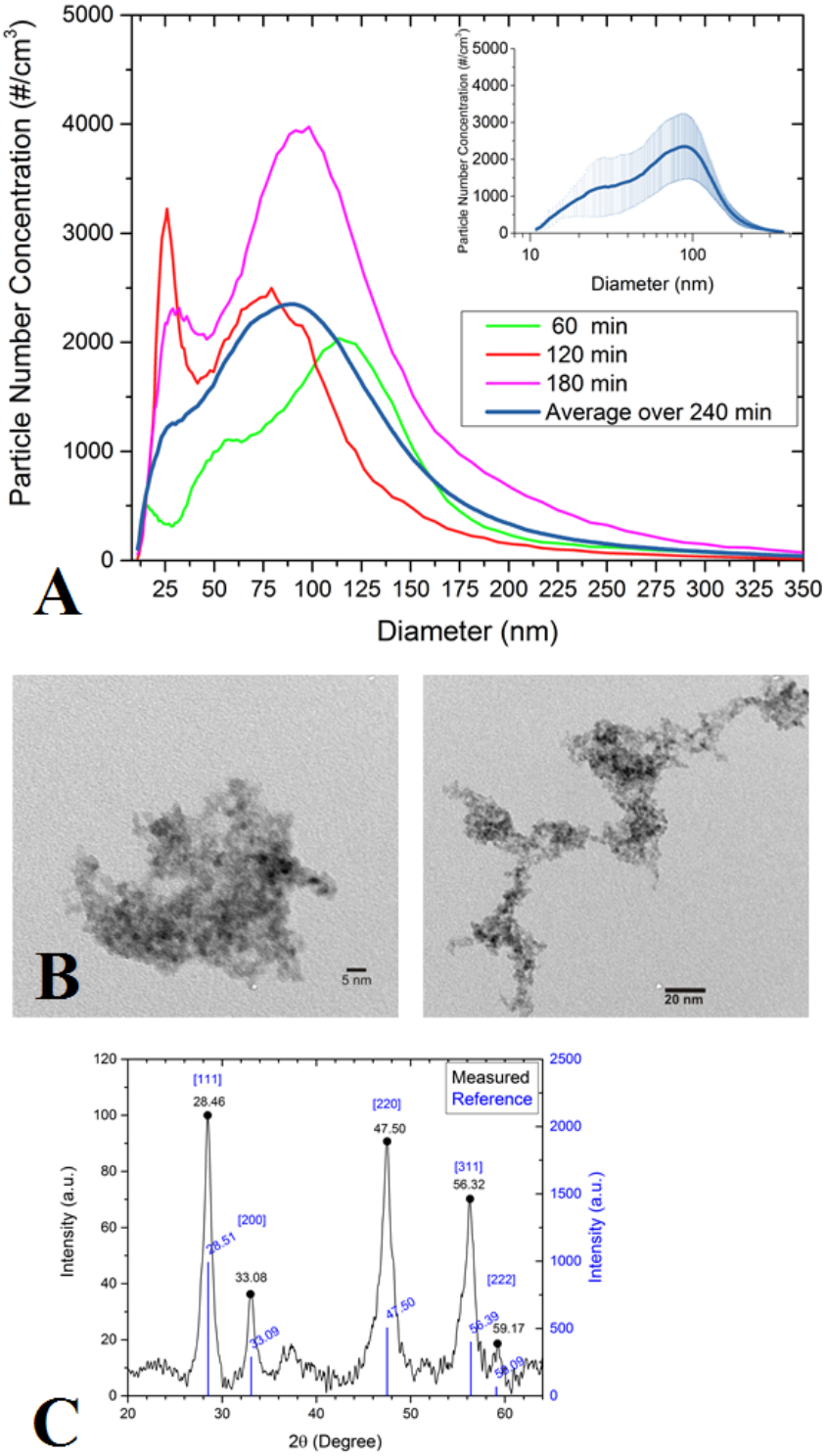

Fig. 3.3 Characterizations for the CeO_2 nanoparticles in this study. (A) Size distributions based on concentration in particle numbers recorded by the SMPS. (B) Bright field TEM images of CeO_2 particles with two magnifications. (C) XRD spectra of the powder sample collected on the impactor surface. A reference XRD peak is presented for comparison. The labels correspond to the peak angles.

3.3.2 Biodistribution of CeO_2 nanoparticles

Table 3.1 summarizes the concentrations of CeO_2 nanoparticles found in the organs. Lungs consistently had the highest concentrations across different runs, followed by feces. A preliminary study measured the evolution of CeO_2 nanoparticles concentrations in feces during the days following exposure (Appendix A3.3): compared to the first day post exposure, concentrations of CeO_2 nanoparticles in feces were reduced by 97% on the fourth day post exposure and remained stable at low concentrations afterwards, as also observed by He et al. (2010). For the extrapulmonary organs (blood, kidneys, heart, brain, liver, and spleen), concentrations in blood showed a slight decrease over time. Concentrations in spleen, liver, and kidneys rose steadily while concentrations in heart remained relatively stable. CeO_2 nanoparticles were detected in the olfactory bulb and in the brain for fresh 1 and fresh 2 runs, while mostly below detection limit for the aged 1 run. The concentrations in the olfactory bulb were exceptionally high for the fresh 2 run (higher than in other extrapulmonary organs by one order of magnitude). For the aged 2 run, the brain had the highest concentrations among all runs, while the concentrations in the olfactory bulb were below detection limit except on one day post exposure. Urine also had concentrations of CeO_2 nanoparticles comparable to blood concentration one day post exposure. The decreasing lung concentrations and the increasing concentrations in extrapulmonary organs may suggest that the CeO_2 nanoparticles deposited in the lungs could have served as a secondary source of exposure to the extrapulmonary organs, either by direct transfer from the lungs or through an indirect route via GI tract. Detailed concentrations for each rat are given in Appendix A3.4.

Combining these concentrations with the different organ weights, we then calculated the masses of CeO_2 nanoparticles and performed a mass balance analysis in Fig. 3.4. The total inhaled amount based on filter packs measured concentrations was lowest

for fresh 1, the highest for fresh 2, and was intermediary for aged 1 and aged 2 runs, with 2.56 μg, 13.35 μg, 7.20 μg, and 6.52 μg, respectively (Fig. 3.4A). One day post exposure, feces dominated the recovered masses (71% – 92%) due to their high weight and high concentrations of CeO_2 nanoparticles (Fig. 3.4A). Although higher in concentrations, the lungs had lower weights than the feces and therefore contributed less than the feces to the total recovered mass, while remaining very important (7% – 18%). Urine and extrapulmonary organs both contributed 4% – 6% to the total recovered mass in run fresh 1 but less than 0.5% of the total recovered mass for the other runs, the absolute recovered mass being approximately the same across the four experiments. The total inhaled amount for nanoparticles smaller than 70 nm based on SMPS measured concentrations for runs fresh 1, fresh 2, aged 1, and aged 2 were 0.42 μg, 0.40 μg, 0.39 μg, and 0.53 μg, respectively (Fig. 3.4B). Interestingly, these absolute amounts of lower size nanoparticle found in the extrapulmonary organs were also rather constant across all runs and varied by less than 65%, while the total inhaled amount varied by a factor of five. This may suggest that only the fraction of CeO_2 nanoparticles that are small enough could penetrate the alveolar wall and find their way into the extrapulmonary organs. The GI tract, muscles, skins, furs, and skeletons of the rats were not analyzed for CeO_2 contents. The unrecorded mass of nanoparticle in these organs could explain the lower than 100% recovery rates for the fresh 1 and fresh 2 runs. The overestimated recovery rates for aged 1 and aged 2 runs could be associated with the variability and uncertainty in feces measurements, or could also reflect additional exposure routes, e.g. deposition on furs and later ingestion.

Table 3.2 Measured concentrations of CeO_2 nanoparticles at different post exposure time in different organs (ng/g) [a, b].

	Fresh 1, filter packs based concentration 172 µg/m^3, SMPS based <70 nm concentration 27.9 µg/m^3			Fresh 2 [c], filter packs based concentration 585 µg/m^3, SMPS based <70 nm concentration 38.9 µg/m^3			Aged 1, filter packs based concentration 483 µg/m^3, SMPS based <70 nm concentration 26.4 µg/m^3			Aged 2, filter packs based concentration 439 µg/m^3, SMPS based <70 nm concentration 35.6 µg/m^3		
Organ	15 min	1 day	7 day	15 min	1 day	7 day	15 min	1 day	7 day	15 min	1 day	7 day
Blood	3.10±0.88	2.90±0.22	1.85±0.07	2.36±0.33	2.32±0.11	2.10±0.35	1.50±0.13	1.76±0.24	0.91±0.33	1.16±0.29	0.57±0.09	0.91±0.35
Lungs	317±129	225±31	93.9±129	1593±144	935±1317	1014±1417	1307±391	495±469	775±325	953±758	1421±250	929±317
Spleen	0.92±0.74	0.21±0.07	2.26±2.73	0.12±0.05	0.46±0.16	3.14±4.39	-	-	-	1.19±0.07	1.55±0.46	1.92±0.24
Liver	0.49±0.12	1.47±0.22	6.65±4.62	0.95±0.22	1.55±1.49	4.46±5.63	0.31±0.21	1.27±0.99	6.36±2.81	0.32±0.15	1.63±0.55	3.57±0.64
Kidneys	0.22±0.06	0.99±0.35	1.67±0.43	0.94±0.03	1.41±0.81	3.47±3.21	0.24±0.09	0.58±0.11	1.73±0.40	1.20±0.16	1.93±0.18	2.96±0.54
Heart	0.13±0.03	0.37±0.38	0.33±0.06	0.61±0.14	0.56±0.13	0.66±0.28	0.25±0.19	0.49±0.45	0.25±0.07	1.36±0.13	1.32±0.15	1.47±0.05
Brain	0.16±0.01	5.55±8.91	0.77±0.11	1.11±0.17	0.95±0.03	1.42±0.19	0.34 [d]	BDL	BDL	1.64±0.47	1.83±0.76	1.41±0.29
Olfactory bulb	0.69±0.07	0.84±0.08	0.69±0.29	13.0±10.6	5.92±3.65	4.69±1.71	BDL	BDL	BDL	BDL	0.92 [d]	BDL
Feces	-	91.6±4.3	-	-	769±431	-	-	672±431	-	-	656±117	-
Urine	-	5.79±3.37	-	-	-	-	-	1.66±1.26	-	-	1.98±2.06	-

[a] All values displayed are mean±standard deviation (n=3).

[b] "BDL" stands for below detection limit; "-" stands for no samples.

[c] The exposure duration for run fresh 2 was six hours, instead of four hours for all other runs. Please refer to text for more details.

[d] Only one sample was above detection limit.

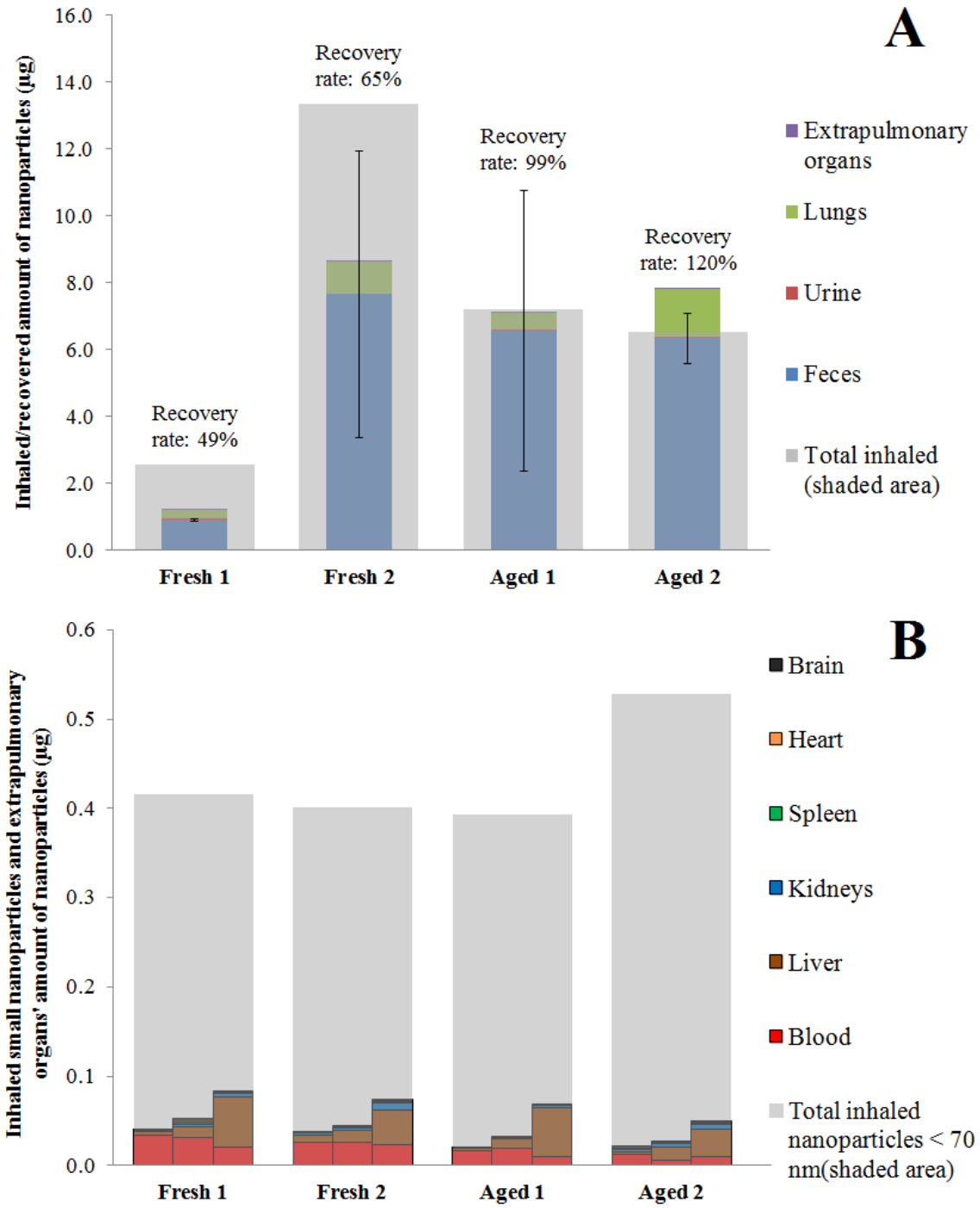

Fig. 3.4 Biodistribution of CeO_2 nanoparticles in different organs. (A) Mass balance of recovered amount on one day post exposure compared to calculated total inhaled amount of nanoparticles, error bars showing one standard deviation on feces. (B) Mass evolution for extrapulmonary organs compared to total inhaled nanoparticles < 70 nm.

3.3.3 PBPK model simulation

Fig. 3.5 shows the evolution of modeled with amount of nanoparticles and compares it with the observed data in the feces (cumulated data), the lungs and the

extrapulmonary organs. Model results are able to reproduce the different observed trends. The CeO_2 nanoparticle levels in the lungs increase rapidly during the exposure period, peak at the end of exposure, and then slowly decrease over time. After eight hours of delay, cumulated CeO_2 nanoparticles amounts in the excreted feces increase rapidly until around the third day after exposure, before entering a phase of much slower increase. The CeO_2 nanoparticles amounts in the extrapulmonary organs are much smaller than those in feces and lungs. These amounts increase quickly during the exposure period like what is seen in the lungs, but keep increasing after exposure until the end of the experiment (Fig. 3.4B and Appendix A3.5) in contrast to the decreasing levels in the lungs.

When examining individual extrapulmonary organs (Fig. A3.2 in Appendix A3.4), the model suggests that the CeO_2 nanoparticles are almost exclusively (over 99%) stored in the PCs in all organs except for the blood for the entire time span of this study. For the blood, during exposure period the transfer of CeO_2 nanoparticles from alveolar region to blood overwhelms the uptake by PCs in the blood. After exposure ends, there are still considerable amounts of CeO_2 nanoparticles not captured by PCs in the blood because the PCs are saturated due to the low uptake capacity of PCs in the blood. These "free" CeO_2 nanoparticles in the blood then circulate to other extrapulmonary organs and are captured by the PCs in those organs over time.

As illustrated in Fig. 3.5 and Fig. 3.6, the model's predictions for the four runs in this study fit generally well with measured data (R^2 ranged from 0.85 to 0.93). The GSD^2 ranged from 4.5 to 11.5, indicating that the accuracies of predictions of individual data points is of maximum one order of magnitude compared to the variation of four orders of magnitude differences between all organs and time points.

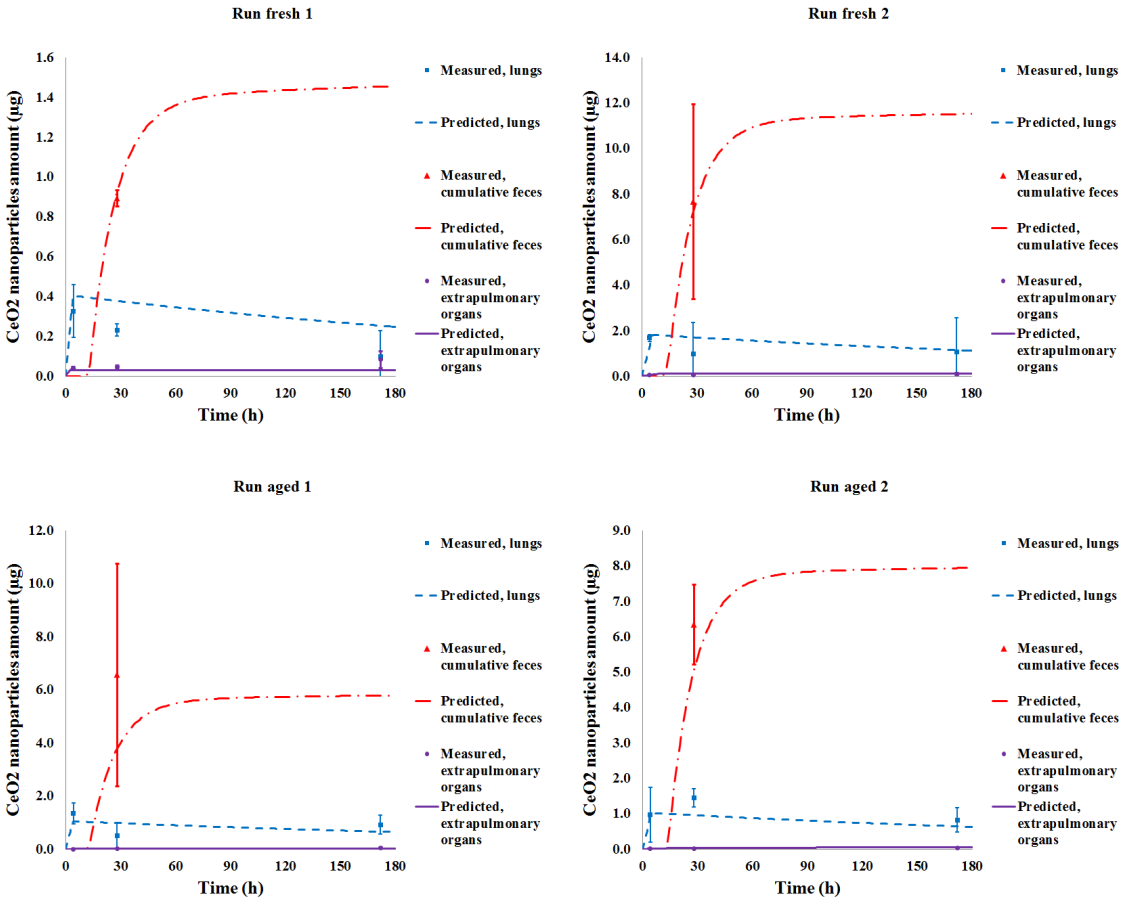

Fig. 3.5 Predicted amounts of CeO_2 nanoparticles in different organs compared to experimentally derived amounts. Error bars represent one standard deviation of measured data.

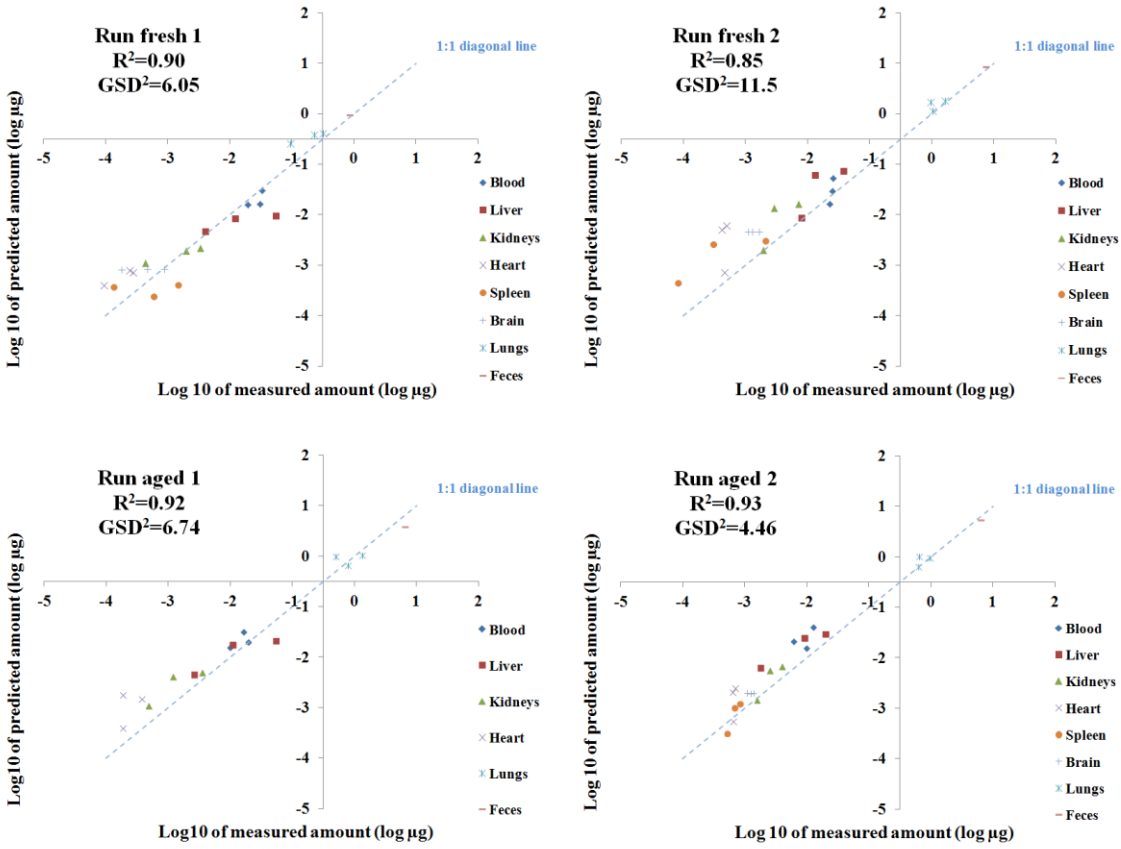

Fig. 3.6 Log_{10} of predicted CeO_2 nanoparticle mass in different organs as a function of log_{10} of measured mass.

3.4 Discussion

The experimental design of this study enabled us to compare freshly generated and UV-light aged CeO_2 nanoparticles with minimal changes in all other conditions. As the other conditions were well controlled, the differences in the characteristics of the fresh and aged CeO_2 nanoparticles can be explained solely by the UV-light aging process. Based on the results obtained from this study, the size distribution, morphology, and crystalline structure of the fresh and aged CeO_2 nanoparticles were similar. Meanwhile, other studies showed that under irradiation, some nanoparticles may have altered surface chemistry that resulted in different toxicity or behaviors in the environment (Badireddy et al. 2014; Rancan et al. 2014). It would be of interest to study the surface chemistry of fresh and aged CeO_2 nanoparticles in the future.

Performing the mass balance analysis is critical to ensure that the majority of introduced CeO_2 nanoparticles were accounted for. More than half of the recovered nanoparticles were found in the feces. Data on the feces showed substantial variations and could explain the near or more than 100% recovery rate observed in the runs for aged CeO_2 nanoparticles. The variation of the feces data may be due to a number of factors such as amount of nanoparticles deposited on rats' fur, the possible behaviors of the rats that may lead to ingestion of fur-deposited nanoparticles during and post exposure, and contamination of the collected sample feces by the fur of the rats or metabolic cages. Similarly, the high concentrations in the urine samples could actually result from contamination by the feces as urine and feces were in contact in the metabolic cages before being analyzed.

Despite the differences in total inhaled dose among the four runs (up to a factor of five difference), the amounts recovered in all the extrapulmonary organs were quite similar (within 65% of each other). In parallel, the amounts of CeO_2 nanoparticles of smaller sizes (70 nm) based on the SMPS's records also showed less than 35% variation. This could indicate that only the smaller nanoparticles could enter from the lungs to the blood circulation. Previous studies also confirmed this observation (Semmler et al. 2004; Takenaka et al. 2001). By filtering nanoparticles down to a gradient of maximum sizes, future research should be conducted to study the relationship between nanoparticle size and uptake in the extrapulmonary organs by inhalation.

Previous intravenous studies of nanoparticles do not support the hypothesis of nanoparticles penetrating the blood-brain-barrier and entering the brain (Hardas et al. 2010; Li et al. 2014). In this study, although the concentrations of CeO_2 nanoparticles we found in the brain and olfactory bulb were not consistently above detection limit,

the detected concentrations in the brain were of the same order of magnitude as that in the blood. This could support the hypothesis proposed by others that nanoparticles can enter the brain through the olfactory bulb (Oberdörster et al. 2004; Elder et al. 2006). Besides the cumulated feces, most of the recovered CeO_2 nanoparticles were found in the lungs for all four runs in this study, which is consistent with previous studies (He et al. 2010; Geraets et al. 2012; Aalapati et al. 2014). In contrast to He et al. (2010), this study showed higher amounts recovered in the feces than in the lungs. This difference can be explained by the difference in the exposure methods – He et al. used intratracheal instillation, which will limit nanoparticle deposition outside the respiratory system and exclude the possibility of direct intake to the GI tract via ingestion during exposure or from the nanoparticles deposited on the fur. Among the extrapulmonary organs, liver and blood had the highest amount of CeO_2 nanoparticles. The amount of nanoparticles in liver, spleen, and kidney increased over time, the amount in blood decreased over time, and the amount in heart and brain stayed relatively stable. These patterns agree with previous pulmonary studies as well in general (He et al. 2010; Geraets et al. 2012) although the blood concentration reported by He et al. (2010) kept increasing and the spleen results from Geraets et al. (2012) did not show any clear time evolution pattern. Aalapati et al. (2014) exposed mice to CeO_2 nanoparticles daily for four weeks and examined the contents in different organs two and four weeks after the last exposure. They found a steady decrease in nanoparticle concentrations in both the lungs and extrapulmonary organs. CeO_2 nanoparticles might have been cleared on a longer time frame. However, this decrease was not found by He et al. (2010) after four weeks of instillation in their study nor by us in our one week post exposure measurements.

The PBPK model in this study accounts for different physiologic mechanisms to predict and explain the dynamics of CeO_2 nanoparticle levels in different organs. In our model, in contrast to Bachler et al (2013), elimination to feces is predominantly originated in the GI tract lumen, not biliary excretion from the liver. This pathway is also supported by the high concentrations of nanoparticles found in the GI tract samples analyzed so far, which was one order of magnitude higher than those in the liver. The sources of nanoparticles in the GI tract lumen are a mixture of direct entry during exposure, ingestion from the deposited nanoparticles on the fur, and the transport of saturated PCs from the pulmonary region by mucociliary movement to the larynx then swallowed down to the GI tract. The first two are responsible for the fast increase of nanoparticles in feces within 24 hours post exposure while the mucociliary clearance of nanoparticles loaded PCs is responsible for the continuous excretion throughout the study. This transport of nanoparticle saturated PCs from the lungs to the GI tract then to feces is also the major contributor of the slow decrease of CeO_2 nanoparticles in the lungs and a widely accepted clearance route for inhaled nanoparticles (Takenaka et al. 2001; Hofmann and Asgharian 2003; Yang et al. 2008). The model predicts the majority of nanoparticles in the lungs are captured by the PCs in the pulmonary region. This agrees well with microscopic evidences from Takenaka et al. (2001).

According to the PBPK model, the majority of nanoparticles entering the blood are coming from the smaller nanoparticles in the pulmonary region during exposure period. This explains the sudden increase in the blood compartment in the model and the highest concentrations observed in the blood 15 min post exposure. After exposure, part of the nanoparticles transported in to the GI tract could be absorbed before being excreted during the fecal retention time. These absorbed nanoparticles

from the GI tract, together with small amounts of nanoparticles that are desorbed from the PCs in the pulmonary region, enter the systemic circulation and drive the levels of nanoparticles in the extrapulmonary organs (except for blood) higher or keep them stable throughout this study. The phagocytosis of nanoparticles is a well-documented phenomenon (Moghimi et al. 2001; Cho et al. 2009; Li et al. 2014) and supports the model's predicts that most of the CeO_2 nanoparticles are captured by PCs in the different organs. It is noteworthy that the level of exposure in this study is much lower than other CeO_2 nanoparticle pulmonary exposure studies (He et al. 2010; Geraets et al. 2012; Aalapati et al. 2014). The concentrations in extrapulmonary organs were also much lower than nanoparticle studies of intravenous injection (Wenger et al. 2011; Yokel et al. 2012; Yokel et al. 2009). Therefore, the PCs in all organs including the pulmonary region in the lungs are not saturated in the current model.

Most PBPK models for nanoparticles are only applicable to intravenous injection (Lin et al. 2008; Lee et al. 2009; Lankveld et al. 2010; Li et al. 2012; Li et al. 2014). Our model is one of the two existing PBPK models that can predict the biodistribution of inhaled nanoparticles (Bachler et al. 2013). Compared to Bachler et al. (2013), our model advances the field by taking into account the dynamic of nanoparticles in the feces directly excreted from the GI tract, which has been shown to be a major deposit of nanoparticles in this study and the results from He et al. (2010). Nevertheless, our model also has several limitations. First, the amount in the liver is systematically underestimated at the end of this study. Our model could not predict an increase over time large enough to reach the measured levels seven days post exposure (Appendix A3.5). We may miss certain physiologic pathways that cause this increase in the liver. For example, the nanoparticles may undergo endocytosis by the M cells in the GI tract for a period of time before being exocytosed and be in contact with the GI tract wall

(Shakweh et al. 2004). This may create a delayed effect for the nanoparticles to be absorbed by the GI tract and make the nanoparticles in the GI tract a source that can slowly release free nanoparticles to the GI tract to absorb over time. Second, the model is able to predict individual data points within one order of magnitude. However, the measured data also displayed large variations identified by large standard deviations (Table 1). These large variations in both the measured data and model predictions could be inherently caused by the exposure conditions as the rats' individual behaviors during and post exposure could result in different intake of CeO_2 nanoparticles.

3.5 Conclusions

CeO_2 nanoparticles were generated and aged under UV-light before being inhaled by rats in one integrated system in this study. Characterizations of the fresh and aged nanoparticles showed little differences in size distribution, morphology, or crystalline structure. The biodistribution of fresh and aged CeO_2 nanoparticles follow the same patterns, with the highest amounts recovered in feces and lungs. The slow decrease of nanoparticle concentrations in the lungs is explained by clearance to the GI tract and then to the feces. For the extrapulmonary organs, the nanoparticles level in the blood peaked at the end of exposure then went down. The PBPK model successfully predicts the dynamic of CeO_2 nanoparticles in various organs measured in this study. The model suggests most of the nanoparticles were captured by PCs, which agrees with the literature. When applying this model to other nanoparticle inhalation studies, the exposure conditions including the size distribution of the nanoparticles should be clearly defined as these would greatly affect model predictions.

Acknowledgement to this chapter:

The content of this chapter will be submitted to the journal of *Particles and Fibre Toxicology* as a full research paper. Author list:

Dingsheng Li, Masako Morishita, James G. Wagner, Mohammad Fatouraie, Margaret Wooldridge, Ethan Eagle, James Barres, Claude Emond, Olivier Jolliet

This study was funded by the U.S. Environmental Protection Agency under EPA STAR Program (grant No. RD-83486001). It is also supported by NSF grant #DMR-0315633. The authors wish to thank Kaitlin Cornwell, David Ciciora, Gina Sancricca, and Kathryn Thompson for their efforts on biological sample preparation.

CHAPTER 4[3]

Adaptation of the physiologically based pharmacokinetic model to other nanoparticles

4.1 Introduction

Nanoparticles have found wide application in multiple industries including drug delivery, fuel efficiency, cosmetics, etc. (Wakefield et al. 2008; Sao et al. 2015; Willhite et al. 2014). The population may be exposed to these nanoparticles either directly when using these nano-engineered products, or indirectly after the nanoparticles have been released into the environment. Various types of nanoparticles exhibit have been found to have different toxic effects in either *in vivo* or *in vitro* studies (Sayes et al. 2006; Aalapati et al. 2014; Zhang et al. 2011). Since negative human health risks result from the combination of exposure and toxicity potentials for nanoparticles as any other hazardous chemical, biodistribution of nanoparticles need to be well understood in order to perform meaningful human health risk assessments. However, tools to systemically and consistently evaluate the biodistribution of different types of nanoparticles are missing so far.

Physiologically based pharmacokinetic (PBPK) models have been used to predict the biodistribution of both drugs and harmful substances inside the body (Krishnan 2007) and can also be adapted to the study of nanoparticles biodistribution. A number of PBPK models emerged for different types of nanoparticles in recent years (Lin et al.

[3] The content of this chapter has been summarized in a conference proceeding paper for the International Conference on Safe Production and Use of Nanomaterials 2012. Li, D.; Emond, C.; Johanson, G.; Jolliet, O. Using a PBPK model to study the influence of different characteristics of nanoparticles on their biodistribution. *J. Phys.: Conf. Ser.* **2013**, *429* 012019.

2008; Lee et al. 2009; Lankveld et al. 2010; Li et al. 2012). However they face one or both of the following limitations: 1) lack the explanation power for certain biobehaviors of nanoparticles such as phagocytosis or mucociliary clearance from the pulmonary regions in the lungs; 2) built around one certain type of nanoparticles and have not demonstrated the ability to be adapted to predict biodistribution of other types of nanoparticles. As a result, it would be hard to use any one of the previous PBPK models for nanoparticles to successfully understanding the biodistribution of different types of nanoparticles via exposure from different routes. In addition, compared to multimedia fate models that can screen the environmental fate and human exposure of thousands of chemicals at a time (Arnot et al. 2006; Rosenbaum et al. 2008; Wambaugh et al. 2013), PBPK modelers have traditionally focused on one single chemical at a time. In the same time, there is a need to develop a PBPK model that can study different types of nanoparticles and identify which parameters can remain constant and which need to be adapted to reflect specific characteristics of the individual type of nanoparticles.

To address this need we aim to adapt the PBPK model developed for intravenous injection of polyethylene glycol-coated polyacrylamide (PAA-peg) nanoparticles and inhaled cerium oxide (CeO_2) nanoparticles to provide a common framework to assess different types of nanoparticles without major changes in the model structure. We aim here in particular to explore whether this framework is a good candidate for a parsimonious PBPK model, able to assess the biodistribution of different types of nanoparticles.

The objectives of this exploratory study are:

1. Extend the current PBPK model framework to other types of nanoparticles with minimum changes to the model itself while maintain the robustness of the model.
2. Evaluate the ability of the model to accommodate for unique characteristics of certain nanoparticles.
3. Explore how different characteristics of the nanoparticles are reflected in the most influential parameters determining the biodistribution

4.2 Methods

4.2.1 Experimental data

We first define a set of criteria to be met for a certain nanoparticles biodistribution dataset to be selected for analysis in this study. 1) The nanoparticles should be clearly characterized with the mean diameter of size, status of surface modification, and administrated dose. This is to ensure the characteristics of different types of nanoparticles can be compared. 2) The data set should present the biodistribution of nanoparticles in the blood and in at least five of the following organs: blood, liver, spleen, lungs, kidneys, heart, carcass, or excreta. This is to ensure the majority of important organs are accounted for. 3) There should be at least three time points when organs were analyzed for nanoparticles levels. This is to ensure a time evolution of the biodistribution in different organs can be deducted. 4) The mass balance based on the administrated dose and amount recovered in the measured organs should give at least a recovery rate of at least 50%, unless very specific reasons were given to account for the missing amount of nanoparticles. This is to ensure a holistic dynamic of nanoparticles between organs can be represented.

Based on the above criteria, the following datasets were selected (Table 4.1). For intravenous pathway: Wenger et al. (2011) presented data for 31 nm polyacrylamide (PAA, in addition to the PAA-peg used in Chapter 2 for model parameterization) nanoparticles administered by intravenous injection to rats; Panagi et al. (2001) provided biodistribution of 114 nm poly(Lactide-co-glycolide)-monomethoxypoly(ethyleneglycol) (PLGA-mPEG) nanoparticles administered by intravenous injection to mice; Liu et al. (2008) provided data for larger size 319 nm coated breviscapine-loaded poly(D, L-lactic acid) (BVP-PLA) nanoparticles administered by intravenous injection to rats; and Lankveld et al. (2010) was selected for three different sizes of silver (Ag) nanoparticles from 20 to 110 nm, administered by intravenous injections to rats. For pulmonary exposure pathway: He et al. (2010) was selected for CeO_2 nanoparticles through intratracheal instillation to rats. These literatures reported studies are compared to the PAA-peg nanoparticles and CeO_2 nanoparticles studies detailed in the previous chapters. Since all four runs of the CeO_2 inhalation study showed similar biodistribution patterns, run fresh 1 is selected because it has more samples measured than the other runs. Table 4.1 summarizes the specifications of each dataset, including the fraction of nanoparticles recovered in the experiment typically ranging from 10% to 100%.

Table 4.1 Specifications of different nanoparticles biodistribution experiments.

Nanoparticles	Size (nm)	Surface modification	Literature source	Animal species	Exposure route	Dose (μg)	Study duration (days)	Time points	Recovery rate
PAA-peg	31	Yes	Wenger et al., 2010	Rats	Single i.v. injection	7000	5	5	~ 100%
PAA	31	No	Wenger et al., 2010	Rats	Single i.v. injection	11300	5	5	~ 100%
PLGA-mPEG	114	Yes	Panagi et al., 2001	Mice	Single i.v. injection	1050	0.125	4	~ 100%
BVP-PLA	319	Yes	Liu et al., 2008	Rats	Single i.v. injection	2200	1	3	6% - 19%
Ag(20)	20	No	Lanveld et al., 2010	Rats	Five repeated i.v. injections	119	17	8	2% - 11%
Ag(80)	80	No	Lanveld et al., 2010	Rats	Five repeated i.v. injections	132	17	8	12% - 33%
Ag(110)	110	No	Lanveld et al., 2010	Rats	Five repeated i.v. injections	138	17	8	10% - 55%
CeO_2 (instilled)	13	No	He et al., 2010	Rats	Single intratracheal instillation	200	28	4	~ 100%
CeO_2 (inhaled)	146	No	Chapter 3 of this thesis	Rats	Four hours nose-only inhalation	2.56	7	3	49%

4.2.2 PBPK models

The PBPK framework and model has been described in details in Chapter 2 and Chapter 3. A brief summary is given in this section.

The PBPK model for intravenous injection consists of 10 compartments: arterial blood, venous blood, lungs, spleen, liver, kidneys, heart, brain, bone marrow, and the rest of the body (skin, muscle, skeleton, etc.). The PBPK model for pulmonary exposure consists of 10 compartments: arterial blood, venous blood, lungs, spleen, liver, kidneys, heart, brain, gastrointestinal tract (GI tract), and the rest of the body (skin, muscle, skeleton, etc.). Within each compartment, there are three sub-compartments representing capillary blood, tissue and phagocytizing cells (PCs) and remaining tissue. The conceptual framework of the model is illustrated in Fig. 4.1 and Fig. 4.2.

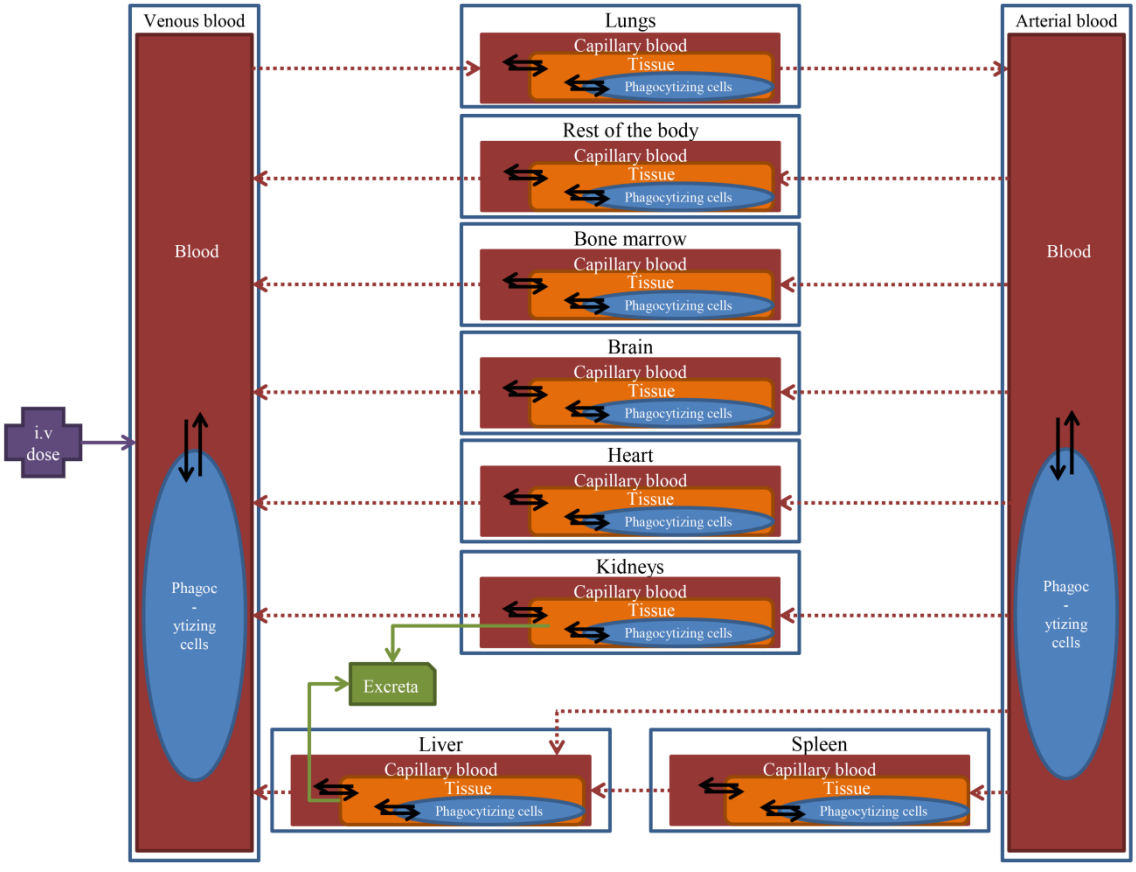

Fig. 4.1 PBPK framework for intravenous injection of nanoparticles.

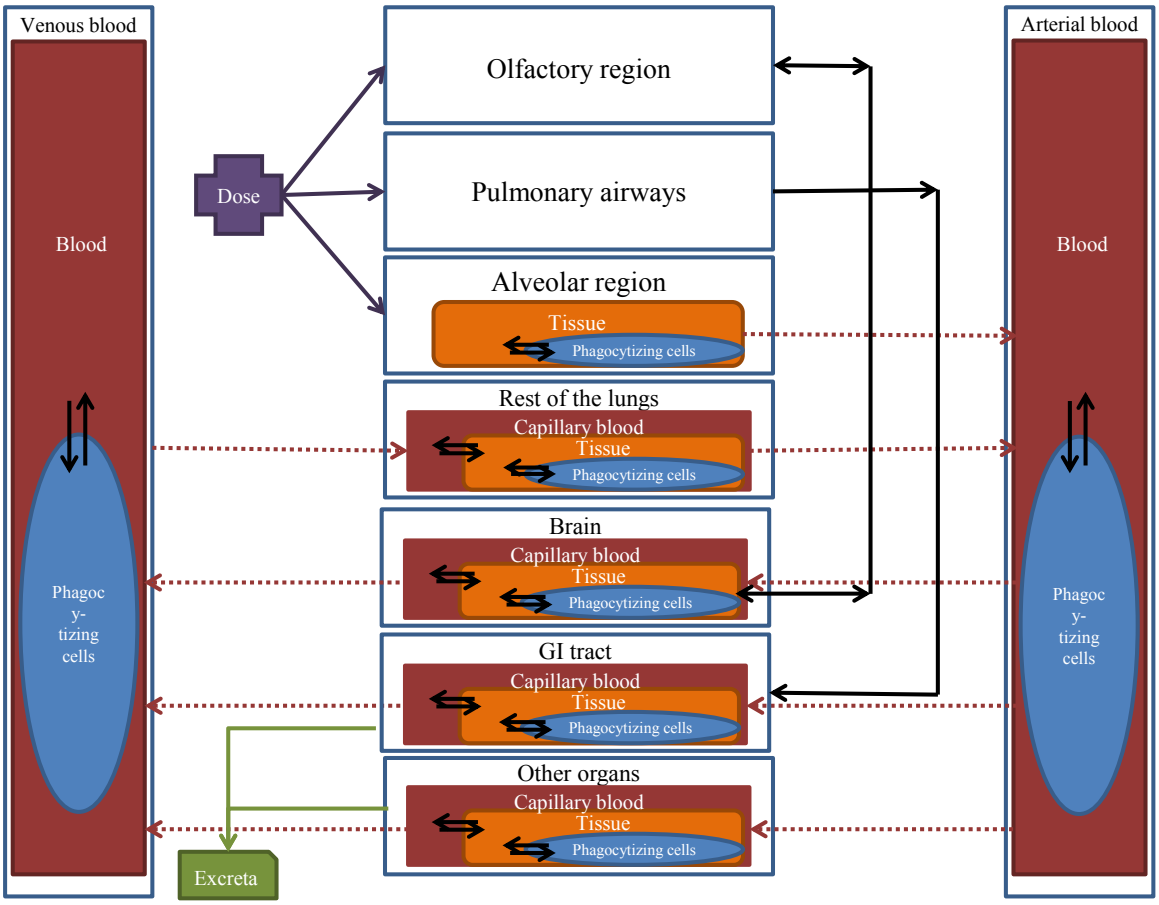

Fig. 4.2 PBPK framework for pulmonary exposure of nanoparticles.

The exchange of nanoparticle between blood and tissue in each organ is described as a flow- and diffusion-limited process, the latter being controlled by permeability parameters, which limits the effective blood flow (Krishnan 2007). The permeability coefficient for the brain compartment is set to zero, under the assumption of a highly efficient blood-brain barrier. The possibility of uneven distribution between blood and tissue at steady-state is taken care of by a blood-tissue partition coefficient.

Some of the nanoparticles that enter the tissue are captured by the tissue PCs. The uptake rate is a function of the efficacy and saturation level of the PCs and decreases as the nanoparticles in the PCs become saturated. For now, we assume that all PCs have the same efficacy and saturation level for a certain type of nanoparticle, independent of their location. However, the numbers of PCs differ between organs, causing different phagocytosis capacity at saturation. To fit a minimum number of

parameters, we will test the hypothesis that the relative saturation capacities of PCs across organs are independent of the nanoparticles types and be kept constant, while the absolute saturation capacities will change between different types of nanoparticles. We also assume that the uptake rate by PCs may also be altered to account for specific nanoparticles properties.

A removal rate of nanoparticles is introduced in the model to account for biliary excretion, urination, and possibly biodegradation for some nanoparticles.

The PBPK model was implemented in Berkely-Madonna^{TM} (version 8.3.18). For intravenous injection datasets, the model was first optimised by fitting the unknown model parameters against the PAA-peg experimental data. For the pulmonary exposure datasets, the inhalation model was first optimized using both the inhalation experiment presented in Chapter 3, and the instilled CeO_2 nanoparticles dataset (He et al. 2010) which provided complementary information on pulmonary region PCs saturation capacities due to its higher dosage. The other biodistribution datasets were used in a second stage to parameterize the model to each type of nanoparticles. During the parameterization process, the maximum parameters were kept identical. Only those parameters that have a physiological relationship with the characteristics of different types of nanoparticles were changed in order to reflect the unique differences across the analyzed nanoparticles. This was done to preserve the parsimony of the common model framework. In addition, this practice could help identify which parameters are closely linked to certain characteristics of the nanoparticles. The parameters that were fitted and varied among different nanoparticles are summarized in Table 4.2 in the Results section of this chapter.

4.2.3 Model evaluation and sensitivity analysis

For model evaluation we determine the deviation from the 1:1 line between the $\log_{10}$ of measured and predicted values, calculating the squared geometric standard deviation on the log as well as the corresponding R^2 (McKone 1993).

Model sensitivity can be evaluated for each model parameter based on the area under the curve (*AUC*) of blood and liver for the entire duration of each study. The *AUC* of blood and lungs are used to evaluate the sensitivity of parameters for the pulmonary exposure studies. To test the sensitivity, each parameter's value is increased by 10% and the *AUC* recalculated. The relative sensitivity is then calculated using the following equation

$$Relative\ sensitivity = \frac{dAUC_i / dp_j}{AUC_i / p_j} \qquad 4.1$$

Where AUC_i represents area under the curve (*AUC*) for compartment *i*, and p_j represents the parameter *j*.

4.3 Results

4.3.1 Comparison of time courses for nanoparticles of intravenous injection

The time courses for all the intravenous injected nanoparticles datasets are shown in Fig. 4.3 below. A first group of nanoparticles with medium or slow kinetic in the blood composed of PAA-peg, PAA, and PLGA-mPEG nanoparticles, exhibited a similar pattern of time courses for all measured organs. The levels of nanoparticles in the blood gradually decreased over time while the levels in the other organs compensated for this loss in the blood, suggesting the transfer of nanoparticles from the blood to the other organs. The richly perfused organs (including the lungs, liver, kidneys, heart, bone marrow, and brain), especially the liver and spleen, in these three datasets all reached a plateau rather quickly (less than about five hours). The time

course for the rest of the body showed different evolutions between the PAA-peg/PAA and the PLGA-mPEG nanoparticles datasets. For the PAA-peg and PAA nanoparticles, the amounts of nanoparticles in the rest of the body continued increasing towards 120 hours after injection and were much higher than those in the richly perfused organs. But in the PLGA-mPEG dataset the removal from the blood was faster, and the rest of the body saturated in less than five hours after injection at a level comparable with the richly perfused organs, suggesting a faster distribution of PLGA-mPEG nanoparticles from the blood to other organs.

A second group of intravenously applied nanoparticles, composed of for BVP-PLA and Ag nanoparticles showed a markedly different behaviour. The levels of nanoparticles in the blood for these two types of nanoparticles dropped over 90% in less than one hour after injection of the dose. Unlike the other intravenous injection datasets, the increase of nanoparticles amounts in other organs measured in the experiments for BVP-PLA and Ag nanoparticles was not large enough to compensate this huge decrease in the blood and resulted in much lower recovery rates of the total administrated dose. This indicates that there is a rapid removal kinetic for the nanoparticles that are not captured by the other organs, with eventually a competition between the rate constants for PCs capture and for removal from blood. In the Ag nanoparticles experiments, we can also see a steady decrease in the liver throughout a much longer timeframe (17 days versus five days at most for the other nanoparticles experiments) that suggest a slow release and elimination of nanoparticles captured by PCs or an elimination of the PCs themselves.

A more detailed examination of the model predicted time courses that differentiate the nanoparticles captured by PCs and those that are not can be found in Appendix A4.1.

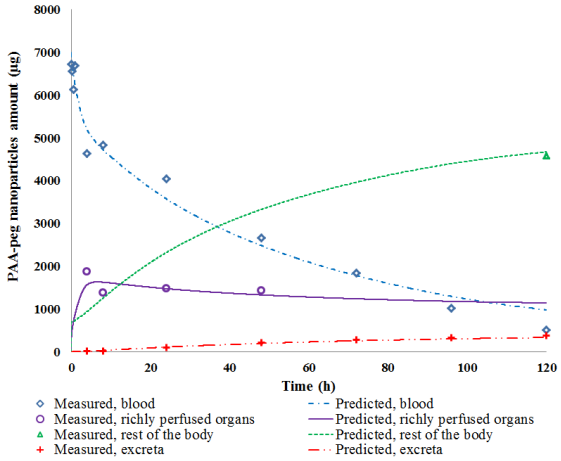
PAA-peg nanoparticles amount (µg)
Time (h)
Measured, blood
Measured, richly perfused organs
Measured, rest of the body
Measured, excreta
Predicted, blood
Predicted, richly perfused organs
Predicted, rest of the body
Predicted, excreta

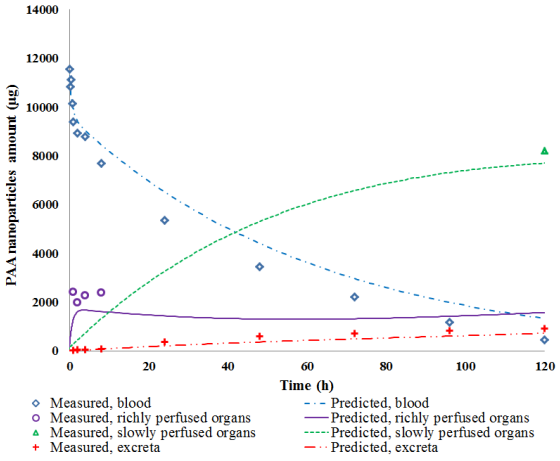
PAA nanoparticles amount (µg)
Time (h)
Measured, blood
Measured, richly perfused organs
Measured, slowly perfused organs
Measured, excreta
Predicted, blood
Predicted, richly perfused organs
Predicted, slowly perfused organs
Predicted, excreta

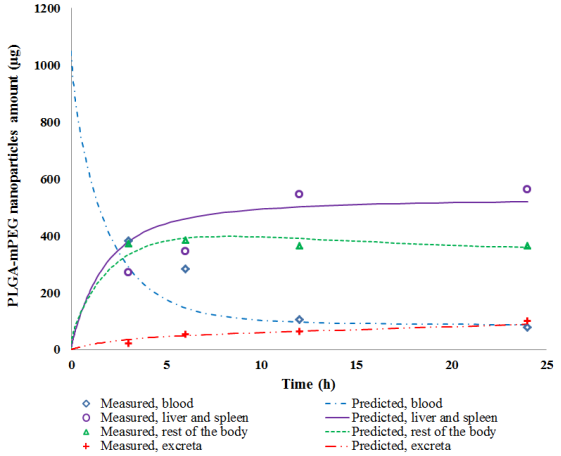
PLGA-mPEG nanoparticles amount (µg)
Time (h)
Measured, blood
Measured, liver and spleen
Measured, rest of the body
Measured, excreta
Predicted, blood
Predicted, liver and spleen
Predicted, rest of the body
Predicted, excreta

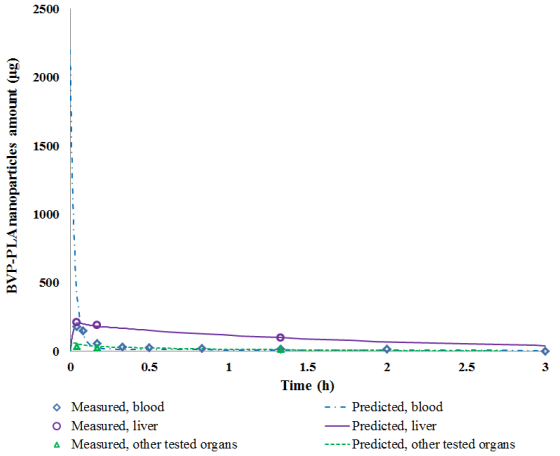
BVP-PLA nanoparticles amount (µg)
Time (h)
Measured, blood
Measured, liver
Measured, other tested organs
Predicted, blood
Predicted, liver
Predicted, other tested organs

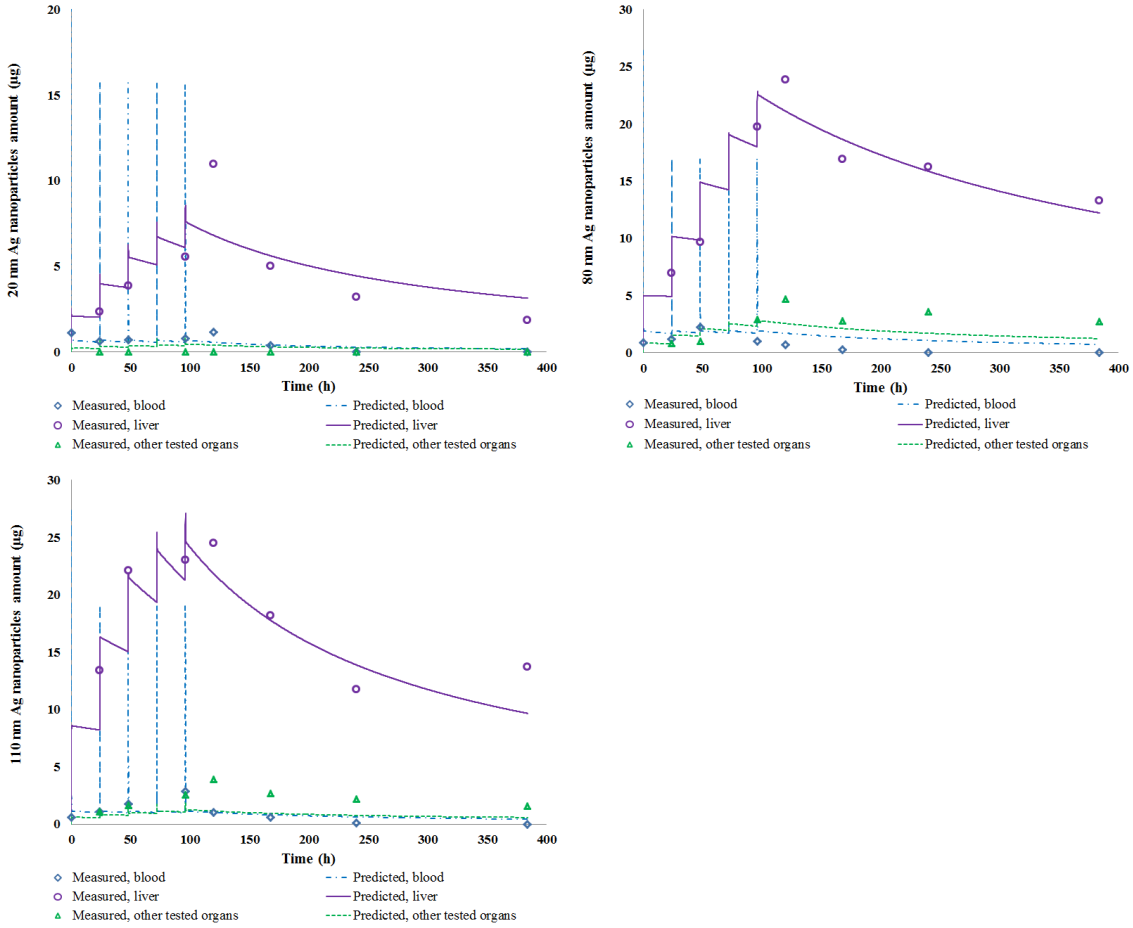

Fig. 4.3 Time courses for PAA-peg, PAA, PLGA-mPEG, BVP-PLA, and Ag nanoparticles of different sizes, intravenous injection.

4.3.2 Comparison of time courses for nanoparticles of pulmonary exposure

The time courses for the intratracheal instilled and inhaled CeO_2 nanoparticles are shown in Fig. 4.4 below. The time courses share a number of similarities: lungs and feces contain the highest amounts of nanoparticles; amount in the lungs slowly decreases after exposure; amount in the cumulated excreted feces increases quickly within two days of exposure, then keeps on increasing but at a much slower pace; the amount of nanoparticles in extrapulmonary organs is very small compared to amounts in lungs and feces. There are also some differences in the time courses for these two experiments: the inhaled CeO_2 nanoparticle experiment shows higher amounts in the feces than lungs but the instilled CeO_2 nanoparticle experiment shows the contrary; the decrease in the lungs is faster for the inhaled CeO_2 nanoparticles as it decreased

by more than 50% during the seven days post exposure, while the decline over the same period of time is only 9% for instilled CeO_2 nanoparticles; the amount of nanoparticles in the extrapulmonary organs is about 4% of the total recovered amount for all organs in the inhaled CeO_2 experiment but is only about 0.1% in the instilled CeO_2 experiment for which the applied doses is much higher.

A more detailed examination of the model predicted time courses that differentiate the nanoparticles captured by PCs and those that are not can be found in Appendix A4.1.

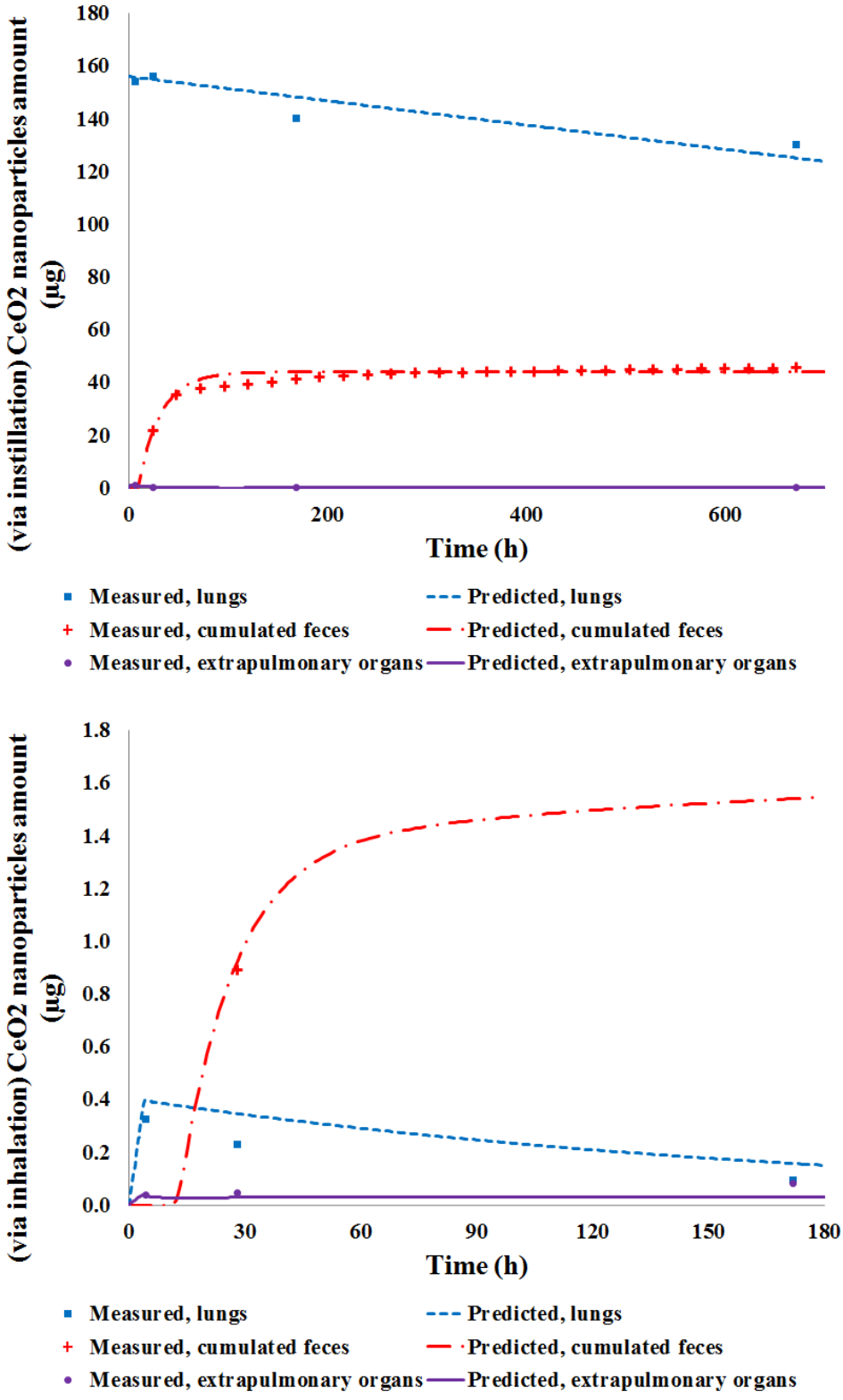

Fig. 4.4 Time courses measured and predicted amounts of CeO_2 nanoparticles exposed via intratracheal instillation and inhaled in lungs, cumulated feces and extrapulmonary organs.

4.3.3 Parameterization of the model

For the different types of nanoparticles in this study, Table 4.2 summarizes all the fitted parameters. Parameters that are totally independent of the type of nanoparticles such as organ weights are not shown in Table 4.2.

Removal rates: The two groups identified in the discussion of the time course showed markedly different removal rates: Those with slower kinetic have low removal rate $k_{removal}$ (PAA-peg, PAA, and PLGA-mPEG) and those with rapid removal consistently have a high $k_{removal}$ (BVP-PLA and Ag).

Uptake capacity at saturation: It was possible to keep the relative saturation capacities of PCs across organs at the same relative value for all studied nanoparticles, confirming that this relative saturation across organs may be independent of the nanoparticles types. When comparing PAA-peg with larger size PLGA-mPEG nanoparticles (both have surface modification and low $k_{removal}$), the *UCS* increased by 340% when size of the nanoparticles increased by 270%, suggesting that larger nanoparticles may have a larger uptake capacity for PCs at saturation. This would be plausible and consistent with the hypothesis that macrophage saturation may be related to the number rather than the mass of nanoparticles as discussed in Chapter 2, but this need to be further confirmed by looking at a larger number of experiments reaching saturation. When comparing PAA-peg and PAA nanoparticles (only difference is with or without surface modification), the *UCS* remained almost the same while k_{ab0} was higher for PAA nanoparticles. Since BVP-PLA and Ag nanoparticles had a high removal rate in the blood, the amount of nanoparticles reached the organs were too low to reach any meaningful saturation level of PCs. Therefore the model is not limited by *UCS* for these nanoparticles.

PCs uptake and desorption rates: It is the competition between k_{ab0} and $k_{removal}$ that is critical in the biodistribution of the nanoparticles that have high $k_{removal}$. In order to

model the decrease in organ amounts of BVP-PLA and Ag nanoparticles, the values of k_{de} for these nanoparticles were many orders of magnitude higher than the other nanoparticles. Interestingly, the amounts of nanoparticles for BVP-PLA and Ag nanoparticles in the brain were too high to be explained solely by the residual blood. Therefore, the permeability coefficient for brain was fitted to a non-zero value, whereas it is set to zero for the other nanoparticles.

Partition coefficient and transfer rates from tracheobronchial region to GI tract: Among parameters directly influencing the biodistribution of nanoparticles in the extrapulmonary organs, P showed great change between the inhaled and instilled CeO_2 nanoparticles, which was 60 times higher for the instilled CeO_2 nanoparticles than the inhaled CeO_2 nanoparticles, possibly associated with the much smaller particle size in the instilled nanoparticles. The values of other parameters for the extrapulmonary organs had similar values for the two experiments. This could indicate that the dynamics of nanoparticles outside the extrapulmonary organs are mostly independent of the nanoparticles in these two experiments. It is noted that k_{gi} was much higher for the instilled CeO_2 experiment than the inhaled CeO_2 experiment. This may be due to the exposure pathway. The tracheobronchial trees may response to the direct instilled solution more intensively and induce a faster transfer process to remove the foreign object. It was possible to keep the same partition coefficient for all organs for most experiments, a second separate partition coefficient value being needed to explain the observed biodistribution for liver and spleen in the BVP-PLA, 20 nm and 80 nm Ag experiments.

Table 4.2 Different nanoparticles and fitted parameters.

Parameters	Description	PAA-peg (31 nm)	PAA (31 nm)	PLGA-mPEG (114 nm)	BVP-PLA (319 nm)	Ag (20 nm)	Ag (80 nm)	Ag (110 nm)	CeO_2 (instilled, 13 nm)	CeO_2 (inhaled, 146 nm)
UCS (unitless) [a]	Uptake capacity at saturation for PCs	1.00	0.96	4.39	**11.7**	**0.71**	**3.99**	**4.02**	**0.23**	**0.23**
kab0 (per h)	Maximum uptake rate by PCs	16.1	20.9	8.4	19.9	16.18	16.1	16.0	0.98	0.98
kabs0 (per h)	Maximum uptake rate by splenic PCs	0.112	0.191	0.800	4.91	4.16	5.00	16.1	1.33	0.540
kde (per h)	Desorption rate by PCs	4.9E-19	4.9E-19	4.9E-19	1.4E+00	5.2E-03	5.6E-03	5.2E-03	4.9E-19	4.9E-19
P (unitless) [b]	Partition coefficient between tissue and blood	0.147	0.192	0.501	**2.10**	**0.63**	0.80	**0.80**	3.49	0.074
$k_{removal}$ (per h)	Removal rate from the body	0.018	0.02	0.116	32.4	14.5	4.96	5.00	0.008	0.008
χ_{rich} (unitless)	Permeability coefficient for richly perfused organs	1.1E-03	4.0E-04	9.9E-03	3.4E-01	4.4E-01	2.8E-01	2.9E-01	1.5E+00	3.1E-01
χ_{rest} (unitless)	Permeability coefficient for rest of the body	8.3E-05	2.7E-04	1.6E-03	3.0E-02	5.6E-08	7.2E-05	3.1E-04	9.9E-04	1.8E-02
χ_{brain} (unitless)	Permeability coefficient for brain	0.0E+00	0.0E+00	0.0E+00	3.3E-01	2.5E-03	2.5E-04	2.5E-03	0.0E+00	0.0E+00
		Parameters specific for pulmonary exposure								
M_{pulcap} (μg/g) [c]	Uptake capacity for PCs in pulmonary region								179	**179**
k_{gi} (per h)	Transfer rate from tracheobronchial region to GI tract								1.613	0.056
k_{headbr} (per h)	Transfer rate from head region to brain								0.004	0.01
k_{brhead} (per h)	Transfer rate from brain to head region								0.04	0.1
CLE_{gif} (per h)	Clearance from GI tract lumen								0.072	0.072

[a] *UCS* is the limiting factor for PAA-peg, PAA, and PLGA-mPEG nanoparticles due to the high doses injected to the blood. For the other nanoparticles, the PCs in all organs are far from saturation and the model is not limited by this parameter.

[b] For BVP-PLA, Ag (20 nm), and Ag (110 nm) nanoparticles, all organs except liver and spleen have a different value for P in order to fit the measured data. These values are 0.46 for BVP-PLA, 0.048 for Ag (20 nm), and 0.064 for Ag (110 nm).

[c] M_{pulcap} is not the limiting factor for CeO_2 (inhaled) since the dose is much lower than CeO_2 (instilled).

4.3.4 Evaluation of the model

Figure 4.5 displays separately for each type of particle and experiment the predicted concentration in each organ against the corresponding measured. The values of R^2 range from 0.69 to 0.97 (Fig. 4.5) indicate that the model predicted the experimental data relatively well across the different organs. Besides of the Ag nanoparticles, the GSD^2 for all nanoparticles fall within 10, indicating that the accuracies of predictions of individual data points are of maximum one order of magnitude. For the Ag nanoparticles, there are outliers in the blood data that induced a much larger GSD^2 (Fig. 4.5). According to the measured data (Lankveld et al. 2010), no nanoparticles were detected in the blood towards the end of the study. Since the limit of detection was not given in the original study, these data points cannot be represented on the log scale graph. In order to make these two data points available on the $\log_{10}$ scale, their values were set to 0.001 μg (smallest value found in blood elsewhere was 0.359 μg, no limit of detection was given in the original study).

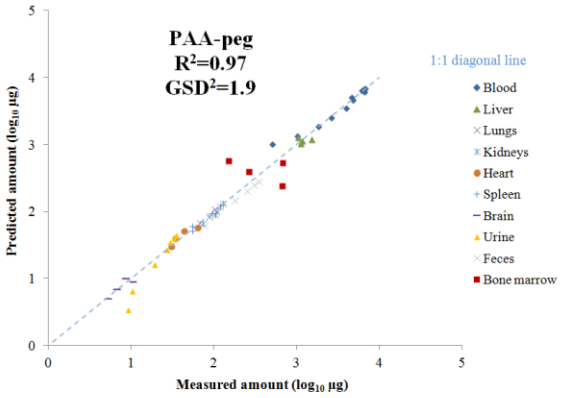
PAA-peg
R²=0.97
GSD²=1.9
1:1 diagonal line
Blood
Liver
Lungs
Kidneys
Heart
Spleen
Brain
Urine
Feces
Bone marrow
Predicted amount (log10 µg)
Measured amount (log10 µg)

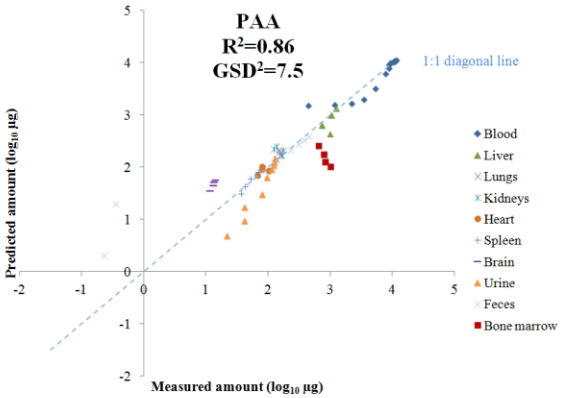
PAA
R²=0.86
GSD²=7.5
1:1 diagonal line
Blood
Liver
Lungs
Kidneys
Heart
Spleen
Brain
Urine
Feces
Bone marrow
Predicted amount (log10 µg)
Measured amount (log10 µg)

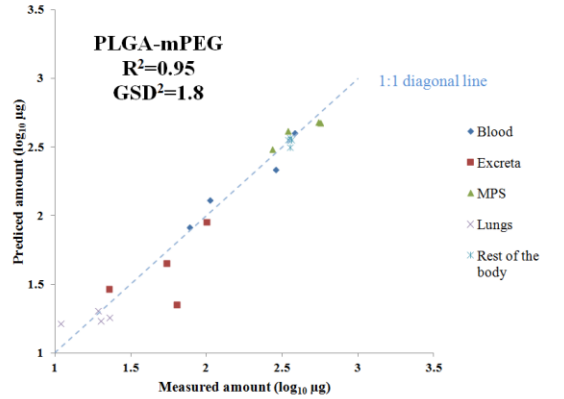
PLGA-mPEG
R²=0.95
GSD²=1.8
1:1 diagonal line
Blood
Excreta
MPS
Lungs
Rest of the body
Predicted amount (log10 µg)
Measured amount (log10 µg)

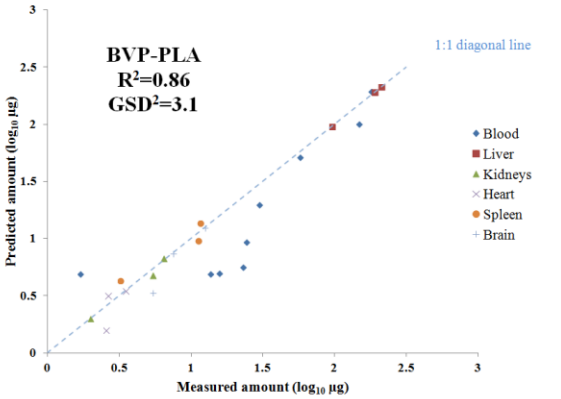
BVP-PLA
R²=0.86
GSD²=3.1
1:1 diagonal line
Blood
Liver
Kidneys
Heart
Spleen
Brain
Predicted amount (log10 µg)
Measured amount (log10 µg)

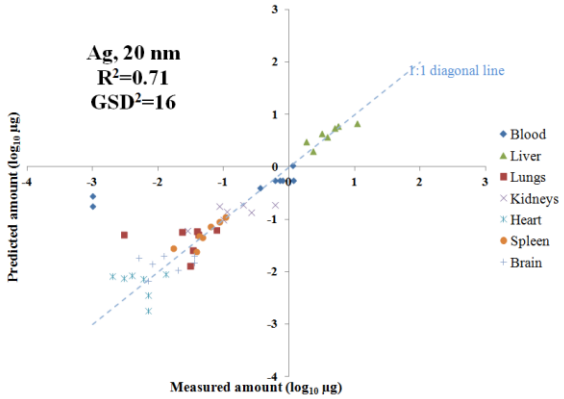
Ag, 20 nm
R²=0.71
GSD²=16
1:1 diagonal line
Blood
Liver
Lungs
Kidneys
Heart
Spleen
Brain
Predicted amount (log10 µg)
Measured amount (log10 µg)

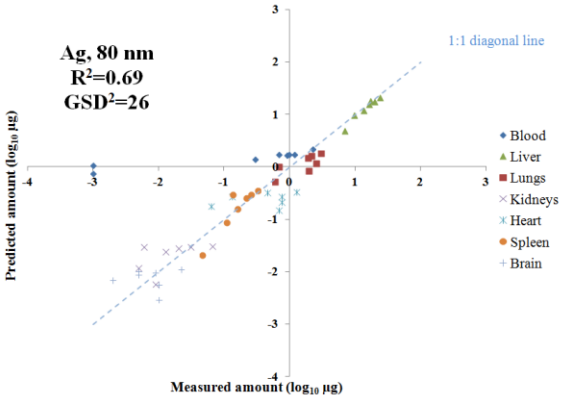
Ag, 80 nm
R²=0.69
GSD²=26
1:1 diagonal line
Blood
Liver
Lungs
Kidneys
Heart
Spleen
Brain
Predicted amount (log10 µg)
Measured amount (log10 µg)

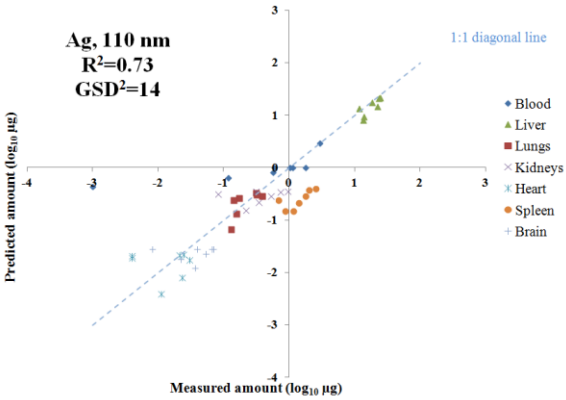
Ag, 110 nm
R²=0.73
GSD²=14
1:1 diagonal line
Blood
Liver
Lungs
Kidneys
Heart
Spleen
Brain
Predicted amount (log10 µg)
Measured amount (log10 µg)

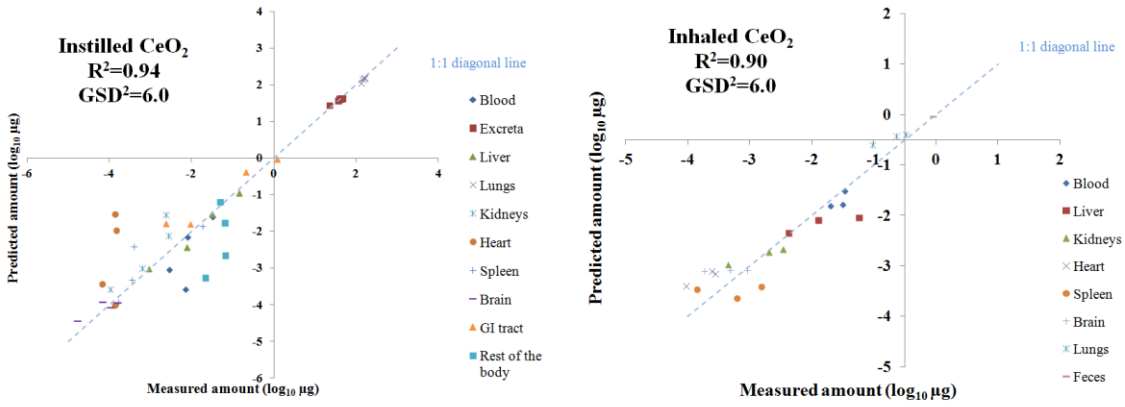

Fig. 4.5 Log_{10} of predicted nanoparticles amount as a function of log_{10} of measured amount.

4.3.5 Sensitivity of the model

The relative sensitivities were calculated according to Eq. 4.1 for all types of nanoparticles in this study and are listed in Table 4.3. For the intravenously injected nanoparticles, the model is most sensitive to the parameter *UCS* for PAA-peg, PAA, and PLGA-mPEG nanoparticles. Although the relative sensitivities for *UCS* to blood for the other nanoparticles have high values, it should be noted that it is only because most of the amount in the blood are stored in PCs for those nanoparticles. k_{ab0} only becomes a sensitive parameter to the model for BVP-PLA. For the nanoparticles with high $k_{removal}$ (BVP-PLA and Ag), the model is sensitive to both $k_{removal,}$ and k_{ab0}, that are of the same order of magnitude and reflect the competition between PCs uptake and direct removal from blood. k_{de} also is a sensitive parameter for these nanoparticles with fast kinetic as it participates indirectly in the competition between $k_{removal}$ and k_{ab0}. The amounts in liver are also sensitive to P for all three Ag nanoparticles, as it heavily influences the biodistribution in organs on the long term, the Ag experiments having the longest duration of measurements.

For the instilled and inhaled CeO_2 nanoparticles, the predicted amount of nanoparticles in the blood is sensitive to the partition coefficient P, especially for the

instilled CeO_2 nanoparticles. In contrast, as can be expected, variations in *P* will not affect the predictions of the amount of nanoparticles in the lungs for either experiment, since this amount is determined by the quantity instilled instillation or the quantity deposited in the respiratory tract in case of inhalation. The instilled CeO_2 nanoparticles had a high enough dose administrated in the experiment to saturate the PCs in the pulmonary region, therefore making M_{pulcap} a sensitive parameter. In contrast, the amount inhaled for the other CeO_2 nanoparticles was too small for the pulmonary region PCs to come close to saturation and the model is not sensitive to M_{pulcap} in this case. Looking at Table 4.3, it may seem that *UCS* is also a very sensitive parameter for both CeO_2 nanoparticles. However, this is because the *UCS* affects the M_{pulcap} just like the uptake capacities of PCs in other organs as well for the instilled CeO_2 nanoparticles and consequently impacts the overall biodistribution by decreasing the free nanoparticles in the pulmonary region that could enter the systemic circulation. Similarly to the Ag nanoparticles, the reason why the amount in blood is sensitive to *UCS* for the inhaled CeO_2 nanoparticles is because most of the amounts in the blood are stored in PCs.

Table 4.3A Relative sensitivities for some parameters [a].

Nanoparticles	*UCS*		k_{ab0}		k_{abs0}		k_{de}		*P*	
	Blood	Liver/lungs	Blood	Liver/lungs	Blood	Liver/lungs	Blood	Liver/lungs	Blood	Liver/lungs
PAA-peg	**-0.19**	**0.67**	0.00	0.00	-0.02	0.00	0.00	0.00	**-0.12**	**0.17**
PAA	**-0.38**	**0.54**	-0.01	0.00	-0.01	0.00	0.00	0.00	**-0.32**	**0.12**
PLGA-mPEG [b]	**-0.73**	**0.44**	-0.06	0.07	-0.01	0.06	-0.01	0.00	**-0.34**	0.10
BVP-PLA	**0.17**	0.01	0.06	**0.67**	0.00	0.00	-0.06	**-0.52**	0.00	-0.01
Ag(20)	**0.81**	0.00	0.08	**0.82**	0.00	0.00	-0.05	**-0.47**	0.02	**0.81**
Ag(80)	**0.89**	-0.01	0.04	**0.63**	0.00	0.00	-0.02	**-0.35**	0.00	**0.63**
Ag(110)	**0.88**	0.00	0.04	**0.66**	0.00	0.00	-0.03	**-0.36**	0.00	**0.66**
CeO_2 (instilled)	**-0.24**	**-0.11**	**0.13**	0.00	-0.04	0.00	0.00	0.00	**-0.58**	0.00
CeO_2 (inhaled)	**0.82**	0.00	-0.01	0.00	0.00	0.00	0.00	0.00	**-0.11**	0.00

[a] The relative sensitivities were calculated by the percentage change divided by the percentage change in the parameter (set at 10%) according to Eq. 4.1. Lungs were analyzed for the CeO_2 nanoparticles instead of the liver. Relative sensitivities with absolute values larger than 0.1 are marked in bold.

[b] Spleen and liver were grouped together in the results of the experiment.

Table 4.3B. Relative sensitivities for some parameters [a].

Nanoparticles	$k_{removal}$		χ_{rich}		χ_{rest}		χ_{brain}	
	Blood	Liver/lungs	Blood	Liver/lungs	Blood	Liver/lungs	Blood	Liver/lungs
PAA-peg	-0.05	-0.02	-0.01	0.02	**-0.49**	**-0.13**	N/A	
PAA	-0.04	-0.03	-0.03	0.04	**-0.31**	**-0.10**	N/A	
PLGA-mPEG [b]	**-0.11**	-0.02	-0.08	**0.11**	**-0.16**	-0.08	N/A	
BVP-PLA	**-0.77**	**-0.87**	0.03	**0.13**	-0.02	-0.04	0.00	0.00
Ag(20)	**-0.24**	**-0.88**	0.01	0.08	0.00	0.00	0.00	0.00
Ag(80)	**-0.12**	**-0.77**	0.01	**0.12**	0.00	0.00	0.00	0.00
Ag(110)	**-0.14**	**-0.79**	0.01	**0.12**	0.00	0.00	0.00	0.00
CeO_2 (instilled)	0.00	0.00	-0.03	0.00	-0.03	0.00	N/A	
CeO_2 (inhaled)	0.00	0.00	0.00	0.00	-0.03	0.00	N/A	

[a] The relative sensitivities were calculated by the percentage change divided by the percentage change in the parameter (set at 10%) according to Eq. 4.1. Lungs were analyzed for the CeO_2 nanoparticles instead of the liver. Relative sensitivities with absolute values larger than 0.1 are marked in bold.

[b] Spleen and liver were grouped together in the results of the experiment.

Table 4.3C. Relative sensitivities for some parameters [a].

Nanoparticles	M_{pulcap}		k_{gi}		k_{headbr}		k_{brhead}		CLE_{gif}	
	Blood	Liver/lungs	Blood	Liver/lungs	Blood	Liver/lungs	Blood	Liver/lungs	Blood	Liver/lungs
CeO_2 (instilled)	**-0.40**	**-0.11**	0.00	0.00	0.00	0.00	0.00	0.00	0.00	0.00
CeO_2 (inhaled)	0.00	0.00	0.00	0.00	0.00	0.00	0.00	0.00	-0.05	0.00

[a] The relative sensitivities were calculated by the percentage change divided by the percentage change in the parameter (set at 10%) according to Eq. 4.1. Lungs were analyzed for the CeO_2 nanoparticles instead of the liver. Relative sensitivities with absolute values larger than 0.1 are marked in bold.

4.4 Discussion

The PBPK model predictions of the nanoparticles biodistribution for these datasets agree relatively well with the measured data when including phagocytosis. The similarities and differences in the biodistribution across the analysed datasets can be explained by the PBPK model framework after considering the specific characteristics of the nanoparticles and the specifications of experiment such as exposure method and administrated dose. The PBPK model indicates that the saturation effect in the richly perfused organs is due to the PCs uptake of nanoparticles. The maximum uptake amount for the PCs determines the saturation level is observed when the administrative dose is high enough.

For the nanoparticles with slow or medium kinetic, the amount of nanoparticles in the rest of the body stopped increasing after about five hours for the PLGA-mPEG experiment instead of following the course in the PAA-peg and PAA experiments. This can be explained by the relatively low uptake rate by PCs and higher permeability coefficients between tissue and capillary blood. The combination of these two factors enables a quicker removal from the blood to the other organs in which the nanoparticles were captured. Also, once captured by the PCs, the nanoparticles will be relatively immobilized, explaining the very low decrease of nanoparticles amounts in the organs (except for blood, which has a low PCs uptake capacity) after saturation across all experiments. The tissue sub-compartment in organs may only accumulate nanoparticles after the PCs sub-compartment are saturated and there are still considerable amounts of nanoparticles in the blood, as shown in the PAA-peg and PAA nanoparticles experiments (Fig. 2.3 and Fig. A4.2).

For the nanoparticle with fast removal, According to (Liu et al. 2008), the core of the BVP-PLA nanoparticles, BVP, has a very short half-life in blood, which is reflected in the sharp decrease in the blood after administration of BVP-PLA nanoparticles and the low recovery rate over all. For the Ag nanoparticle, it is suggested by Lankveld et al. (2010) that the administered silver nanoparticles could be transformed into silver ions inside the body, a transformation associated with a dramatic change in behaviour. This would possibly explain the fast decrease in the blood and the lower recovery rates. These specific characteristics of the BVP-PLA and Ag nanoparticles also lend support to having a high removal rate in the PBPK model. In addition, both of these studies conducted a short term (less than an hour) kinetic study of the blood concentration following injection and confirmed this fast remove phenomenon. The data from BVP-PLA and Ag nanoparticles support the model having a permeability coefficient for the brain, indicating the blood brain barrier could be breached, which seems contradictory to other researches (Sadauskas et al. 2007; Hardas et al. 2010). However, the BVP-PLA nanoparticles were releasing BVP that are not nanoparticles (Liu et al. 2008) and are known to enhance the permeability of blood-brain barrier (Liu et al. 2002). Some other studies also suggest that silver nanoparticles could cross the blood-brain barrier by transcytosis or increasing the permeability of brain microvessel endothelial cells (Trickler et al. 2010).

The difference in behaviour between the instilled and inhaled CeO_2 nanoparticles can be associated to the difference between the exposure pathways. When instilled, the nanoparticles have little chance of entering the GI tract directly and the transfer to feces will occur through the slow clearance from the pulmonary region by mucociliar movements. But inhalation exposure could have a direct transfer into the GI tract. In addition, nanoparticles deposited on the fur during inhalation experiments could also

serve as a secondary exposure source, as rats will unintentionally ingest the nanoparticles when licking their fur. These differences resulted in a higher fraction of the administrated dose in the GI tract for the inhaled CeO_2 nanoparticle, leading to a higher amount of nanoparticles in the feces than the lungs. On the contrary, the instilled CeO_2 nanoparticles are directly instilled in the lung, thus the higher concentration in lung than in feces. In addition, the administrated dose in the instilled CeO_2 experiment was almost 100 times higher than the dose in the inhaled CeO_2 experiment. This resulted in the saturation of PCs in the pulmonary region for in the instilled experiment but not in the inhaled experiment. As a result, for the instilled CeO_2 nanoparticle, there were abundant free nanoparticles in the pulmonary region to migrate into the systemic circulation, causing a steady rise of nanoparticles amount in the extrapulmonary organs. In contrast, for the inhaled CeO_2 nanoparticles, the amount deposited in the pulmonary region was almost totally captured by the PCs in vicinity and limited their transfer through the alveolar wall into the blood stream. This explains why the inhaled CeO_2 experiment did not show the steady increase of nanoparticles amount across all extrapulmonary organs. Without the direct transport of free nanoparticles from the air in the pulmonary region during exposure, we would have seen much lower amount in the extrapulmonary organs for the inhaled CeO_2 nanoparticles.

By examining the differences in certain parameters in the model for different nanoparticles, we may explore the relationship between the characteristics of nanoparticles and the determinants of their biodistribution. Choi et al. (2014) also observed a positive correlation between size of the nanoparticles and uptake by PCs. This could indicate that the PCs are saturated by the number of nanoparticles rather than absolute mass, as deducted in Chapter 2 of this thesis. An alternative explanation

would be the larger nanoparticles may more easily attach to the PCs, as suggested by previous studies (Tabata and Ikada 1988; Champion et al. 2008). The results of parameterization of the model for the experiments in this study do not disprove this positive correlation, but cannot strongly confirm it either because most experiments did not administrated a dose high enough for the PCs to reach saturation. Compared to the other nanoparticles in this study, the BVP-PLA and Ag nanoparticles are removed from the body three to four orders of magnitude faster than the other nanoparticles in this study. The high removal rates are justified by the short half-life of BVP for BVP-PLA nanoparticles and possibility of conversion to ionic form for silver nanoparticles (Liu et al. 2008; Lankveld et al. 2010).

Interestingly, even with the same core and no surface modifications, the partition coefficient between tissue and blood for the instilled CeO_2 nanoparticles is much larger than that for the inhaled CeO_2 nanoparticles. Literatures suggest that the partition coefficient may be linked with the biocorona formation around nanoparticles (Nel et al. 2009; Lundqvist et al. 2008) with size and surface properties playing a main role (Lundqvist et al. 2008). The differences between the partition coefficients between these two types of CeO_2 nanoparticles may therefore be caused by their different sizes, since there are little differences in other characteristics of these two nanoparticles. The PAA and PAA-peg nanoparticles also have different partition coefficients. In this case, the difference may be linked to the different surface properties since the size of these two nanoparticles are the same. The relationship between a specific characteristic of nanoparticles with the partition coefficient is less clear for PLGA-mPEG, BVP-PLA, and Ag nanoparticles, as they differ from each other in core, size, and surface modifications.

The model's sensitivity to *UCS* for most nanoparticles in this study reflects the role of PCs, as a major reservoir for nanoparticles. The reason for the model for BVP-PLA is not sensitive to *UCS* but to k_{ab0} can be explained by the short duration of the BVP-PLA nanoparticles study, which lasted only for three hours while experiments for the other nanoparticles were at least 24 hours. It is possible that the PCs cannot be saturated within three hours in the BVP-PLA nanoparticles study and therefore making the *UCS* an insensitive parameter but the k_{ab0} a sensitive one.

4.5 Conclusions and outlook

The PBPK model framework developed in Chapter 2 and 3 can be extended to other nanoparticles with little modifications and maintain its robustness in predictability. It is found that the main differences in biodistribution of the nine nanoparticles examined here can be explained either by the exposure procedure or certain characteristics of the different nanoparticles. By adjusting only the parameters linked with unique characteristics of the nanoparticles, the model offers insights on how these characteristics may affect the nanoparticles biodistribution.

For further study, it is worth designing more detailed experiments to test the hypothesis of increase in nanoparticle size would increase the uptake capacity of PCs. Since a very fast removal of the Ag nanoparticles from the body was observed but little is known about their fate, it would also be of interest to pay more attention to the excretion within one hour of dosing since for the Ag nanoparticles and identify what form – nanoparticles or ions – there are in the excreta.

Acknowledgements to this chapter:

This chapter is based on a conference paper titled "Using a PBPK model to study the influence of different characteristics of nanoparticles on their biodistribution" published in *Journal of Physics: Conference Series*.

This study was supported by U.S. EPA grant EPA-G2010-STAR-N1, the Swedish Council for Working Life and Social Research, and BioSimulation Consulting Inc., DE, USA.

CHAPTER 5

Conclusions

This thesis developed a PBPK model that describes the biodistribution of PAA-peg nanoparticles through intravenous injection and CeO_2 nanoparticles via inhalation. The model was able to represent well the time evolution observed in collected experimental data. Though multiple parameters needed to be fitted, the physiologically sound mechanisms used to build the model offer explanations of most phenomena observed in the biodistribution of nanoparticles. The parsimonious design allows the model to be extended to different types of nanoparticles by modifying a limited number of parameters, while maintaining its robustness in predictions. We first discuss hereby the lessons learned, potential, and limitations of this model, regarding its ability to answer the three scientific questions raised in Chapter 1 about phagocytosis, exposure by inhalation and the influence of particles characteristics. We then discuss the need and ideas for future research opportunities stemming from this thesis. We finally look at perspectives and outlook.

5.1 Lessons learned, potential, and limitations

Lessons regarding the biodistribution of nanoparticles inside the body can be learned from the PBPK model developed in this study. In the meanwhile, there are still several limitations exist that prevent the model to reach its full potential. These lessons, potential, and limitations revolve around three topics in this thesis, which are accounting for phagocytosis in the biodistribution of nanoparticles, relating inhaled

nanoparticles to extrapulmonary uptake, and connecting biodistribution with nanoparticles characteristics.

5.1.1 Accounting phagocytosis in the biodistribution of nanoparticles

A sub-compartment of PCs for specifically addressing phagocytosis of the nanoparticles, which is an experimentally proved nano-specific phenomena, is incorporated for each organ in the PBPK model developed in this thesis. By accounting for phagocytosis, the PBPK model is adequate to explain the organ saturation effect observed in measured data. Within 15 hours, most nanoparticles are captured by the PCs unless the given dose is much above the saturation level. Depending on the dose administrated, PCs could be the major reservoir of nanoparticles in the body. When the administrated dose is not high enough to saturate the PCs within organs or there is a high removal rate directly from the blood, the uptake rate of PCs exhibits a greater role in the biodistribution of nanoparticles, especially for the short-term duration after exposure.

Although different types of PCs could have different uptake limits and rates for the same nanoparticles, this thesis uses a single uptake rate for all PCs in all organs (except for the spleen, which has a different structure that can delay the contact between nanoparticles and splenic PCs). This single uptake rate is a proxy of the average of uptake rates for different types of PCs weighted by their relative population in the organs. The results show this single uptake rate is sufficient to model the biodistribution of nanoparticles. The relative uptake capacities of the PCs across organs should be independent of the type of nanoparticles that enters the body. This is because the relative uptake capacities are a representation of the abundance of PCs in different organs and should be only dependent on the animal species of study. The parameterization of uptake capacities of PCs in the PBPK model agree well with

known physiology – spleen, liver, lungs (especially the pulmonary region) are rich in PCs and they indeed are the organs with highest values for the parameter of uptake capacities. Although these relative uptake capacities of the PCs may stay the same no matter what type of nanoparticles the animal is exposed to, the absolute amount of nanoparticles each PC can uptake could vary due to different sizes, surface modifications, and other factors.

There are several limitations of this PBPK model and phagocytosis sub-model. 1) Many model parameters, such as the partition coefficient, permeability coefficient, uptake rate and capacity of PCs, are fitted based on the experimental data, instead of having experimentally validated values. This increases the uncertainty of the model. 2) During the optimization process, some parameters are not limited by the measured data and could have a wide range of possible values. This was the case for the uptake capacity of PCs in the blood, which later needed to be refitted when extending the original model based on the PAA-peg nanoparticles study to other biodistribution data, thus the interest to have the model robustness tested on several types of particles. 3) Although the sub-compartment of PCs could explain some of the biobehavior of nanoparticles, the dynamic of the interactions between PCs and nanoparticles in this model is still in a rather crude phase and has much room for improvement. Specifically, the current sub-module of PCs does not reflect the two-step phagocytosis process suggested by experiments (Luciani et al. 2009); it also does not differentiate the uptake rate and capacities of different types of PCs which could be a major barrier when there is a need to model specific areas of a target organ.

5.1.2 Relating inhaled nanoparticles to extrapulmonary uptake

As shown in Chapter 2, the biodistribution of fresh and aged CeO_2 nanoparticles followed the same patterns, with the highest amounts recovered in feces and lungs.

The slow decrease of nanoparticle levels in the lungs is explained by mucociliar clearance to the GI tract and then to the feces. This indicates the crucial need for the PBPK model to include the transfer of nanoparticles from the respiratory system to GI tract. For the extrapulmonary organs, the nanoparticle level in the blood peaked at the end of exposure and decreased afterwards. A detailed mass balance analysis of the size distribution and the amount of nanoparticles recovered from the extrapulmonary region suggests that the extrapulmonary uptake of nanoparticles could be size dependent. In the intratracheal instillation of CeO_2 nanoparticles He et al. (2010) also found the lungs and cumulated feces with the highest amount of nanoparticles. The instillation study showed an increase of nanoparticle amounts in the extrapulmonary organs over time which could be explained by the much higher dose administrated in the pulmonary region. When applied to intratracheal instillation of CeO_2 nanoparticles, the model is able to explain well the similarity and differences between the two datasets, modifying only a few parameters.

Several important lessons are also learned from conducting first hand a CeO_2 inhalation study. First, controlling the size of nanoparticles that the animals are exposed to is crucial for the quality of results, since large aggregates may have been stored in the facility and released in an unpredictable and uncontrollable manner. In this specific CeO_2 specific experiment presented in Chapter 3, it was not possible to properly relate the size distribution recorded by the SMPS to the exposed contents to the rats as measured by the filter packs, until the cascade impactor was added upstream of the exposure chamber. In the early stage of the experiment, the filter packs were receiving nanoparticle aggregates larger than 500 nm in diameter and randomly reported high and variable exposure concentration, while the SMPS was more stable since it already filtered nanoparticles larger than 500 nm. Second,

multiple and most contributing organs should all be collected and analyzed, in order to ensure a sufficiently high recovery rate and to provide a holistic understanding of the relative change of nanoparticles amount in different organs. If feces had not been collected and analyzed in the CeO_2 experiments, the majority of the inhaled dose would not have been accounted for. This would have generated large uncertainties regarding the fate of the nanoparticles, and prevented understanding of how they are removed from the body.

Two major challenges still exist for modeling the extrapulmonary uptake. 1) Although the hypothesis that only nanoparticles below a certain size (< 70 nm) could penetrate the alveolar wall and enter the systemic circulation can explain the mass balance from the CeO_2 nanoparticles inhalation study in Chapter 3, there is no direct evidence to confirm this hypothesis so far. If this hypothesis does not hold, then it would mean the model is missing some other mechanism for the extrapulmonary uptake from inhalation and would not perform well with nanoparticles with different size distributions. 2) The measured data from the CeO_2 inhalation studies clearly show a steady increase in the liver and kidney over time, but the model cannot predict this effectively. It is possible that this increase in extrapulmonary organs has its source in the nanoparticles stored in the GI tract lumen as discussed in Chapter 3. However, certain mechanisms could be missing in the current model and causing the model to perform poorly for absorption from the GI tract. This will be an even greater challenge when applying the current model to nanoparticles with ingestion as the primary exposure route.

5.1.3 Connecting biodistribution with nanoparticles characteristics

Extending the PBPK model to various biodistribution datasets for nanoparticles allows the exploration of relationship between the key determinants of biodistribution

and the nanoparticles characteristics or the exposure conditions. The nanoparticles core, sizes, surface modifications, direct removal from the blood, and administrated dose levels are found to have impacts on the biodistribution. Most interestingly, the parameterization of the model may suggest there is a positive correlation between the sizes of nanoparticles and the uptake capacities of PCs. The kinetics of biodistribution will also be different and more dependent on the uptake rate by PCs when the administrated dose is not high enough to saturate the PCs within organs. The detailed sensitivity analysis of the model for different datasets is important to help us identify the most influential parameters governing the biodistribution. A closer examination of these parameters could then inform us about why they are important, and may lead to proposals of innovative hypotheses to be explored in the future.

Some weaknesses in the model need also to be emphasized. 1) In its current state, the model is not able to extrapolate a quantitative relationship between values of certain parameters with nanoparticles characteristics quantitatively, e.g. the uptake capacities of PCs and the size of nanoparticles. This creates the need to optimize the model for all parameters every time when used to study the biodistribution of a different nanoparticle. 2) When optimizing for some datasets in Chapter 4, the model has to sacrifice some of its parsimony in order to fit the data (different partition coefficients for liver/spleen and other organs for BVP-PLA and Ag nanoparticles). This could indicate that there are other underlying factors or phenomena in the biodistribution of nanoparticles that are not captured by this model. 3) Finally, the present approach has considered each nanoparticle individually, whereas nanoparticle mixtures could lead to synergistic effects, e.g. linked to the PCs saturation effects. Studying some mixtures could be of special interest for drug delivery as suggested by Wenger et al. (2011) and the present PBPK model could be used to test and design further

experiments, for example saturating PCs in untargeted organs and cells with inactive nanoparticles prior to injecting chemotherapy nanoparticles which would then better reach the targeted organs.

5.2 Future research opportunities

The research of this thesis not only made progress to build an innovative PBPK model for nanoparticles and answered the scientific questions proposed at the beginning, but also generated some research ideas that could further advance our knowledge on the biodistribution of nanoparticles. The three most important challenges still to be solved are: modeling the detail dynamics of interaction between nanoparticles and PCs, identifying the influence of nanoparticles size on extrapulmonary uptake from inhalation exposure, and characterizing the relationship between nanoparticles properties and the phagocytosis process.

5.2.1 Dynamics of interaction between nanoparticles and phagocytizing cells

As shown in this thesis, the interactions between PCs and nanoparticles play a crucial role in the biodistribution of nanoparticles. It is therefore of high interest to study these interactions in a more extensive way. To better improve the parameterization of the sub-model of PCs, experiments exposing macrophages to both fresh and aged CeO_2 nanoparticles *in vitro* will be conducted to study the kinetic of absorption/desorption and internalization of nanoparticles to PCs. This may allow us to better characterize this important biobehaviors of nanoparticles in the body.

It is hypothesized that the capture of nanoparticles by macrophages is a two-step process (Luciani et al. 2009). The first step is passive adsorption of nanoparticles to the surface of macrophages and the second step is active internalization into the macrophages. Each step has an amount limit for adsorption/internalization and a rate

for these processes. Under a temperature of 4 ˚C, the macrophage may become inactive and the internalization will not take place. The *in vitro* study will first expose macrophages to a gradient of concentrations of CeO_2 nanoparticles at 4 ˚C and 37 ˚C for four hours. The contents of nanoparticles in the macrophages will then be analyzed. The content should increase as the exposed concentration increases until saturation is reached. The differentiation of 4 ˚C and 37 ˚C will then provide the saturation level for surface adsorption alone and the combined saturation level for adsorption and internalization. Then, another group of macrophages will be exposed to CeO_2 nanoparticles at concentration over the saturation levels, again at 4 ˚C and 37 ˚C degree. The exposure duration will last from 5 min to 16 hours. The results will then provide information regarding the adsorption rate alone with the 4 ˚C data and internalization rate after considering the 37 ˚C data.

Once these parameters have been determined, a feasibility study we have carried out has shown that it will be possible to substitute the model equation representing the particulate mass balance in PCs by an equation adapted from Luciani et al. (2009).

5.2.2 Influence of size on extrapulmonary uptake from inhalation

The importance of nanoparticle size for inhalation exposure is two-fold: deposition fraction of the inhaled nanoparticles in different regions of the respiratory system, and the potential of penetrating the alveolar wall and entering the systemic circulation directly from the air during the inhalation exposure period. By filtering nanoparticles down to a gradient of maximum sizes, future research should be conducted to study the relationship between nanoparticles size and uptake in the extrapulmonary organs by inhalation. Another possible approach would consist of examining the nanoparticle sizes on each side of the alveolar wall to determine how well the alveolar wall able to block larger nanoparticles from passing through this wall. In addition, the sizes and

morphology of nanoparticles in the pulmonary region could be changed due to aggregation in the microenvironment of alveolar sacs. In order to better understand the relationship of size and extrapulmonary uptake of nanoparticles from inhalation, it would be worth documenting any differences in size and other characteristics between nanoparticles in the ambient air and those in the pulmonary region.

5.2.3 Relationship between nanoparticles characteristics and phagocytosis

The possible positive correlation between nanoparticles size and uptake capacities of PCs is a topic to be studied in more detail and quantitatively. In Chapter 4, there were not enough qualified biodistribution data to confirm this correlation with confidence when parameterizing the model. More experiments with high enough dose to saturate PCs in the organs are needed to better characterize this relationship. Given the importance of phagocytosis, quantitatively identifying this relationship would help us better parameterize the model and predict the biodistribution of different nanoparticles. It should also be noted that other characteristics such as surface modifications could influence phagocytosis of the nanoparticles and may need to be taken into account when examining the data.

5.3 Outlook and perspectives

Toxicity of nanoparticles has been a popular topic in the scientific community for more than a decade and has generated a wealth of data. In order to fully evaluate the potential human health risks imposed by various nanoparticles, both the toxicity and exposure should be well characterized. However, research on the biodistribution of nanoparticles is far less sufficient and systematic. When conducting literature review of the biodistribution studies on nanoparticles, I found many of the studies not considering the mass balance of the administered dose. Some biodistribution studies

only consisted of two time points, making it impossible to infer the full dynamics from their results. These issues make it difficult for other researchers to fully leverage the results from these previous studies. Therefore I would suggest future research consider having at least three time point measurements, and include enough organs analyses to account for at least 50% of the dose. On the brighter side, nanoparticle characterizations are better documented in more recent published results than they were in the past. However, the influences of different characteristics of nanoparticles, such as size, surface modifications, shape, core, etc, on biodistribution still lack the attention they need compared to recent studies on the toxicity of nanoparticles.

In terms of PBPK modeling, the importance of phagocytosis is receiving more and more attention. Failure to address this critical phenomenon for nanoparticles would prevent modelers from developing a comprehensive PBPK model that can be applied to a number of different types of nanoparticles without heavily optimizing many of the models parameters for each biodistribution dataset. As a consequence, the model would inevitably lose robustness in predictability of other datasets when overfitted for one set of data. If a "more general" PBPK model for nanoparticles emerges in the future, I envision it to be a parsimonious one whose parameters will be a function of a limited number of nanoparticle properties, similar to those for modeling the environmental fate of chemicals. It will be built under an overarching framework to achieve a screening level precision of the biodistribution of nanoparticles once the dose, exposure route, and key characteristics of the nanoparticles are given. If the modeler wishes to go into more depth for a specific type of nanoparticle, then details and modifications could be added to the parsimonious model.

As a researcher that has addressed not only PBPK modeling but also environmental fate modeling (see e.g. Appendix 5), I have a vision for a more comprehensive model,

linking toxicity tests and toxicodynamic approaches, PBPK models, and environmental fate models. This would extend beyond nanoparticles to human health impact assessment for chemicals in general. The environmental fate model would allow us to estimate the intake rate of a certain chemical. The PBPK model then takes up the task to predict the specific concentrations in the target organs based on the results of the environmental fate model. Once the concentrations in the organs are evaluated, it would be then possible to link these concentrations to *in vitro* toxicity tests to see if those concentrations are at alarming levels. A quantitative estimate of the health impact to individual persons of this chemical could be obtained by integrating the toxicity data, PBPK model, and environmental fate model with just the physicochemical properties and *in vitro* toxicity data of that chemical as input. Going further, incorporating quantitative structure-activity relationship (QSAR) models into this system would even allow us to predict the human health impacts of new chemicals that are artificially created on a global scale. All of the above is for one single chemical. It should be noted that the current trend for environmental fate model, toxicity tests, and QSAR are on the tract towards high-throughput methodology. Developing high-throughput PBPK models would complete the picture above and make possible the screening for human health risks of thousands of chemicals, new or old.

APPENDIX 1

Honors, publications, and conference presentations

A1.1 Honors and grants

2014, 2nd place, Poster Competition, 19th Annual Environmental Health Sciences Symposium, Department of Environmental Health Sciences

2014, 3rd place, AATC and Charles River Best Abstract Award, American Association of Chinese in Toxicology

2014, Graduate Student Travel Support, Society of Toxicology, $1 000

2013, Rackham International Research Award, University of Michigan, $6 000

2013, Rackham Graduate Student Research Grant, University of Michigan, $3 000

2011 – 2014, Rackham Conference Travel Grant, University of Michigan, $2 900

2012, Graduate Student Award, Society of Toxicology, $1 000

2011, 1st place, Student Poster Award, International Society of Exposure Science, $500

2010, Risk Science Center Fellowship, Risk Science Center, $8 000

A1.2 Publications (corresponding author underlined)

Li, D.; Huijbregts, M.; Jolliet, O. Health impacts of polycyclic aromatic hydrocarbon for source-specific mixtures. *Int. J. Life Cycle Ass.* **2015**, *20(1)*, 87-99.

Li, D.; Johanson, G.; Emond, C.; Carlander, U.; Philbert, M.; Jolliet, O. Physiologically based pharmacokinetic modeling of polyethylene glycol-coated polyacrylamide nanoparticle in rats. *Nanotoxicology* **2014**, *8(S1)*, 128-137. .

Li, D.; Emond, C.; Johanson, G.; Jolliet, O. Using a PBPK model to study the influence of different characteristics of nanoparticles on their biodistribution. *J. Phys.: Conf. Ser.* **2013**, *429* 012019.

Wenger, Y.; **Li, D.**; Jolliet, O. Indoor intake fraction and surface sorption of air organic compounds for life cycle assessment. *Int. J. Life Cycle Ass.* **2012**, *17*(7), 919-931.

Wu, B.; Liu, Z.; Xu, Y.; **Li, D.**; Li, M. Combined toxicity of cadmium and lead on the earthworm *Eisenia fetida* (Annelida, Oligochaeta). *Ecotox. Environ. Safe.* **2012**, *81*, 122-126.

Rosenbaum, R.; Huijbregts, M.; Henderson, A.; Margni, M.; McKone, T.; van de Meent, D.; Hauschild, M.; Shaked, S.; **Li, D.**; Gold, L.; Jolliet, O. USEtox human exposure and toxicity factors for comparative assessment of toxic emissions in life cycle analysis: sensitivity to key chemical properties. *Int. J. Life Cycle Ass.* **2011**, *16*, 710-727.

Li, D.; Liu, Z. T.; Cui, Y.B.; Li, W. L.; Fang, Hao.; Li, M.; Kong, Z.M. Toxicity of cyanobacterial bloom extract from Taihu Lake on mouse, *Mus musculus*. *Ecotoxicology* **2011**, *20*(5), 1018-1025.

Hu, C.W.; Li, M.; Cui, Y.B.; **Li, D.;** Chen, J.; Yang, L.Y. Toxicological effects of TiO_2 and ZnO nanoparticles in soil on earthworm *Eisenia fetida*. *Soil Biol. Biochem.* **2010**, *42*(4), 586-591.

Li, M.; Liu, Z.T.; Xu, Y.; Cui, Y.B.; **Li, D.**; Kong, Z.M. Comparative effects of Cd and Pb on biochemical response and DNA damage in the earthworm *Eisenia fetida* (*Annelida, Oligochaeta*). *Chemosphere* **2009**, *74*(5), 621-625.

A1.3 Conference presentations (presenter underlined)

Li, D.; Barres, J.,; Eagle, E.; Emond, C.; Morishita, M.; Wagner, J.G.; Wooldridge, M.; Jolliet, O. (2014). Physiologically Based Pharmacokinetic Modeling of Cerium Oxide Nanoparticles by Inhalation Exposure in Rats [*platform presentation*]. In 24th ISES Conference; Oct 12-16; Cincinnati, United States.

Veltman, K.; Henderson, A.; Asselin-Balencon, A.; Chase, L.; Duval, B.; Izaur-ralde, C.; Jones, C.; Li, C.; **Li, D.**; Salas, W.; Vadas, P.; Jolliet, O. (2014). Comparison of process-based model to quantify major nutrient flows and greenhouse gas emissions of milk production [*poster presentation*]. In: LCA Food 2014; Oct 8-10; San Francisco, United States.

Li, D.; Barres, J.,; Carlander, U.; Eagle, E.; Emond, C.; Johanson, G.; Morishita, M.; Wagner, J.G.; Wooldridge, M.; Jolliet, O. (2014). Physiologically Based Pharmacokinetic Modeling of Cerium Oxide Nanoparticles by Pulmonary Exposure in Rats [*poster presentation*]. In: SOT 53rd Annual Meeting; May 24-27; Phoenix, United States.

Li, D.; Johanson, G.; Emond, C.; Carlander, U.; Jolliet, O. (2013). Physiologically Based Pharmacokinetic Modeling of Cerium Oxide Nanoparticles in Rats [*platform presentation*]. In: ISES-ISEE-ISIAQ 2013 Conference; Aug 20-23; Basel, Switzerland.

Li, D.; Johanson, G.; Emond, C.; Carlander, U.; Jolliet, O. (2013). Physiologically Based Pharmacokinetic Modelling of Polyethylene Glycol-coated Plyacrylamide Nanoparticle in Rats [*poster presentation*]. In: 23rd SETAC Europe Conference; May 12-16; Glasgow, United Kingdom.

Ernstoff, A.; **Li, D.**; Jolliet, O. (2012). Direct Consumer Exposure during Use of Personal Care Products, Plasticizers and Flooring Materials [*platform presentation*]. In: 10th International Conference on EcoBalance; Nov 20-23; Yokohama, Japan.

Li, D.; Emond, C.; Johanson, G.; Jolliet, O. (2012). Using a PBPK Model to Study the Influence of Different Characteristics of Nanoparticles on their Biodistribution [*platform presentation*]. In: International Conference on Safe Production and Use of Nanomaterials 2012; Nov 13-15; Minatec, France.

Li, D.; Johanson, G.; Emond, C.; Carlander, U.; Jolliet, O. (2012). Influence of Size and Surface Modifications of Nanoparticles on their Uptake and Biodistribution [*platform and poster presentations*]. In: 22nd ISES Conference; Oct 28-Nov 1; Seattle, United States.

Li, D.; Huijbregts, M.; Jolliet, O. (2012). Health Impacts of Polycyclic Aromatic Hydrocarbon Mixtures - Importance of Fate, Exposure, Effect, and Emission Profile [*platform presentation*]. In: 22nd ISES Conference; Oct 28-Nov 1; Seattle, United States.

Ernstoff, A.; Henderson, A.; Chuang, S.; Jolliet, O.; **Li, D.** (2012). Assessing Direct Impact of Products on Consumer in LCA [*platform presentation*]. In: In: 22nd ISES Conference; Oct 28-Nov 1; Seattle, United States.

Li, D.; Chuang, S.; Henderson, A.D.; Jolliet, O. (2012). Comparison of Far Field and Near Field Exposure from Consumer Products for Chemical Exposure Prioritization [*platform presentation*]. In: 22nd SETAC Europe Conference; May 20-24; Berlin, Germany.

Jolliet, O.; **Li, D.**; McKone, T. (2012). Rapid Exposure-Based Prioritization of Environmental Chemicals Using USEtox [*platform presentation*]. In: SOT 51st Annual Meeting; Mar 11-15; San Francisco, United States.

Li, D.; Emond, C.; Johanson, G.; Jolliet, O. (2012). PBPK Modeling of Polyacrylamide Nanoparticle Biodistribution in Rats [*poster presentations*]. In: SOT 51st Annual Meeting; Mar 11-15; San Francisco, United States.

Li, D.; Emond, C.; Johanson, G.; Jolliet, O. (2011). PBPK Modeling of Polyacrylamide Nanoparticle Biodistribution in Rats [*platform and poster presentations*]. In: 21st ISES Conference; Oct 23-27; Baltimore, United States.

Li, D.; Jolliet, O. (2011). Life Cycle Impact of Floorings? The Importance of Direct Indoor Exposures [*platform presentation*]. In: 21st ISES Conference; Oct 23-27; Baltimore, United States.

Li, D.; Huijbregts, M.; Jolliet, O. (2011). Improving Human Toxicity Assessment for Polycyclic Aromatic Hydrocarbons (PAHs) from Primary Aluminum Production [*platform presentation*]. In: The American Center for Life Cycle Assessment LCA XI Conference; Oct 4-6; Chicago, United States.

Wenger, Y.; **Li, D.**; Jolliet, O. (2011). Integrating Indoor Exposure and LCA for SVOCs [*platform presentation*]. In: SVOCs in the Indoor Environment: Mechanistic Insights to Support Sustainable Product Design, Safe Use and Improved Public Health; Jan 5-7; Research Triangle Park, United States.

Li, D.; Henderson, A.; Jolliet, O. (2010). Targeting Purchasing Policy Changes Using Input/ Output LCA for a Large Academic Institution [*platform presentation*]. In: The American Center for Life Cycle Assessment LCA X Conference; Nov 2-4; Portland, United States.

APPENDIX 2

Physiologically based pharmacokinetic modeling of polyethylene glycol-coated polyacrylamide nanoparticles in rats

A2.1 Mathematical representation of the model

A2.1.1 Dynamics of the nanoparticles in tissues, as a function of capillary blood concentrations

The dynamic of nanoparticles in the tissue sub-compartment in different organs can be summarized as follow. The sources of nanoparticles for tissues are capillary blood which is part of the systemic circulation. Parts of the nanoparticles will be exchanged back to capillary blood and return to the systemic circulation while other parts are captured by phagocytizing cells (PCs). For those captured by PCs, desorption is also possible to re-enter the tissue. In certain organs, excretion out of the organ is a clearance route. The equation describing these processes is:

$$\frac{dM_t}{dt} = \overbrace{PA_t \times (C_{t,b} - C_t / P)}^{net\ transfer\ with\ capillary\ blood} - \overbrace{(W_t \times C_t \times k_{t,ab} - M_{t,m} \times k_{de})}^{interaction\ with\ PCs} - \overbrace{\frac{dM_{e,ex}}{dt}}^{clearance\ by\ excretion} \quad \text{A2.1}$$

where

M_t [μg] – Amount of nanoparticles in the tissue of organ *t*.

W_t [g] – Weight of organ *t*.

C_t [μg per g] – Concentration of nanoparticles in the tissue of organ *t*.

$C_{t,b}$ [μg per g] – Concentration of nanoparticles in the capillary blood of organ *t*.

PA_t [mL per hour] – Permeability coefficient-surface area cross-product. It is approximated as the product of permeability coefficient between capillary blood and tissue and regional blood flow, $\chi_a \times Q_t$, in this model, assuming the surface area is proportional to the regional blood flow.

P [unitless] – Partition coefficient of nanoparticles between tissue and blood.

$M_{t,m}$ [μg] – Amount of nanoparticles captured by PCs in organ t.

$k_{t,ab}$ [per hour] – Current uptake rate of nanoparticles by PCs in organ t.

k_{de} [per hour] – Desorption rate of nanoparticles from PCs to tissue.

$M_{e,ex}$ [μg] – Amount to excreta from source e. e only applies to tissue in liver and capillary blood in kidneys.

A2.1.2 Dynamics of the nanoparticles in capillary blood, as a function of concentrations in arterial and venous blood

The nanoparticle concentration in capillary blood is determined by the concentrations in the arterial blood and in the tissue. The interaction between capillary blood and tissue can be described as:

$$\frac{dM_{t,b}}{dt} = Q_t \times (C_{art} - C_{t,b}) - PA_t \times (C_{t,b} - C_t / P)$$

A2.2

where

$M_{t,b}$ [μg] – Amount of nanoparticles in the capillary blood of organ t.

Q_t [mL per hour] – Blood flow through organ t.

C_{art} [μg per g] – Concentration of nanoparticles in arterial blood.

C_t [μg per g] – Concentration of nanoparticles in the tissue of organ t.

Tissue uptake of nanoparticles from the capillary blood is modeled as a diffusion limited process, therefore the movement of the nanoparticles from capillary blood to

the cellular matrix of the tissue is proportional to the permeability coefficient-surface area cross-product (Krishnan 2007) which can be expressed as a proportion of the blood flow Q_t, assuming the surface area is proportional to the regional blood flow:

$$PA_t = \chi_\alpha \times Q_t$$

A2.3

with χ_α the permeability coefficient between capillary blood and organ *t*. This parameter has specific values for the rest of the body (χ_{rest}) and brain (χ_b) and the same generic value for the richly perfused organs (χ_{rich}), which are spleen, liver, bone marrow, lungs, heart, kidneys, and brain.

We can simplify the model by eliminating the specific sub-compartment of capillary blood and calculate concentration of the capillary blood as a function of the arterial blood, assuming $C_{t,b}$ is in quasi steady state equilibrium between C_{art} and C_t. We then have:

$$Q_t \times (C_{art} - C_{t,b}) = PA_t \times (C_{t,b} - C_t / P)$$

A2.4

Combining Eq. A2.3 and Eq. A2.4 we have the concentration in organ capillary blood $C_{t,b}$ as:

$$C_{t,b} = \frac{C_{art} + \chi_\alpha \times C_t / P}{(1 + \chi_\alpha)}$$

A2.5

Eq. A2.5 applies for all organs in the systemic circulation except for the lungs because the lungs receive the collective venous blood. Therefore we have the concentration in lungs capillary blood $C_{lu,b}$ as a function of venous blood:

$$C_{lu,b} = \frac{C_{ven} + \chi_{rich} \times C_{lu} / P}{(1 + \chi_{rich})}$$

A2.6

where

C_{ven} [μg per g] – Concentration of nanoparticles in venous blood.

χ_{rich} [mL per hour] – Permeability coefficient between capillary blood and richly perfused organs.

A2.1.3 Dynamics of the nanoparticles in arterial and venous blood

For the arterial blood we have:

$$\frac{dM_{art}}{dt} = Q_{tot} \times (C_{lu,b} - C_{art}) - (W_{art} \times C_{art} \times k_{blood,ab} - M_{art,m} \times k_{de})$$

A2.7

where

M_{art} [μg] – Amount of nanoparticles in arterial blood.

Q_{tot} [mL per hour] – Total cardiac output.

W_{art} [μg] – Weight of arterial blood.

$k_{blood,ab}$ [per hour] – Uptake rate of PCs in blood, mathematical description can be found later in this section.

$M_{art,m}$ [μg] – Amount of nanoparticles captured by PCs in arterial blood.

k_{de} [per hour] – Desorption rate from PCs.

And the concentration of nanoparticles in the arterial blood C_{art} is:

$$C_{art} = \frac{M_{art}}{W_{art}}$$

A2.8

The dynamic of nanoparticles in the venous blood is:

$$\frac{dM_{ven}}{dt} = \sum (Q_t \times C_{t,b}) - Q_{tot} \times C_{ven} - (W_{ven} \times C_{art} \times k_{blood,ab} - M_{ven,m} \times k_{de})$$

A2.9

where

M_{ven} [μg] – Amount of nanoparticles in venous blood.

C_{ven} [μg per g] – Concentration of nanoparticles in the venous blood.

W_{ven} [g] – Weight of venous blood.

$M_{ven,m}$ [μg] – Amount of nanoparticles captured by PCs in venous blood.

The initial value for M_{ven} is the injected dose. And the concentration of nanoparticles in the venous blood C_{ven} is:

$$C_{ven} = \frac{M_{ven}}{W_{ven}}$$

A2.10

Approximately, arterial blood takes up 20% of the total blood and venous blood takes up 80% of the total blood (Despopoulos and Silbernagl 2003). We also assume the PCs in arterial and venous blood are distributed in this 20/80 ratio. Therefore, W_{art} = 0.2 × W_{blood}, $M_{art,m}$ = 0.2 × $M_{blood,m}$, W_{ven} = 0.8 × W_{blood}, $M_{ven,m}$ = 0.8 × $M_{blood,m}$, where W_{blood} is the weight of total blood and $M_{blood,m}$ is the amount of nanoparticles captured by PCs in the total blood.

A2.1.4 Dynamics of the nanoparticles in tissues, as a direct function of arterial and venous concentrations

By introducing Eq. A2.5 to Eq. A2.1 we can directly express the dynamic of amount of nanoparticles in different organs (except for lungs) other than the blood as a function of the arterial blood, eliminating the sub-compartment of capillary blood and simplifying the model as follows:

$$\frac{dM_t}{dt} = \frac{\chi_\alpha \times Q_t}{(1+\chi_\alpha)}(C_{art} - C_t / P) - (W_t \times C_t \times k_{t,ab} - M_{t,m} \times k_{de}) - \frac{dM_{e,ex}}{dt}$$

A2.11

The amount of nanoparticles in the lungs is related to the venous blood instead of the arterial blood and can be described as:

$$\frac{dM_{lu}}{dt} = \frac{\chi_{rich} \times Q_{tot}}{(1+\chi_{rich})}(C_{ven} - C_{lu} / P) - (W_{lu} \times C_{lu} \times k_{lu,ab} - M_{lu,m} \times k_{de})$$

A2.12

where

M_{lu} [μg] – Amount of nanoparticles in the tissue of lungs.

W_{lu} [g] – Weight of lungs.

C_{lu} [μg per g] – Concentration of nanoparticles in lungs.

$M_{lu,m}$ [μg] – Amount of nanoparticles captured by PCs in lungs.

$k_{lu,ab}$ [per hour] – Current uptake rate of nanoparticles by PCs in lungs.

In addition, the outflow from the spleen feeds directly into the liver, instead of joining the venous blood in circulation.

A2.1.5 Capture of nanoparticles by phagocytizing cells

The PCs capture nanoparticles from the tissue and in the meanwhile, desorption from the PCs will release part of the captured nanoparticles back to the tissue. The PCs capture the nanoparticles in a saturable manner. That is, as the amount captured approaches the capacity for the PCs in the various organs, the uptake rate $k_{t,ab}$ will decrease and eventually the capture of nanoparticles will be in a dynamic balance with the desorption. The equation describing these behaviors is:

$$\frac{dM_{t,m}}{dt} = W_t \times C_t \times k_{t,ab} - M_{t,m} \times k_{de}$$

A2.13

The initial uptake rate is assumed to be equal for all organs, while saturation levels of PCs will be adjusted for each compartment independently, reflecting the potential variation in PCs density in various organs. Thus the uptake rate is related to the amount of nanoparticles already captured and the maximum uptake capacity in different organs:

$$k_{t,ab} = k_{ab0} \times (1 - \frac{M_{t,m}}{M_{t,cap} \times W_t})$$

A2.14

where

k_{ab0} [per hour] – Maximum uptake rate by PCs.

$M_{t,cap}$ [μg] – PCs uptake capacity for nanoparticles per organ t weight.

A2.1.6 Excretion

The excretion of nanoparticles is assumed to be a first order elimination from the tissue of liver and capillary blood of kidneys. This is summarized as below:

$$\frac{dM_{ex}}{dt} = \sum \frac{dM_{e,ex}}{dt} = M_l \times CLE_f + M_{k,b} \times CLE_u$$

A2.15

where

M_{ex} [μg] – Amount in excreta.

CLE_f [per hour] – Clearance rate to feces from liver tissue.

CLE_u [per hour] – Clearance rate to urine from capillary blood in kidneys.

A2.1.7 Codes of the model

Codes of the model in Berkeley-Madonna™ (version 8.3.18) and acslX™ (version 3.0.2.1) are available by request (Dingsheng Li, email: dingsli@umich.edu).

A2.2 Linear regression of the model's prediction against measured data

Fig. A2.1 shows the statistical analysis of the model's prediction versus measured data. The R^2 is 0.97. The standard error on the residuals (McKone 1993) on the $\log_{10}$ of predicted and measured values is 0.14, corresponding to a squared geometric standard deviation of 1.9 which means the model is able to predict masses of PAA-peg nanoparticles within a factor of 1.9. The coefficient of a linear regression between the $\log_{10}$ of predicted and measured values is 0.99.

For excreta, the feces have an approximate 8 h of delay from the removal from the system until actual sampling. Therefore the measured results' corresponding time are modified when being compared to the predicted results, e.g. the original measured nanoparticles amount in feces at 24 h is being compared to the model's prediction for feces at 16 h. The original experiment only measured 0.02 g of the bone marrow (Wenger et al. 2011) while the bone marrow weights about 3% of the rat's body weight (Travlos 2006). This means that 99.7% of the bone marrow was included in the rest of the body in the original experiment. Therefore when comparing predicted results to experimental one, we first estimate the nanoparticle amount in the total bone marrow by multiplying the concentrations found in parts of the bone marrow in the experiment with the total amount of bone marrow (3% of body weight). Then we sum 99.7% of the predicted nanoparticles mass in the bone marrow with the rest of the body to predict the total nanoparticles mass in the rest of the body. According to model results, bone marrow contributes to 8.7% of the nanoparticles found in the rest of the body. In addition, we sum the amount of nanoparticles found in the lymph nodes, which is less than 0.1% of the injected dose, with the rest of the body.

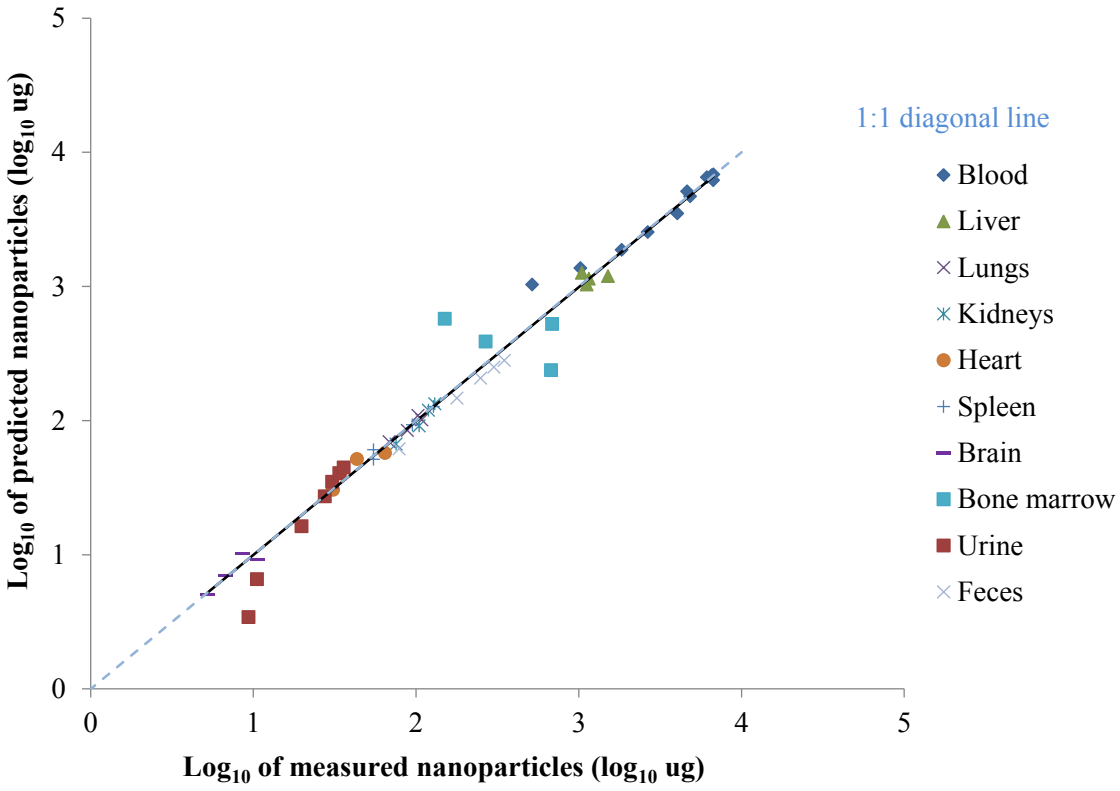

Fig. A2.1 Log_{10} of predicted PAA-peg nanoparticle mass in blood and different organs as a function of log_{10} of measured mass.

A2.3 Sensitivity study of the rest of the body to permeability coefficient

The richly perfused organs are only sensitive to their corresponding permeability coefficient in the short-term. However, the permeability coefficient between capillary blood and the rest of the body is a very sensitive parameter to the rest of the body in this model. The corresponding relative sensitivities (definition and calculation can be found in the main text) for the 10 hours *AUC* and 120 hours *AUC* for the rest of the body are 0.28 and 0.41 respectively, compared to values of 0.20 and 0.02 for 10 hours *AUC* and 120 hours *AUC* for the liver in respond to 1% change in the permeability coefficient between capillary blood and the liver.

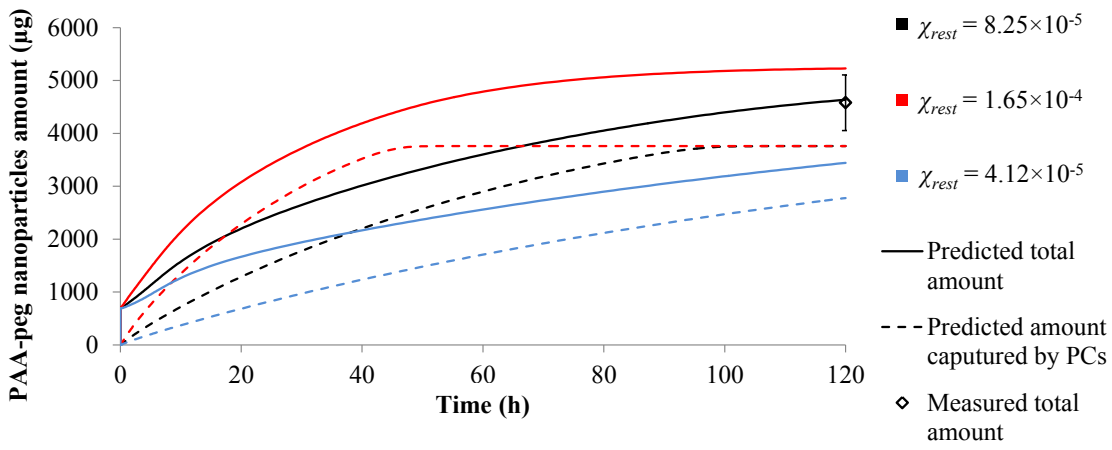

Fig. A2.2 Sensitivity analysis of the model for the rest of the body to permeability coefficient between capillary blood and tissue in rest of the body (χ_{rest}). Error bars showing the standard deviation of measured data. "PCs" is the abbreviation for phagocytizing cells. Reference values from Table 2.1 are in black and sensitivity study are shown in red and blue.

APPENDIX 3

Physiologically based pharmacokinetic modeling of cerium oxide nanoparticles by inhalation exposure in rats

A3.1 Calculation of deposition fractions in different regions of the respiratory system

We combined two sets of information to calculate the deposition fractions of nanoparticles in the head region, tracheobronchial region, and the pulmonary region. First we gathered the detailed size distribution of nanoparticles in the study with the scanning mobility particle sizer (SMPS), which are shown in Fig. A3.1 below.

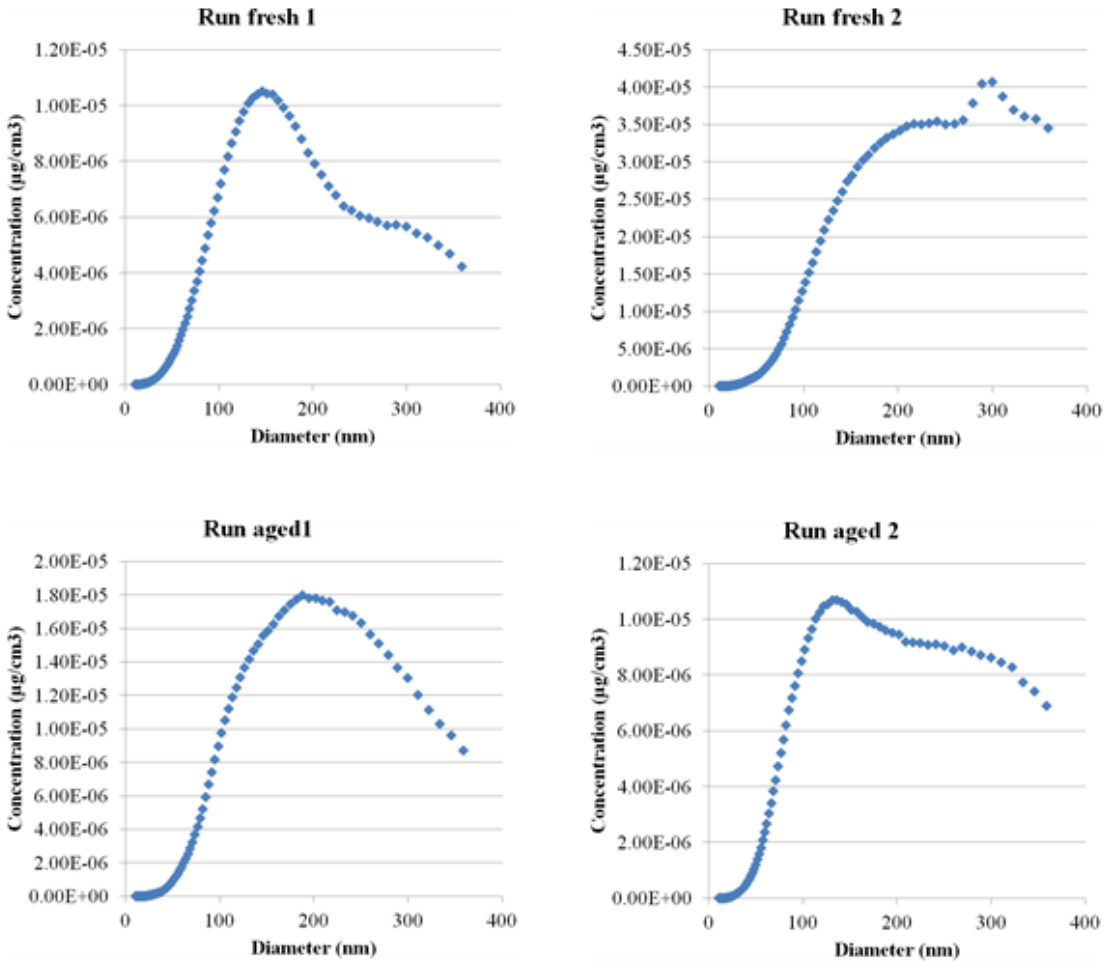

Fig. A3.1 Size distribution of the mass based concentration of CeO_2 nanoparticles for four runs based on SMPS collected data.

Second, we utilized the Multiple-Path Particle Dosimetry Model (MPPD v2.11) to obtain the deposition fractions in different regions of the respiratory system for the size range of nanoparticles in this study, assuming the density of CeO_2 nanoparticles in this study was 6.96 g/cm^3. Then we matched the percentage of a certain size of nanoparticles in the study with the deposition fractions of the corresponding size in the MPPD model results. By repeating this process for the whole size distribution, we arrived with the cumulated deposition fractions of the inhaled nanoparticles for the different regions of the respiratory system.

A3.2 Mathematical representation of the model

A3.2.1 Calculation of total inhaled nanoparticles

The total amount of nanoparticles inhaled, expressed in μg, during the study is described by the following equation:

$$intake = Conc \times ExpedT \times BF \times TV \times InsFr$$

A3.1

where

intake [μg] – Total inhaled amount of nanoparticles during the study.

Conc [μg/m^3] – Concentration of nanoparticles in the air.

ExpedT [hour] – Exposed duration.

BF [per hour] – Breathing frequency.

TV [m^3] – Tidal volume.

InsFr [unitless] – Inspiratory fraction

The values for *Conc* and *ExpedT* follow the study settings. The values for *BF*, *TV*, and *InsFr* were taken from the default values for rats in the MPPD model.

Inflows and outflows in different regions of the respiratory system and GI tract lumen

After inhaled, the nanoparticles enter different regions of the respiratory system. They can they exchange with nearby organs. The GI tract lumen is relevant here also because nanoparticles can either be directly deposited in the GI tract lumen during inhalation, or swallowed down after mucociliar clearance from the pulmonary region. The inflows and outflows for the different regions of the respiratory system and GI tract lumen are described as below.

Pulmonary region

$$\frac{dM_{pul}}{dt} = \frac{intake}{ExpedT} \times fr_{pul} - M_{pul} \times fr_s \times k_{pulb} - \frac{dM_{pul,m}}{dt}$$

A3.2

where

M_{pul} [µg] – Amount of nanoparticles in the pulmonary region.

fr_{pul} [unitless] –Fraction of nanoparticles deposited in the pulmonary region.

fr_s [unitless] –Fraction of nanoparticles smaller than 70 nm.

k_{pulb} [per hour] – Transfer rate from pulmonary region blood.

The last term describes the interaction with phagocytizing cells (PCs), which is described in details in the following sections.

Tracheobronchial region

$$\frac{dM_{tra}}{dt} = \frac{intake}{ExpedT} \times fr_{tra} - M_{pulm} \times k_{pulmtra} - M_{tra} \times k_{gi}$$

A3.3

where

M_{tra} [µg] – Amount of nanoparticles in the tracheobronchial region.

fr_{tra} [unitless] –Fraction of nanoparticles deposited in the tracheobronchial region.

M_{pulm} [µg] – Amount of nanoparticles in the pulmonary region PCs.

$k_{pulmtra}$ [per hour] – Transfer rate of saturated PCs from pulmonary region to tracheobronchial region.

k_{gi} [per hour] – Transfer rate nanoparticles from tracheobronchial region to GI tract.

Head region

$$\frac{dM_{head}}{dt} = \frac{intake}{ExpedT} \times fr_{head} - M_{head} \times k_{headbr} + M_{br} \times k_{brhead} - M_{head} \times CLE_{head}$$

A3.4

where

M_{head} [µg] – Amount of nanoparticles in the head region.

fr_{head} [unitless] –Fraction of nanoparticles deposited in the head region.

k_{headbr} [per hour] – Transfer rate of nanoparticles from head region to brain.

M_{br} [μg] – Amount of nanoparticles in the brain tissue.

k_{brhead} [per hour] – Transfer rate of nanoparticles from brain to head region.

CLE_{head} [per hour] – Clearance rate from head region.

GI tract lumen

$$\frac{dM_{gilumen}}{dt} = \frac{intake}{ExpedT} \times fr_{gi} + M_{tra} \times k_{gi} - M_{gilumen} \times CLE_{fgi} - M_{gilumen} \times k_{giab} \quad \text{A3.5}$$

where

$M_{gilumen}$ [μg] – Amount of nanoparticles in the GI tract lumen.

fr_{gi} [unitless] –Fraction of nanoparticles directly deposited in the GI tract lumen.

CLE_{fgi} [per hour] – Clearance rate from the GI tract to feces.

k_{giab} [per hour] – Absorption rate of nanoparticles from the GI tract to the liver.

Note that the first two terms has a delay of two hours in time for the nanoparticles to come down from larynx to the GI tract lumen.

A3.2.2 Dynamics of the nanoparticles in tissues, as a function of capillary blood concentrations

The dynamic of nanoparticles in the tissue sub-compartment in different organs can be summarized as follow. The sources of nanoparticles for tissues are capillary blood which is part of the systemic circulation. Parts of the nanoparticles will be exchanged back to capillary blood and return to the systemic circulation while other parts are captured by PCs. For those captured by PCs, desorption is also possible to re-enter the tissue. In certain organs, excretion out of the organ is a clearance route. The equation describing these processes is:

$$\frac{dM_t}{dt} = \overbrace{PA_t \times (C_{t,b} - C_t / P)}^{net\ transfer\ with\ capillary\ blood} - \overbrace{(W_t \times C_t \times k_{t,ab} - M_{t,m} \times k_{de})}^{interaction\ with\ PCs} - \overbrace{\frac{dM_{e,ex}}{dt}}^{clearance\ by\ excretion} \quad \text{A3.6}$$

where

M_t [μg] – Amount of nanoparticles in the tissue of organ *t*.

W_t [g] – Weight of organ *t*.

C_t [μg per g] – Concentration of nanoparticles in the tissue of organ *t*.

$C_{t,b}$ [μg per g] – Concentration of nanoparticles in the capillary blood of organ *t*.

PA_t [mL per hour] – Permeability coefficient-surface area cross-product. It is approximated as the product of permeability coefficient between capillary blood and tissue and regional blood flow, $\chi_\alpha \times Q_t$, in this model, assuming the surface area is proportional to the regional blood flow.

P [unitless] – Partition coefficient of nanoparticles between tissue and blood.

$M_{t,m}$ [μg] – Amount of nanoparticles captured by PCs in organ *t*.

$k_{t,ab}$ [per hour] – Current uptake rate of nanoparticles by PCs in organ *t.*

k_{de} [per hour] – Desorption rate of nanoparticles from PCs to tissue.

$M_{e,ex}$ [μg] – Amount to excreta from source *e*. *e* only applies to tissue in liver and capillary blood in kidneys. The elimination of nanoparticles directly from the GI tract is described separately

A3.2.3 Dynamics of the nanoparticles in capillary blood, as a function of concentrations in arterial and venous blood

The nanoparticle concentration in capillary blood is determined by the concentrations in the arterial blood and in the tissue. The interaction between capillary blood and tissue can be described as:

$$\frac{dM_{t,b}}{dt} = Q_t \times (C_{art} - C_{t,b}) - PA_t \times (C_{t,b} - C_t / P)$$

A3.7

where

$M_{t,b}$ [μg] – Amount of nanoparticles in the capillary blood of organ *t*.

Q_t [mL per hour] – Blood flow through organ *t*.

C_{art} [μg per g] – Concentration of nanoparticles in arterial blood.

C_t [μg per g] – Concentration of nanoparticles in the tissue of organ *t*.

Tissue uptake of nanoparticles from the capillary blood is modeled as a diffusion limited process, therefore the movement of the nanoparticles from capillary blood to the cellular matrix of the tissue is proportional to the permeability coefficient-surface area cross-product (Krishnan 2007) which can be expressed as a proportion of the blood flow Q_t, assuming the surface area is proportional to the regional blood flow:

$$PA_t = \chi_\alpha \times Q_t$$

A3.8

with χ_α the permeability coefficient between capillary blood and organ *t*. This parameter has a specific value for the brain (χ_b) and the same generic value for the richly perfused organs (χ_{rich}), which are lungs, spleen, liver, kidneys, heart, and the GI tract.

We can simplify the model by eliminating the specific sub-compartment of capillary blood and calculate concentration of the capillary blood as a function of the arterial blood, assuming $C_{t,b}$ is in quasi steady state equilibrium between C_{art} and C_t. We then have:

$$Q_t \times (C_{art} - C_{t,b}) = PA_t \times (C_{t,b} - C_t / P)$$

A3.9

Combining Eq. A3.8 and Eq. A3.9 we have the concentration in organ capillary blood $C_{t,b}$ as:

$$C_{t,b} = \frac{C_{art} + \chi_{\alpha} \times C_t / P}{(1 + \chi_{\alpha})}$$

A3.10

Eq. A3.10 applies for all organs in the systemic circulation except for the lungs because the lungs receive the collective venous blood. Therefore we have the concentration in lungs capillary blood $C_{lu,b}$ as a function of venous blood:

$$C_{lu,b} = \frac{C_{ven} + \chi_{rich} \times C_{lu} / P}{(1 + \chi_{rich})}$$

A3.11

where

C_{ven} [μg per g] – Concentration of nanoparticles in venous blood.

χ_{rich} [mL per hour] – Permeability coefficient between capillary blood and richly perfused organs.

Dynamics of the nanoparticles in arterial and venous blood

In addition to the systemic circulation, the arterial blood is also receiving inputs of nanoparticles penetrating the alveolar wall from the pulmonary region. Therefore we have the arterial blood as:

$$\frac{dM_{art}}{dt} = \frac{intake}{ExpedT} \times fr_s \times fr_{airblood} + M_{pul} \times fr_s \times k_{alvlub} + Q_{tot} \times (C_{lu,b} - C_{art}) - (W_{art} \times C_{art} \times k_{blood,ab} - M_{art,m} \times k_{de})$$

A3.12

where

M_{art} [μg] – Amount of nanoparticles in arterial blood.

$fr_{airblood}$ [unitless] – Direct transferred fraction of nanoparticles from the pulmonary region to the blood during exposure.

Q_{tot} [mL per hour] – Total cardiac output.

W_{art} [μg] – Weight of arterial blood.

$k_{blood,ab}$ [per hour] – Uptake rate of PCs in blood, mathematical description can be found later in this section.

$M_{art,m}$ [μg] – Amount of nanoparticles captured by PCs in arterial blood.

k_{de} [per hour] – Desorption rate from PCs.

And the concentration of nanoparticles in the arterial blood C_{art} is:

$$C_{art} = \frac{M_{art}}{W_{art}}$$

A3.13

The dynamic of nanoparticles in the venous blood is:

$$\frac{dM_{ven}}{dt} = \sum (Q_t \times C_{t,b}) - Q_{tot} \times C_{ven} - (W_{ven} \times C_{art} \times k_{blood,ab} - M_{ven,m} \times k_{de})$$

A3.14

where

M_{ven} [μg] – Amount of nanoparticles in venous blood.

C_{ven} [μg per g] – Concentration of nanoparticles in the venous blood.

W_{ven} [g] – Weight of venous blood.

$M_{ven,m}$ [μg] – Amount of nanoparticles captured by PCs in venous blood.

The initial value for M_{ven} is the injected dose. And the concentration of nanoparticles in the venous blood C_{ven} is:

$$C_{ven} = \frac{M_{ven}}{W_{ven}}$$

A3.15

Approximately, arterial blood takes up 20% of the total blood and venous blood takes up 80% of the total blood (Despopoulos and Silbernagl 2003). We also assume the PCs in arterial and venous blood are distributed in this 20/80 ratio. Therefore, W_{art} =

$0.2 \times W_{blood}$, $M_{art,m} = 0.2 \times M_{blood,m}$, $W_{ven} = 0.8 \times W_{blood}$, $M_{ven,m} = 0.8 \times M_{blood,m}$, where W_{blood} is the weight of total blood and $M_{blood,m}$ is the amount of nanoparticles captured by PCs in the total blood.

A3.2.4 Dynamics of the nanoparticles in tissues, as a direct function of arterial and venous concentrations

By introducing Eq. A3.10 to Eq. A3.6 we can directly express the dynamic of amount of nanoparticles in different organs (except for lungs) other than the blood as a function of the arterial blood, eliminating the sub-compartment of capillary blood and simplifying the model as follows:

$$\frac{dM_t}{dt} = \frac{\chi_\alpha \times Q_t}{(1+\chi_\alpha)}(C_{art} - C_t / P) - (W_t \times C_t \times k_{t,ab} - M_{t,m} \times k_{de}) - \frac{dM_{e,ex}}{dt}$$

A3.16

The amount of nanoparticles in the lungs is related to the venous blood instead of the arterial blood and can be described as:

$$\frac{dM_{lu}}{dt} = \frac{\chi_{rich} \times Q_{tot}}{(1+\chi_{rich})}(C_{ven} - C_{lu} / P) - (W_{lu} \times C_{lu} \times k_{lu,ab} - M_{lu,m} \times k_{de})$$

A3.17

where

M_{lu} [µg] – Amount of nanoparticles in the tissue of lungs.

W_{lu} [g] – Weight of lungs.

C_{lu} [µg per g] – Concentration of nanoparticles in lungs.

$M_{lu,m}$ [µg] – Amount of nanoparticles captured by PCs in lungs.

$k_{lu,ab}$ [per hour] – Current uptake rate of nanoparticles by PCs in lungs.

In addition, the outflows from the spleen and GI tract feed directly into the liver, instead of joining the venous blood in circulation.

A3.2.5 Capture of nanoparticles by phagocytizing cells

The PCs capture nanoparticles from the tissue and in the meanwhile, desorption from the PCs will release part of the captured nanoparticles back to the tissue. The PCs capture the nanoparticles in a saturable manner. That is, as the amount captured approaches the capacity for the PCs in the various organs, the uptake rate $k_{t,ab}$ will decrease and eventually the capture of nanoparticles will be in a dynamic balance with the desorption. The equation describing these behaviors is:

$$\frac{dM_{t,m}}{dt} = W_t \times C_t \times k_{t,ab} - M_{t,m} \times k_{de}$$

A3.18

The initial uptake rate is assumed to be equal for all organs, while saturation levels of PCs will be adjusted for each compartment independently, reflecting the potential variation in PCs density in various organs. Thus the uptake rate is related to the amount of nanoparticles already captured and the maximum uptake capacity in different organs:

$$k_{t,ab} = k_{ab0} \times (1 - \frac{M_{t,m}}{M_{t,cap} \times W_t})$$

A3.19

where

k_{ab0} [per hour] – Maximum uptake rate by PCs.

$M_{t,cap}$ [µg] – PCs uptake capacity for nanoparticles per organ *t* weight.

A3.2.6 Elimination

Parts of the nanoparticles are assumed to be excreted by a first order elimination from the head region, GI tract lumen, tissue of liver, and capillary blood of kidneys. This is summarized as below:

$$\frac{dM_{ex}}{dt} = \sum \frac{dM_{e,ex}}{dt} = M_l \times CLE_f + M_{k,b} \times CLE_u + M_{head} \times CLE_{head} + M_{gilum} \times CLE_{fgi}$$

A3.20

where

M_{ex} [μg] – Amount in excreta.

CLE_f [per hour] – Clearance rate to feces from liver tissue.

CLE_u [per hour] – Clearance rate to urine from capillary blood in kidneys.

A3.2.7 Codes of the model

Codes of the model in Berkeley-Madonna™ (version 8.3.18) are available by request to the corresponding author (Dingsheng Li, email: dingsli@umich.edu).

A3.3 Time evolution for concentration in feces from a preliminary study

Data showed a rapid decrease in concentrations until the fourth day then stayed stead at lower levels.

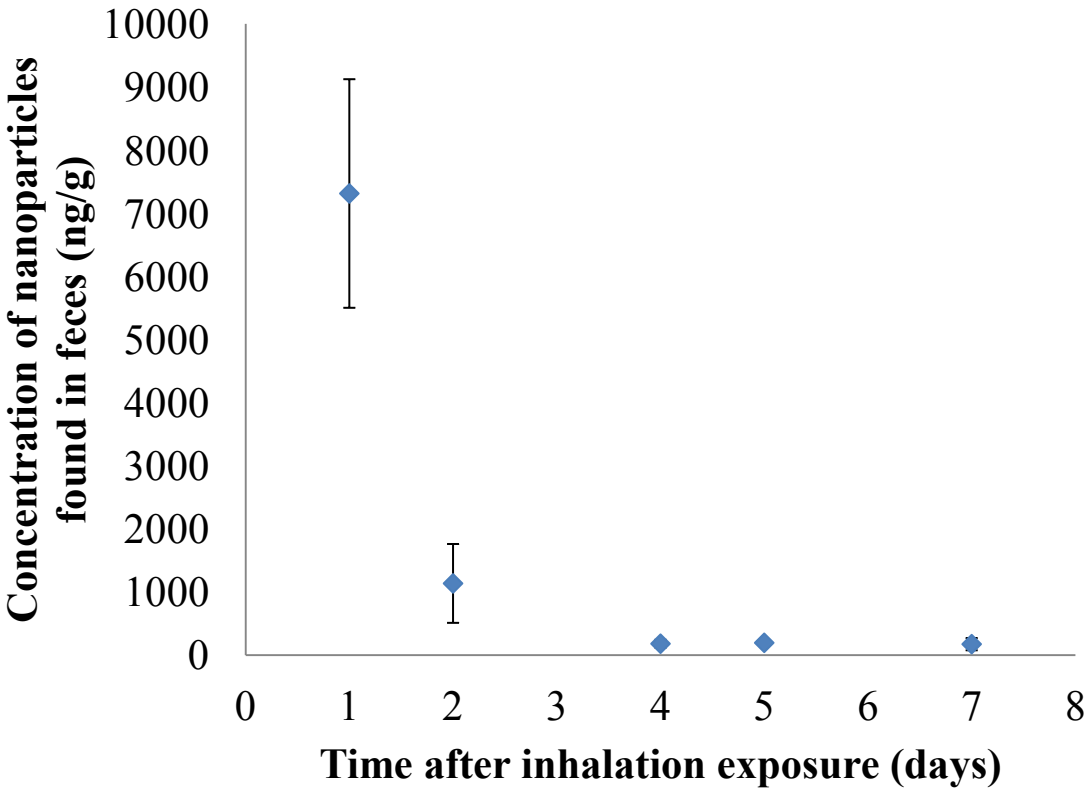

Fig. A3.2 Concentrations found in feces in the preliminary study. Error bars representing one standard deviation on the means.

A3.4 Individual organ concentrations of CeO_2 nanoparticles for all runs

The following tables show the individual organ concentrations of CeO_2 nanoparticles for all runs. Rat 9-892 in run fresh 1, 13-892 in run fresh 2 was deemed as outliers due to exceptionally high concentrations in the heart and feces respectively. These concentrations violated the mass balance by themselves and therefore the data from these two rats were discarded from further analysis of the data.

Run fresh 1

Rat ID	Exposure duration (hrs)	Necropsy post exposure	Lung (µg/kg)	Liver (µg/kg)	Kidney (µg/kg)	Heart (µg/kg)	Brain (µg/kg)	Spleen (µg/kg)	Olfactory (µg/kg)	Feces (µg/kg)	Urine (ng/mL)	Serum (ng/mL)
1-892	4	15 min	261	0.6	0.17	0.10	0.17	0.38	0.8	-	-	3.5
2-892	4	15 min	465	0.4	0.29	0.14	0.16	1.76	0.7	-	-	2.1
3-892	4	15 min	226	0.4	0.21	0.14	0.16	0.60	0.6	-	-	3.7
4-892	4	24 hrs	229	1.7	1.28	0.16	0.13	0.28	0.9	91	1.9	3.1
5-892	4	24 hrs	193	1.2	0.59	0.15	0.69	0.20	0.8	88	7.4	2.7
6-892	4	24 hrs	255	1.5	1.09	0.81	15.83	0.14	0.8	96	8.1	-
7-892	4	7 days	185	9.9	1.98	0.29	0.69	4.19	0.9	-	-	1.9
8-892	4	7 days	3	3.4	1.37	0.37	0.85	0.33	0.5	-	-	1.8
9-892	4	7 days	4	0.1	0.17	1214.80	6.33	BID	87.2	-	-	2.3

*BID: below detection limit

- no sample

Run fresh 2

Rat ID	Exposure duration (hrs)	Necropsy post exposure	Lung (µg/kg)	Liver (µg/kg)	Kidney (µg/kg)	Heart (µg/kg)	Brain (µg/kg)	Spleen (µg/kg)	Olfactory (µg/kg)	Feces (µg/kg)	Urine (ng/mL)	Serum (ng/mL)
10-892	6	15 min	1645	0.9	0.92	0.76	1.23	0.15	7.7	-	-	2.3
11-892	6	15 min	1431	1.2	0.98	0.58	1.19	0.15	25.2	-	-	2.7
12-892	6	15 min	1704	0.8	0.94	0.49	0.92	BID	6.2	-	-	2.0
13-892	6	24 hrs	1540	2.3	1.57	0.53	0.97	0.23	3.1	9654	-	2.1
14-892	6	24 hrs	4	0.5	0.84	0.47	0.93	0.57	10.0	465	-	2.4
15-892	6	24 hrs	1866	2.6	1.99	0.65	0.96	0.35	4.6	1074	-	2.2
16-892	6	7 days	2017	8.4	5.74	0.86	1.29	BID	5.9	-	-	2.3
17-892	6	7 days	13	0.5	1.20	0.46	1.55	6.24	3.5	-	-	1.9

*BID: below detection limit

- no sample

Run aged 1

Rat ID	Exposure duration (hrs)	Necropsy post exposure	Lung (µg/kg)	Liver (µg/kg)	Kidney (µg/kg)	Heart (µg/kg)	Brain (µg/kg)	Spleen (µg/kg)	Olfactory (µg/kg)	Feces (µg/kg)	Urine (ng/mL)	Serum (ng/mL)
1-893	4	15 min	1136	0.55	0.25	0.11	BID	--	BID	-	-	1.4
2-893	4	15 min	1754	0.19	0.31	0.16	BID	--	BID	-	-	1.4
3-893	4	15 min	1031	0.18	0.15	0.47	0.34	--	BID	-	-	1.6
4-893	4	24 hrs	507	1.32	0.48	0.81	BID	--	BID	235	3.1	1.5
5-893	4	24 hrs	20	0.25	0.57	BID	BID	--	BID	686	0.9	2.0
6-893	4	24 hrs	958	2.22	0.70	0.17	BID	--	BID	1096	1.0	1.8
7-893	4	7 days	647	5.98	1.93	0.22	BID	--	BID	-	-	0.6
8-893	4	7 days	1145	3.76	1.98	0.32	BID	--	BID	-	-	1.3
9-893	4	7 days	533	9.34	1.26	0.20	BID	--	BID	-	-	0.9

*BID: below detection limit

- no sample

-- under analysis

Run aged 2

Rat ID	Exposure duration (hrs)	Necropsy post exposure	Lung (µg/kg)	Liver (µg/kg)	Kidney (µg/kg)	Heart (µg/kg)	Brain (µg/kg)	Spleen (µg/kg)	Olfactory (µg/kg)	Feces (µg/kg)	Urine (ng/mL)	Serum (ng/mL)
10-893	4	15 min	1289	0.43	1.38	1.50	2.12	1.28	BID	-	-	1.5
11-893	4	15 min	1484	0.22	1.14	1.25	1.18	1.15	BID	-	-	1.0
12-893	4	15 min	85	BID	1.07	1.32	1.61	1.15	BID	-	-	1.0
13-893	4	24 hrs	1706	1.07	2.06	1.22	1.24	1.14	0.9	785	1.1	0.7
14-893	4	24 hrs	1322	2.16	2.00	1.50	2.68	2.05	BID	630	4.3	0.5
15-893	4	24 hrs	1236	1.68	1.72	1.26	1.55	1.46	BID	554	0.5	0.5
16-893	4	7 days	571	2.98	2.53	1.43	1.08	2.17	BID	-	-	1.0
17-893	4	7 days	1043	4.24	2.80	1.52	1.50	1.87	BID	-	-	0.5
18-893	4	7 days	1174	3.50	3.56	1.45	1.63	1.71	BID	-	-	1.2

*BID: below detection limit

- no sample

-- reanalysis

A3.5 Individual organ time courses simulated by the PBPK model

The following figures show the model's simulations on individual organs for each run, compared to the measured data. The simulations on organs are further differentiated into PCs captured and the total in the organ. Amount captured by PCs in organ *t* and the total amount in organ *t* have the symbols of *Mtm* and *Mtt*, respectively. The measured data are circles on the figure. X-axis is time in hours, with 0 hour the start of the exposure. Y-axis is the amount of nanoparticles, with the unit of μg. The number 1, 2, 3, and 4 at the end of each symbol indicates which run this simulation and data are for. 1: fresh 1; 2: fresh 2; 3: aged 1; 4: aged 2. Organs with in sufficient measurement data are only shown the model simulation results. The feces are not shown too since they are represented in Fig. 3.5 in Chapter 3 and they don't have PCs sub-compartment. The order of figures in each run's results is: blood, spleen, liver, brain, heart, kidneys, and lungs.

From these results, we can see the model predicts PCs capturing almost all of the nanoparticles in the organs. There are some free nanoparticles in organs during exposure period and shortly after, but diminish over time.

A3.5.1 Run fresh 1

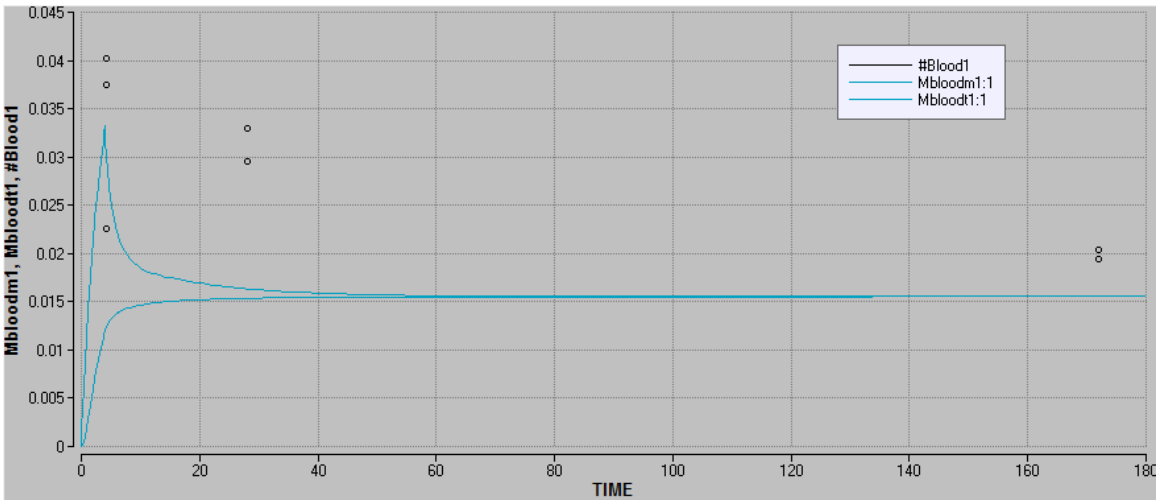

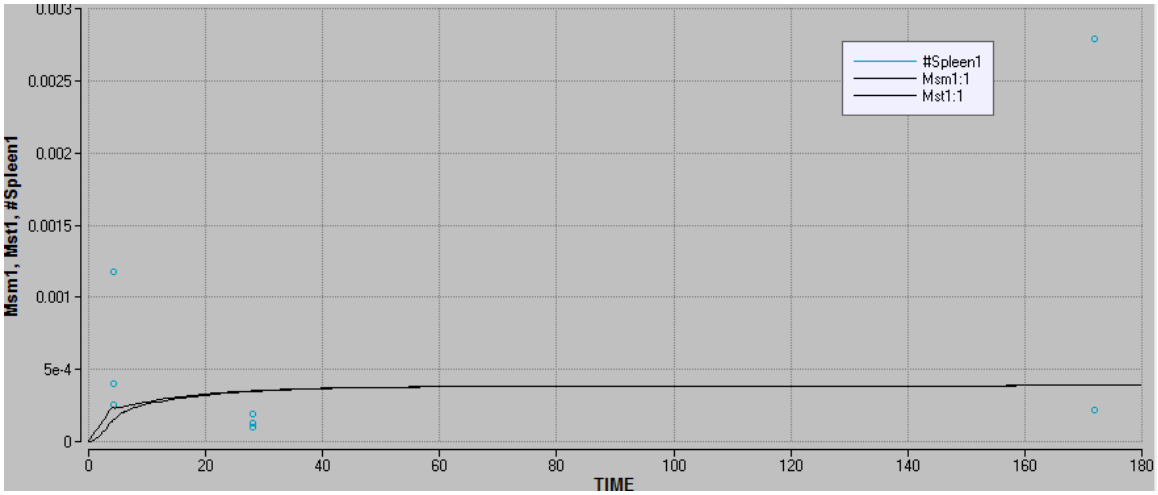
#Spleen1
Msm1:1
Mst1:1
Msm1, Mst1, #Spleen1
TIME

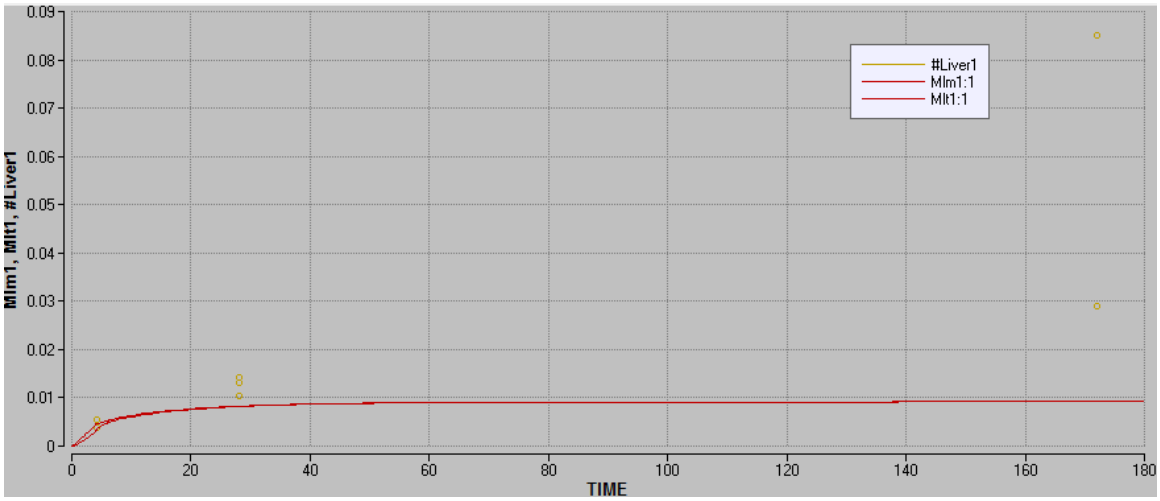
#Liver1
Mlm1:1
Mlt1:1
Mlm1, Mlt1, #Liver1
TIME

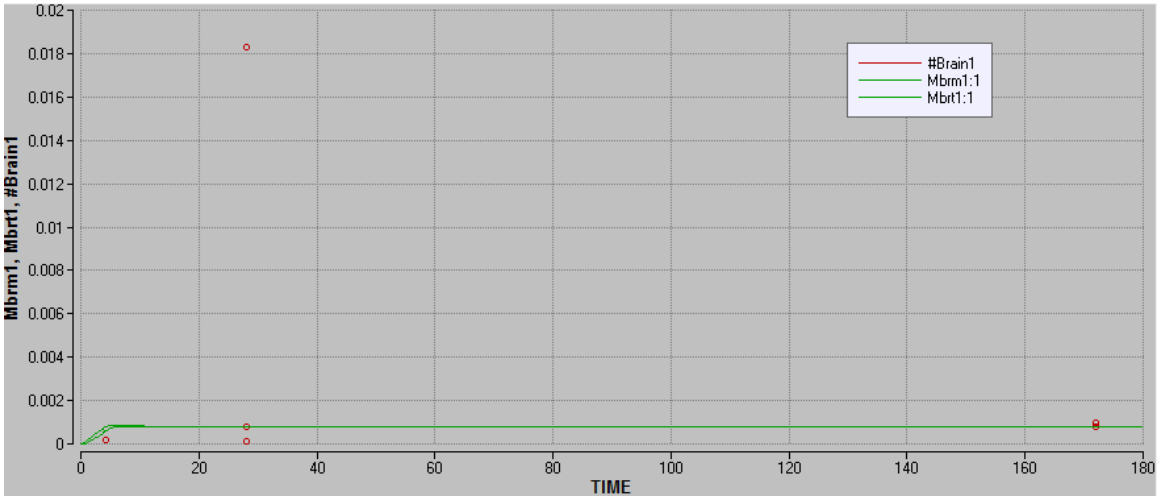
#Brain1
Mbrm1:1
Mbrt1:1
Mbrm1, Mbrt1, #Brain1
TIME

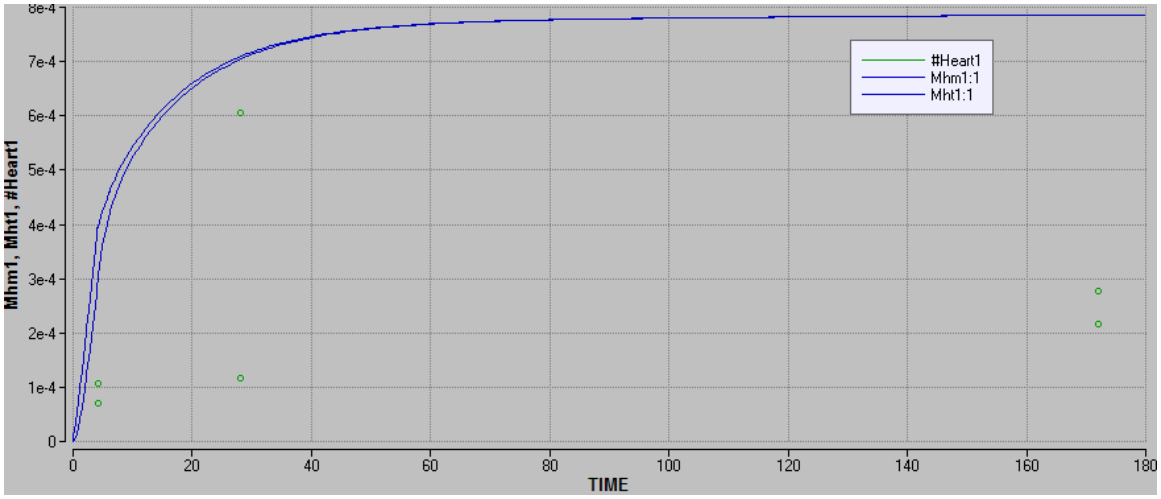

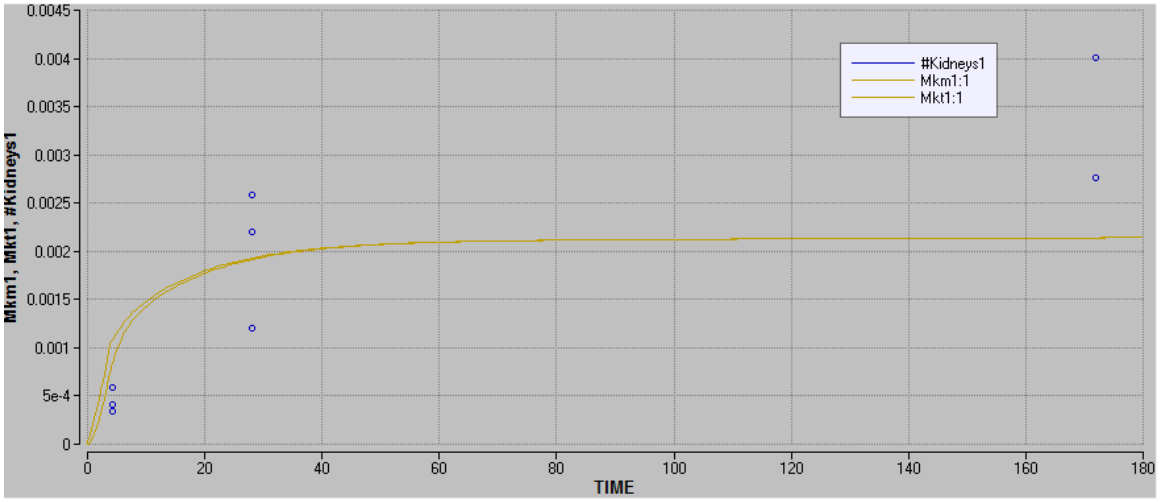

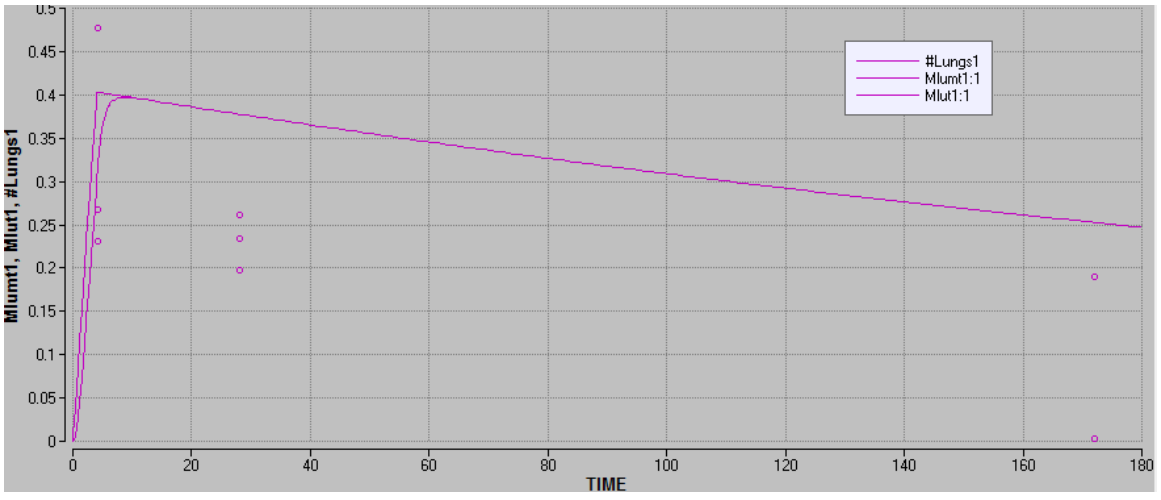

Fig. A3.3 Individual organ time course for run fresh 1.

A3.5.2 Run fresh 2

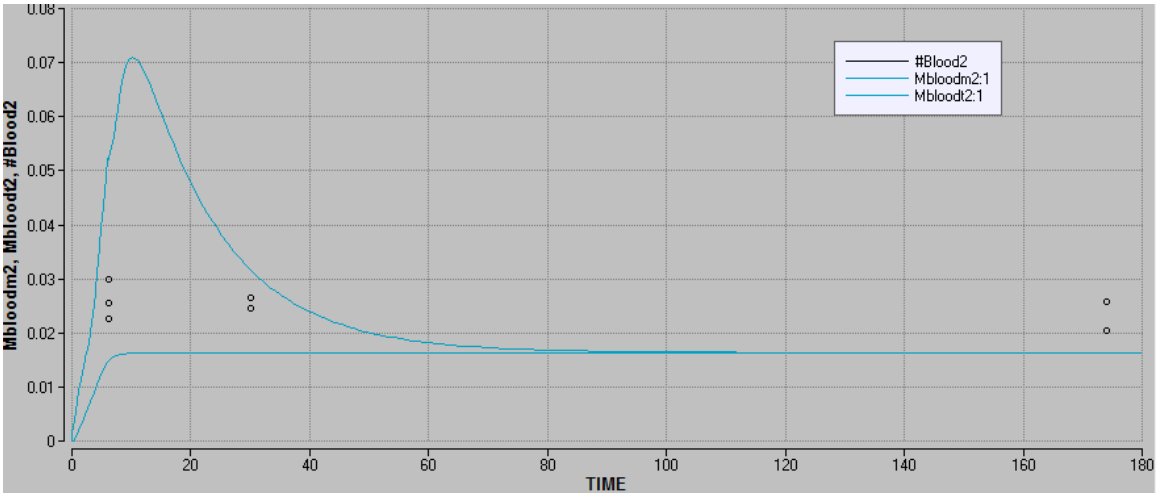
#Blood2
Mbloodm2:1
Mbloodt2:1
Mbloodm2, Mbloodt2, #Blood2
TIME

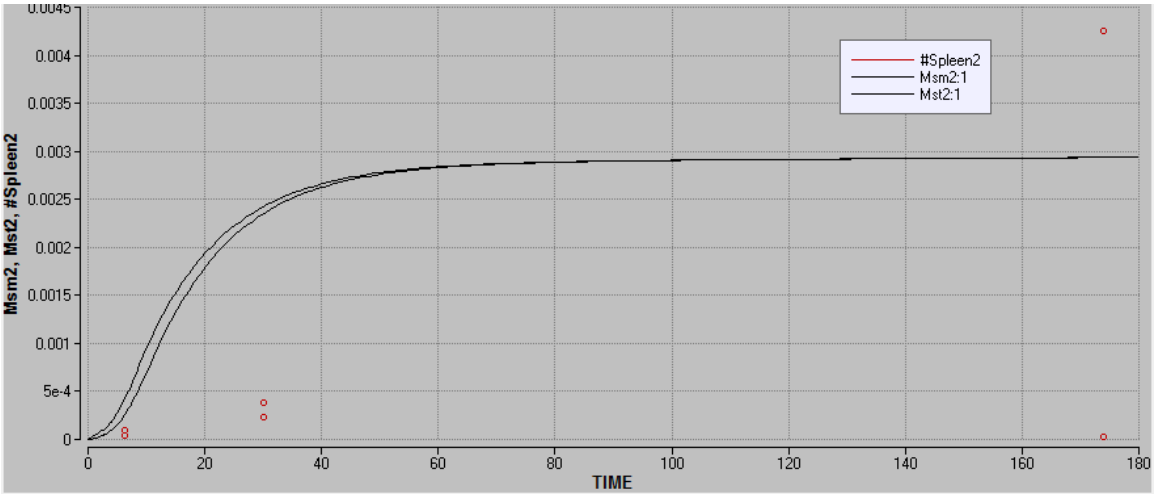
#Spleen2
Msm2:1
Mst2:1
Msm2, Mst2, #Spleen2
TIME

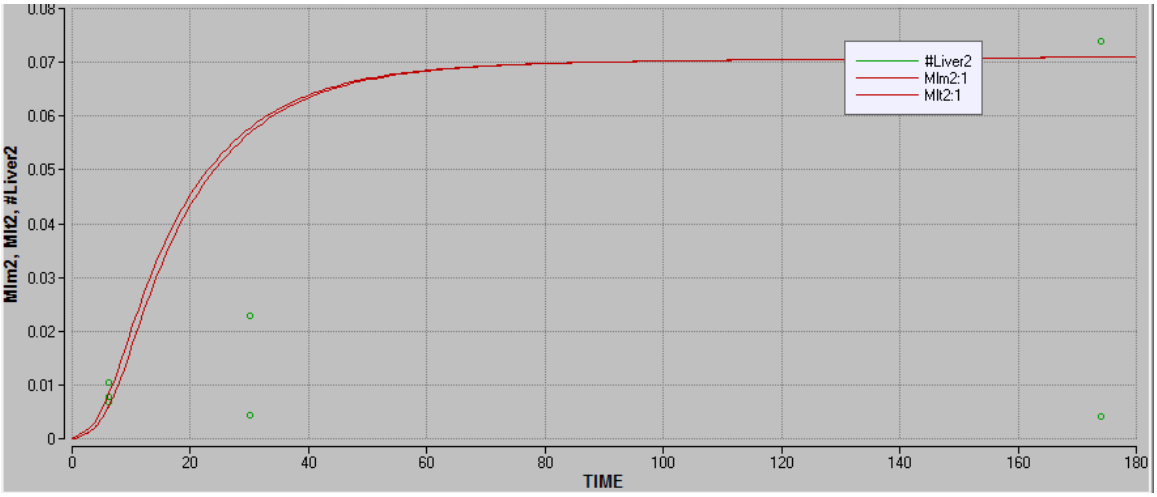
#Liver2
Mlm2:1
Mlt2:1
Mlm2, Mlt2, #Liver2
TIME

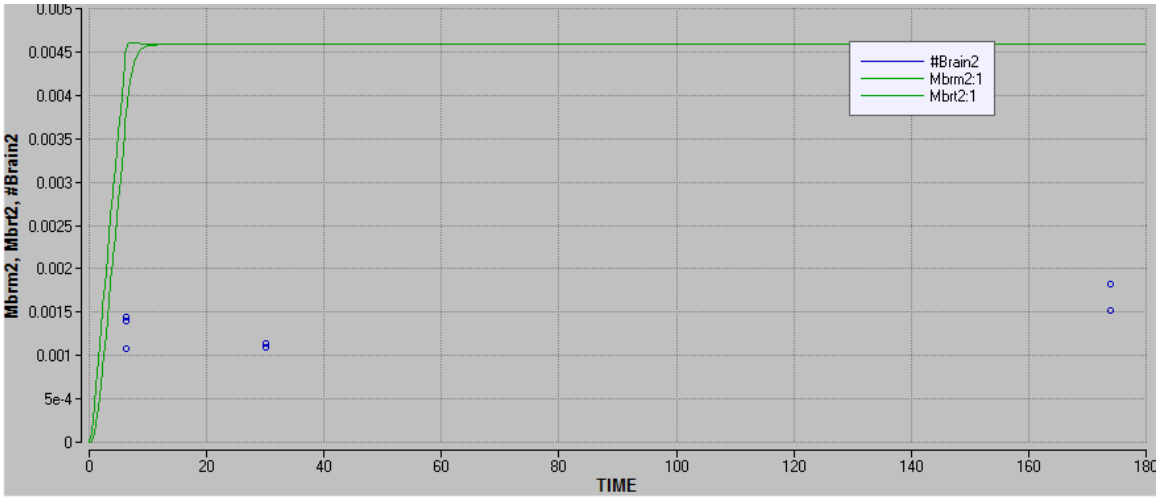
#Brain2
Mbrm2:1
Mbrt2:1
Mbrm2, Mbrt2, #Brain2
TIME

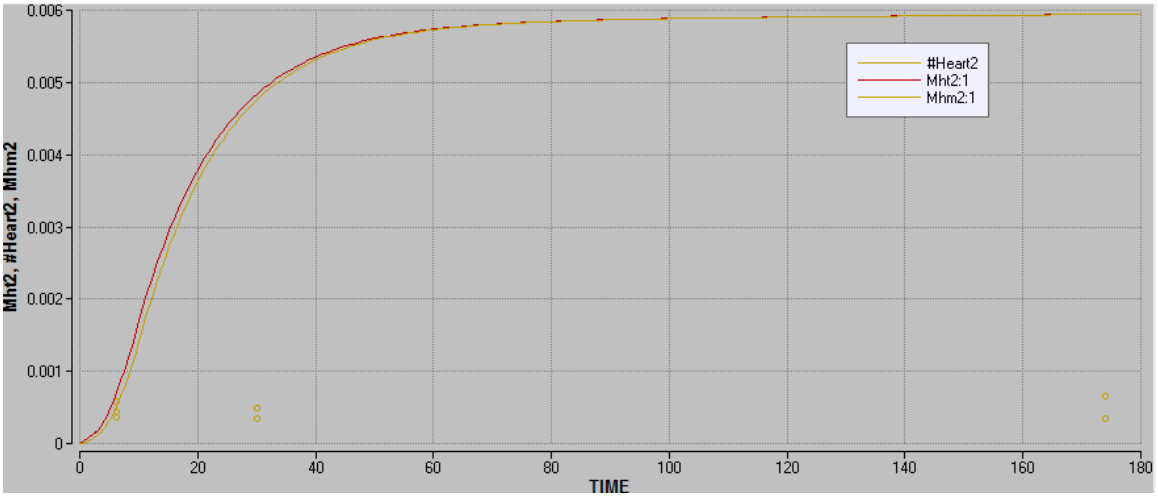
#Heart2
Mht2:1
Mhm2:1
Mht2, #Heart2, Mhm2
TIME

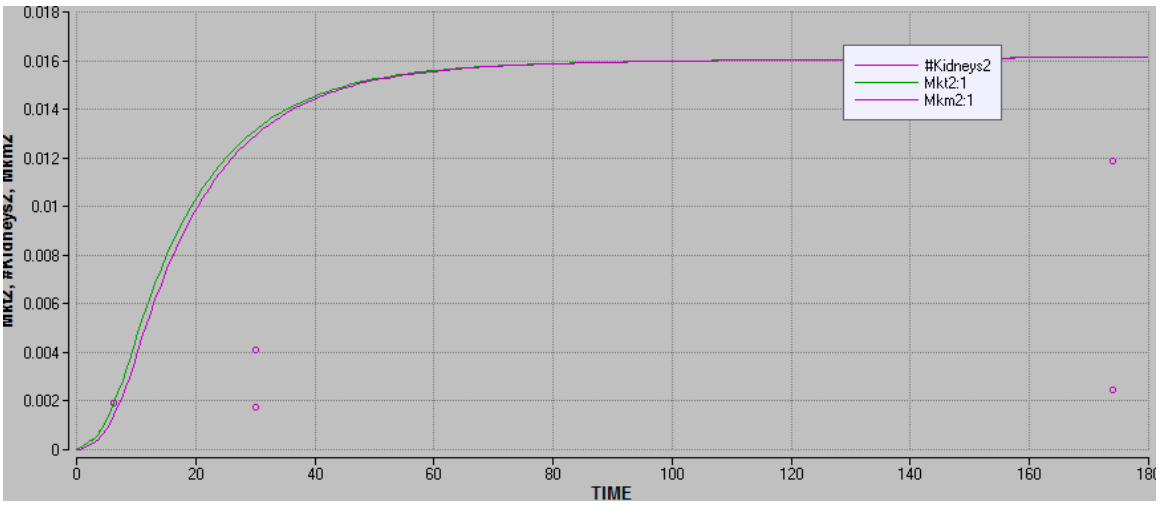
#Kidneys2
Mkt2:1
Mkm2:1
TIME

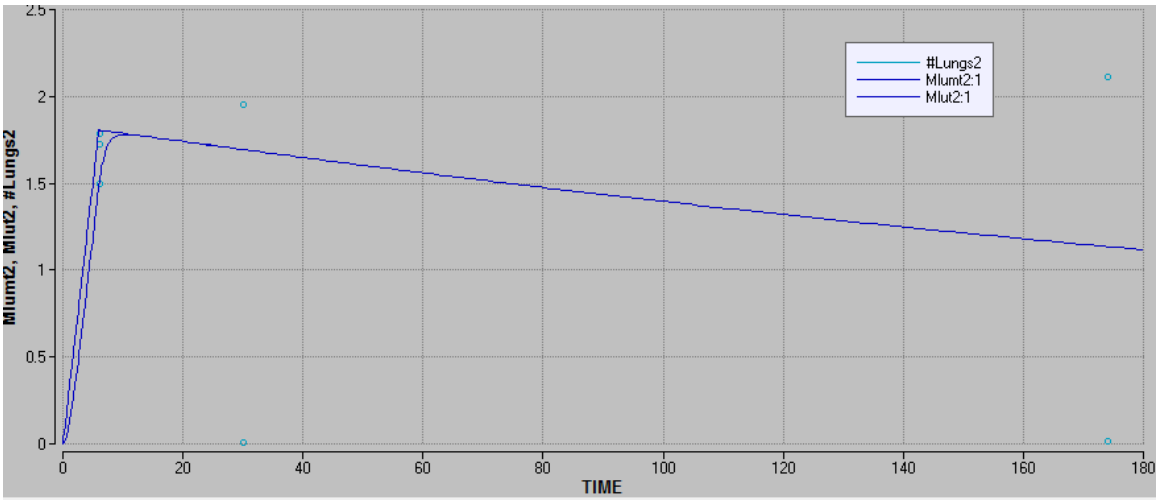

Fig. A3.4 Individual organ time course for run fresh 2.

A3.5.3 Run aged 1

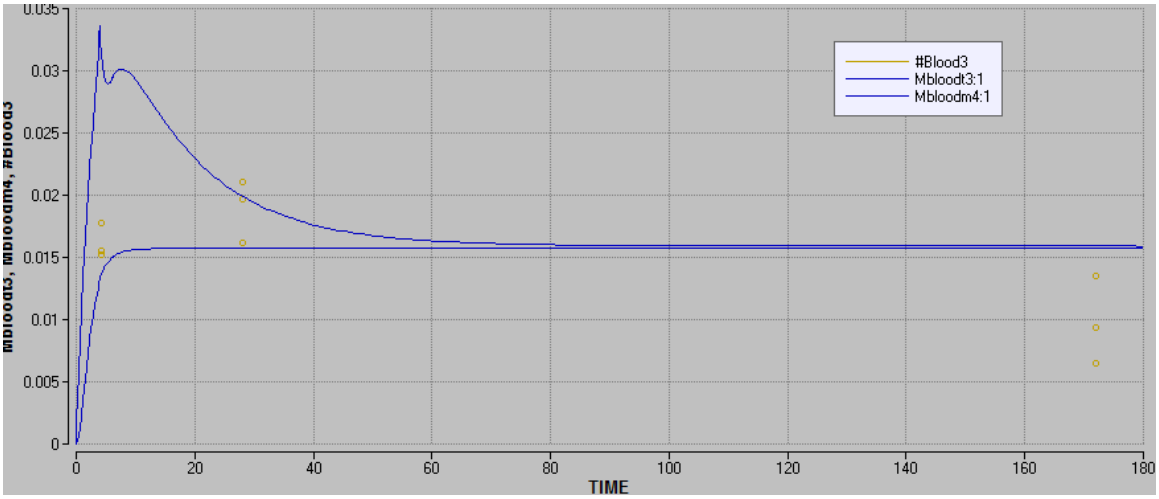

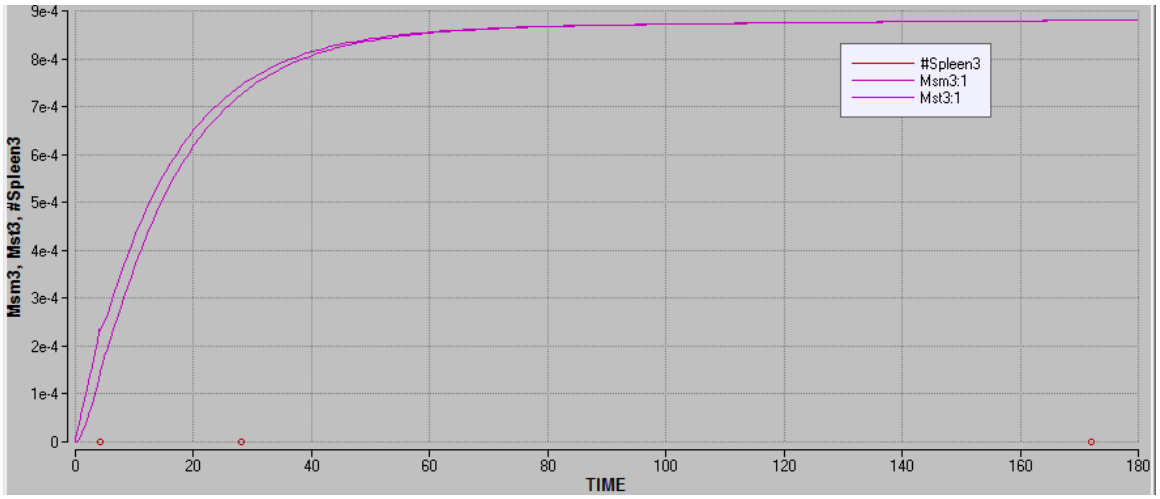

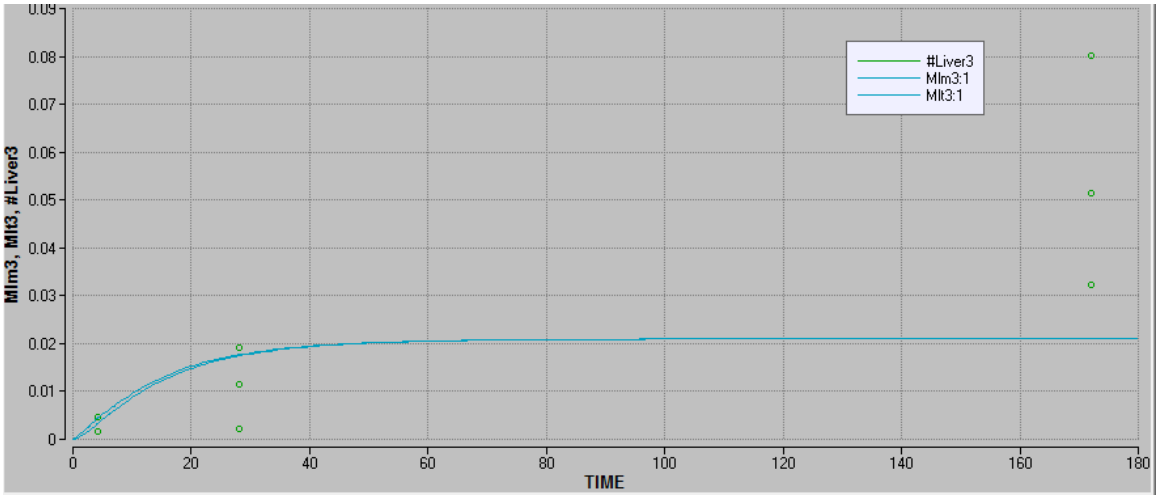
#Liver3
Mlm3:1
Mlt3:1
Mlm3, Mlt3, #Liver3
TIME

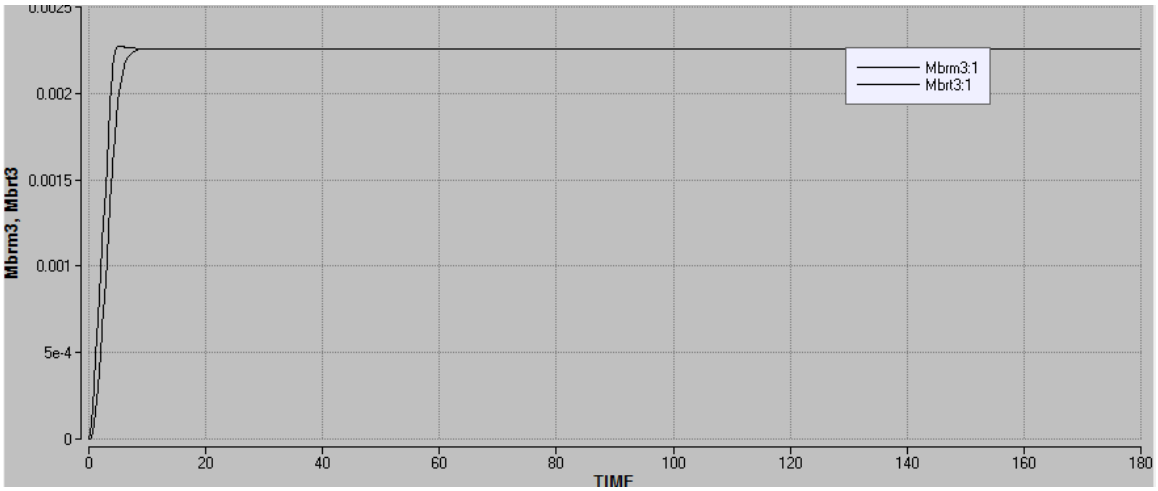
Mbrm3:1
Mbrt3:1
Mbrm3, Mbrt3
TIME

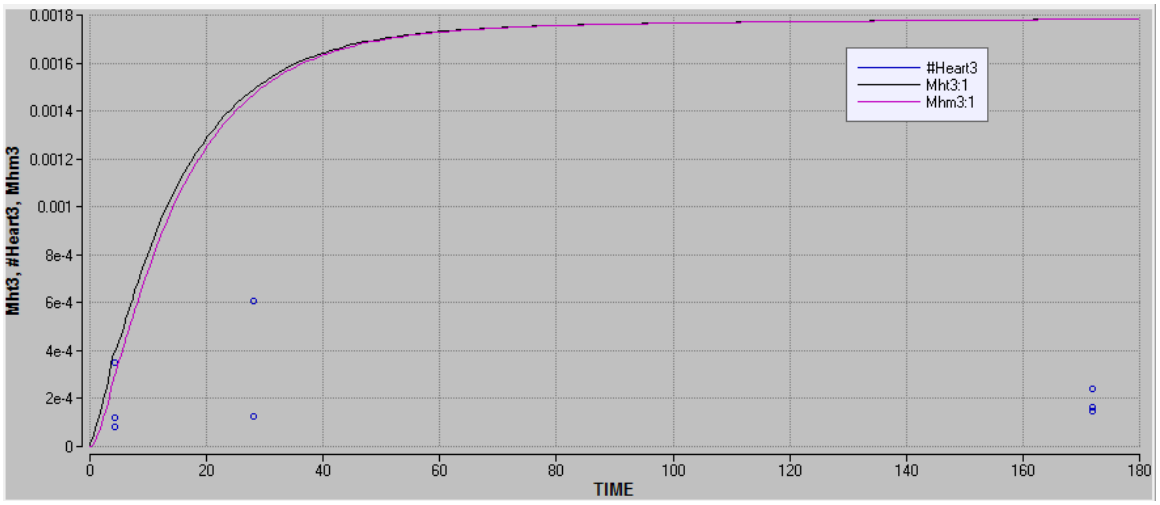
#Heart3
Mht3:1
Mhm3:1
Mht3, #Heart3, Mhm3
TIME

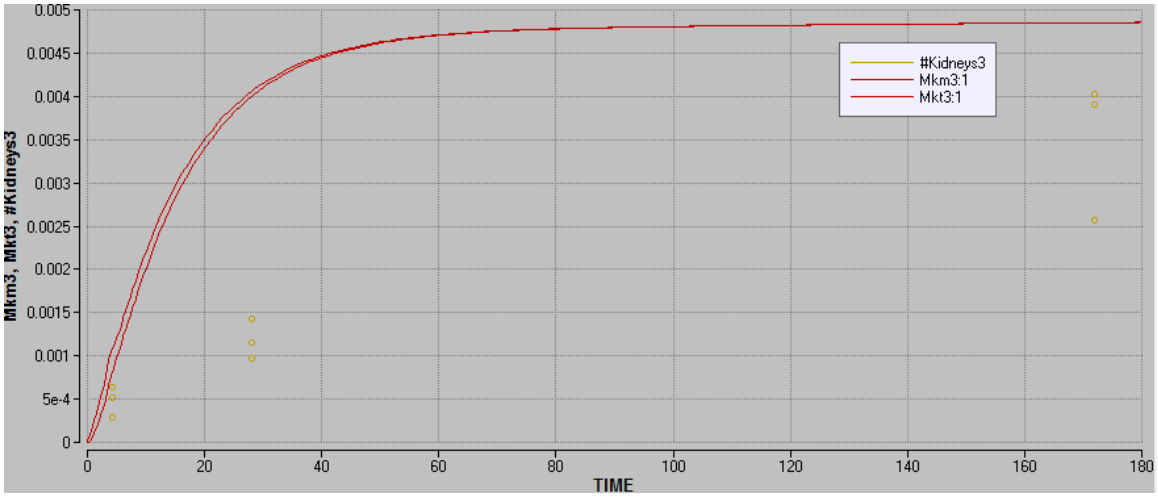

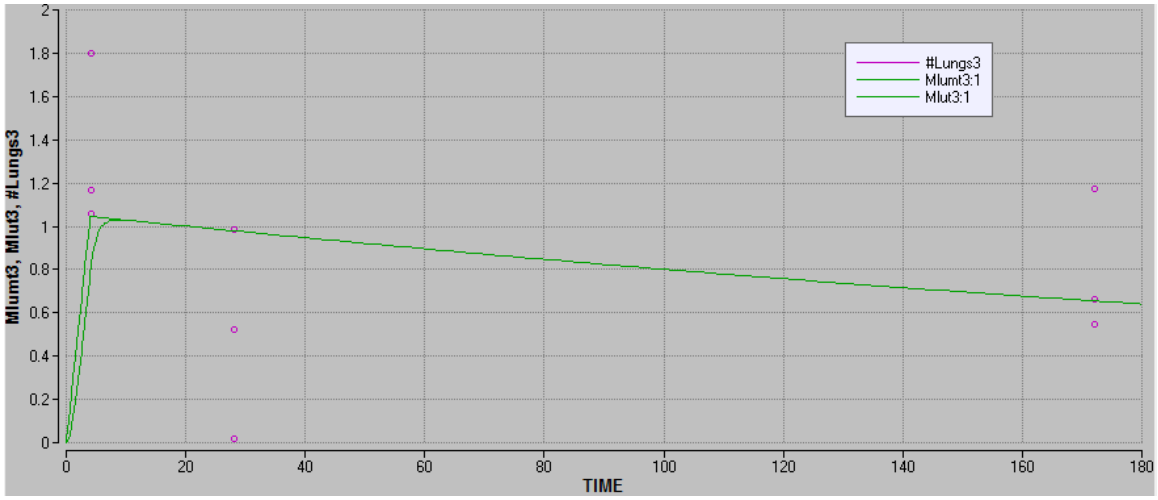

Fig. A3.5 Individual organ time course for run aged 1.

A3.5.4 Run aged 2

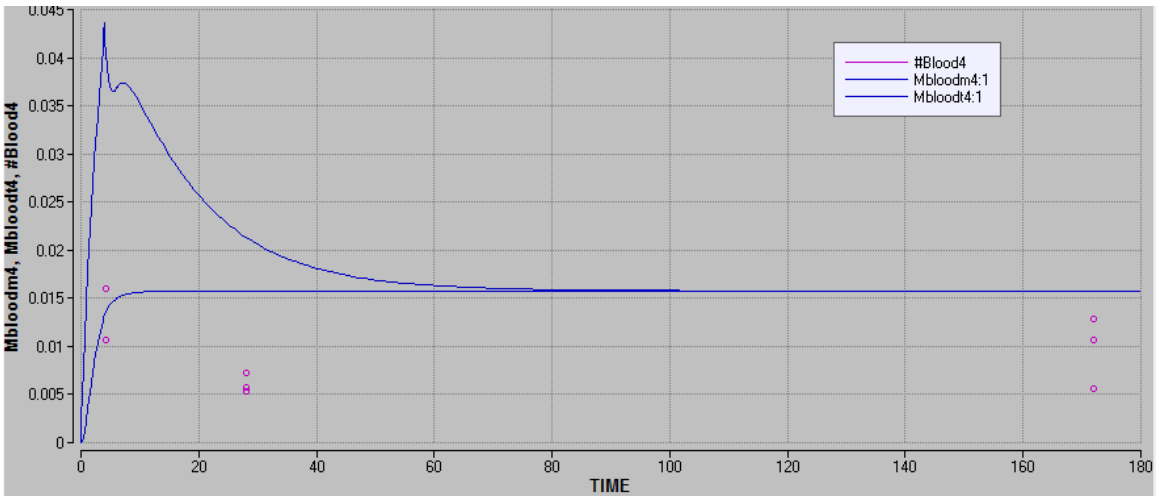

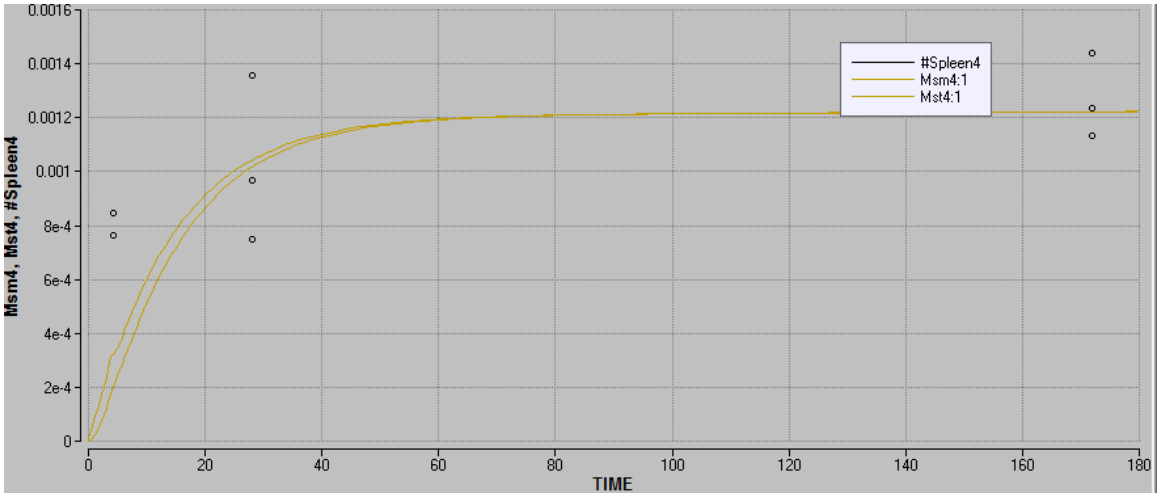
Msm4, Mst4, #Spleen4
TIME
#Spleen4
Msm4:1
Mst4:1

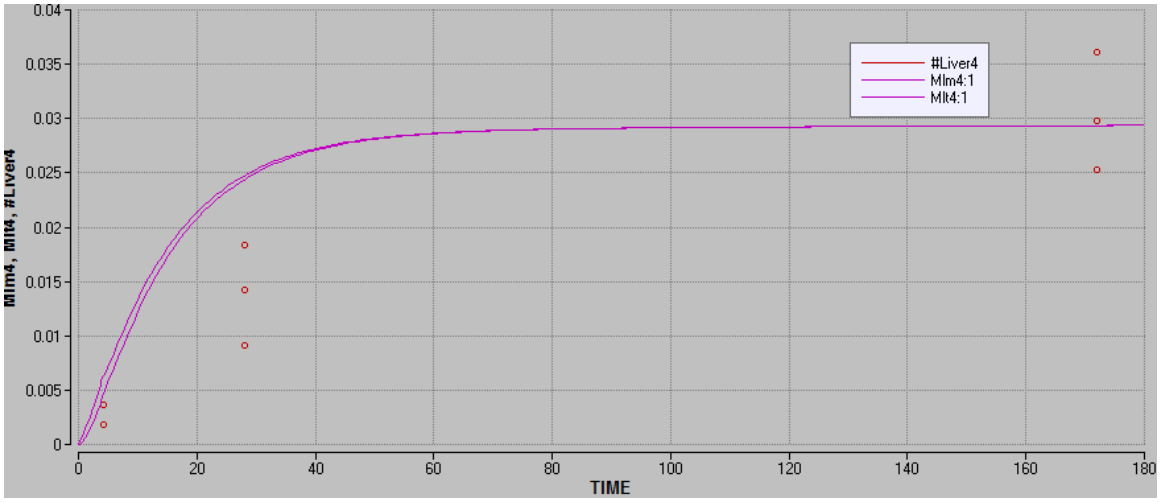
Mlm4, Mlt4, #Liver4
TIME
#Liver4
Mlm4:1
Mlt4:1

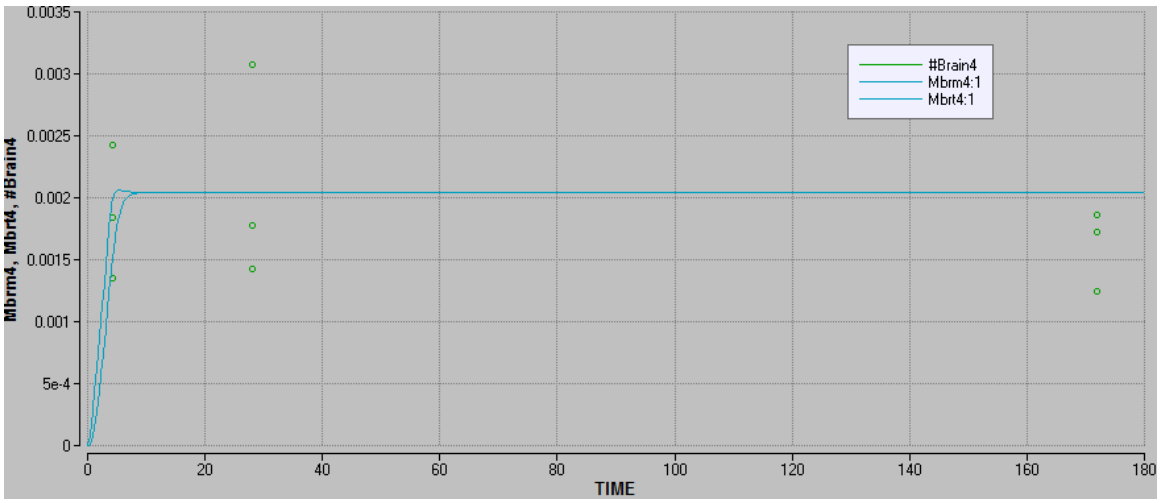
Mbrm4, Mbrt4, #Brain4
TIME
#Brain4
Mbrm4:1
Mbrt4:1

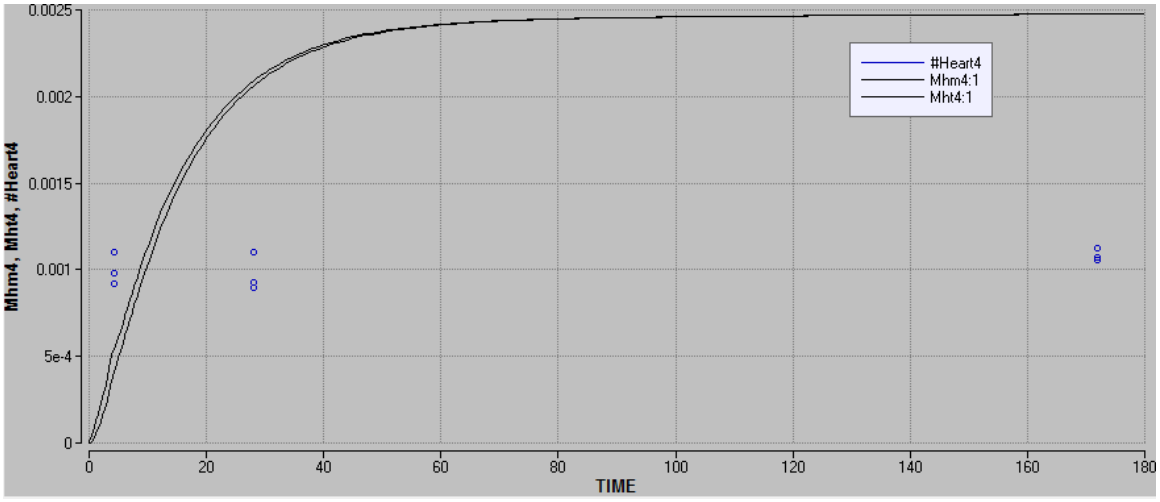

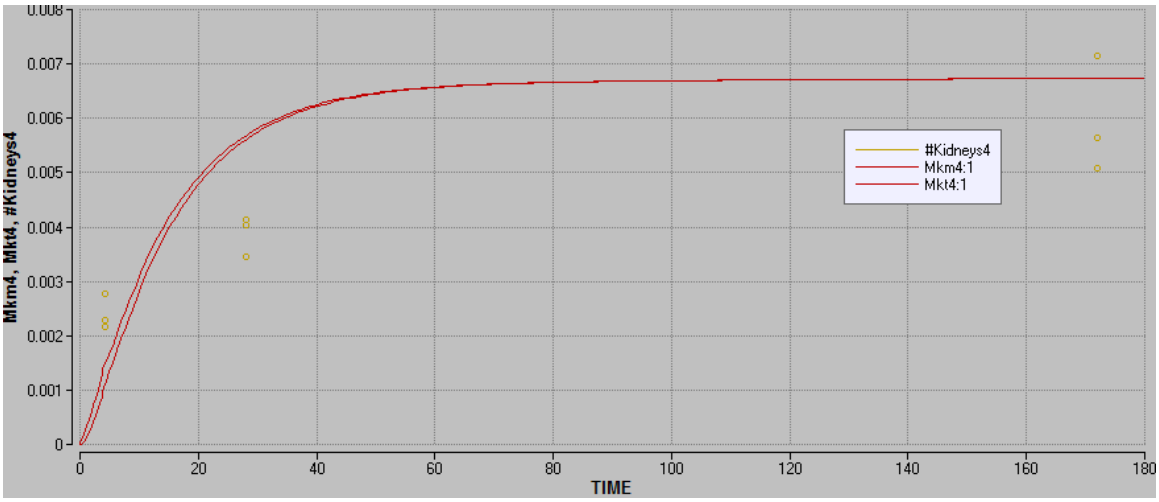

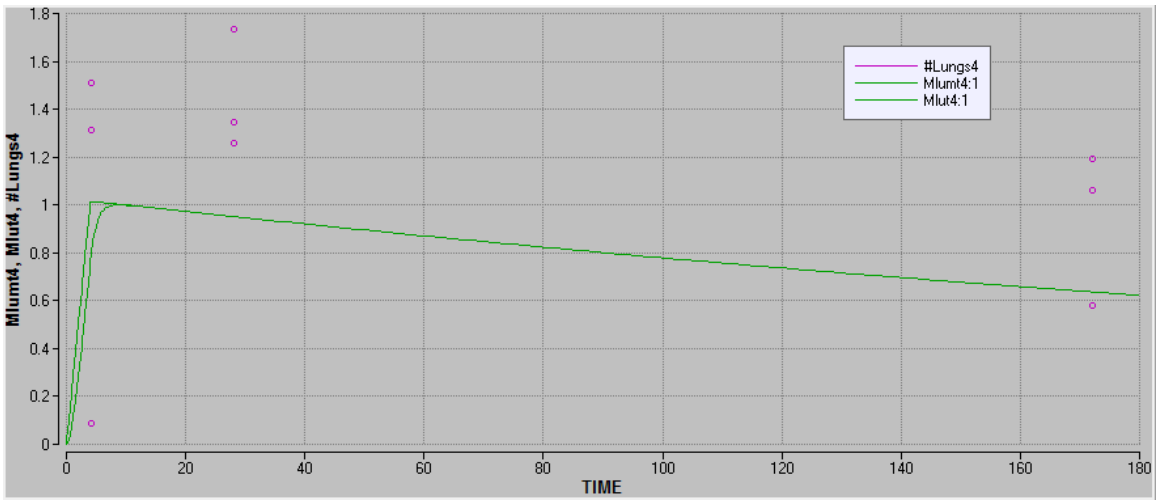

Fig. A3.6 Individual organ time course for run aged 2.

APPENDIX 4

Adaptation of the physiologically based pharmacokinetic model to other nanoparticles

A4.1 Individual organ time courses simulated by the PBPK model

The following figures show the model's simulations on individual organs for each run, compared to the measured data. The simulations on organs are further differentiated into PCs captured and the total in the organ. Amount captured by PCs in organ *t* and the total amount in organ *t* have the symbols of *Mtm* and *Mtt*, respectively. The measured data (mean) are circles on the figure. X-axis is time in hours, with 0 hour the start of the exposure. Y-axis is the amount of nanoparticles, with the unit of µg.

A4.1.1 PAA-peg

Please refer to Fig. 2.3 in Chapter 2.

A4.1.2 PAA

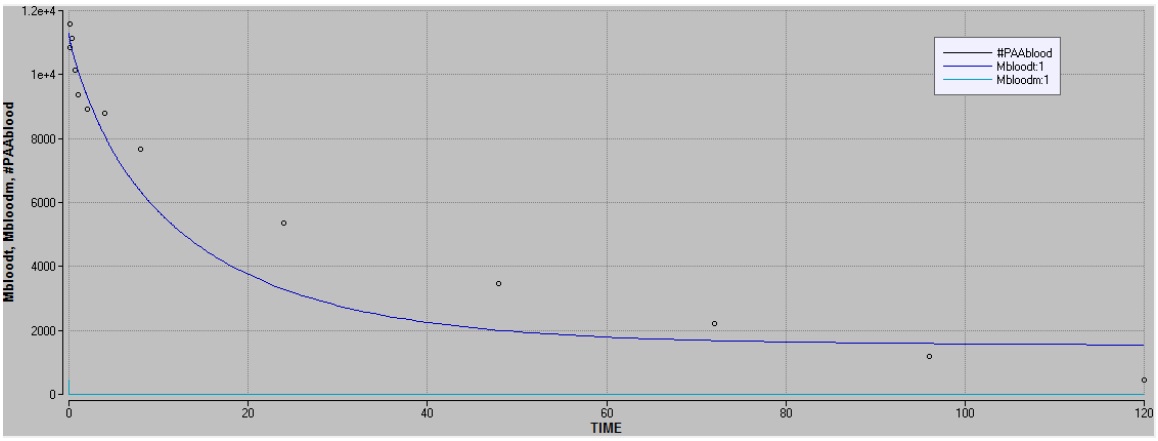

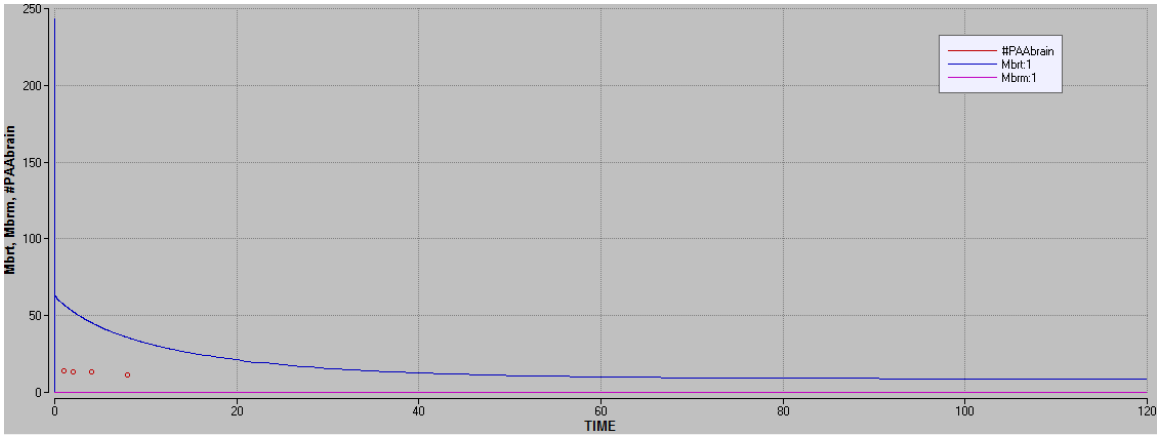
#PAAbrain
Mbrt:1
Mbrm:1
Mbrt, Mbrm, #PAAbrain
TIME

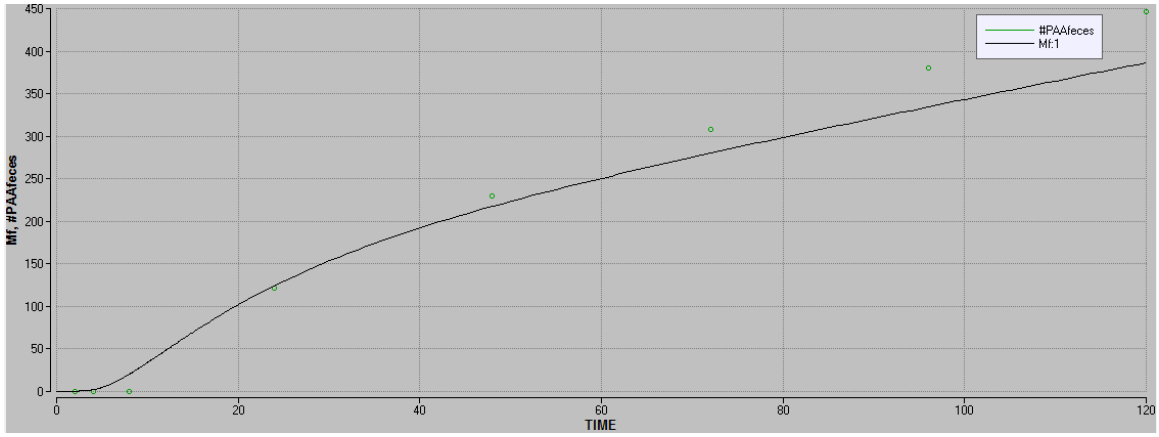
#PAAfeces
Mf:1
Mf, #PAAfeces
TIME

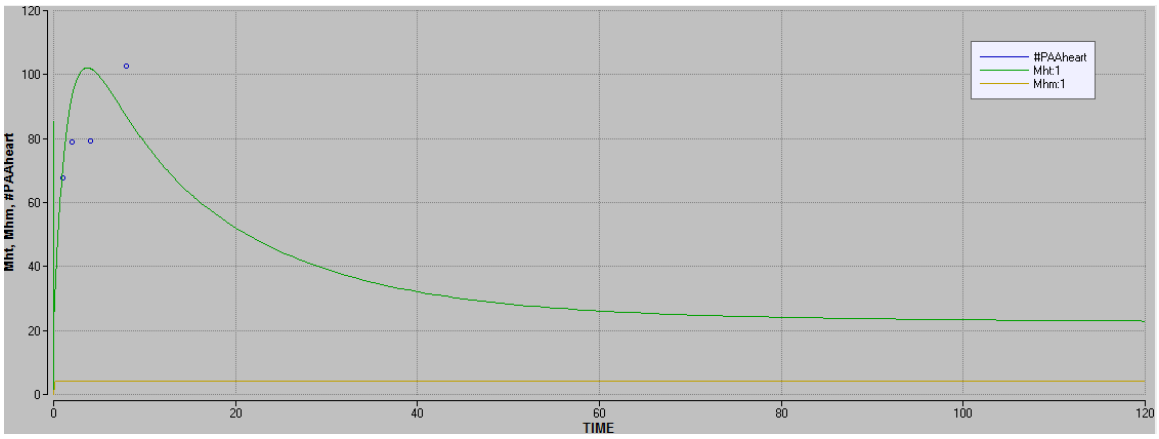
#PAAheart
Mht:1
Mhm:1
Mht, Mhm, #PAAheart
TIME

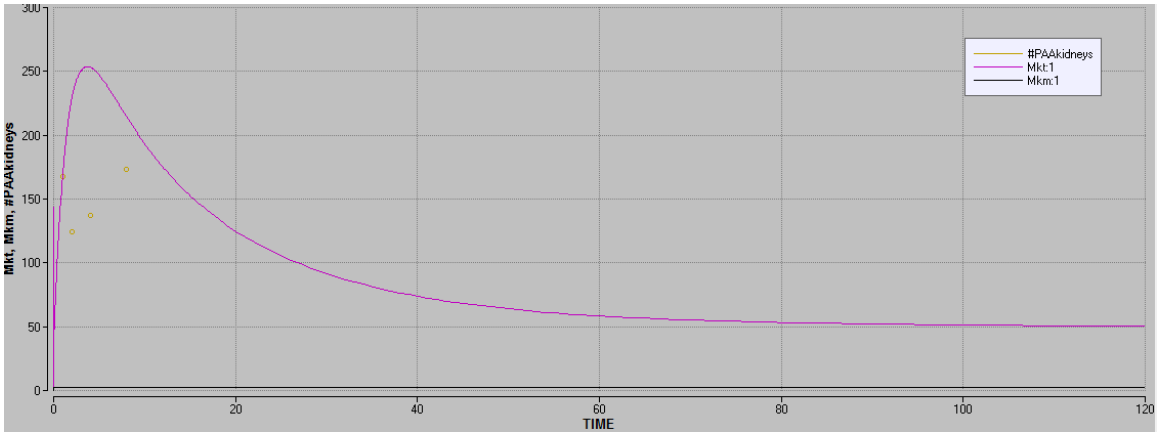
#PAAkidneys
Mkt:1
Mkm:1
Mkt, Mkm, #PAAkidneys
TIME

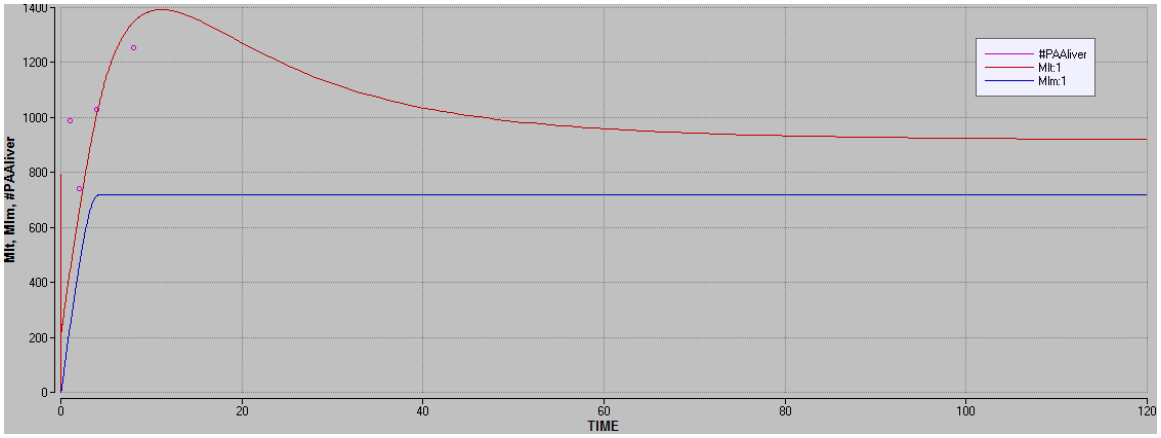
#PAAliver
Mlt:1
Mlm:1
Mlt, Mlm, #PAAliver
TIME

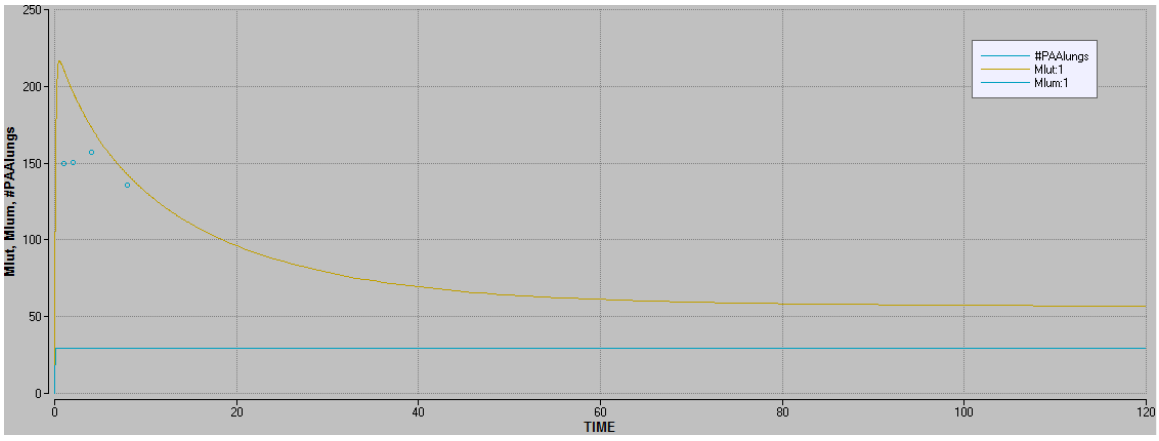
#PAAlungs
Mlut:1
Mlum:1
Mlut, Mlum, #PAAlungs
TIME

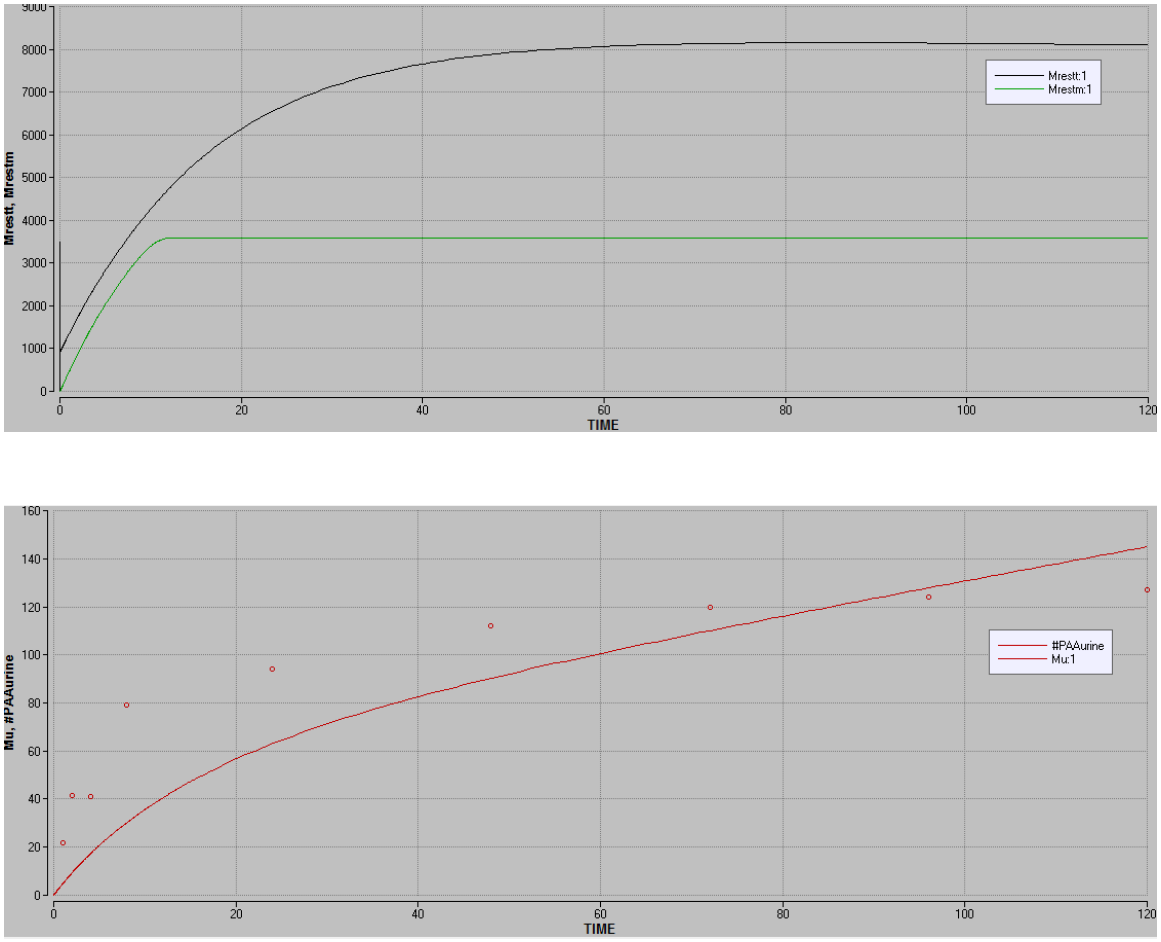

Fig. A4.1 Individual time courses for PAA nanoparticles. For the rest of the body, only one time point data available at 120 hours with a value of 8204 µg.

A4.1.3 PLGA-mPEG

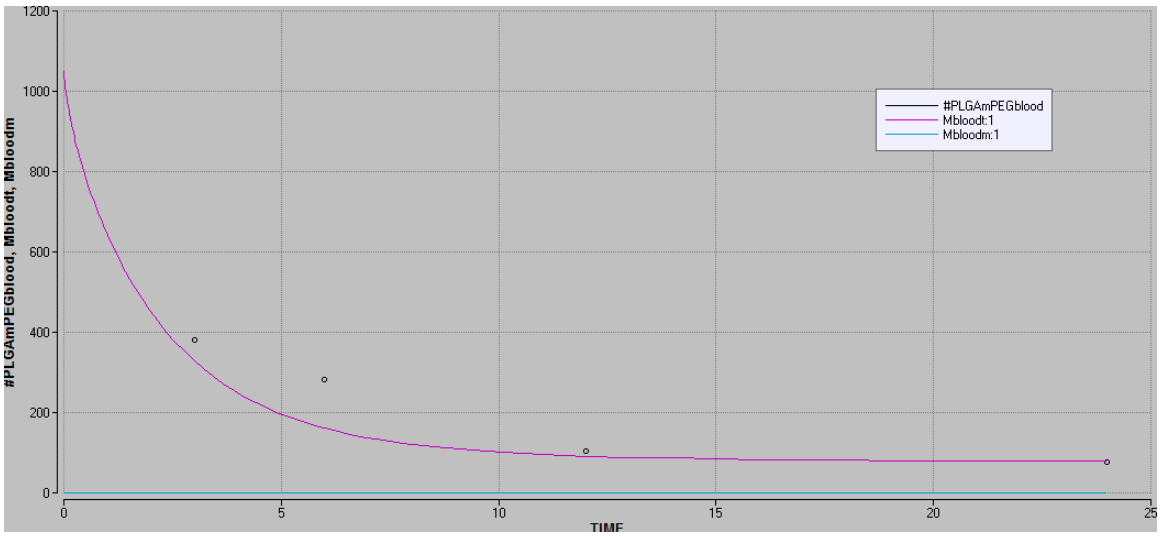

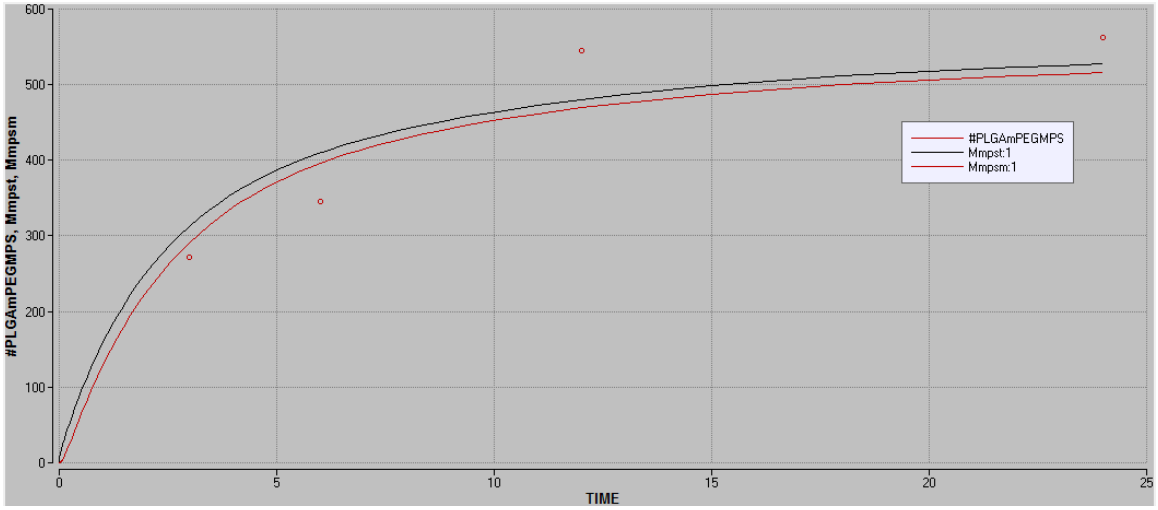
#PLGAmPEGMPS, Mmpst, Mmpsm
TIME
#PLGAmPEGMPS
Mmpst:1
Mmpsm:1

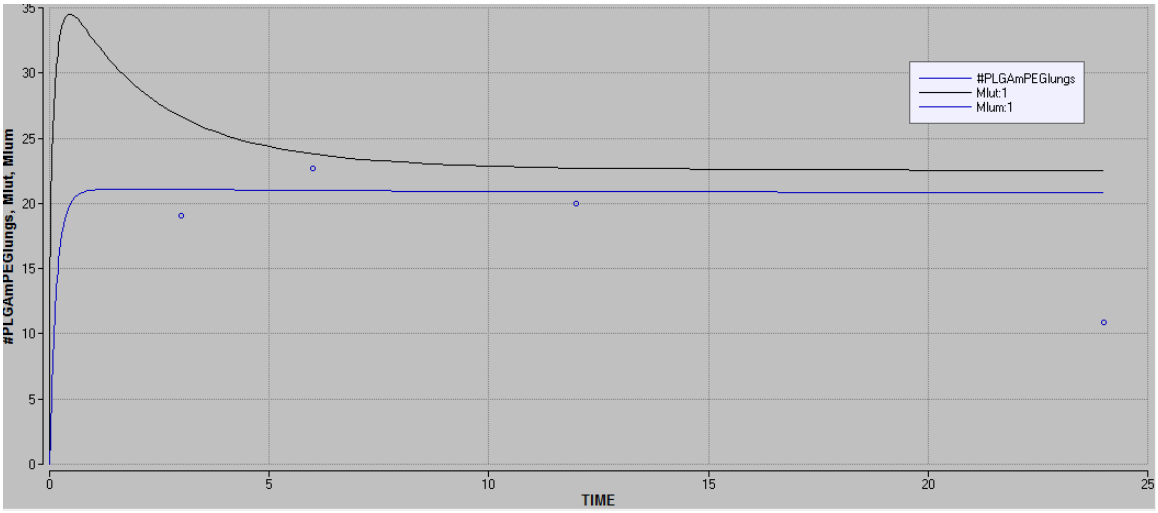
#PLGAmPEGlungs, Mlut, Mlum
TIME
#PLGAmPEGlungs
Mlut:1
Mlum:1

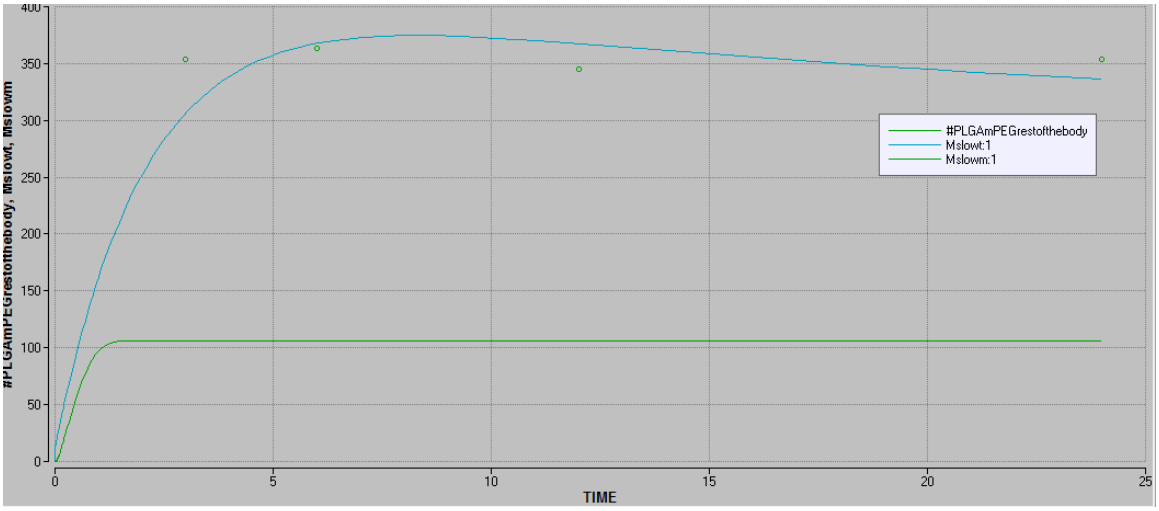
#PLGAmPEGrestofthebody, Mslowt, Mslowm
TIME
#PLGAmPEGrestofthebody
Mslowt:1
Mslowm:1

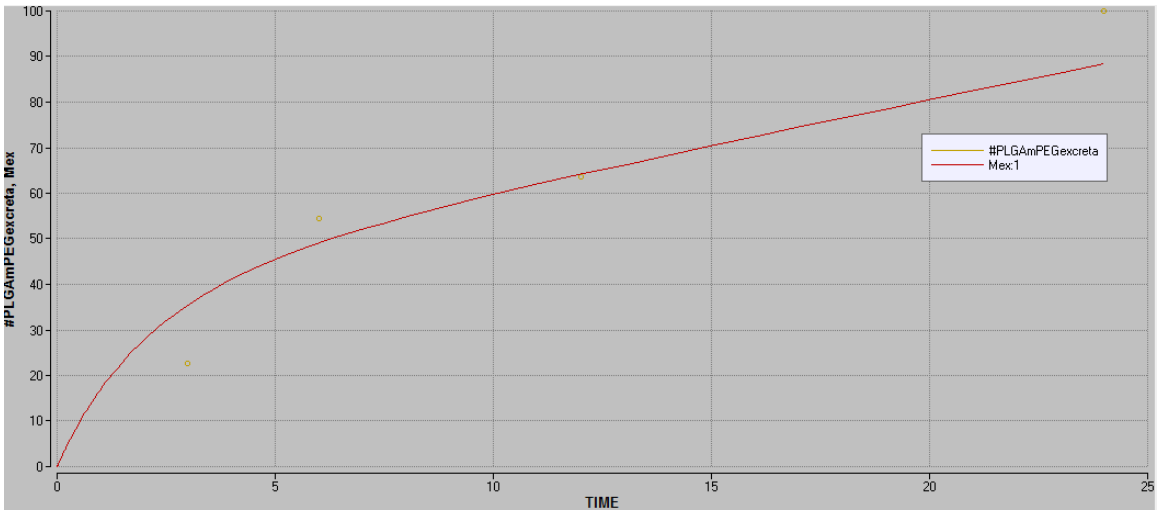

Fig. A4.2 Individual time courses for PLGA-mPEG nanoparticles.

A4.1.4 BVP-PLA

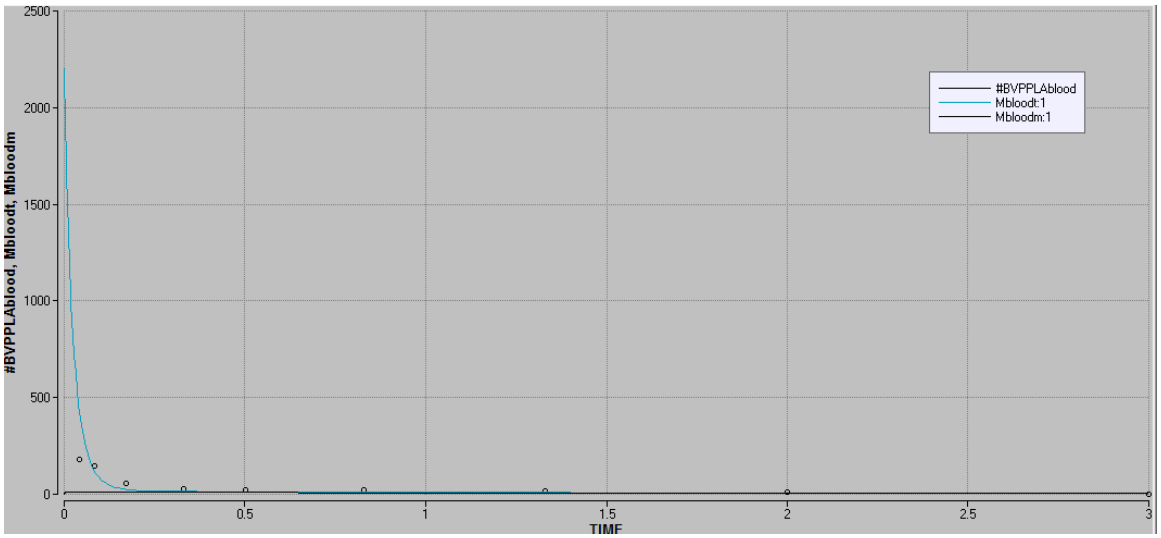

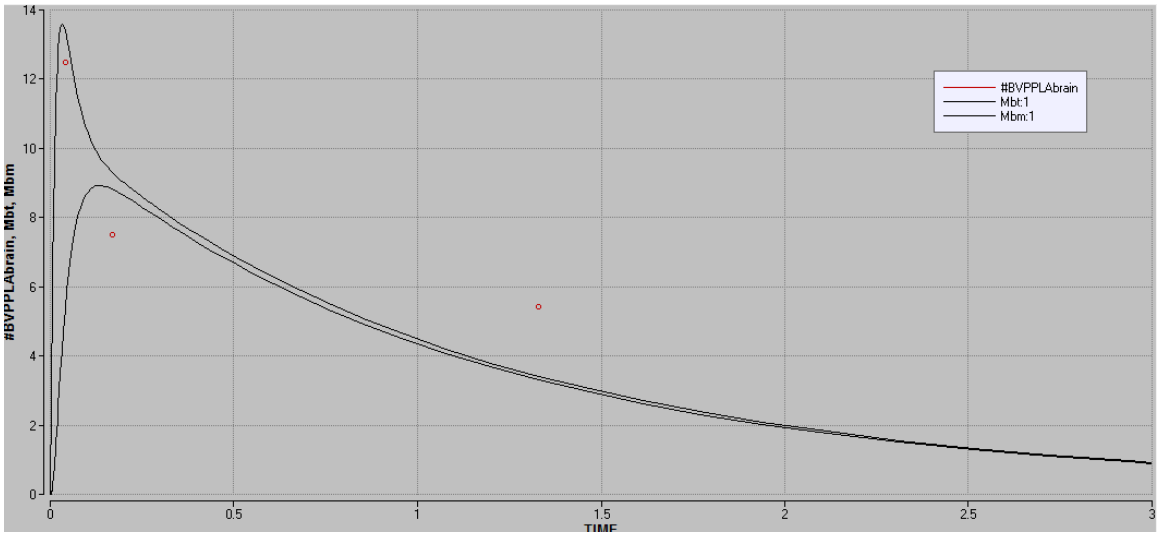
#BVPPLAbrain, Mbt, Mbm
#BVPPLAbrain
Mbt:1
Mbm:1
TIME

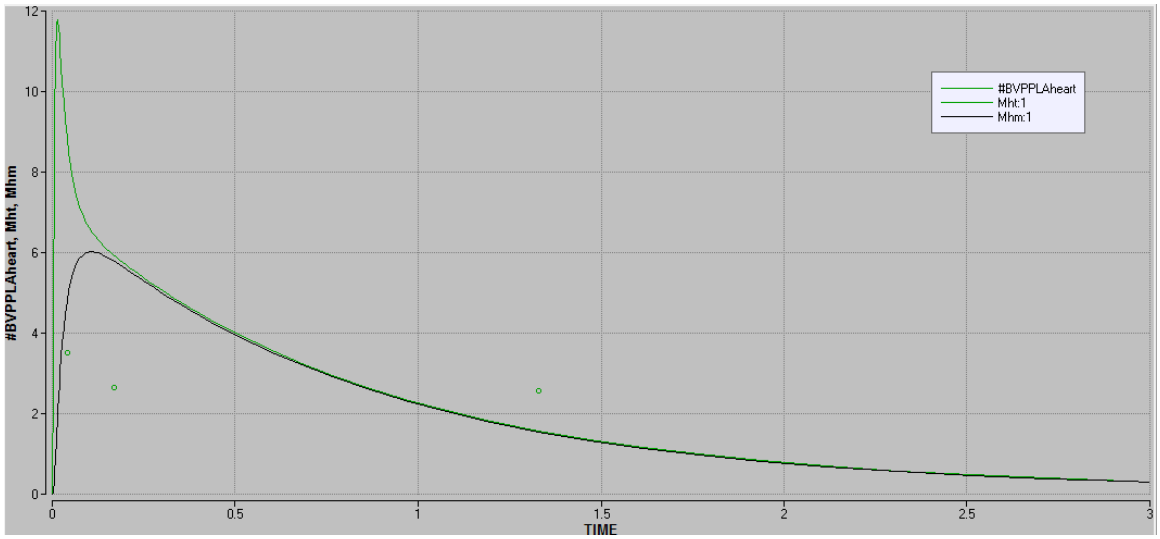
#BVPPLAheart, Mht, Mhm
#BVPPLAheart
Mht:1
Mhm:1
TIME

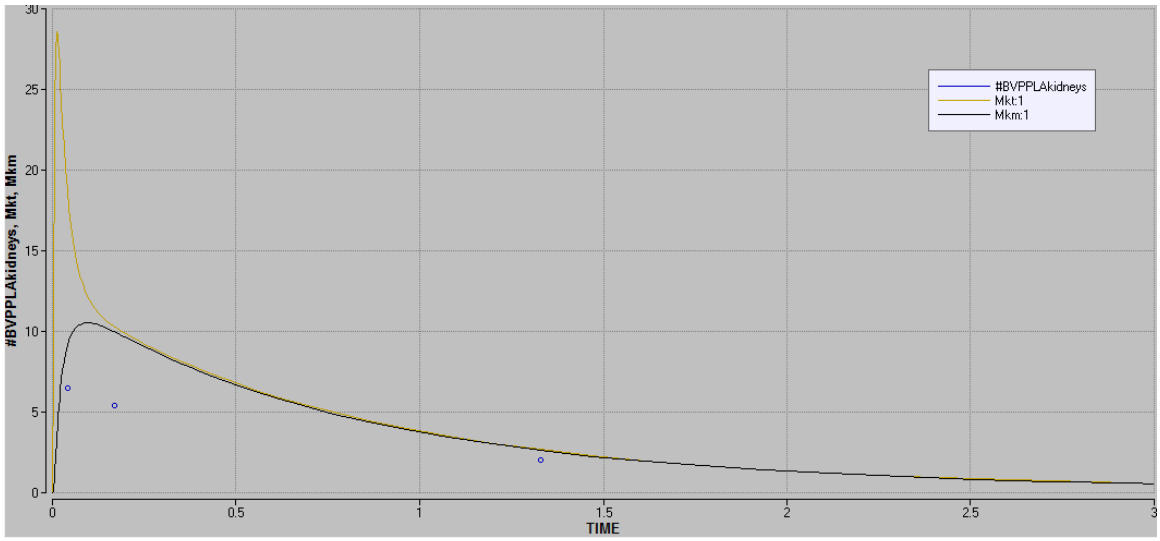
#BVPPLAkidneys, Mkt, Mkm
#BVPPLAkidneys
Mkt:1
Mkm:1
TIME

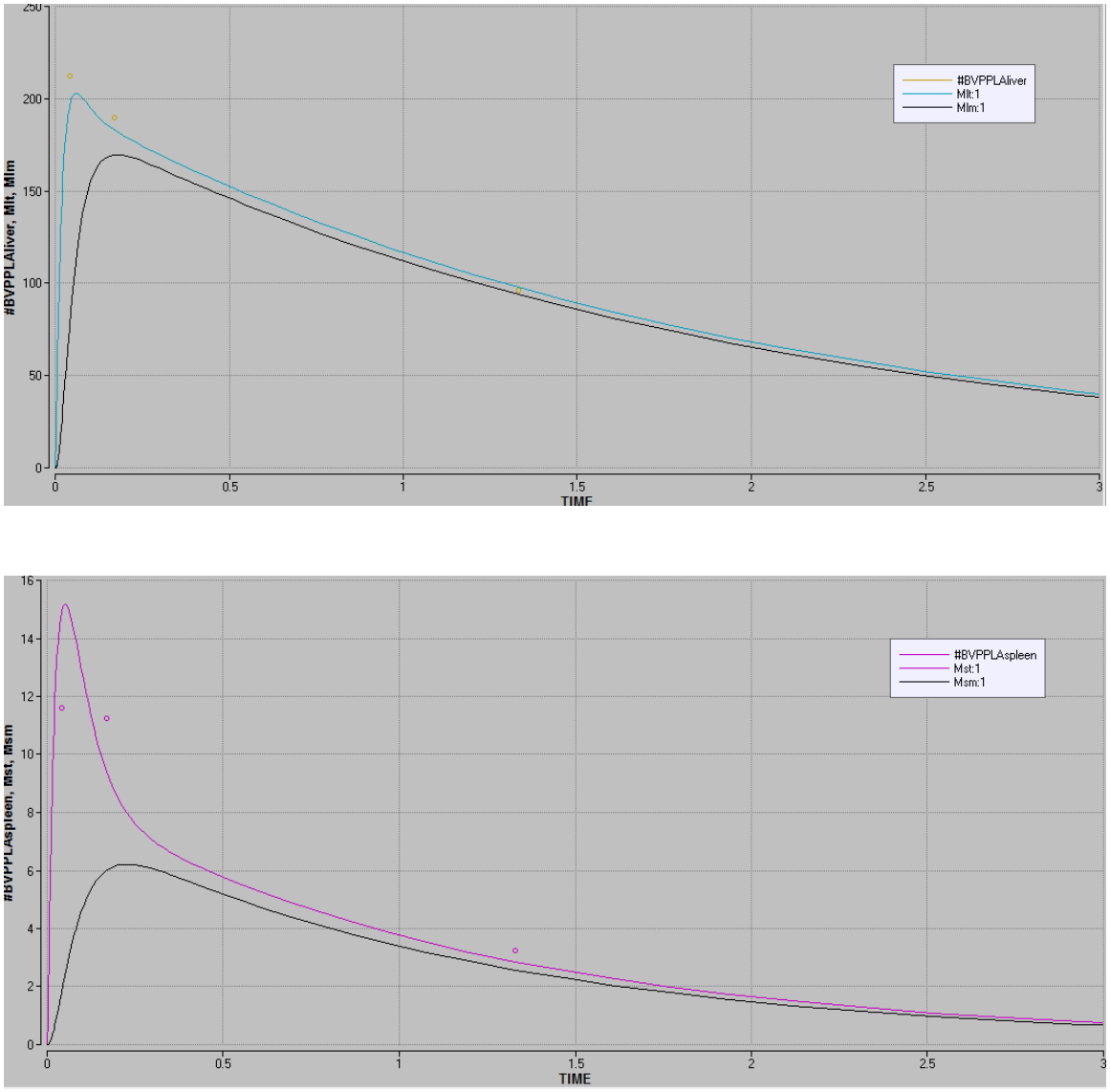

Fig. A4.3 Individual time courses for BVP-PLA nanoparticles.

A4.1.5 Ag, 20 nm

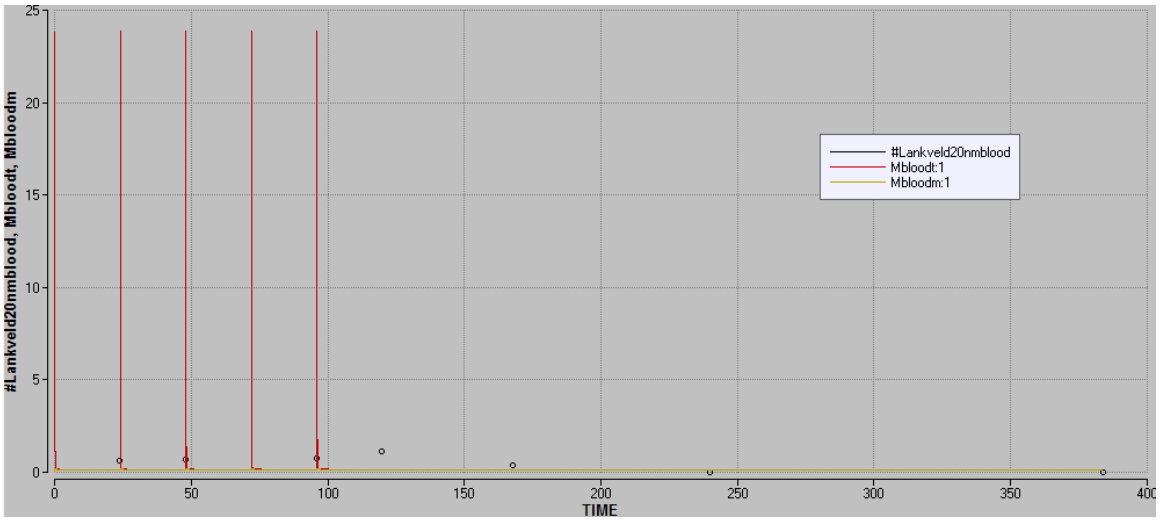
#Lankveld20nmblood, Mbloodt, Mbloodm
#Lankveld20nmblood
Mbloodt:1
Mbloodm:1
TIME

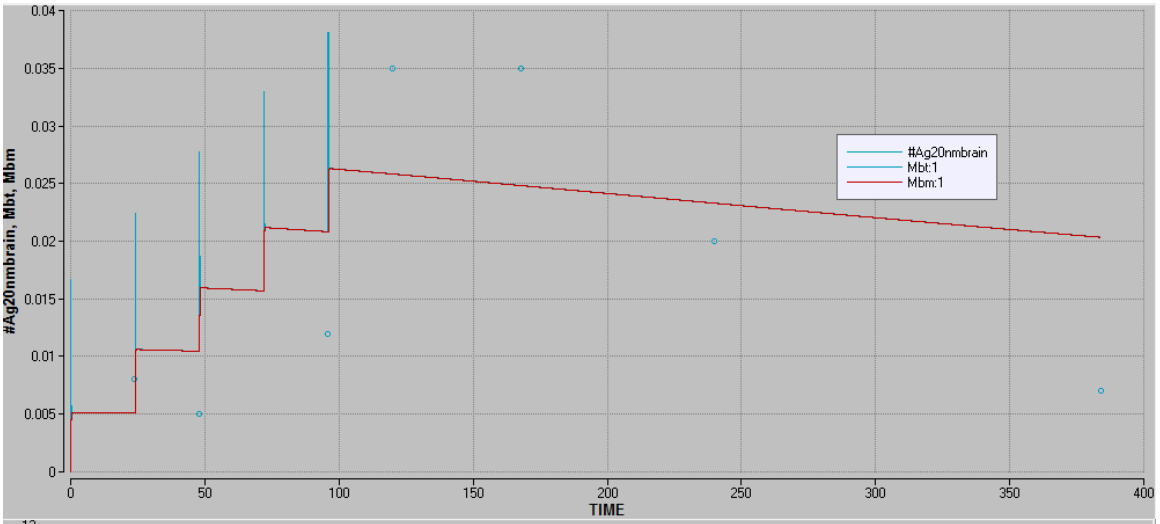
#Ag20nmbrain, Mbt, Mbm
#Ag20nmbrain
Mbt:1
Mbm:1
TIME

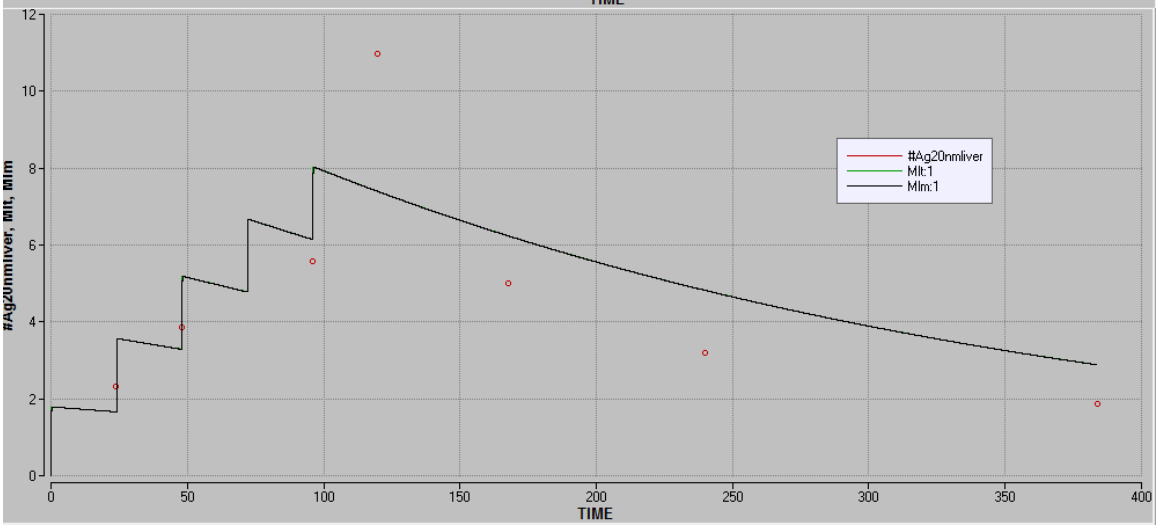
#Ag20nmliver, Mlt, Mlm
#Ag20nmliver
Mlt:1
Mlm:1
TIME

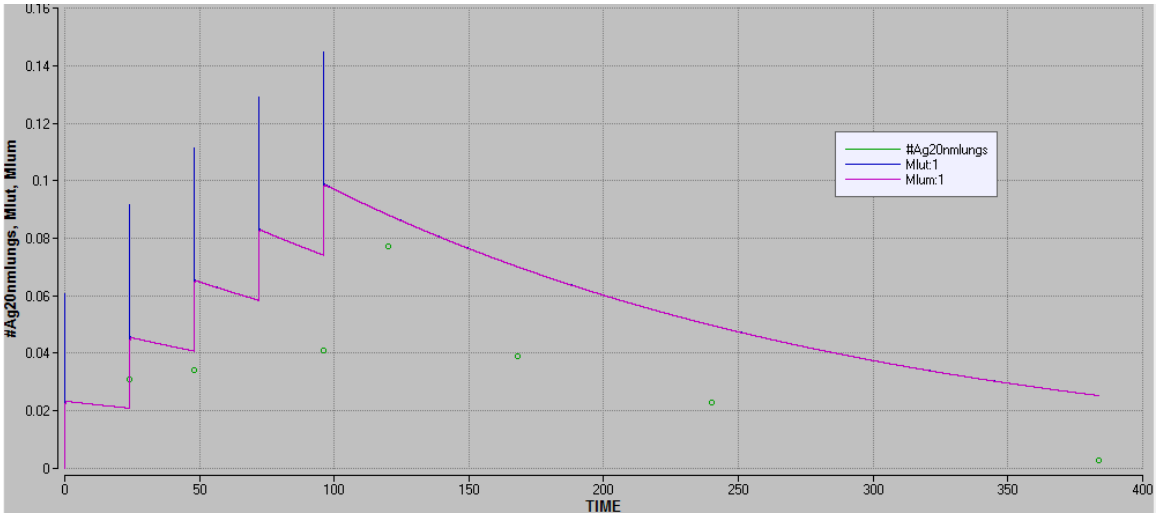
#Ag20nmlungs, Mlut, Mlum
TIME
#Ag20nmlungs
Mlut:1
Mlum:1

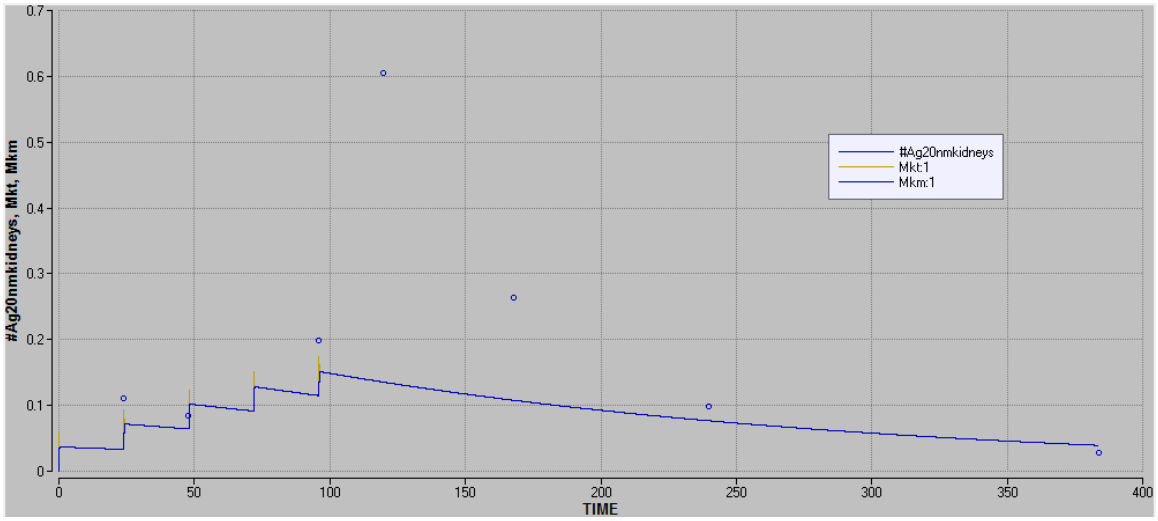
#Ag20nmkidneys, Mkt, Mkm
TIME
#Ag20nmkidneys
Mkt:1
Mkm:1

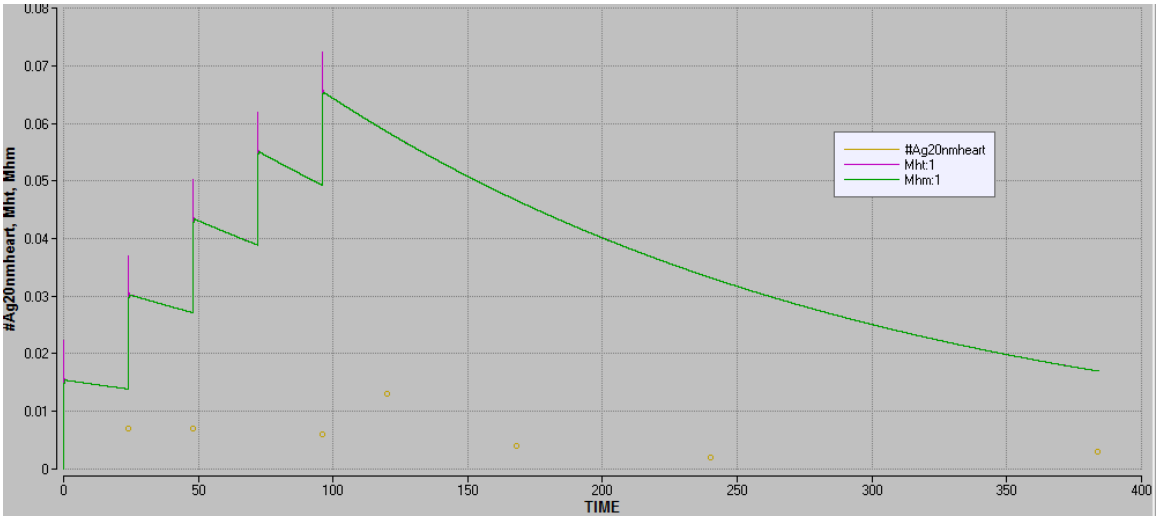
#Ag20nmheart, Mht, Mhm
TIME
#Ag20nmheart
Mht:1
Mhm:1

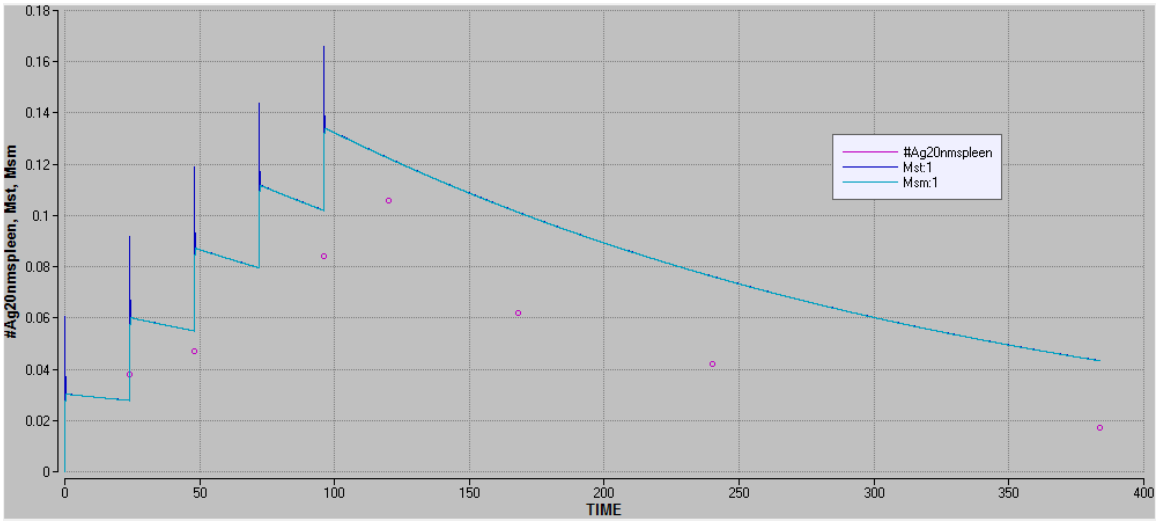

Fig. A4.4 Individual time courses for Ag (20 nm) nanoparticles.

A4.1.6 Ag, 80 nm

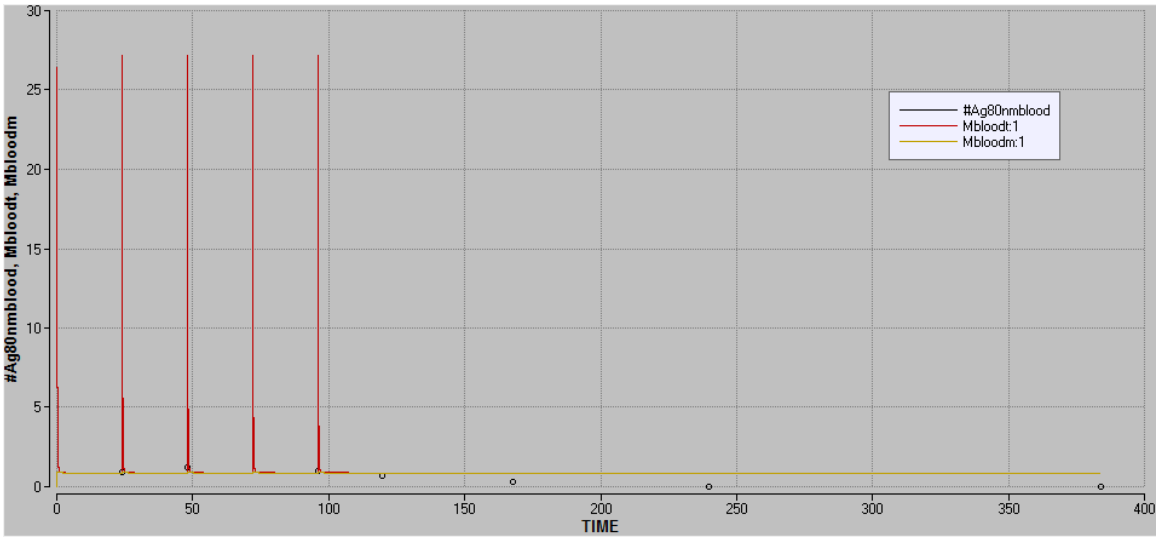

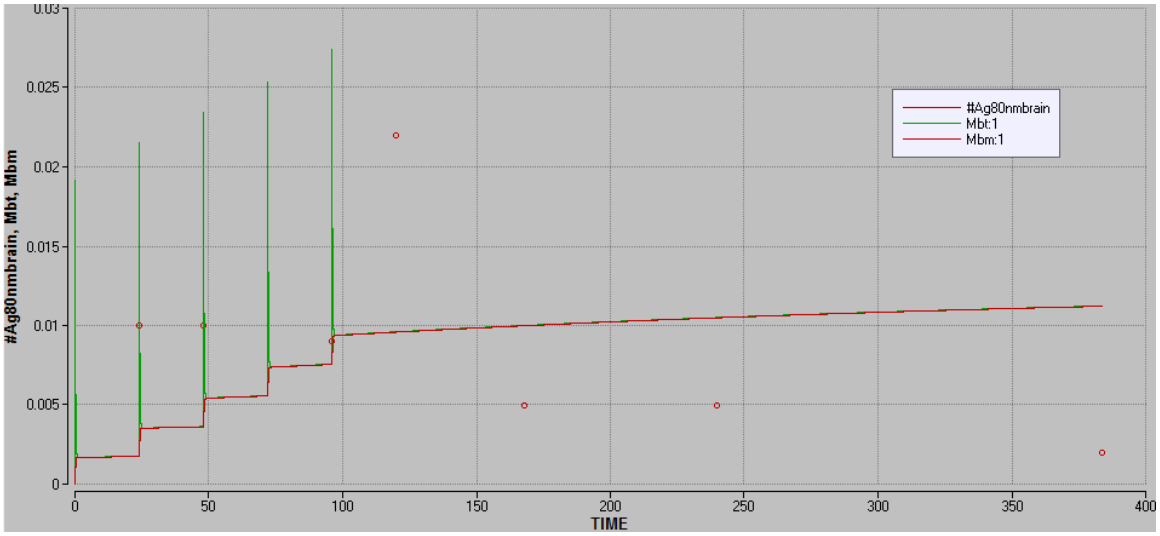
#Ag80nmbrain
Mbt:1
Mbm:1
#Ag80nmbrain, Mbt, Mbm
TIME

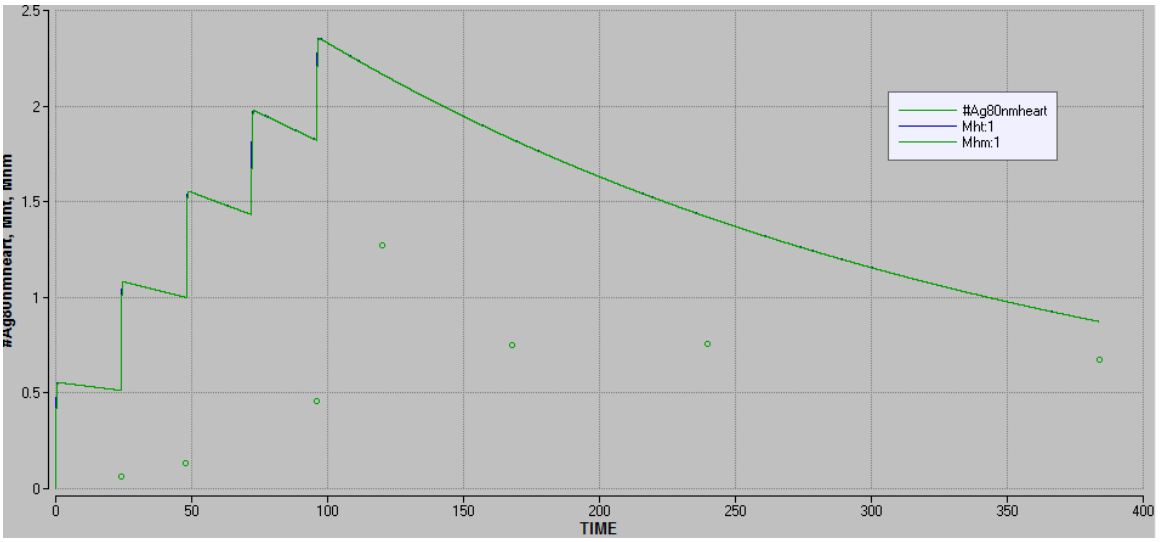
#Ag80nmheart
Mht:1
Mhm:1
#Ag80nmheart, Mht, Mhm
TIME

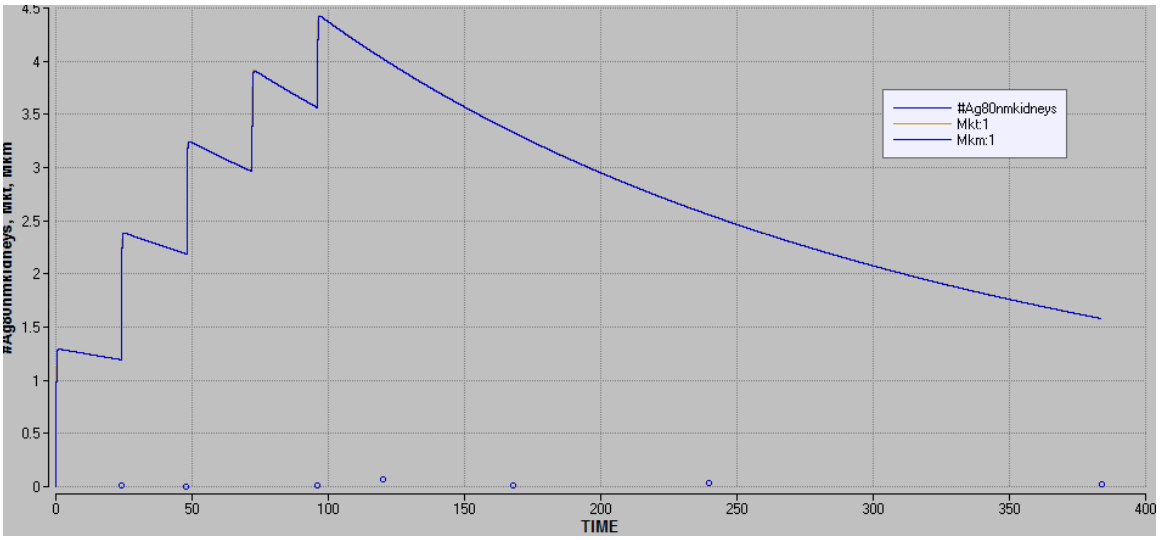
#Ag80nmkidneys
Mkt:1
Mkm:1
#Ag80nmkidneys, Mkt, Mkm
TIME

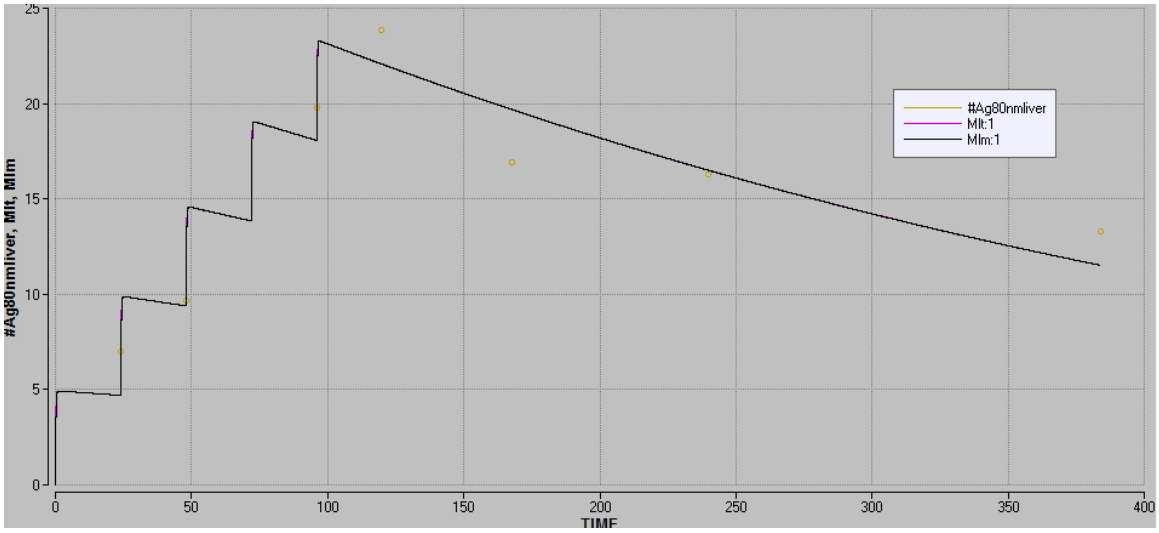

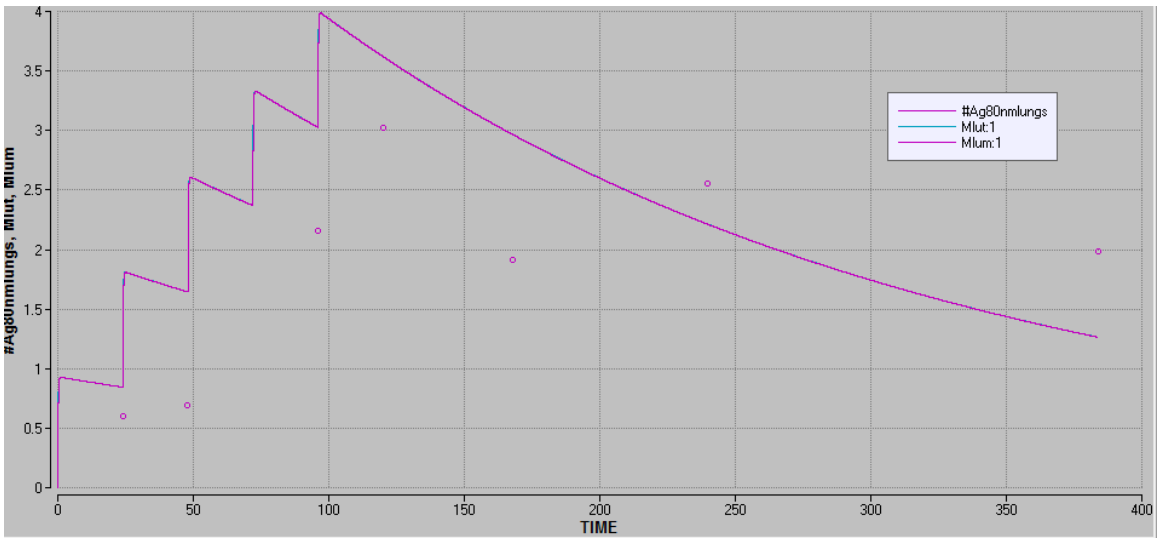

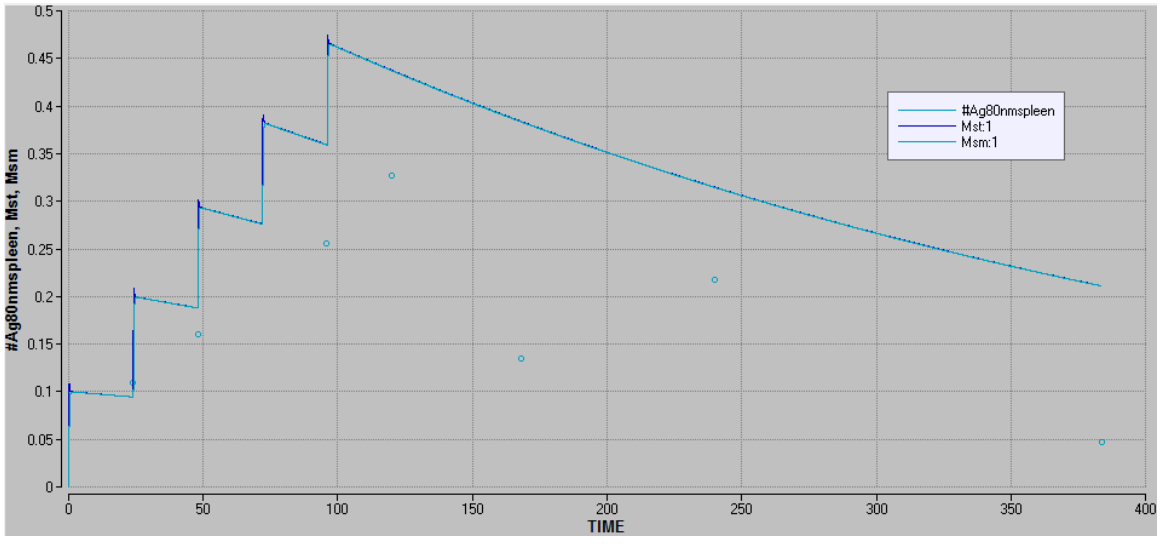

Fig. A4.5 Individual time courses for Ag (80 nm) nanoparticles.

A4.1.7 Ag, 110 nm

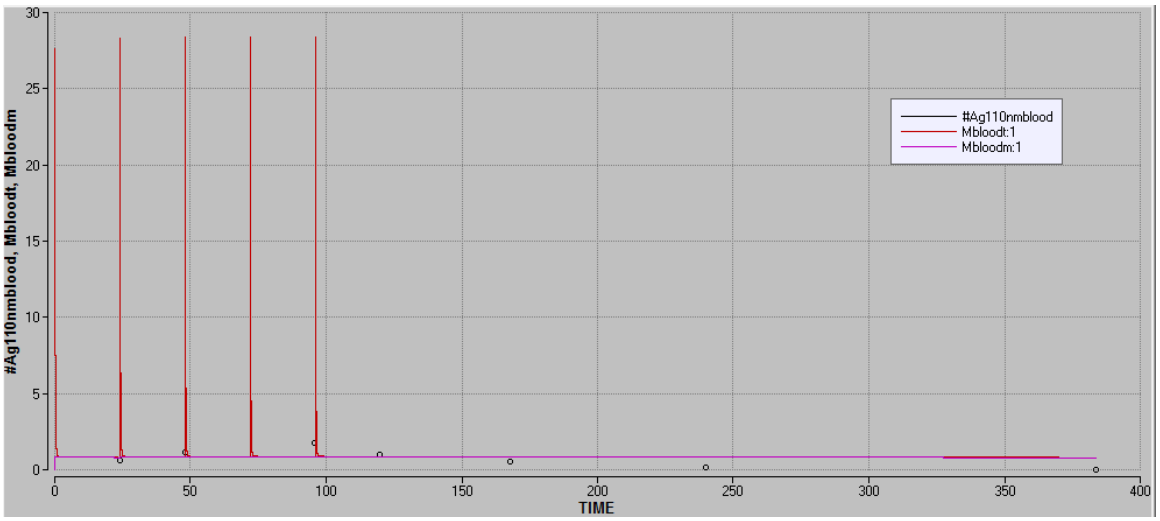

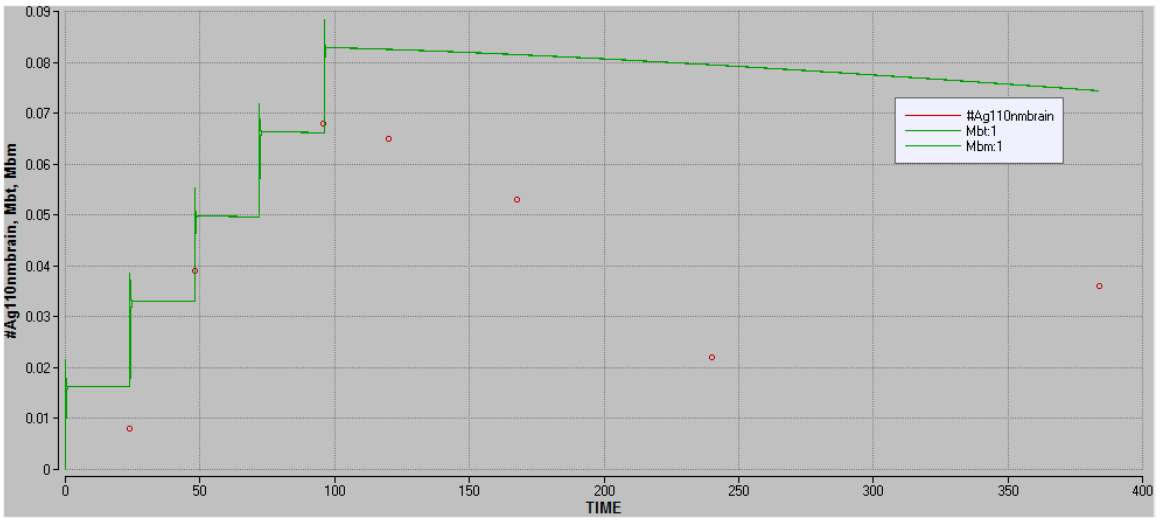

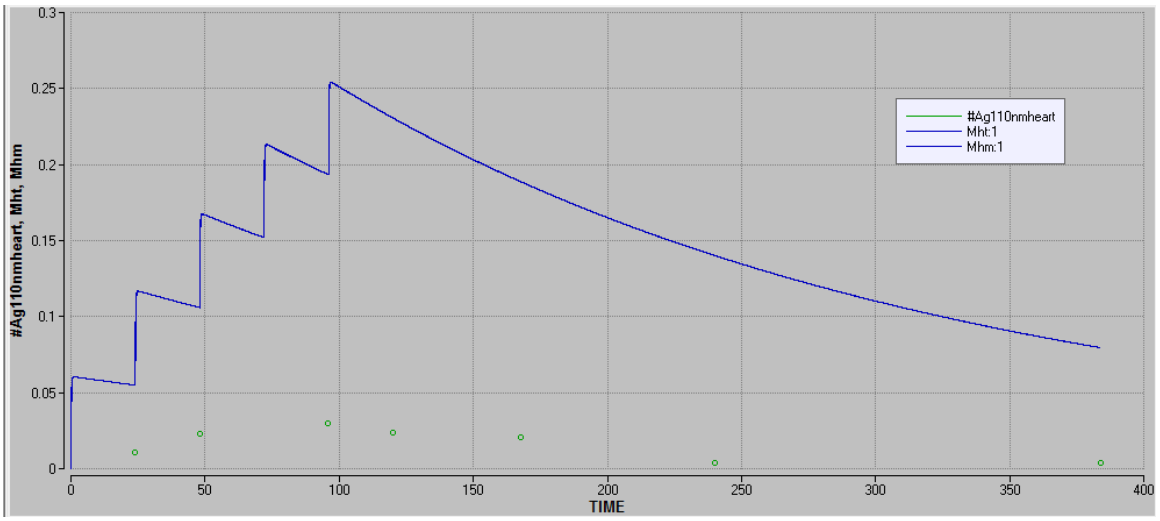

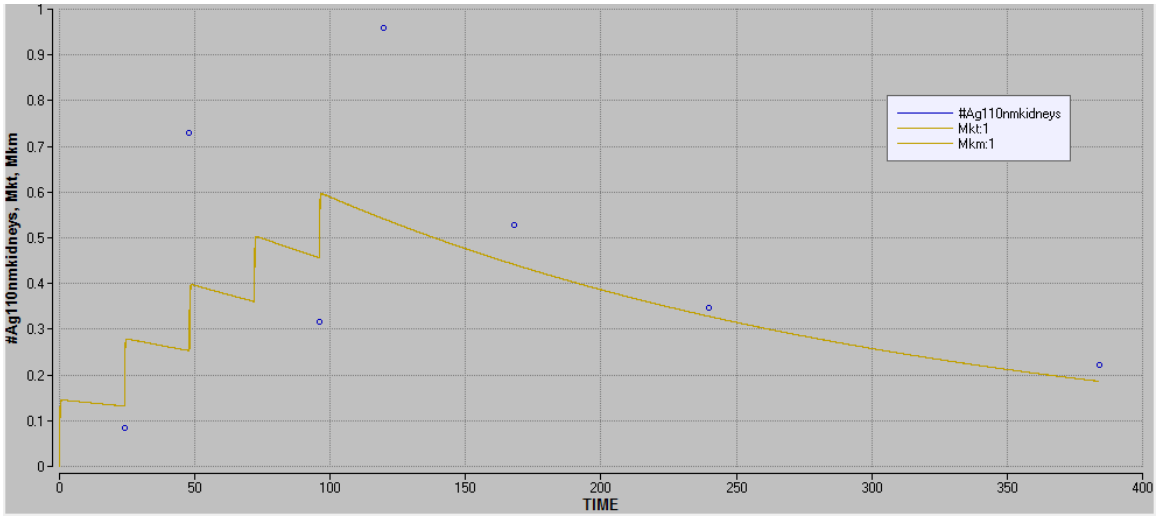
#Ag110nmkidneys, Mkt, Mkm
TIME
#Ag110nmkidneys
Mkt:1
Mkm:1

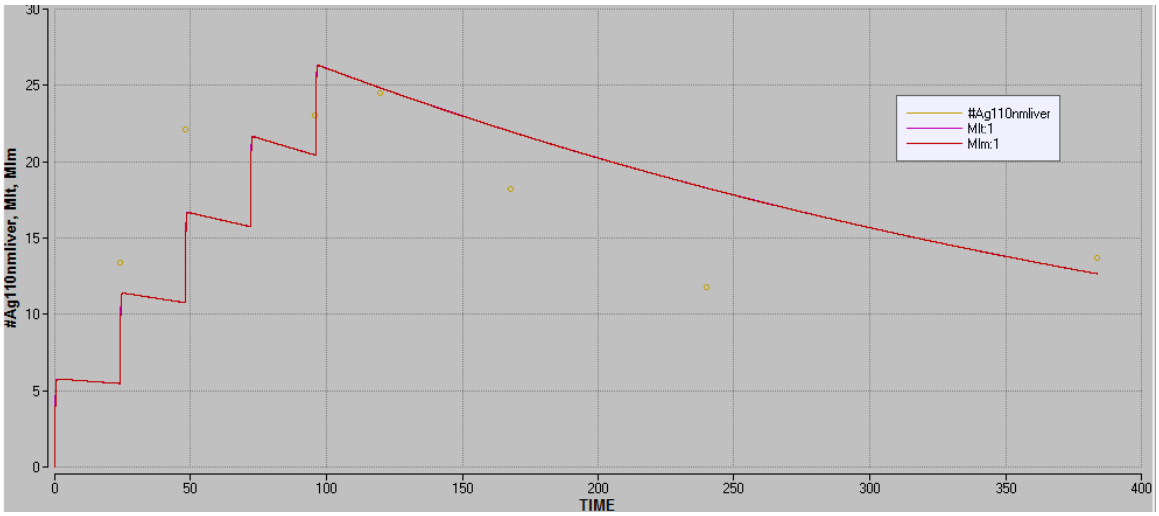
#Ag110nmliver, Mlt, Mlm
TIME
#Ag110nmliver
Mlt:1
Mlm:1

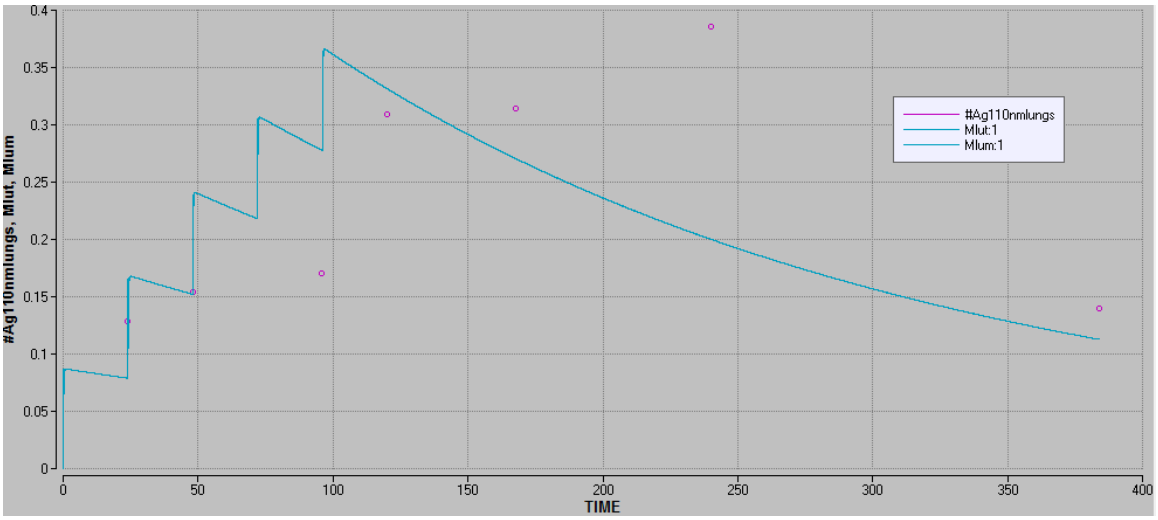
#Ag110nmlungs, Mlut, Mlum
TIME
#Ag110nmlungs
Mlut:1
Mlum:1

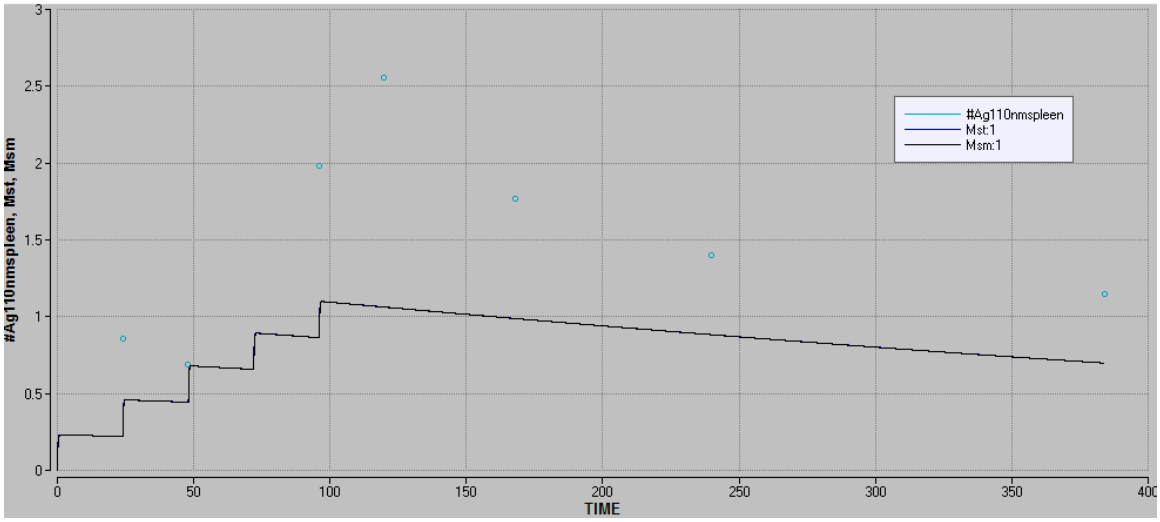

Fig. A4.6 Individual time courses for Ag (110 nm) nanoparticles.

A4.1.8 CeO_2, instilled

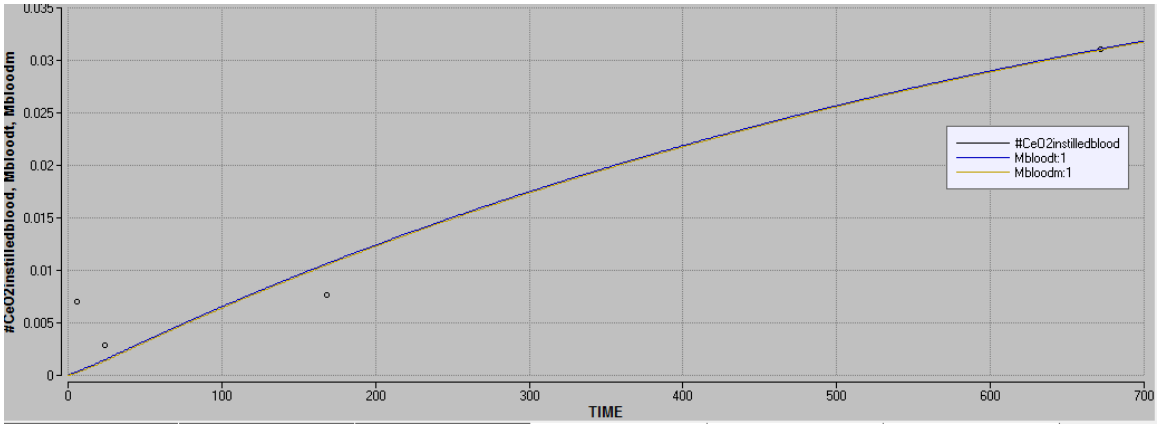

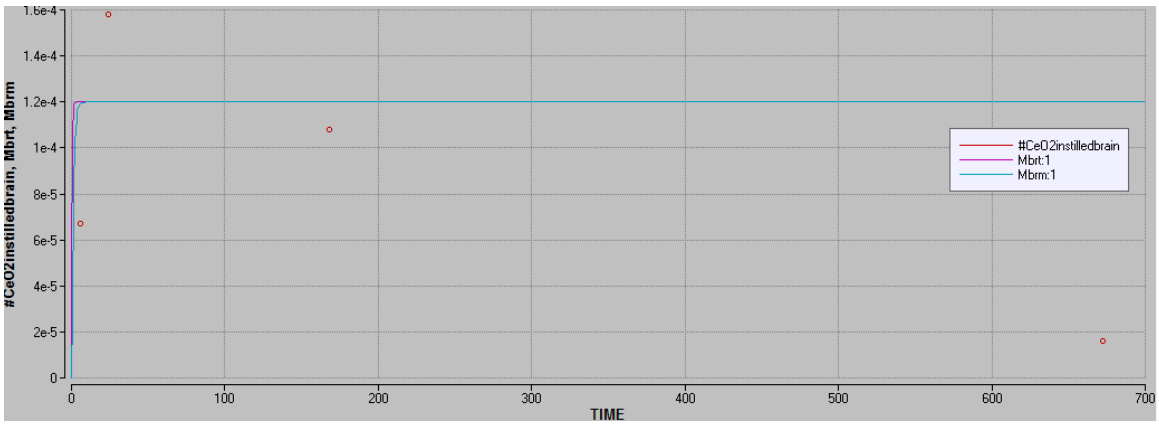

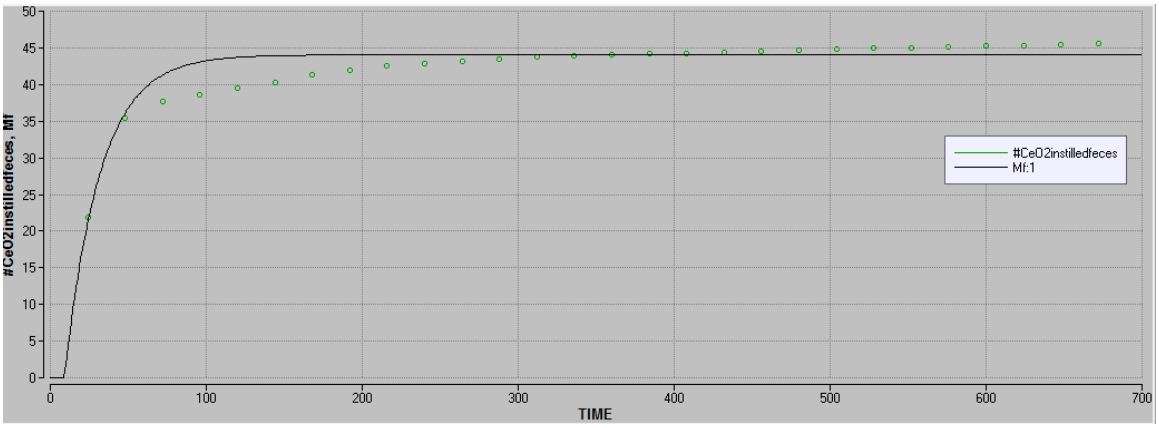
#CeO2instilledfeces, Mf
TIME
#CeO2instilledfeces
Mf:1

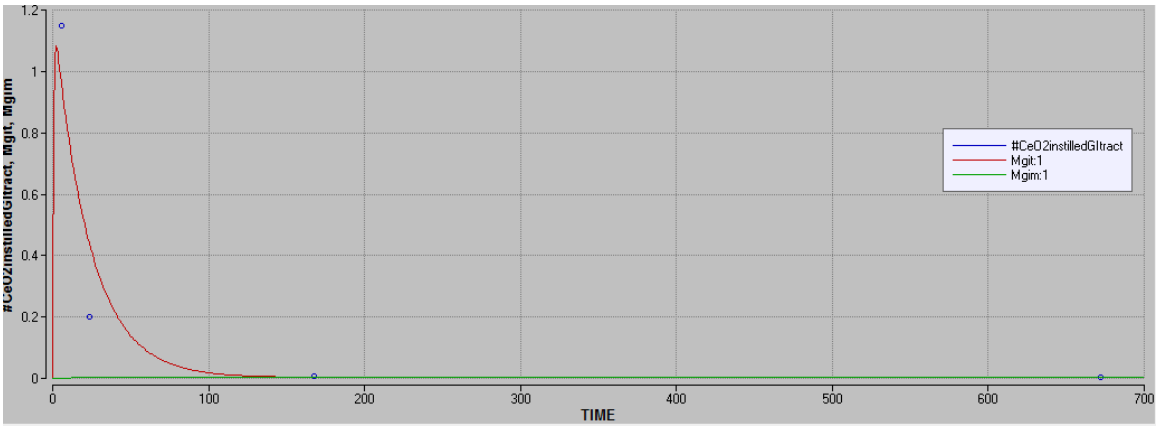
#CeO2instilledGItract, Mgit, Mgim
TIME
#CeO2instilledGItract
Mgit:1
Mgim:1

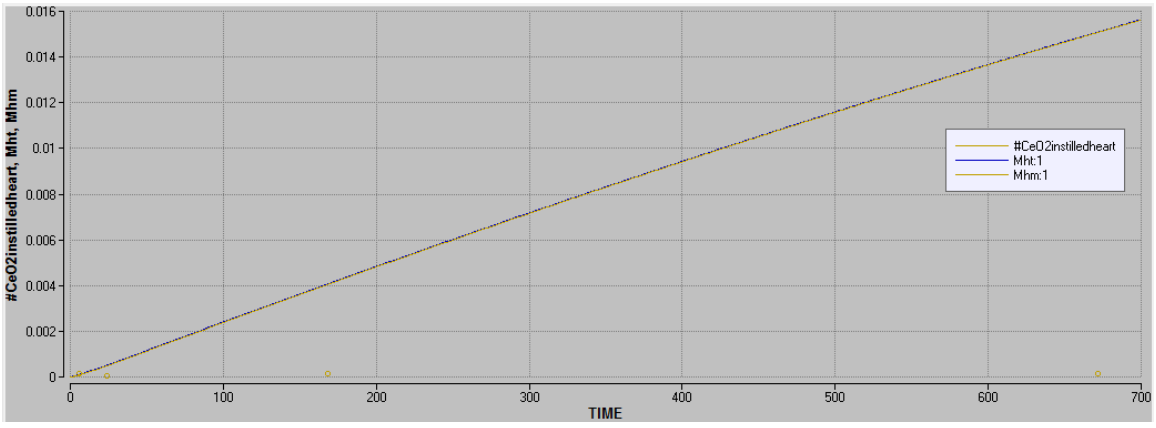
#CeO2instilledheart, Mht, Mhm
TIME
#CeO2instilledheart
Mht:1
Mhm:1

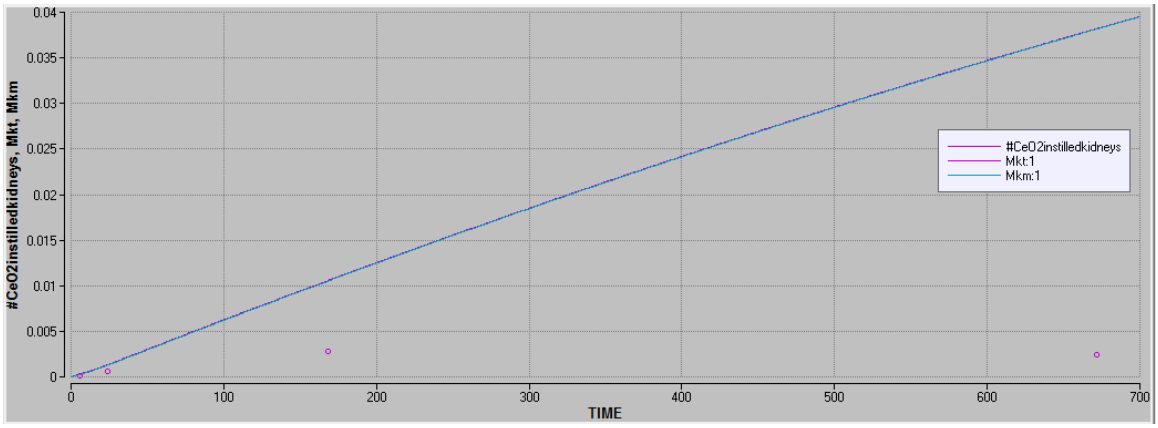
#CeO2instilledkidneys, Mkt, Mkm
TIME
#CeO2instilledkidneys
Mkt:1
Mkm:1

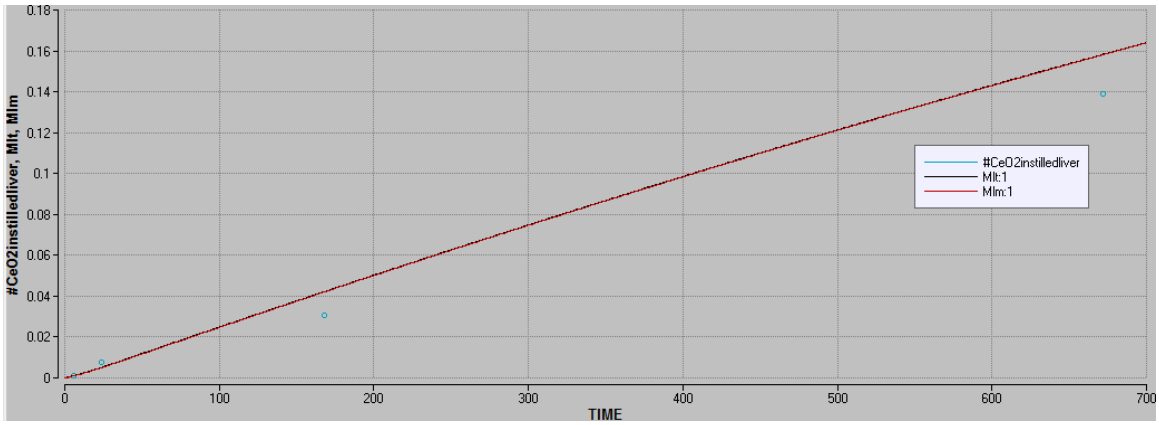
#CeO2instilledliver, Mlt, Mlm
TIME
#CeO2instilledliver
Mlt:1
Mlm:1

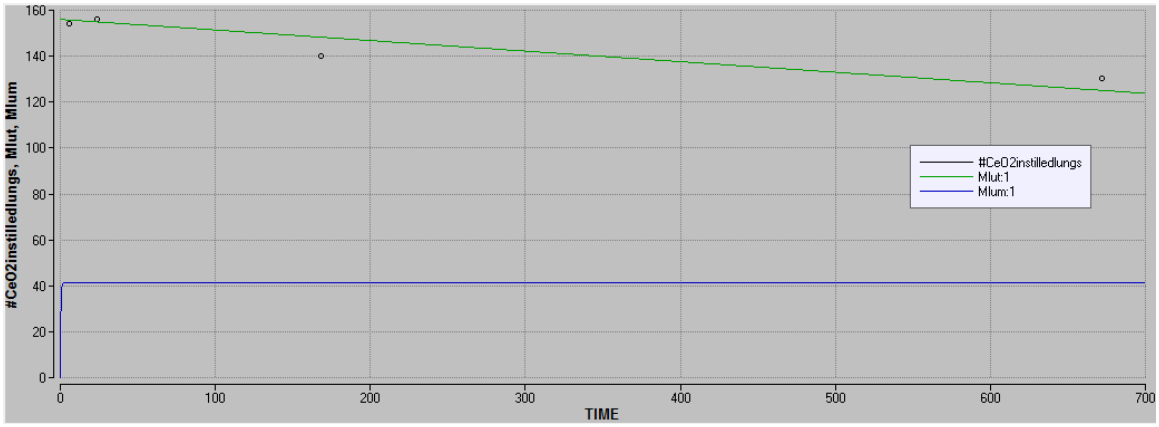
#CeO2instilledlungs, Mlut, Mlum
TIME
#CeO2instilledlungs
Mlut:1
Mlum:1

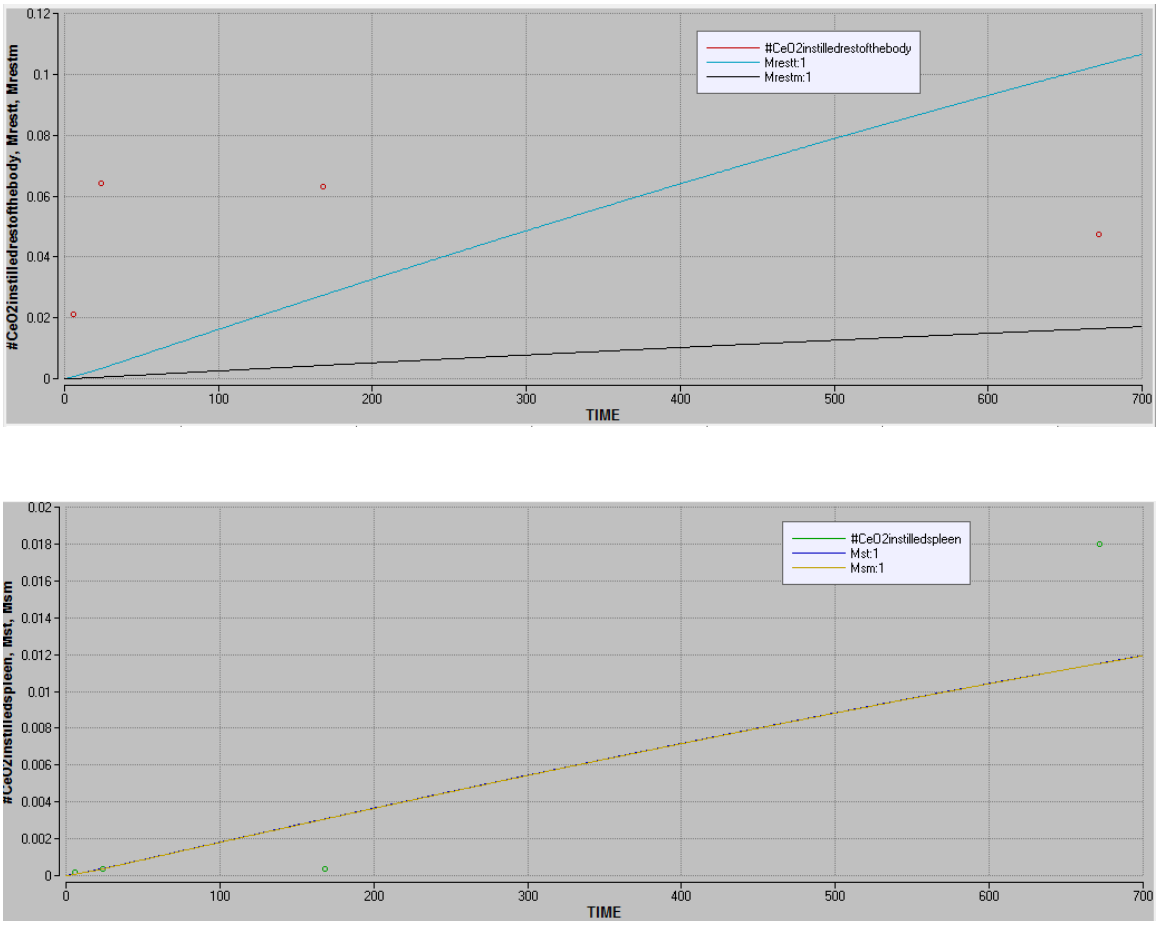

Fig. A4.7 Individual time courses for CeO_2 (instilled) nanoparticles.

A4.1.9 CeO_2, inhaled

Please refer to Appendix A3.5.1 for details.

APPENDIX 5

Life cycle health impacts of polycyclic aromatic hydrocarbon for source-specific mixtures

A5.1 Introduction

Polycyclic aromatic hydrocarbons (PAHs) in the environment are emitted as by-products from incomplete combustion of fossil fuels or wood (Li et al. 2006). Several PAHs are classified as carcinogenic or probably/possibly carcinogenic to humans by the International Agency for Research on Cancer (IARC 2010). Depending on the Life Cycle Impact Assessment (LCIA) method used, PAHs may be considered to be the dominant contributors to human health impacts for several products and services (Kohler and Künniger 2003; Andersen and Shier 2009; Amienyo et al. 2013). For instance, using the CML 2001 method (Guinée 2001), Amienyo et al. (2013) compared the impacts on human toxicity of different soft drink packaging finding that PAHs contributed 97% of the impact from aluminum cans. However, several factors generate large uncertainties in assessing the human health impact of PAHs in LCIA that may bias product comparison.

On the fate and exposure side, estimates of half-lives for the PAHs vary among frequently referred sources (Howard et al. 1991; Mackay et al. 2006; U.S. EPA 2009), which result in very different residence times for PAHs in the environment. In addition, estimated PAH concentrations in environmental and food media from different models are inconsistent with measured concentrations (Lang et al. 2007; Prevedouros et al. 2004). These discrepancies lead to inconsistent predictions of

intake for the population. An additional difficulty is the partition behaviors of PAHs between gas or dissolved phase and particle bound phase could be significantly affected by black carbon and should be considered in modeling the fate of PAHs (Hauck et al. 2007; Armitage et al. 2008; Prevedouros et al. 2008).

On the effect side, current LCIA models such as USEtox (Ralph K Rosenbaum et al. 2008), IMPACT 2002 (Pennington et al. 2005), and USES-LCA (Huijbregts et al. 2000) use animal experiment data to estimate the human toxicity of PAHs whereas human epidemiological data is preferred if available (Rosenbaum et al. 2011). The World Health Organization (WHO 2000) and other studies (Gibbs 1997; Armstrong et al. 2004; Armstrong and Gibbs 2009) have given estimated unit risks or relative risks for PAH mixtures based on epidemiological data. However, these estimates are solely attributed to benzo[a]pyrene while other PAHs' contributions to the impact of the PAH mixture are also relevant to quantify in LCIAs (Pennington et al. 2006) and could have in addition an interaction with the effective dose-response of benzo[a]pyrene. Thus, it is necessary to develop effect factors for all relevant PAHs based on these available epidemiological data accounting for possible interactions between different PAHs in estimating dose-responses.

The goal of this study is to assess the life cycle human health impact of PAH mixtures by refining estimates of fate, exposure, and effects of the 16 PAHs listed as Priority Pollutants by the U.S. Environmental Protection Agency (U.S. EPA 2013). It specifically aims to a) address the influence of black carbon adsorption and photolysis on the multimedia multi-pathway intake fractions of individual PAHs; b) to recalculate the effect factors and compare the human health impact per kg emitted of 16 PAHs for different models; c) to derive impact per kg emitted – so-called

characterization factors – for source-specific PAHs mixtures; and d) to illustrate this study's use and importance in assessing human health impact in LCIA.

To this end, we first incorporate black carbon adsorption and photolysis of PAHs in the USEtox multimedia model (Ralph K Rosenbaum et al. 2008). We then show the influences of these new and updated model specifications on the intake fractions, the effect factors, and the characterization factors for health impacts on humans by PAHs. The characterization factors for PAHs are applied to specific PAH mixtures from the aluminum industry, domestic combustion, and the general world emission. We ultimately illustrate the importance of the proposed refined treatment of PAHs in a case study, comparing results of the newly developed factors to those of earlier LCIA methods.

A5.2 Methods

A5.2.1 General framework

A general framework using a multimedia model evaluating toxicity of different chemicals was developed and peer-reviewed by an independent expert panel in a UNEP-SETAC workshop (Jolliet et al. 2006). This framework was described by (Rosenbaum et al. 2007) and adopted in this study. Impact per kg emitted, the so-called characterization factor (*CF*, in cases/$kg_{emitted}$), is a product of the fate factor (*FF*, in day), exposure factor (*XF*, in 1/day), and effect factor (*EF*, in cases/kg_{intake}). The total health impact score (*S*, in cases) due to a given emission of PAHs (*M*, in $kg_{emitted}$) is then derived by multiplying the characterization factor with the corresponding emission for a given technology:

$$S = CF \times M = (FF \times XF \times EF) \times M = (iF \times EF) \times M$$

A5.1

The result of *XF* and *FF* can be expressed as intake fraction (*iF*, $kg_{intake}/kg_{emitted}$) which is defined as the fraction of the mass released to the environment that is taken in by the population integrated over time (Bennett et al. 2002).

The UNEP-SETAC USEtox model (Ralph K Rosenbaum et al. 2008) is used as a starting point for the improvement for the PAHs characterization factors for human health. IMPACT 2002 (Pennington et al. 2005) and USES-LCA (Huijbregts et al. 2000), which have explicit calculation of fate in vegetation and utilize alternative landscape parameters, are used to compare results between different models.

A5.2.2 Fate and exposure

Evaluating the fate of chemicals in the environment requires considering the chemicals' physico-chemical properties and degradation half-lives. Currently, the chemical properties of PAHs in USEtox are based on Estimation Programs Interface Suite™ v4.00 (U.S. EPA 2009) (EPI Suite™ v4.00) although more up-to-date data exists for these chemical properties (Ma et al., 2010). USEtox also does not include the influences of black carbon adsorption and photolysis that are shown to be important in the fate of PAHs in other studies (Hauck et al. 2007; Prevedouros et al. 2008; Chen et al. 2001; Hauck et al. 2008).

An updated comprehensive review of physico-chemical properties for 15 PAHs (all 16 PAHs except for dibenz[a,h]anthracene) was done by Ma et al. (2010) and provides the molecular weight (*MW*), octanol-water partition coefficient (*Kow*), octanol-air partition coefficient (*Koa*), Henry's Law constant at 25 ˚C (K_H25), vapor pressure at 25 ˚C (*Pvap25*), solubility at 25 ˚C (*Sol25*), and sub-cooled liquid vapor pressure (*Subcooled VP*) values used in our study. Soil Absorption Coefficient (*Koc*) is not included by Ma et al. (2010) therefore we estimate from *Kow* according to the method proposed by Doucette (2000), which is used by EPI Suite™ v4.00 (U.S. EPA

2009). The physico-chemical properties for dibenz[a,h]anthracene are directly taken from EPI Suite™ v4.00 (U.S. EPA 2009). The values of these parameters are provided in Table S1 in the electronic supplementary material (ESM). For discussion purposes, the 16 PAHs can be differentiated into two groups based on their number of rings and their affinity to lipids. Benzo[g,h,i]perylene, indeno[1,2,3-cd]-pyrene, dibenz[a,h]anthracene, benzo[a]pyrene, benzo[b]fluoranthene, benzo[k]fluoranthene, benz[a]anthracene, chrysene, pyrene, and fluoranthene have 4 rings or more and have a higher affinity to lipids (*Kow*>90 000) while the others have 2 or 3 rings and are less lipophilic and more volatile.

Black carbon can be emitted as a byproduct of incomplete combustion, which is one of the major sources of PAHs. In addition, black carbon is known to strongly absorb other pollutants (Ni et al. 2014). The presence of black carbon may increase the fractions of PAHs bound to particles affecting the fate and bioavailability of PAHs. Several black carbon inclusive multimedia models have been proposed (Hauck et al. 2007; Armitage et al. 2008; Prevedouros et al. 2008; Lohmann and Lammel 2004). In this study, the model and parameters from Koelmans et al. (2006) and Prevedouros et al. (2008) supplemented with the data of Total Suspended Particulate (TSP) from other literature sources (Lohmann and Lammel 2004; Gustafsson et al. 2001) are implemented in USEtox to examine the effects of black carbon on the fate of the 16 PAHs (see section 10 in the ESM for details of the implementation).

Degradations of PAHs in air, water, sediment, soil, and plants are considered in this study. As for air, photo-oxidation with radical species and photolysis are the major mechanisms responsible for the breakdowns of PAHs (Chen et al. 2001; Atkinson 1987). Photo-oxidation rates are taken from EPI Suite™ v4.00 (U.S. EPA 2009), which reflects a 24 hour average value. Photolysis rates are corrected from rates

obtained in laboratory conditions by Chen et al. (2001), applying a factor of four to reflect photolysis rates in the natural environment. This correction accounts for a factor two between the day/night cycle under ambient conditions, and is multiplied by another factor 2 to account for the difference in the light intensity of the incubator model used by Chen et al. (2001) and the annual average light intensity at 25 degrees north latitude (National Aeronautics and Space Administration 2012). For surface water, biodegradation and photolysis are the dominant removal mechanisms (Lane and Katz 1977). Biodegradation rates are taken from Howard et al. (1991). For photolysis in water, degradation rates depend on the water depth. Deeper water bodies have less sunlight penetration and result in lower photolysis degradation rates of PAHs (Schwarzenbach et al. 2003). Since most reported photolysis degradation rates were obtained experimentally in vials (Lane and Katz 1977; Muel and Saguem 1985; Fukuda et al. 1988), it is necessary to adjust these values for water depths. We follow Schwarzenbach et al. (2003) by considering the ratio between light absorption rates at a given water depth to that at near-surface. This ratio, known as the screening factor, is a function of maximum adsorption wavelength, attenuation coefficient and water depth (Schwarzenbach et al. 2003). The photolysis rates in water obtained in laboratory conditions are further corrected in the same manner for photolysis rates in air by a factor of four. Based on the findings of previous studies (Behymer and Hites 1985; Larson and Weber 1994), we assume that PAHs will not be subject to photo-oxidation in air or photolysis in both air and water when bound to particles. Compiled data for half-lives for PAHs in different media used in this study are listed in Table S2 in the ESM.

A5.2.3 Effect factors

To evaluate the health impacts of individual PAHs, we multiply the effect factor of benzo[a]pyrene by the PAH specific Toxicity Equivalence Factor (TEF_i) that expresses the toxicity of an individual PAH *i* in kg benzo[a]pyrene equivalent:

$$EF_i = TEF_i \times EF_{B[a]P}$$

A5.2

As described by Nisbet and LaGoy (1992), U.S. EPA (1993), and U.S. EPA (2010), *TEF*s are derived from available toxicology data to assess the health impacts of chemicals with similar structures, using benzo[a]pyrene as a reference substance (see Table S3 in the ESM). For carcinogenic effects, we use the *TEF*s from the (U.S. EPA 1993) due to their prevalent use in worldwide regulatory guidance (Jennings 2012) and we then consider alternative *TEF*s in a sensitivity study.

Currently, the USEtox toxicity database includes carcinogenic effect factors only for benzo[a]pyrene and naphthalene, and non-carcinogenic factors for pyrene, fluoranthene, anthracene, fluorene, and acenaphthene. All these human health effect factors were extrapolated from chronic animal experiments. To decrease the uncertainty from animal-human extrapolation, we can take advantage of epidemiological data that are available for impacts of benzo[a]pyrene and PAHs. The carcinogenic factor for benzo[a]pyrene is therefore recalculated based on residential related lifetime lung cancer risks from Gibbs (1997). We use the unit risks data from Gibbs (1997) because these data consider the differences between occupational and residential settings, as well as the background lung cancer rates that are critical in calculating effect factors, but are lacking in other studies using relative risks (Armstrong et al. 2004; Armstrong and Gibbs 2009). We calculate the effect factor of a PAH mixture ($EF_{mixture}$) expressed in cases per kg inhaled by multiplying the unit risk by the corresponding breathing rate and exposure duration (Gibbs, 1997). Both

the unit risk and initial effect factor are calculated assuming that all effects were attributed to benzo[a]pyrene as did Gibbs (1997). In reality, workers had also been exposed to other PAHs in addition to benzo[a]pyrene. To avoid double counting when also assessing the impacts of other PAHs, we first need to separate the contribution of benzo[a]pyrene alone from the contribution of the other PAHs by accounting for the industry-specific emission profile. Since the emission profile is available for coke ovens (Petry et al. 1996; Strunk et al. 2002; Yang et al. 2007), we use as a starting point the unit risk (*UR*) of being exposed to PAHs emitted from coke oven recalculated by Gibbs (1997) as $UR^{mixture}_{attributedto\ B[a]P}$= 7.8 ng/m^3 per 100 000 persons in the general population exposed over lifetime ($IR \times T_{lifetime}$). This value is itself based on one of the largest and most detailed PAH-related epidemiology study by Costantino et al. (1995). Considering separately the contribution of each PAH, the effect of the mixture entirely attributed to benzo[a]pyrene can be disaggregated into:

$$f_{B[a]P} \times EF^{mixture}_{attributedto\ B[a]P} = \sum f_i \times EF_i = \sum f_i \times TEF_i \times EF_{B[a]P}$$

A5.3

Thus the effect factor for benzo[a]pyrene alone ($EF_{B[a]P}$) is a function of the *TEF* and the fraction (f_i) of each PAH *i* in the mixture emitted for the considered coke oven technology:

$$EF_{B[a]P} = EF^{mixture}_{attributedto\ B[a]P} \times \frac{f_{B[a]P}}{\sum f_i \times TEF_i} = UR^{mixture}_{attributedto\ B[a]P} \times IR \times T_{lifetime} \times \frac{f_{B[a]P}}{\sum f_i \times TEF_i}$$

A5.4

The detailed calculations can be found in section 11 of the (ESM).

For non-carcinogenic effects of PAHs we use the default USEtox effect factors that are available for pyrene, fluoranthene, anthracene, fluorene, acenaphthene, and naphthalene (Ralph K Rosenbaum et al. 2008) .

A5.2.4 Sensitivity analysis on the characterization factors

To explore the sensitivity of results to changes in the updated parameters, the characterization factors from this updated USEtox model are respectively compared to those of the adapted model without black carbon adsorption or without photolysis. Alternative values of *TEF*s are also explored to examine the impacts of different *TEF*s on the characterization factors of PAHs.

A5.2.5 Source-specific emission profiles

Given the emission profile of a certain source, the total impact per kg emitted or characterization factor (*CF*) of a PAH mixture from source or technology *j* can be calculated as:

$$CF^{j}_{PAH\,mixture} = \sum_{i} CF_i \times f_i^j$$

A5.5

where CF_i is the characterization factor of the individual PAH *i* and f_i^j is the mass fraction of emitted PAH *i* of the total PAH mixture from source *j*.

The total health impact ($S_{PAH\,mixture}$) of the mixture that may involve various sources *j* for the whole product/region of interest is given by multiplying the PAH mixture *CF* of each specific source by the total PAH mass emitted by this source (m^j_{total}) and summing them up across all sources:

$$S_{\text{PAH mixture}} = \sum_{j} CF^{j}_{\text{PAH mixture}} \times m^{j}_{\text{total}}$$

A5.6

We then can derive *CF*s for different sources that represent important contribution, to PAHs emissions (Shen et al., 2013) and for which we have detailed emission profile, i.e for aluminum production and domestic combustion. For aluminum, anode plants

and Søderberg plants are responsible for most of the PAHs emissions during aluminum production (European Aluminium Association 2008). Their specific emission profiles are introduced in equation (5) to derive *CF*s. For domestic combustion, straw, wood, and sawdust briquettes, and kerosene are considered (Oanh et al. 2002). The worldwide PAH mixture emission profile in 2007 (Shen et al. 2013) is employed to provide a general *CF* when the source emission profile cannot be determined. For aluminum production, the ratio of rural/urban air emission is assumed to be 48:52, which is equal to the world rural/urban population ratio in 2011 (The World Bank 2013). For domestic combustion it is assumed all PAHs are entirely emitted to rural air. For the worldwide mixture, the sources of PAH mixtures were adapted from Shen et al. (2013) – we then assume PAHs emitted from biofuel burning, open straw burning, and wild fire are 100% emitted to rural air, while PAHs emitted from domestic coal burning, industrial sources, traffic oil, and consumer products are emitted to rural and urban air also based on rural/urban population ratio in year 2011 (The World Bank 2013). The emission profiles of aluminum production, domestic combustion, and worldwide can be found in Table S4-b in the ESM.

2.6 Life cycle case study

The method in this study is compared with three other LCIA methods, namely CML 2001 (Guinée 2001), ReCiPe (Goedkoop et al. 2008), and the USEtox-based IMPACT World + (Bulle et al. 2012) to examine the changes in human health impacts for the production of one kg primary aluminum. Inventory data are taken from Ecoinvent 2.2 (Frischknecht et al. 2005).

A5.3 Results

A5.3.1 Intake fractions

Intake fractions (*iF*s) via inhalation and ingestion from emission to rural air calculated using the USEtox default scenario and three updated scenarios with black carbon adsorption, new degradation data including photolysis, and these two modifications altogether are shown in Fig. A5.1.

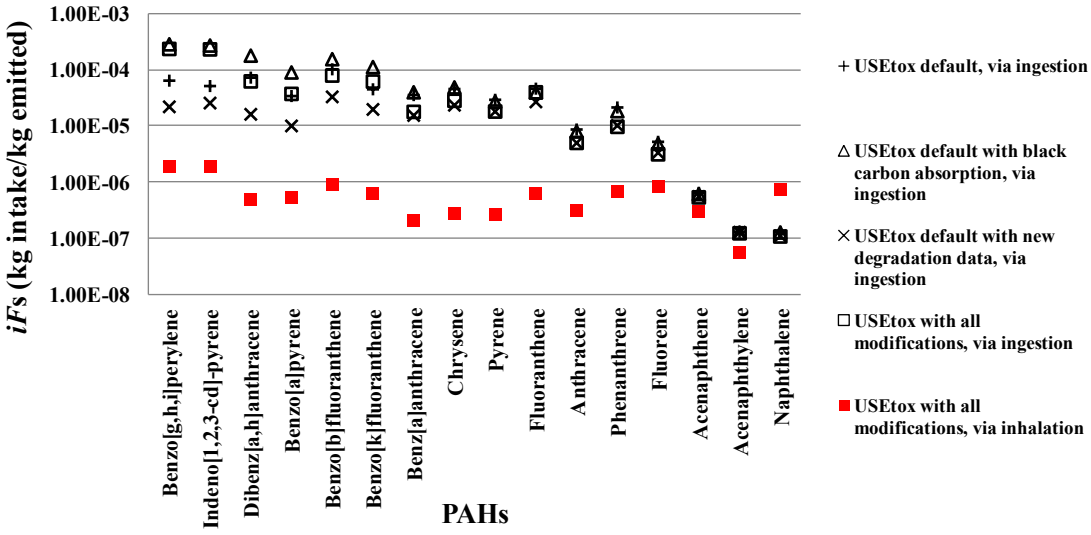

Fig. A5.1 Intake fractions (*iF*s, kgintake/kgemitted) from emission to rural air of the 16 PAHs ordered in decreasing *Kow/Koa* (from left to right) calculated by USEtox under different scenarios.

Accounting for photolysis alone reduces ingestion *iF*s by 36% - 78% for all PAHs except for acenaphthene, acenaphthylene, and naphthalene, which only have reductions of 2% - 15% (Fig. A5.1). Since photolysis generally gives a half-life much lower than biodegradation (Table S2 in ESM), the residence time in water for PAHs decreases up to seven-fold after adding photolysis. This explains the decreases in the *iF*s. On the contrary, accounting for black carbon adsorption alone results in 1.5- to 5.3-fold higher ingestion *iF*s for benzo[g,h,i]perylene, indeno[1,2,3-cd]-pyrene, dibenz[a,h]anthracene, benzo[a]pyrene, benzo[b]fluoranthene, and benzo[k]fluoranthene (Fig. 1). The inclusion of black carbon adsorption lowers the gaseous/dissolved fractions of PAHs and reduces the photo-oxidation rates in air and photolysis rates in both air and water. For water, the increased adsorption to black carbon also increases PAHs dry deposition from air and net sedimentation in water. In

addition, the bioavailability of PAHs in water decreases after adsorbing to black carbon and lowers the *iF*s of relevant pathways (drinking water, fish consumption, etc.). However, the major contributor to the ingestion *iF*s is exposed produce (grain, vegetables, etc.), which is directly related to the PAHs in air, so the reduction of *iF*s in water related pathways does not affect the overall *iF*s significantly.

Overall, when accounting for photolysis and black carbon (USEtox with all modifications in Fig. 1), the *iF*s via ingestion are not substantially changed for the PAHs with three rings or less, but *iFs* are increased by up to 350% for the most lipophilic PAHs. Considering both modifications, *iF*s of the 16 PAHs via inhalation vary from 5.6×10^{-8} $kg_{intake}/kg_{emitted}$ for acenaphthylene to 1.9×10^{-6} $kg_{intake}/kg_{emitted}$ for indeno[1,2,3-cd]-pyrene. Except for fluorene, acenaphthene, acenaphthylene, and naphthalene, *iF*s via ingestion are higher by one to two orders of magnitude than via inhalation, and span more than three orders of magnitude. Results from different USEtox scenarios show similar trends among the 16 PAHs (Fig. A5.1).

The variations of *iF*s among the different model scenarios can be explained by the influences from photolysis inclusion and black carbon adsorption as a function of the fractions in gaseous/dissolved phases and of the half-lives for each PAH in air and water. The inclusion of photolysis has a direct decreasing effect on the half-lives of PAHs but this effect is interactive with the fraction gaseous/dissolved phase that is also affected by the black carbon adsorption. For PAHs with low *Koa* and *Kow*, the inclusion of black carbon adsorption decreases their gaseous phase fraction by only less than 1% and decreases their fractions in dissolved phase by 7% - 34%, and thus has little influence on their *iF*s. On the contrary, accounting for black carbon adsorption strongly affects the fate of PAHs with high *Koa* and *Kow*: Fractions in gaseous phase decrease by as much as 98% and fractions in dissolved phase decrease

by 48% - 79%. This in turn inhibits their degradation processes, extending their persistency in the environment, and thus increases their *iF*s. For example, taking the black carbon adsorption effect into account reduces the fraction of benzo[g,h,i]perylene in the gaseous phase in air from 87% to 1.8% and its fraction in dissolved phase from 27% to 5.6%, resulting in a 4.4 fold increase in its *iF*.

The *iF*s from emission to urban air are also calculated and range from 1.1×10^{-5} to 2.5×10^{-5} $kg_{intake}/kg_{emitted}$ (Table A5.1). These are one to three orders of magnitude higher than the inhalation *iF*s for emission to rural air. The significant increases of inhalation *iF*s for urban areas make inhalation an exposure pathway comparable to ingestion for PAHs with high *Kow* and the dominant pathway for PAHs with low *Kow*. The comparison between this study and the IMPACT 2002 and USES-LCA models show very similar trends and a consistent relative ranking in *iFs* between the three models. For the inhalation *iF*s of PAHs, the three models are in relatively good agreement with each other. For ingestion, results from this study are generally higher by one order of magnitude than those from USES-LCA, while IMPACT 2002 provides systematically higher values due to differences in the vegetation modeling. Details can be found in Fig. S1 of the ESM.

A5.3.2 Carcinogenic effect factors

The updated cancer effect factor (*EF*) for benzo[a]pyrene of 73 cases/$kg_{intake,}$ based on epidemiological data, is 61 times higher than the default USEtox cancer *EF* of 1.2 cases/kg_{intake}, which is based on animal toxicity data. By applying the *TEF*s, the proposed cancer *EF*s for the 16 PAHs ranged from 7.3×10^{-2} to 73 cases/kg_{intake} (Table A5.1). Although the *TEF* of dibenz[a,h]anthracene was assigned as 1 by U.S. EPA (1993) and widely employed among worldwide regulatory guidance (Jennings 2012), Nisbet and LaGoy (1992) proposed a higher value of 5. Moreover, U.S. EPA

recommended a value of 10 of *TEF* for dibenz[a,h]anthracene and a set of varying *TEF*s for other PAHs in a recent report (U.S. EPA 2010) (this report is still in external review status and we therefore do not use it as our base scenario). Also, U.S. EPA (2010) reported a higher *TEF* for benzo[b]flourene (value of 0.8) and a lower *TEF* for benzo[k]flourene (value of 0.03). A sensitivity study is performed to investigate *EF* responses to the change of the *TEF*s. Increasing the *TEF* for dibenz[a,h]anthracene indirectly leads to a decrease of the relative importance of benzo[a]pyrene when accounting for PAH emission profiles from coke ovens that underlie the epidemiological data. This results in a decrease in the *EF* of benzo[a]pyrene from 73 to 54 cases/kg_{intake} (-26%) with *TEF* values given by Nisbet and LaGoy (1992) and to 27 cases/kg_{intake} (-63%) with *TEF* values given by U.S. EPA (2010). The sensitivity to dibenz[a,h]anthracene *TEF* is of special interest: Changing only dibenz[a,h]anthracene *TEF* from 1 to 5 or 10 only results in an increase of the impact per kg dibenz[a,h]anthracene intake by 268% and 505% due to the parallel decrease in the reference *EF* for benzo[a]pyrene. When dibenz[a,h]anthracene *TEF* is changed to 10 and the other PAHs *TEF*s are also changed to U.S. EPA (2010), the impact per kg dibenz[a,h]anthracene intake only increases by 274% compared to U.S. EPA (1993).

A5.3.3 Health impacts per kg emitted of individual PAHs

Combining *iF*s and *EF*s enables us to analyze the cancer cases per kg emitted for the individual PAHs, or the so-called characterization factors (Fig. A5.2). Default characterization factors are only shown for PAHs for which cancer effect data are readily available in the USEtox database. The influence of black carbon adsorption and photolysis on these characterization factors corresponds to the patterns of *iF*s via ingestion from emission to rural air, confirming that ingestion is the major exposure

route for rural emissions. For benzo[a]pyrene, the increases in *iF*s and *EF*s lead to a final characterization factor 66 times higher than the default 4.1×10^{-5} cancer cases/kg benzo[a]pyrene emitted. For naphthalene, the modifications in both fate and *EF* result in a characterization factors increased by 17% compared to its default value.

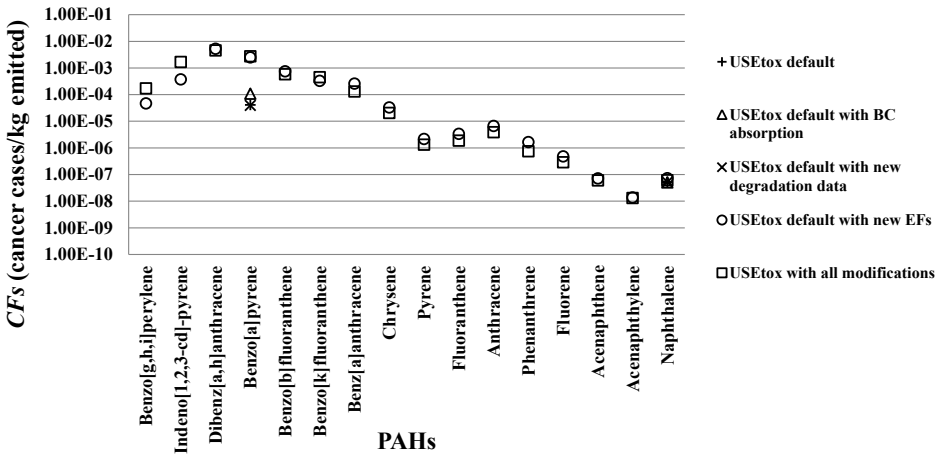

Fig. A5.2 Characterization factors (*CF*s, cancer cases/kgemitted) for emissions to rural air of the 16 PAHs ordered in decreasing *Kow/Koa* (from left to right) calculated by USEtox under different scenarios. In its default version USEtox has carcinogenic characterization factors only for benzo[a]pyrene and naphthalene.

Table A5.1 Intake fractions, effect factors and characterization factors calculated by USEtox with all modifications.

PAHs	Intake fractions [a] ($kg_{intake}/kg_{emitted}$)			Effect factors [b, c] ($cases/kg_{intake}$)		Characterization factors [d] ($cases/kg_{emitted}$)	
	Inhalation		Ingestion	Cancer	Non-cancer	Rural	Urban
	Rural	Urban					
B[ghi]Pe	1.9E-06	2.5E-05	2.3E-04	7.3E-01	n/a	1.7E-04	1.8E-04
I[cd]P	1.9E-06	2.5E-05	2.3E-04	7.3E+00	n/a	1.7E-03	1.8E-03
dB[ah]An	4.9E-07	2.1E-05	6.3E-05	7.3E+01	n/a	4.6E-03	5.4E-03
B[a]P	5.3E-07	2.2E-05	3.7E-05	7.3E+01	n/a	2.7E-03	3.9E-03
B[b]F	9.0E-07	2.3E-05	8.1E-05	7.3E+00	n/a	6.0E-04	6.9E-04
B[k]F	6.3E-07	2.2E-05	6.2E-05	7.3E+00	n/a	4.5E-04	5.6E-04
B[a]An	2.0E-07	1.8E-05	1.8E-05	7.3E+00	n/a	1.3E-04	2.3E-04
Cry	2.8E-07	1.9E-05	2.8E-05	7.3E-01	n/a	2.1E-05	3.1E-05
P	2.6E-07	1.9E-05	1.8E-05	7.3E-02	6.0E-03	1.3E-06	2.4E-06
F	6.3E-07	2.2E-05	4.2E-05	7.3E-02	3.6E-03	3.1E-06	4.3E-06
An	3.2E-07	2.0E-05	4.9E-06	7.3E-01	4.5E-04	3.8E-06	1.8E-05
Ph	6.7E-07	2.2E-05	1.0E-05	7.3E-02	n/a	7.8E-07	2.3E-06
Fl	8.4E-07	2.3E-05	3.2E-06	7.3E-02	3.6E-03	2.9E-07	1.9E-06
Ace	2.9E-07	2.0E-05	5.5E-07	7.3E-02	2.6E-03	6.1E-08	1.5E-06
Acy	5.6E-08	1.1E-05	1.3E-07	7.3E-02	n/a	1.3E-08	8.0E-07

Nap	7.2E-07	2.3E-05	1.1E-07	7.3E-02	7.2E-02	6.1E-08	1.7E-06

[a] The intake fractions via ingestion from emission to urban air is within 30% deviation from the intake fractions via ingestion from emission to rural air, therefore only the intake fraction via inhalation from emission to urban air are shown.
[b] The effect factors for inhalation and ingestion is considered the same when more specific experimental values are not available according to Rosenbaum et al. (2008).
[c] For naphthalene, the non-carcinogenic effect factor for ingestion is 1.3E-2 cases/kg_{intake} based on experiments.
[d] Only carcinogenic effect is accounted.

A5.3.4 Health impact: Application to mixture and specific emission profiles

Figure 3 shows that benzo[a]pyrene and dibenz[a,h]anthracene have a major contribution to the total characterization factors (58% – 91%) for the aluminum production, straw combustion, wood combustion, sawdust briquettes combustion, and unspecified sources derived from worldwide PAH emissions. The large contribution of benzo[k]fluoranthene for kerosene combustion is due to the high percentage of benzo[k]fluoranthene in the PAH emission from kerosene combustion (10.8%) and its relatively high *TEF* (0.1). Results for *CF*s are not very sensitive to the variation in *TEF*s from 1 to 10 for dibenz[a,h]anthracene nor from the variation from 0.1 to 0.8 for benzo[b]fluoranthene (details shown in Table A5.2). A more detailed analysis of 205 countries and regions PAH mixtures can be found in Fig. S2 in the ESM and Table S9.

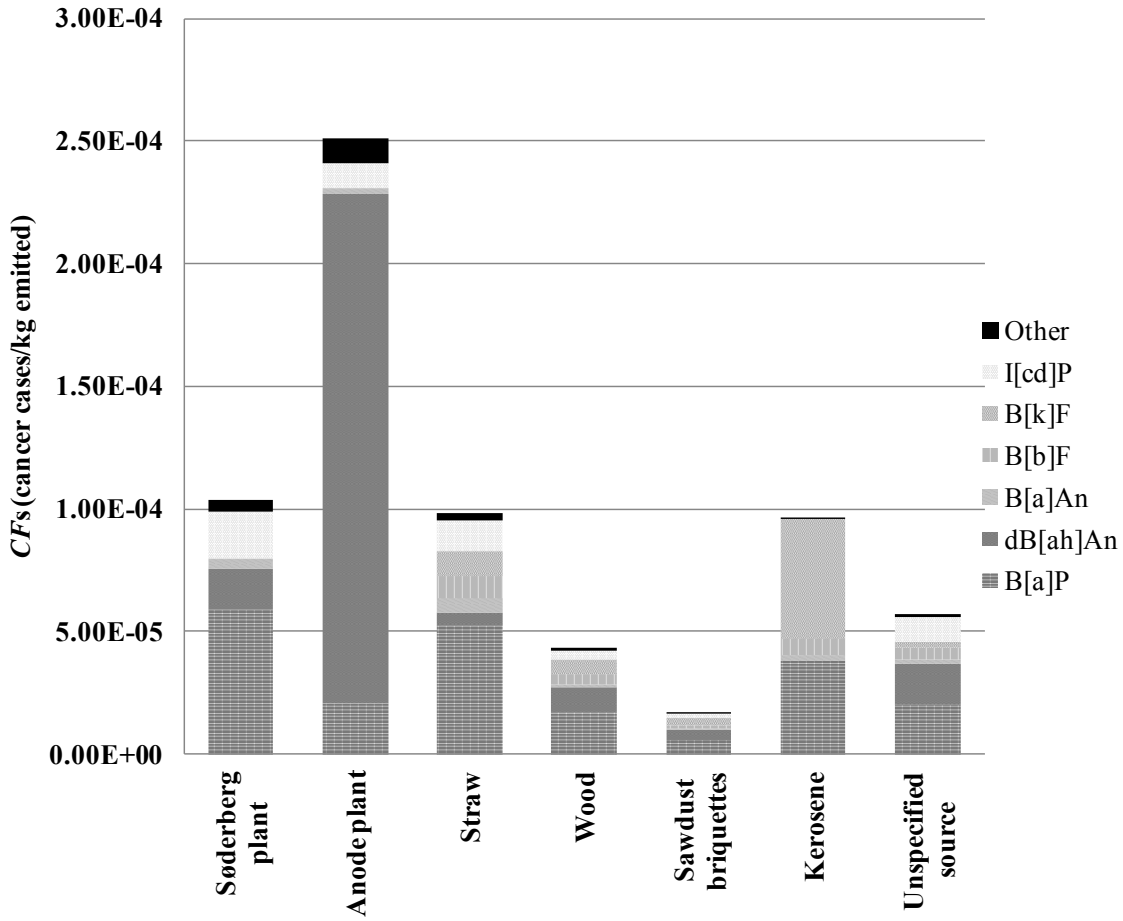

Fig. A5.3 Characterization factors (*CF*s, cancer cases/kg$_{emitted}$) calculated by USEtox for the emission of 16 PAH mixtures from aluminum production, domestic combustion, and worldwide emission (unspecified source).

Comparing various sources only based on their impacts per kg$_{emitted}$ as described by the *CF*s may however be misleading, since overall quantities of PAHs emitted to meet a given function (production of a functional unit of one ton aluminum or of one MJ domestic heat) could depend on the considered sources. Figure 4 shows the impacts of a) aluminum production and b) domestic combustion on this functional basis. Although the *CF* for the PAH mixture of the anode plant is 101% higher than that of the Søderberg plant, the mass of the PAH mixture emitted per ton of aluminum produced is 69% lower and the resulting impact of PAHs per ton of aluminum produced by anode plant is only 64% of the Søderberg plant. For domestic combustion, straw combustion has much higher impact per MJ heat produced, even if

its *CF* is of the same order of magnitude as other fuels. This is because of a low heat value and a much higher overall mass of PAHs emitted (detailed calculations in Table S5 in the ESM).

Table A5.2 Sensitivity of *CF*s to *TEF* value for PAHs mixtures from USEtox.

Products/regions	Sources	*CF*s [a] (cases/$kg_{emitted}$)	*CF*s for sensitivity study 1 [b] (cases/$kg_{emitted}$)	*CF*s for sensitivity study 2 [c] (cases/$kg_{emitted}$)
Aluminum production	Søderberg plant	1.04E-04	1.25E-04	1.12E-04
	Anode plant	2.51E-04	7.97E-04	8.01E-04
Domestic combustion	Straw	9.80E-05	8.76E-05	8.30E-05
	Wood	4.33E-05	6.23E-05	7.05E-05
	Sawdust briquettes	1.67E-05	2.46E-05	2.43E-05
	Kerosene	9.64E-05	7.09E-05	5.26E-05
Worldwide	Various	5.73E-05	8.93E-05	8.98E-05

[a] (U.S. EPA 1993). [b] (Nisbet and Lagoy 1992). [c] (U.S. EPA 2010)

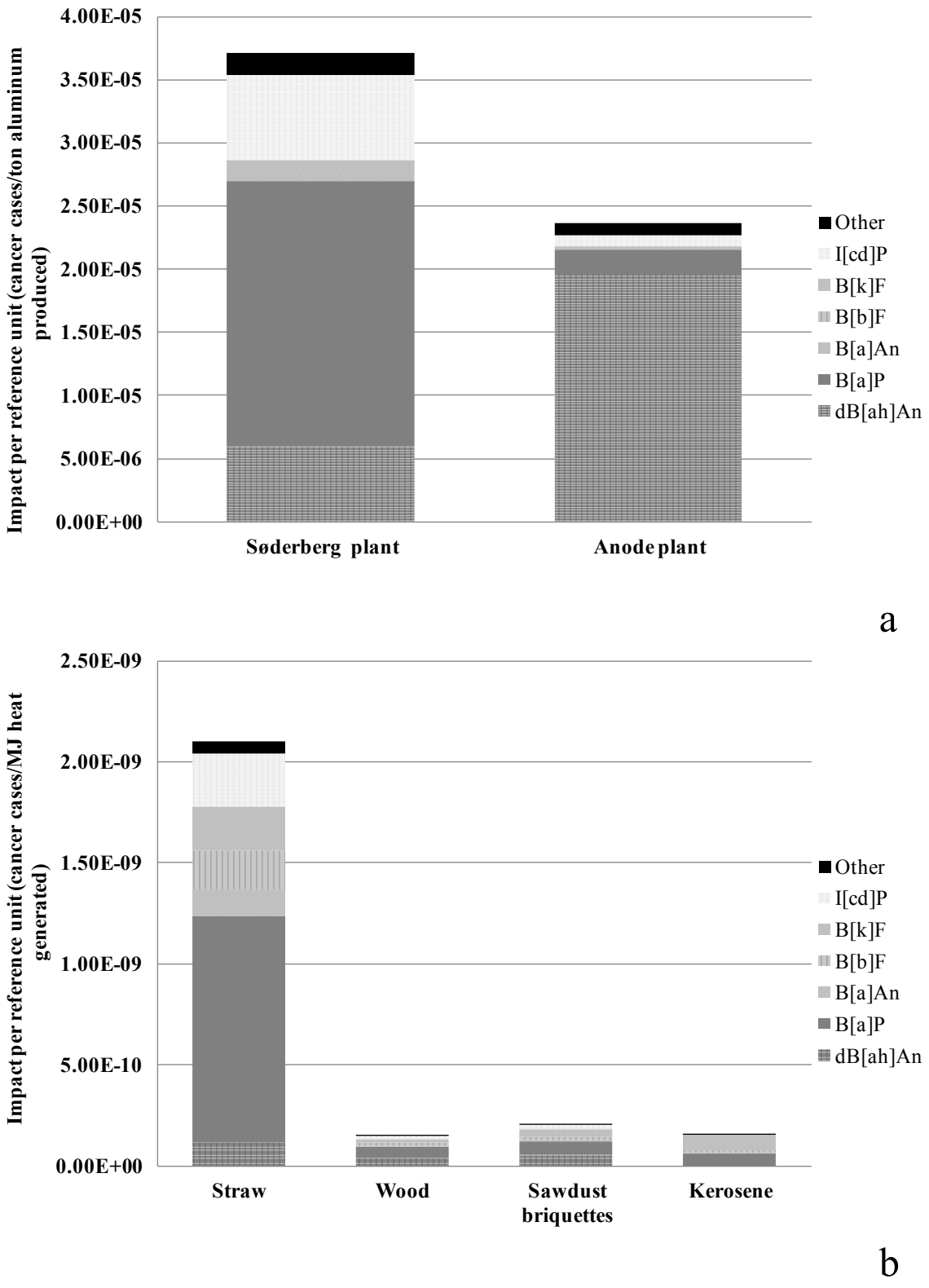

Fig. A5.4 Impacts per reference unit calculated by USEtox for the emission of 16 PAH mixture from a) aluminum production (cancer cases per kg production); and b) domestic combustion (cancer cases per MJ production).

The high percentages of dibenz[a,h]anthracene and benzo[a]pyrene in the PAH mixture emitted from aluminum anode plant production resulted in much higher *CF*s

compared to the Söderberg plant, domestic combustion, and the PAH mixture emission from an unspecified worldwide source. Although having much lower effect factors due to lower *TEF*s, benzo[b]fluoranthene and benzo[k]fluoranthene still constitute a large part of the PAH mixture *CFs* from straw burning and kerosene burning. This shows the importance of identifying the emission profile of a PAH mixture to estimating its health impacts. When the specific emission profile cannot be obtained, the worldwide unspecified source of the PAH mixture can be used as a generic estimate of health impact for PAH mixture with a *CF* of 5.7×10^{-5} cancer cases/$kg_{emitted}$. Considering a global emission of 5.1×10^{8} kg PAH/year (Shen et al. 2013), we obtain a total burden of disease of PAH emitted to air of the order of magnitude of 30 000 cancer cases per year worldwide.

A5.3.5 Non-carcinogens

This study does not extend its scope to the exploration of non-carcinogenic effects in details. Based on the current non-carcinogenic *EF*s available in the USEtox database, the magnitude of non-carcinogenic *EF*s are comparable to the carcinogenic *EF*s for naphthalene (see Table A5.1). To examine the potential contribution of non-carcinogenic effects to the overall impact of PAH emissions, we introduce a severity factor which translates cases of diseases into Disability-Adjusted Life Year (DALY) for the *EF* according to Huijbregts et al. (2005). The carcinogenic effect of PAHs is induced respiratory cancer, therefore a severity factor of 16.5 DALY/case is applied (Huijbregts et al. 2005). As a sensitivity study, the generic severity factor of 2.7 DALY/case is applied to the non-carcinogenic effect of PAHs (Huijbregts et al. 2005). After applying the severity factors, the non-carcinogenic health impacts from PAHs with non-carcinogenic data are one to four orders of magnitude lower than their carcinogenic health impacts. Details can be found in Table S6 in the ESM.

A5.3.6 Case study

The results of the life cycle case study for one kg primary aluminum are presented in Figure 5. The overall human health impacts composite toxicity effects and health effects by primary/secondary particulate matters induced by the emission of various chemicals in the life cycle. More specifically, contributors of the toxicity effects are grouped into four categories, namely PAHs, other organics, and inorganics. While CML 2001 assigns 89% of the total human health impact to PAHs, this fraction was less than 1% for the other methods in this case study. Compared to the original USEtox results employed by IMPACT World +, the modifications made in this study increase the relative contribution of PAHs to the total impact from 0.002% (IMPACT World + with USEtox default) to 0.7% (IMPACT World + with USEtox modified). USEtox gives a much higher value of impact per kg emitted for arsenic and therefore the contribution of human health impacts by inorganics in IMPACT World + with USEtox default versus modified are 93% and 92%, respectively. In contrast, the ReCiPe suggests 36% of the total human health impacts are caused by toxicity induced by inorganics, while the rest are health effects by primary/secondary particulate matters.

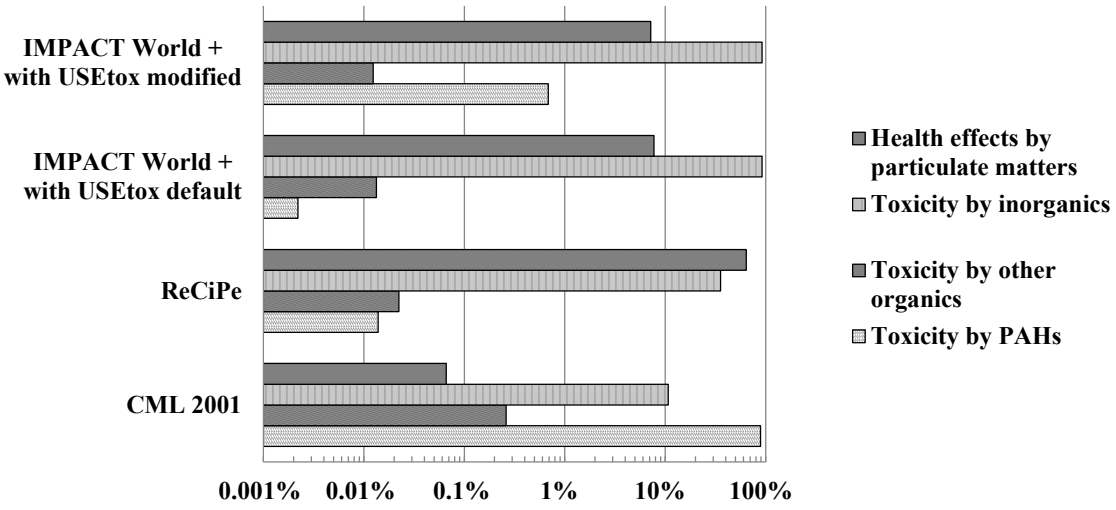

Fig. A5.5 Contributions from different categories to the total human health impacts of the life cycle case study for 1 kg primary aluminum estimated by CML 2001, ReCiPe, IMPACT World + with USEtox default, and IMPACT World + with USEtox modified.

A5.4 Discussion

A5.4.1 Factors influencing the intake fraction of PAHs

The differentiated effects of black carbon adsorption on the fate of PAH as a function of their physico-chemical properties are in agreement with previous studies (Hauck et al. 2007; Prevedouros et al. 2008; 2008). The intake fraction of benzo[a]pyrene via ingestion calculated in this study (3.7×10^{-5} $kg_{intake}/kg_{emitted}$) is in the lower end of the intake fraction ranges calculated based on monitored concentration in foods in the United States, aproximately 1.4×10^{-5} to 8.0×10^{-4} $kg_{intake}/kg_{emitted}$ (Kazerouni et al. 2001), and Europe, aproximately 7.0×10^{-5} to 1.8×10^{-3} $kg_{intake}/kg_{emitted}$ (Pennington et al. 2006).

In addition to black carbon, other particles related to PAH emissions (e.g. aluminum oxide in aluminum production) could also adsorb PAHs and further decrease their fractions in gaseous/dissolved phases and thus influence their intake fractions. There are limitations in estimating the photolysis half-lives in real world from values

obtained in experiments either in labs or outdoors. Detailed knowledge of the experimental values, light intensity, and longitude of locations of the experiments should be taken into consideration to adjust the estimates of real world photolysis half-lives if available. It should also be noted that in this study neither the role of dermal absorption or indoor exposure are considered.

The degradation of PAHs in vegetation could also play a critical role in human's exposure since the intake fraction via ingestion is dominated by exposed produce. Currently the USEtox model is extrapolating the vegetation degradation rate from the soil degradation rate. Several studies (Wild et al. 2005; Chen et al. 2010; 2011) tested the degradation of fluoranthene, anthracene, phenanthrene, and fluorene on plant surfaces and within plants and linked them with photodegradation. Substituting these measured values with the extrapolated vegetation degradation rates in the current USEtox model, the intake fractions via ingestion of fluoranthene, anthracene, phenanthrene, and fluorene decreased two to nine fold (Fig. S3 in ESM). It can, however, not be assumed that photolysis is the major factor in vegetation degradation for all PAHs. The four PAHs with measured degradation rates in vegetation are all with low *Kow*. The PAHs with much higher *Kow* may have a larger fraction transferred into the cellular structure, blocking the photolysis to a greater extent which is supported by the experimental values from Wild et al. (2005). Biodegradation within the plant may therefore be a dominant removal pathway for PAHs with high *Kow*.

A5.4.2 Effect factors for PAH mixtures.

Although benzo[a]pyrene is one of the most important PAH in terms of assessing the health impacts of PAH mixtures, benchmarking PAH mixtures' health impacts based on the concentrations of benzo[a]pyrene alone could lead to incomplete estimates

(Gibbs 1997; Armstrong et al. 2004; Armstrong and Gibbs 2009; Costantino et al. 1995). It is therefore essential to account for the full PAHs emission profile when interpreting results of epidemiological studies and translating them into health risk estimates for individual PAHs.

PAHs can react with oxidants (OH, NO_3, O_3) in the atmosphere and form nitrated PAHs (NPAHs), which are also recognized as carcinogens (Albinet et al. 2007; Huang et al. 2014). From the perspective of *TEF*s, some of the NPAHs may even be more toxic than their PAH precursors (RIDEM, 2008). This transformation of PAHs to NPAHs is not considered in the present study, similarly to the way other toxics are treated in most LCIA methods. To ensure that the human health impacts of PAH mixtures are not underestimated, further research is needed to characterize the fraction of each PAH degraded into its degradation compounds, as well as the fate, exposure and effect of these compounds.

A5.4.3 Importance of emission profile

As shown in this study, the intake fractions and effect factors of different PAH species vary by orders of magnitudes and therefore result in great variations in the health impacts of individual PAHs. It is important to acknowledge these differences when conducting LCIA practices. For example, although the anode plant emits much less PAHs in quantities than Søderberg plant for producing one ton of aluminum, the larger percentages of benzo[a]pyrene and dibenz[a,h]anthracene in the mixture make the overall impact of PAHs mixture higher and may counter the advantage of a lower emission to some extent. Mitigation strategies for reducing PAHs emissions should therefore focus on the dominant PAHs in priority.

We recommend for LCIA application that practitioners prioritize collection of information on the emission profile for the technology responsible for the PAHs main

emissions in order to apply individual PAH characterization factors. In cases where this is not possible, the practitioner may use in priority the generic world estimate for PAH mixtures of 5.7×10^{-5} cancer cases/$kg_{emitted.}$ The country specific *CF*s provided in Table S9 are primarily useful to assess the impacts of overall PAHs emissions for a given region (rather than source specific emissions) or to test the sensitivity of the generic world characterization factor to regional variations.

Finally, if the assessment method assigns the impact of benzo[a]pyrene to all PAHs - as does the CML 2001 method (Guinée 2001) - the health impact of PAHs could be highly overestimated and bias the overall impacts of product life cycle with PAH emissions.

A5.5 Conclusions

This study demonstrates the importance of including black carbon adsorption and photolysis in predicting the fate of PAHs, which have been neglected in LCIA practices. Employing these modifications leads to predictions closer to measured values of intake fractions for benzo[a]pyrene, showing its potential for other PAHs. This study also provides a method based on the Toxicity Equivalence Factors (*TEF*s) to incorporate the emission profile to the epidemiology data and shows the contributions of PAHs other than benzo[a]pyrene, especially dibenz[a,h]anthracene, benzo[b]fluoranthene, and benzo[k]fluoranthene, depending on the emission profile, are not negligible. Although the *TEF* values vary among different reports (U.S. EPA 1993; Nisbet and Lagoy 1992; U.S. EPA 2010), the resulting effect factors are much less variable once health effect is attributed to the whole mixture and not just to benzo[a]pyrene. This also means that it is essential both for LCIA and epidemiological studies to report emissions and concentrations not only for

benzo[a]pyrene but also for the other PAHs and at least for dibenz[a,h]anthracene, benzo[b]fluoranthene, and benzo[k]fluoranthene.

The new factors, especially the effect factors, proposed in this study lead to substantial changes for the health impacts of PAHs in LCIA results for aluminum and other products emitting PAHs during their production when compared to the default USEtox. Our health impacts estimate for PAH mixture falls intermediary between the CML 2001 and ReCiPe. This study offers a method that can assess the health impacts of all 16 individual PAHs. Combined with the knowledge of source-specific emission profiles of the product of interest, the health impacts of PAH mixtures can be evaluated more comprehensively and avoid biased results that are based solely on benzo[a]pyrene or total PAH emission quantities. Given the importance of emission profiles of PAH mixtures, we thus recommend future LCIA studies to include emissions of individual PAHs, and specifically of dibenz[a,h]anthracene, benzo[b]fluoranthene, and benzo[k]fluoranthene in addition to benzo[a]pyrene.

Electronic supplementary material

The electronic supplementary material contains the physico-chemical properties, degradation rates, *TEF*s, emission profiles of the 16 PAHs used in this study, results of the calculated degradation half-lives in air and water, comparison of *iF*s calculated in this study and from IMPACT 2002 and USES-LCA, sensitivity of the choice of *TEF*s, detailed implementation of black carbon adsorption model, and the calculation of unit risk for benzo[a]pyrene. In a separated excel file with the detailed calculation for the half-lives in air and water can be found.

Acknowledgments

This study was partially funded by the International Aluminium Institute. We would like to thank Eirik Nordheim, Marlen Bertram, Chris Bayliss, and Christian Leroy for their input regarding aluminum production and related PAH emission. We thank Philip Howard for his comments on the degradation rate calculations. We are also thankful for Shu Tao's help on the global PAH emissions data and discussion on partition behaviors of PAHs. We appreciate Alexi Ernstoff and Susan Csiszar's help in improving the English and content of the manuscript.

References

Oberdörster G, Oberdörster E, Oberdörster J. 2005. Nanotoxicology: an emerging discipline evolving from studies of ultrafine particles. Environmental Health Perspectives 113(7): 823-839.
Oberdorster G, Maynard A, Donaldson K, Castranova V, Fitzpatrick J, Ausman K, et al. 2005. Principles for characterizing the potential human health effects from exposure to nanomaterials: elements of a screening strategy. Particle and fibre toxicology 2: 8-8.
Nel A, Xia T, Madler L, Li N. 2006. Toxic potential of materials at the nanolevel. Science 311(5761): 622-627.
Smith DM, Simon JK, Baker Jr JR. 2013. Applications of nanotechnology for immunology. Nature Reviews Immunology 13(8): 592-605.
Chakrabarti MH, Brandon NP, Hajimolana SA, Tariq E, Yufit V, Hashim MA, et al. 2014. Application of carbon materials in redox flow batteries. J Power Sources 253: 150-166.
Chen H, Seiber JN, Hotze M. 2014. ACS select on nanotechnology in food and agriculture: A perspective on implications and applications. Journal of Agricultural and Food Chemistry 62(6): 1209-1212.
Irzhak A, Koledov V, Zakharov D, Lebedev G, Mashirov A, Afonina V, et al. 2014. Development of laminated nanocomposites on the bases of magnetic and non-magnetic shape memory alloys: Towards new tools for nanotechnology. J Alloy Compd 586: S464-S468.
Wijnhoven SWP, Peijnenburg WJGM, Herberts CA, Hagens WI, Oomen AG, Heugens EHW, et al. 2009. Nano-silver – a review of available data and knowledge gaps in human and environmental risk assessment. Nanotoxicology 3(2): 109-138.
Sayes CM, Wahi R, Kurian PA, Liu YP, West JL, Ausman KD, et al. 2006. Correlating nanoscale titania structure with toxicity: a cytotoxicity and inflammatory response study with human dermal fibroblasts and human lung epithelial cells. Toxicological Sciences 92(1): 174-185.
Warheit DB, Webb TR, Reed KL, Frerichs S, Sayes CM. 2007. Pulmonary toxicity study in rats with three forms of ultrafine-TiO2 particles: differential responses related to surface properties. Toxicology 230(1): 90-104.
Yu Y, Duan J, Yu Y, Li Y, Liu X, Zhou X, et al. 2014. Silica nanoparticles induce autophagy and autophagic cell death in HepG2 cells triggered by reactive oxygen species. Journal of hazardous materials 270: 176-186.
Lee S, Chung H, Kim S, Lee I. 2013. The genotoxic effect of ZnO and CuO nanoparticles on early growth of buckwheat, Fagopyrum Esculentum. Water Air and Soil Pollution 224(9).
Martinez Paino IM, Marangoni VS, Silva de Oliveira RdC, Greggi Antunes LM, Zucolotto V. 2012. Cyto and genotoxicity of gold nanoparticles in human hepatocellular carcinoma and peripheral blood mononuclear cells. Toxicology Letters 215(2): 119-125.

Wu W-T, Liao H-Y, Chung Y-T, Li W-F, Tsou T-C, Li L-A, et al. 2014. Effect of nanoparticles exposure on fractional exhaled nitric oxide (FENO) in workers exposed to nanomaterials. International journal of molecular sciences 15(1): 878-894.
Lee J, Chatterjee DK, Lee MH, Krishnan S. 2014. Gold nanoparticles in breast cancer treatment: Promise and potential pitfalls. Cancer letters 347(1): 46-53.
Walser T, Limbach LK, Brogioli R, Erismann E, Flamigni L, Hattendorf B, et al. 2012. Persistence of engineered nanoparticles in a municipal solid-waste incineration plant. Nature Nanotechnology 7(8): 520-524.
Sun TY, Gottschalk F, Hungerbuhler K, Nowack B. 2014. Comprehensive probabilistic modelling of environmental emissions of engineered nanomaterials. Environmental Pollution 185: 69-76.
Warheit DB, Sayes CM, Reed KL, Swain KA. 2008. Health effects related to nanoparticle exposures: environmental, health and safety considerations for assessing hazards and risks. Pharmacology & Therapeutics 120(1): 35-42.
Khanna I, Kumar A. 2014. Including nanoparticle mixtures in human health risk assessment. Integrated environmental assessment and management 10(1): 144-144.
Maynard AD. 2007. Nanotechnology: The next big thing, or much ado about nothing? Annals of Occupational Hygiene 51(1): 1-12.
Maynard AD, Warheit DB, Philbert MA. 2011. The New Toxicology of Sophisticated Materials: Nanotoxicology and Beyond. Toxicological Sciences 120: S109-S129.
Oberdorster G, Ferin J, Lehnert BE. 1994. Correlation between particle-size, in-vivo particle persistence, and lung injury. Environmental Health Perspectives 102: 173-179.
Maynard AD, Kuempel ED. 2005. Airborne nanostructured particles and occupational health. Journal of Nanoparticle Research 7(6): 587-614.
Shvedova AA, Kisin ER, Mercer R, Murray AR, Johnson VJ, Potapovich AI, et al. 2005. Unusual inflammatory and fibrogenic pulmonary responses to single-walled carbon nanotubes in mice. American Journal of Physiology-Lung Cellular and Molecular Physiology 289(5): L698-L708.
Oberdörster G, Sharp Z, Atudorei V, Elder A, Gelein R, Lunts A, et al. 2002. Extrapulmonary translocation of ultrafine carbon particles following whole-body inhalation exposure of rats. Journal of Toxicology and Environmental Health, Part A 65(20): 1531-1543.
Nemmar A, Hoet PHM, Vanquickenborne B, Dinsdale D, Thomeer M, Hoylaerts MF, et al. 2002. Passage of inhaled particles into the blood circulation in humans. Circulation 105(4): 411-414.
Semmler M, Seitz J, Erbe F, Mayer P, Heyder J, Oberdorster G, et al. 2004. Long-term clearance kinetics of inhaled ultrafine insoluble iridium particles from the rat lung, including transient translocation into secondary organs. Inhalation Toxicology 16(6-7): 453-459.
He X, Zhang H, Ma Y, Bai W, Zhang Z, Lu K, et al. 2010. Lung deposition and extrapulmonary translocation of nano-ceria after intratracheal instillation. Nanotechnology 21(28).
Geraets L, Oomen AG, Schroeter JD, Coleman VA, Cassee FR. 2012. Tissue Distribution of Inhaled Micro- and Nano-sized Cerium Oxide Particles in Rats: Results From a 28-Day Exposure Study. Toxicological Sciences 127(2): 463-473.

Aalapati S, Ganapathy S, Manapuram S, Anumolu G, Prakya BM. 2014. Toxicity and bio-accumulation of inhaled cerium oxide nanoparticles in CD1 mice. Nanotoxicology 8(7): 786-798.
Bockmann J, Lahl H, Eckert T, Unterhalt B. 2000. Titanium blood levels of dialysis patients compared to healthy volunteers. Pharmazie 55(6): 468-468.
Kreyling WG, Semmler M, Erbe F, Mayer P, Takenaka S, Schulz H, et al. 2002. Translocation of ultrafine insoluble iridium particles from lung epithelium to extrapulmonary organs is size dependent but very low. Journal of Toxicology and Environmental Health-Part A 65(20): 1513-1530.
Kreyling WG, Semmler-Behnke M, Seitz J, Scymczak W, Wenk A, Mayer P, et al. 2009. Size dependence of the translocation of inhaled iridium and carbon nanoparticle aggregates from the lung of rats to the blood and secondary target organs. Inhalation Toxicology 21 Suppl 1: 55-60.
Oberdörster G, Sharp Z, Atudorei V, Elder A, Gelein R, Kreyling W, et al. 2004. Translocation of inhaled ultrafine particles to the brain. Inhalation Toxicology 16(6-7): 437-445.
Elder A, Gelein R, Silva V, Feikert T, Opanashuk L, Carter J, et al. 2006. Translocation of inhaled ultrafine manganese oxide particles to the central nervous system. Environmental Health Perspectives 114(8): 1172-1178.
Moghimi SM, Hunter AC, Murray JC. 2001. Long-circulating and target-specific nanoparticles: theory to practice. Pharmacological Reviews 53(2): 283-318.
Liu MX, Li HF, Luo G, Liu QF, Wang YM. 2008. Pharmacokinetics and biodistribution of surface modification polymeric nanoparticles. Archives of Pharmacal Research 31(4): 547-554.
Krishnan K. 2007. Physiologically based pharmacokinetic and toxicokinetic models. In: Principles and Methods of Toxicology, Part 5th (Hayes AW, ed). Boca Raton:CRC press, 231-292.
Grillo JA, Zhao P, Bullock J, Booth BP, Lu M, Robie-Suh K, et al. 2012. Utility of a physiologically-based pharmacokinetic (PBPK) modeling approach to quantitatively predict a complex drug-drug-disease interaction scenario for rivaroxaban during the drug review process: implications for clinical practice. Biopharmaceutics & Drug Disposition 33(2): 99-110.
Lipscomb JC, Haddad S, Poet T, Krishnan K. 2012. Physiologically-based pharmacokinetic (PBPK) models in toxicity testing and risk assessment. Advances in experimental medicine and biology 745: 76-95.
Lu Y, Rieth S, Lohitnavy M, Dennison J, El-Masri H, Barton HA, et al. 2008. Application of PBPK modeling in support of the derivation of toxicity reference values for 1,1,1-trichloroethane. Regul Toxicol Pharmacol 50(2): 249-260.
Teorell T. 1937. Kinetics of distribution of substances administered to the body I The extravascular modes of administration. Archives Internationales De Pharmacodynamie Et De Therapie 57: 205-225.
Jain RK, Gerlowski LE, Weissbrod JM, Wang J, Pierson Jr RN. 1981. Kinetics of uptake, distribution, and excretion of zinc in rats. Annals of Biomedical Engineering 9(4): 347-361.
Gerlowski LE, Jain RK. 1983. Physiologically based pharmacokinetic modeling - principles and applications. Journal of Pharmaceutical Sciences 72(10): 1103-1127.
Ramsey JC, Andersen ME. 1984. A physiologically based description of the inhalation pharmacokinetics of styrene in rats and humans. Toxicology and Applied Pharmacology 73(1): 159-175.

Lin P, Chen JW, Chang LW, Wu JP, Redding L, Chang H, et al. 2008. Computational and ultrastructural toxicology of a nanoparticle, Quantum Dot 705, in mice. Environmental Science & Technology 42(16): 6264-6270.
Lee HA, Leavens TL, Mason SE, Monteiro-Riviere NA, Riviere JE. 2009. Comparison of quantum dot biodistribution with a blood-flow-limited physiologically based pharmacokinetic model. Nano Letters 9(2): 794-799.
Lankveld DPK, Oomen AG, Krystek P, Neigh A, Troost – de Jong A, Noorlander CW, et al. 2010. The kinetics of the tissue distribution of silver nanoparticles of different sizes. Biomaterials 31(32): 8350-8361.
Li M, Panagi Z, Avgoustakis K, Reineke J. 2012. Physiologically based pharmacokinetic modeling of PLGA nanoparticles with varied mPEG content. International Journal of Nanomedicine 7: 1345-1356.
Cho M, Cho W-S, Choi M, Kim SJ, Han BS, Kim SH, et al. 2009. The impact of size on tissue distribution and elimination by single intravenous injection of silica nanoparticles. Toxicology Letters 189(3): 177-183.
Wilhelm C, Gazeau F, Roger J, Pons JN, Bacri JC. 2002. Interaction of anionic superparamagnetic nanoparticles with cells: kinetic analyses of membrane adsorption and subsequent internalization. Langmuir 18(21): 8148-8155.
Luciani N, Gazeau F, Wilhelm C. 2009. Reactivity of the monocyte/macrophage system to superparamagnetic anionic nanoparticles. Journal of Materials Chemistry 19(35): 6373.
Wenger Y, Schneider RJ, Reddy GR, Kopelman R, Jolliet O, Philbert MA. 2011. Tissue distribution and pharmacokinetics of stable polyacrylamide nanoparticles following intravenous injection in the rat. Toxicology and Applied Pharmacology 251(3): 181-190.
Abbott LC, Maynard AD. 2010. Exposure assessment approaches for engineered nanomaterials. Risk Analysis 30(11): 1634-1644.
Li M, Al-Jamal KT, Kostarelos K, Reineke J. 2010. Physiologically based pharmacokinetic modeling of nanoparticles. ACS Nano 4(11): 6303-6317.
Cassee FR, van Balen EC, Singh C, Green D, Muijser H, Weinstein J, et al. 2011. Exposure, health and ecological effects review of engineered nanoscale cerium and cerium oxide associated with its use as a fuel additive. Critical Reviews in Toxicology 41(3): 213-229.
Lee JH, Kwon M, Ji JH, Kang CS, Ahn KH, Han JH, et al. 2011. Exposure assessment of workplaces manufacturing nanosized TiO(2) and silver. Inhalation Toxicology 23(4): 226-236.
Weinberg H, Galyean A, Leopold M. 2011. Evaluating engineered nanoparticles in natural waters. TrAC Trends in Analytical Chemistry 30(1): 72-83.
Zhang HF, He XA, Zhang ZY, Zhang P, Li YY, Ma YH, et al. 2011. Nano-CeO2 exhibits adverse effects at environmental relevant concentrations. Environmental Science & Technology 45(8): 3725-3730.
Panagi Z, Beletsi A, Evangelatos G, Livaniou E, Ithakissios DS, Avgoustakis K. 2001. Effect of dose on the biodistribution and pharmacokinetics of PLGA and PLGA-mPEG nanoparticles. International Journal of Pharmaceutics 221(1-2): 143-152.
Khlebtsov N, Dykman L. 2011. Biodistribution and toxicity of engineered gold nanoparticles: a review of in vitro and in vivo studies. Chemical Society Reviews 40(3): 1647.

Kuruppuarachchi M, Savoie H, Lowry A, Alonso C, Boyle RW. 2011. Polyacrylamide nanoparticles as a delivery system in photodynamic therapy. Molecular Pharmaceutics 8(3): 920-931.
Nel AE, Maedler L, Velegol D, Xia T, Hoek EMV, Somasundaran P, et al. 2009. Understanding biophysicochemical interactions at the nano-bio interface. Nature Materials 8(7): 543-557.
Lundqvist M, Stigler J, Elia G, Lynch I, Cedervall T, Dawson KA. 2008. Nanoparticle size and surface properties determine the protein corona with possible implications for biological impacts. Proceedings of the National Academy of Sciences of the United States of America 105(38): 14265-14270.
Mason RP, Moisey DM, Shajenko L. 1992. Cholesterol alters the binding of Ca-2+ channel blockers to the membrane lipid bilayer. Molecular Pharmacology 41(2): 315-321.
Demoy M, Andreux JP, Weingarten C, Gouritin B, Guilloux V, Couvreur P. 1999. Spleen capture of nanoparticles: influence of animal species and surface characteristics. Pharmaceutical Research 16(1): 37-41.
Moghimi SM. 2002. Chemical camouflage of nanospheres with a poorly reactive surface: towards development of stealth and target-specific nanocarriers. Biochimica Et Biophysica Acta-Molecular Cell Research 1590(1-3): 131-139.
Chithrani BD, Chan WC. 2007. Elucidating the mechanism of cellular uptake and removal of protein-coated gold nanoparticles of different sizes and shapes. Nano Letters 7(6): 1542-1550.
Keighron JD, Ewing AG, Cans A-S. 2012. Analytical tools to monitor exocytosis: a focus on new fluorescent probes and methods. Analyst 137(8): 1755-1763.
Smith EA, Prues SL, Oehme FW. 1996. Environmental degradation of polyacrylamides .1. Effects of artificial environmental conditions: temperature, light, and pH. Ecotoxicology and Environmental Safety 35(2): 121-135.
Smith EA, Prues SL, Oehme FW. 1997. Environmental degradation of polyacrylamides .2. Effects of environmental (outdoor) exposure. Ecotoxicology and Environmental Safety 37(1): 76-91.
Travlos GS. 2006. Normal structure, function, and histology of the bone marrow. Toxicologic Pathology 34(5): 548-565.
Brown RP, Delp MD, Lindstedt SL, Rhomberg LR, Beliles RP. 1997. Physiological parameter values for physiologically based pharmacokinetic models. Toxicology and Industrial Health 13(4): 407-484.
Bernareggi A, Rowland M. 1991. Physiologic modeling of cyclosporine kinetics in rat and man. Journal of Pharmacokinetics and Biopharmaceutics 19(1): 21-50.
Brookes M. 1967. Blood flow rates in compact and cancellous bone and bone marrow. Journal of Anatomy 101: 533-&.
McKone TE. 1993. The precision of QSAR methods for estimating intermedia transfer factors in exposure assessments. SAR and QSAR in environmental research 1(1): 41-51.
Yokel RA, Au TC, Macphail R, Hardas SS, Butterfield DA, Sultana R, et al. 2012. Distribution, elimination, and biopersistence to 90 Days of a systemically introduced 30 nm ceria-engineered nanomaterial in rats. Toxicological sciences : an official journal of the Society of Toxicology 127(1): 256-268.
Sadauskas E, Wallin H, Stoltenberg M, Vogel U, Doering P, Larsen A, et al. 2007. Kupffer cells are central in the removal of nanoparticles from the organism. Particle and fibre toxicology 4: 10.

Lang CH, Dobrescu C. 1991. Sepsis-induced increase in glucose-uptake by macrophage-rich tissues persist during hypoglycemia. Metabolism-Clinical and Experimental 40(6): 585-593.
Hyafil F, Cornily J-C, Feig JE, Gordon R, Vucic E, Amirbekian V, et al. 2007. Noninvasive detection of macrophages using a nanoparticulate contrast agent for computed tomography. Nature Medicine 13(5): 636-641.
Chithrani BD, Ghazani AA, Chan WCW. 2006. Determining the size and shape dependence of gold nanoparticle uptake into mammalian cells. Nano Letters 6(4): 662-668.
Alpini G, Phillips JO, Vroman B, Larusso NF. 1994. Recent advances in the isolation of liver-cells. Hepatology 20(2): 494-514.
Wilhelm C, Billotey C, Roger J, Pons JN, Bacri JC, Gazeau F. 2003. Intracellular uptake of anionic superparamagnetic nanoparticles as a function of their surface coating. Biomaterials 24(6): 1001-1011.
Robert D, Pamme N, Conjeaud H, Gazeau F, Iles A, Wilhelm C. 2011. Cell sorting by endocytotic capacity in a microfluidic magnetophoresis device. Lab on a Chip 11(11): 1902-1910.
Hardas SS, Butterfield DA, Sultana R, Tseng MT, Dan M, Florence RL, et al. 2010. Brain distribution and toxicological evaluation of a systemically delivered engineered nanoscale ceria. Toxicological Sciences 116(2): 562-576.
Walkey CD, Olsen JB, Guo HB, Emili A, Chan WCW. 2012. Nanoparticle size and surface chemistry determine serum protein adsorption and macrophage uptake. Journal of the American Chemical Society 134(4): 2139-2147.
Wang Y, Yuan L, Yao C, Ding L, Li C, Fang J, et al. 2014. A combined toxicity study of zinc oxide nanoparticles and vitamin C in food additives. Nanoscale 6(24): 15333-15342.
Choi S-J, Oh J-M, Choy J-H. 2009. Toxicological effects of inorganic nanoparticles on human lung cancer A549 cells. Journal of Inorganic Biochemistry 103(3): 463-471.
Kendall M, Holgate S. 2012. Health impact and toxicological effects of nanomaterials in the lung. Respirology 17(5): 743-758.
Wakefield G, Wu X, Gardener M, Park B, Anderson S. 2008. Envirox fuel-borne catalyst: Developing and launching a nano-fuel additive. Technology Analysis & Strategic Management 20(1): 127-136.
Thill A, Zeyons O, Spalla O, Chauvat F, Rose J, Auffan M, et al. 2006. Cytotoxicity of CeO2 nanoparticles for Escherichia coli. Physico-chemical insight of the cytotoxicity mechanism. Environmental Science & Technology 40(19): 6151-6156.
Yokel RA, Florence RL, Unrine JM, Tseng MT, Graham UM, Wu P, et al. 2009. Biodistribution and oxidative stress effects of a systemically-introduced commercial ceria engineered nanomaterial. Nanotoxicology 3(3): 234-248.
Li D, Johanson G, Emond C, Carlander U, Philbert M, Jolliet O. 2014. Physiologically based pharmacokinetic modeling of polyethylene glycol-coated polyacrylamide nanoparticles in rats. Nanotoxicology 8: 128-137.
Bachler G, von Goetz N, Hungerbuehler K. 2013. A physiologically based pharmacokinetic model for ionic silver and silver nanoparticles. International Journal of Nanomedicine 8: 3365-3382.
Bakrania SD, Perez C, Wooldridge MS. 2007a. Methane-assisted combustion synthesis of nanocomposite tin dioxide materials. Proceedings of the Combustion Institute 31: 1797-1804.

Bakrania SD, Miller TA, Perez C, Wooldridge MS. 2007b. Combustion of multiphase reactants for the synthesis of nanocomposite materials. Combustion and Flame 148(1-2): 76-87.
Miller TA, Bakrania SD, Perez C, Wooldridge MS. 2005. A new method for direct preparation of tin dioxide nanocomposite materials. Journal of Materials Research 20(11): 2977-2987.
Hall DL, Wang AA, Joy KT, Miller TA, Wooldridge NS. 2004. Combustion synthesis and characterization of nanocrystalline tin and tin oxide (SnOx, x=0-2) particles. Journal of the American Ceramic Society 87(11): 2033-2041.
U.S. EPA. 1999. Reference Method for the Determination of Fine Particulate Matter as PM2.5 in the Atmosphere. EPA 40 CFR Pat 50. Washington DC.
Harkema J, Keeler G, Wagner J, Morishita M, Timm E, Hotchkiss J, et al. 2004. Effects of inhaled urban air particulates on normal and hypersecretory airways in rats. (Health Effects Institute Research Report 120). Boston MA:Health Effects Institute.
Morishita M, Keeler GJ, Wagner JG, Marsik FJ, Timm EJ, Dvonch JT, et al. 2004. Pulmonary retention of particulate matter is associated with airway inflammation in allergic rats exposed to air pollution in urban Detroit. Inhalation Toxicology 16(10): 663-674.
Badireddy AR, Budarz JF, Marinakos SM, Chellam S, Wiesner MR. 2014. Formation of Silver Nanoparticles in Visible Light-Illuminated Waters: Mechanism and Possible Impacts on the Persistence of AgNPs and Bacterial Lysis. Environmental Engineering Science 31(7): 338-349.
Rancan F, Nazemi B, Rautenberg S, Ryll M, Hadam S, Gao Q, et al. 2014. Ultraviolet radiation and nanoparticle induced intracellular free radicals generation measured in human keratinocytes by electron paramagnetic resonance spectroscopy. Skin Research and Technology 20(2): 182-193.
Takenaka S, Karg E, Roth C, Schulz H, Ziesenis A, Heinzmann U, et al. 2001. Pulmonary and systemic distribution of inhaled ultrafine silver particles in rats. Environmental Health Perspectives 109: 547-551.
Hofmann W, Asgharian B. 2003. The effect of lung structure on mucociliary clearance and particle retention in human and rat lungs. Toxicological Sciences 73(2): 448-456.
Yang W, Peters JI, Williams RO, III. 2008. Inhaled nanoparticles - A current review. International Journal of Pharmaceutics 356(1-2): 239-247.
Shakweh M, Ponchel G, Fattal E. 2004. Particle uptake by Peyer's patches: a pathway for drug and vaccine delivery. Expert opinion on drug delivery 1(1): 141-163.
Sao R, Vaish R, Sinha N. 2015. Multifunctional Drug Delivery Systems Using Inorganic Nanomaterials: A Review. Journal of Nanoscience and Nanotechnology 15(3): 1960-1972.
Willhite CC, Karyakina NA, Yokel RA, Yenugadhati N, Wisniewski TM, Arnold IMF, et al. 2014. Systematic review of potential health risks posed by pharmaceutical, occupational and consumer exposures to metallic and nanoscale aluminum, aluminum oxides, aluminum hydroxide and its soluble salts. Critical Reviews in Toxicology 44: 1-80.
Arnot JA, Mackay D, Webster E, Southwood JM. 2006. Screening level risk assessment model for chemical fate and effects in the environment. Environmental Science & Technology 40(7): 2316-2323.

Rosenbaum RK, Bachmann TM, Gold LS, Huijbregts MAJ, Jolliet O, Juraske R, et al. 2008. USEtox-the UNEP-SETAC toxicity model: recommended characterisation factors for human toxicity and freshwater ecotoxicity in life cycle impact assessment. International Journal of Life Cycle Assessment 13(7): 532-546.
Wambaugh JF, Setzer RW, Reif DM, Gangwal S, Mitchell-Blackwood J, Arnot JA, et al. 2013. High-Throughput Models for Exposure-Based Chemical Prioritization in the Expo Cast Project. Environmental Science & Technology 47(15): 8479-8488.
Liu H, Yang X, Xu H. 2002. Advances in studies on Erigeron breviscapus. Chinese Traditional and Herbal Drugs 33(6): 566-568.
Trickler WJ, Lantz SM, Murdock RC, Schrand AM, Robinson BL, Newport GD, et al. 2010. Silver Nanoparticle Induced Blood-Brain Barrier Inflammation and Increased Permeability in Primary Rat Brain Microvessel Endothelial Cells. Toxicological Sciences 118(1): 160-170.
Choi J-S, Cao J, Naeem M, Noh J, Hasan N, Choi H-K, et al. 2014. Size-controlled biodegradable nanoparticles: Preparation and size-dependent cellular uptake and tumor cell growth inhibition. Colloids and Surfaces B: Biointerfaces 122(0): 545-551.
Tabata Y, Ikada Y. 1988. EFFECT OF THE SIZE AND SURFACE-CHARGE OF POLYMER MICROSPHERES ON THEIR PHAGOCYTOSIS BY MACROPHAGE. Biomaterials 9(4): 356-362.
Champion JA, Walker A, Mitragotri S. 2008. Role of particle size in phagocytosis of polymeric microspheres. Pharmaceutical Research 25(8): 1815-1821.
Despopoulos A, Silbernagl S. 2003. Color atlas of physiology. Stuttgart ; New York: Thieme.
Li J, Zhang G, Li XD, Qi SH, Liu GQ, Peng XZ. 2006. Source seasonality of polycyclic aromatic hydrocarbons (PAHs) in a subtropical city, Guangzhou, South China. Sci Total Environ 355(1-3): 145-155.
IARC. 2010. Some Non-heterocyclic Polycyclic Aromatic Hydrocarbons and Some Related Exposures. Lyon: International Agency for Research on Cancer.
Kohler M, Künniger T. 2003. Emissions of polycyclic aromatic hydrocarbons (PAH) from creosoted railroad ties and their relevance for life cycle assessment (LCA). Holz als Roh-und werkstoff 61(2): 117-124.
Andersen J, Shier D. 2009. The green guide to specification: an environmental profiling system for building materials and components. Bracknell: HIS BRE Press.
Amienyo D, Gujba H, Stichnothe H, Azapagic A. 2013. Life cycle environmental impacts of carbonated soft drinks. The International Journal of Life Cycle Assessment 18(1): 77-92.
Guinée J. 2001. Handbook on life cycle assessment—operational guide to the ISO standards. The International Journal of Life Cycle Assessment 6(5): 255-255.
Howard PH, Boethling RS, Jarvis WF, Meylan WM, Michalenko EM. 1991. Handbook of environmental degradation rates. Boca Raton: CRC press.
Mackay D, Shiu WY, Ma KC, Lee SC. 2006. Polynuclear Aromatic Hydrocarbons (PAHs) and Related Aromatic Hydrocarbons. In: Handbook of Physical-Chemical Properties and Environmental Fate for Organic Chemicals, Vol. 1, Part 2nd. Boca Raton:CRC press, 617-919.
U.S. EPA. 2009. Estimation Programs Interface Suite™ for Microsoft® Windows. Washington, DC.

Lang C, Tao S, Wang XJ, Zhang G, Li J, Fu JM. 2007. Seasonal variation of polycyclic aromatic hydrocarbons (PAHs) in Pearl River Delta region, China. Atmos Environ 41(37): 8370-8379.
Prevedouros K, Brorstrom-Lunden E, Halsall CJ, Jones KC, Lee RGM, Sweetman AJ. 2004. Seasonal and long-term trends in atmospheric PAH concentrations: Evidence and implications. Environ Pollut 128(1-2): 17-27.
Hauck M, Huijbregts MAJ, Koelmans AA, Moermond CTA, van den Heuvel-Greve MJ, Veltman K, et al. 2007. Including sorption to black carbon in modeling bioaccumulation of polycyclic aromatic hydrocarbons: Uncertainty analysis and comparison to field data. Environmental Science & Technology 41(8): 2738-2744.
Armitage JM, Cousins IT, Persson NJ, Gustafsson O, Cornelissen G, Saloranta T, et al. 2008. Black carbon-inclusive modeling approaches for estimating the aquatic fate of dibenzo-p-dioxins and dibenzofurans. Environmental Science & Technology 42(10): 3697-3703.
Prevedouros K, Palm-Cousins A, Gustafsson O, Cousins IT. 2008. Development of a black carbon-inclusive multi-media model: Application for PAHs in Stockholm. Chemosphere 70(4): 607-615.
Rosenbaum RK, Bachmann TM, Gold LS, Huijbregts MA, Jolliet O, Juraske R, et al. 2008. USEtox—the UNEP-SETAC toxicity model: recommended characterisation factors for human toxicity and freshwater ecotoxicity in life cycle impact assessment. The International Journal of Life Cycle Assessment 13(7): 532-546.
Pennington DW, Margni M, Ammann C, Jolliet O. 2005. Multimedia fate and human intake modeling: Spatial versus nonspatial insights for chemical emissions in Western Europe. Environmental Science & Technology 39(4): 1119-1128.
Huijbregts MAJ, Thissen U, Guinee JB, Jager T, Kalf D, van de Meent D, et al. 2000. Priority assessment of toxic substances in life cycle assessment. Part I: Calculation of toxicity potentials for 181 substances with the nested multi-media fate, exposure and effects model USES-LCA. Chemosphere 41(4): 541-573.
Rosenbaum RK, Huijbregts MAJ, Henderson AD, Margni M, McKone TE, van de Meent D, et al. 2011. USEtox human exposure and toxicity factors for comparative assessment of toxic emissions in life cycle analysis: sensitivity to key chemical properties. Int J Life Cycle Ass 16(8): 710-727.
WHO. 2000. Organic pollutants. In: Air quality guidelines for Europe, Part 2nd. Copenhagen:World Health Organization, 58-121.
Gibbs G. 1997. Estimating residential polycyclic aromatic hydrocarbon (PAH) related lung cancer risks using occupational data. Ann Occup Hyg 41(inhaled particles VIII): 49-53.
Armstrong B, Hutchinson E, Unwin J, Fletcher T. 2004. Lung cancer risk after exposure to polycyclic aromatic hydrocarbons: A review and meta-analysis. Environmental Health Perspectives 112(9): 970-978.
Armstrong BG, Gibbs G. 2009. Exposure-response relationship between lung cancer and polycyclic aromatic hydrocarbons (PAHs). Occup Environ Med 66(11): 740-746.
Pennington DW, Margni M, Payet J, Jolliet O. 2006. Risk and regulatory hazard-based toxicological effect indicators in life-cycle assessment (LCA). Hum Ecol Risk Assess 12(3): 450-475.
U.S. EPA. year. Priority pollutants. Available: http://water.epa.gov/scitech/methods/cwa/pollutants.cfm [accessed April 12 2013].

Jolliet O, Rosenbaum R, Chapman PM, McKone T, Margni M, Scheringer M, et al. 2006. Establishing a framework for life cycle toxicity assessment - Findings of the Lausanne review workshop. Int J Life Cycle Ass 11(3): 209-212.
Rosenbaum RK, Margni M, Jolliet O. 2007. A flexible matrix algebra framework for the multimedia multipathway modeling of emission to impacts. Environment International 33(5): 624-634.
Bennett DH, McKone TE, Evans JS, Nazaroff WW, Margni MD, Jolliet O, et al. 2002. Defining intake fraction. Environmental Science & Technology 36(9): 206a-211a.
Chen JW, Quan X, Yan Y, Yang FL, Peijnenburg WJGM. 2001. Quantitative structure-property relationship studies on direct photolysis of selected polycyclic aromatic hydrocarbons in atmospheric aerosol. Chemosphere 42(3): 263-270.
Hauck M, Huijbregts MAJ, Armitage JM, Cousins IT, Ragas AMJ, van de Meent D. 2008. Model and input uncertainty in multi-media fate modeling: Benzo[a]pyrene concentrations in Europe. Chemosphere 72(6): 959-967.
Ma YG, Lei YD, Xiao H, Wania F, Wang WH. 2010. Critical Review and Recommended Values for the Physical-Chemical Property Data of 15 Polycyclic Aromatic Hydrocarbons at 25 degrees C. J Chem Eng Data 55(2): 819-825.
Doucette WJ. 2000. Soil and sediment sorption coefficients. In: Handbook of Property Estimation Methods for Chemicals, (Boethling RS, Mackay D, eds). Boca Raton:CRC press, 141-188.
Lohmann R, Lammel G. 2004. Adsorptive and absorptive contributions to the gas-particle partitioning of polycyclic aromatic hydrocarbons: State of knowledge and recommended parametrization for modeling. Environmental Science & Technology 38(14): 3793-3803.
Koelmans AA, Jonker MTO, Cornelissen G, Bucheli TD, Van Noort PCM, Gustafsson O. 2006. Black carbon: The reverse of its dark side. Chemosphere 63(3): 365-377.
Gustafsson O, Bucheli TD, Kukulska Z, Andersson M, Largeau C, Rouzaud JN, et al. 2001. Evaluation of a protocol for the quantification of black carbon in sediments. Global Biogeochem Cy 15(4): 881-890.
Atkinson R. 1987. A Structure-Activity Relationship for the Estimation of Rate Constants for the Gas-Phase Reactions of Oh Radicals with Organic-Compounds. Int J Chem Kinet 19(9): 799-828.
Lane D, Katz M. 1977. The photomodification of benzo[a]pyrene, benzo[a]fluorantheme and benzo[k]fluoranthene under simulated atmospheric conditions. In: Fate of Pollutants in the Air and Water Environments, Part II, (Suffet I, ed). New York:Wiley - Interscience.
Schwarzenbach RP, Gschwend PM, Imboden DM. 2003. Direct Photolysis. In: Environmental Organic Chemistry, Part 2nd. New York:Wiley, 611-654.
Muel B, Saguem S. 1985. Determination of 23 Polycyclic Aromatic-Hydrocarbons in Atmospheric Particulate Matter of the Paris Area and Photolysis by Sunlight. Int J Environ an Ch 19(2): 111-131.
Fukuda K, Inagaki Y, Maruyama T, Kojima HI, Yoshida T. 1988. On the Photolysis of Alkylated Naphthalenes in Aquatic Systems. Chemosphere 17(4): 651-659.
Behymer TD, Hites RA. 1985. Photolysis of Polycyclic Aromatic-Hydrocarbons Adsorbed on Simulated Atmospheric Particulates. Environmental Science & Technology 19(10): 1004-1006.

Larson RA, Weber EJ. 1994. Reaction Mechanisms in Environmental Organic Chemistry. Boca Raton: CRC Press.
U.S. EPA. 1993. Provisional guidance for quantitative risk assessment of polycyclic aromatic hydrocarbons. EPA600/R93/089. Washington, DC.
Jennings AA. 2012. Worldwide regulatory guidance values for surface soil exposure to carcinogenic or mutagenic polycyclic aromatic hydrocarbons. J Environ Manage 110: 82-102.
Petry T, Schmid P, Schlatter C. 1996. The use of toxic equivalency factors in assessing occupational and environmental health risk associated with exposure to airborne mixtures of polycyclic aromatic hydrocarbons (PAHs). Chemosphere 32(4): 639-648.
Strunk P, Ortlepp K, Heinz H, Rossbach B, Angerer J. 2002. Ambient and biological monitoring of coke plant workers - determination of exposure to polycyclic aromatic hydrocarbons. International Archives of Occupational and Environmental Health 75(5): 354-358.
Yang X, Zheng J, Bai Y, Tian F, Yuan J, Sun J, et al. 2007. Using lymphocyte and plasma Hsp70 as biomarkers for assessing coke oven exposure among steel workers. Environmental Health Perspectives 115(11): 1573-1577.
Costantino JP, Redmond CK, Bearden A. 1995. Occupationally Related Cancer Risk among Coke-Oven Workers - 30 Years of Follow-Up. J Occup Environ Med 37(5): 597-604.
European Aluminium Association. 2008. Environmental Profile Report for the European Aluminium Industry. Brussels:European Aluminium Association.
Oanh NTK, Nghiem L, Phyu YL. 2002. Emission of polycyclic aromatic hydrocarbons, toxicity, and mutagenicity from domestic cooking using sawdust briquettes, wood, and kerosene. Environmental Science & Technology 36(5): 833-839.
Shen H, Huang Y, Wang R, Zhu D, Li W, Shen G, et al. 2013. Global atmospheric emissions of polycyclic aromatic hydrocarbons from 1960 to 2008 and future predictions. Environmental Science & Technology 47(12): 6415-6424.
The World Bank. year. World Development Indicators. Available: http://data.worldbank.org/indicator [accessed April 12 2013].
Goedkoop MJ, Heijungs R, Huijbregts MAJ, De Schryver A, Van Zelm R. 2008. First edition Report I: Characterisation. (A life cycle impact assessment method which comprises harmonised category indicators at the midpoint and the endpoint level
).ReCiPe.
Bulle C, Jolliet O, Humbert S, Rosenbaum R, Margni M. IMPACT World +: A new global regionalized life cycle impact assessment method. In: Proceedings of the International Conference on Ecobalance, 2012. Yokohama, Japan.
Frischknecht R, Jungbluth N, Althaus HJ, Doka G, Dones R, Heck T, et al. 2005. The ecoinvent database: Overview and methodological framework. Int J Life Cycle Ass 10(1): 3-9.
Nisbet ICT, Lagoy PK. 1992. Toxic Equivalency Factors (Tefs) for Polycyclic Aromatic-Hydrocarbons (Pahs). Regul Toxicol Pharm 16(3): 290-300.
U.S. EPA. 2010. Development of a Relative Potency Factor (RPF) Approach for Polycyclic Aromatic Hydrocarbon (PAH) Mixtures (External Review Draft). Washington, DC.
Huijbregts MAJ, Rombouts LJA, Ragas AMJ, van de Meent D. 2005. Human-toxicological effect and damage factors of carcinogenic and noncarcinogenic

chemicals for life cycle impact assessment. Integrated environmental assessment and management 1(3): 181-244.
Kazerouni N, Sinha R, Hsu CH, Greenberg A, Rothman N. 2001. Analysis of 200 food items for benzo[a]pyrene and estimation of its intake in an epidemiologic study. Food Chem Toxicol 39(5): 423-436.
Wild E, Dent J, Thomas GO, Jones KC. 2005. Real-time visualization and quantification of PAH photodegradation on and within plant leaves. Environmental Science & Technology 39(1): 268-273.
Chen L, Zhang Y, Liu BB. 2010. In situ simultaneous determination the photolysis of multi-component PAHs adsorbed on the leaf surfaces of living Kandelia candel seedlings. Talanta 83(2): 324-331.
Chen L, Wang P, Liu JB, Liu BB, Zhang Y, Zhang SZ, et al. 2011. In Situ Monitoring the Photolysis of Fluoranthene Adsorbed on Mangrove Leaves Using Fiber-Optic Fluorimetry. J Fluoresc 21(2): 765-773.